THE UNIVERSITY *of* EDINBURGH

Studying the Growth of Galaxies with JWST

T. W. Kemp

Doctor of Philosophy
The University of Edinburgh
October 2019

Lay Summary

Since the formation of the Universe, known as the Big Bang, the structure and contents of the Universe have changed dramatically. In the first 500 million years, the Universe went through a complex transitional phase from the smallest particles combining to begin building the objects that we recognise as stars and galaxies today. Initially, the Universe was a rapidly expanding hot mess of excited particles. Much work through simulations and observations has been done to try and track how these particles have evolved into the vast, dark empty space that we currently see today. We now know a significant amount of information about the structure of the Universe. An eclectic mix of billions of galaxies populates the Universe, with each of these galaxies containing billions of stars with orbiting planets.

To directly observe these objects, we need powerful telescopes both from the ground and from space. Technological advances have enabled us to observe these objects extremely far away when the Universe was younger and smaller. As light travels at a finite speed, the light we observe these objects show us how these galaxies actually were billions of years ago. The Hubble Space Telescope (*HST*) has observed a few hundred galaxies back to within 1 billion years of the Big Bang, while ground-based observations with Subaru, the Canda-France-Hawaii Telescope (CFHT) and the Visible and Infrared Survey Telescope for Astronomy (VISTA) have provided multi-wavelength observations of millions of galaxies. The dynamic range of the data has allowed the extensive study of the formation and evolution of galaxies across cosmic time.

The James Webb Space Telescope *(JWST* or *Webb)* is a large (6.5m primary mirror) infrared ($0.6 < \lambda < 30\mu$m) telescope, expected to launch in 2021. *JWST* provides the next step in delving further back than even *HST*. In this thesis, I asses the capabilities of *JWST* in studying galaxies to the highest redshift in an

attempt to uncover the most efficient method of observing and analysing galaxies through cosmic history. In particular, I investigate the capabilities of the Mid-InfaRed Instrument (MIRI) onboard *JWST*, and assess its ability to observe dusty star-forming galaxies in the young Universe. In order to accomplish this, I built a piece of software that can simulate *JWST* MIRI observations in all of the available observing modes. To contextualise this with current observations, we attempt to determine, in practice, how useful this may be by calculating the total number of galaxies we know of that MIRI will be vital in observing.

Abstract

The James Webb Space Telescope (*JWST* or *Webb*) is a large (6.5m diameter primary mirror) infrared ($0.6 < \lambda < 30\mu$m) space telescope. It impressive size and wavelength coverage will revolutionise the field of galaxy formation and evolution, enabling the community to push back the observational frontier to within a few 100 million years of the Big Bang. With *JWST* expected to launch in 2021, a detailed understanding of its capabilities is essential to guarantee the success of the mission. In this thesis, I present a new analysis of how best *JWST* can be utilised to study the evolution and formation of galaxies across cosmic time. Primarily this work uses simulated *JWST* and ancillary *HST* observations in an attempt to assess *JWST's* capabilities, specifically its ability to study high-mass, high-redshift, dusty star-forming galaxies in the Universe. Additionally, I use currently available data from the UV/optical to sub-mm to perform a new study of the prevalence of high-mass, high-redshift, dusty star-forming galaxies accessible before the launch of *JWST*.

Firstly, I introduce a piece of software that I have built to simulate observations that will be made using the Mid-infrared Instrument (MIRI) onboard *JWST*. This piece of software is capable of simulating all of MIRI's available observing modes: MIRI Imager, Low-Resolution Spectrograph (LRS), Medium Resolution Spectrometer (MRS). I then use this software to show the potential for measurements of the Hα emission line in high-redshift star-forming galaxies using the MRS IFU. At redshifts $z > 6.7$, MIRI is the only instrument onboard *JWST* that can directly observe Hα, a sensitive star-formation indicator, tracing very recent star-formation. I show that with approximately $\simeq$ 6-hour integration time with the MIRI MRS, the Hα emission line in the brightest known $z \simeq 7$ galaxies can be detected to a SNR of approximately $\simeq 11$. Therefore, I conclude that the MIRI MRS could be an impressive tool for determining the star-formation rates of high-redshift galaxies in the epoch of reionisation. Secondly, I present an

overview of the Public Release Imaging for Extragalactic Research (PRIMER) proposal submitted as part of the Director's Discretionary Early Release Science (DD-ERS) programme for Cycle-1 of *JWST*. PRIMER is a large (52hr), deep, fully-sampled NIRCam and MIRI imaging programme, designed to efficiently ($\approx$ 75% observing efficiency) observe the faintest galaxies in the best-studied available (Non-GTO Covered) equatorial *HST* CANDELS field, COSMOS. As well as detailing the science goals and observational design of this programme, I place it in the context of other planned *JWST* programmes (ERS & GTO) focussed on observations of high-redshift galaxies.

Thirdly, I present a new analysis of the potential power of deep, near-infrared, imaging surveys with the *JWST* to improve our knowledge of galaxy evolution. In this work, I properly simulate what can be achieved with *realistic* survey strategies, and utilise rigorous signal:noise calculations to calculate the resulting posterior constraints on the physical properties of galaxies. I explore a broad range of assumed input galaxy types (> 20,000 models, including extremely dusty objects) across a wide redshift range (out to $z \simeq 12$), while at the same time considering a realistic mix of galaxy properties based on our current knowledge of the evolving population (as quantified through the Empirical Galaxy Generator: EGG). While our main focus is on imaging surveys with NIRCam, spanning $\lambda_{obs} = 0.8 - 5.0\,\mu$m, an important goal of this work is to quantify the impact/added-value of: i) parallel imaging observations with MIRI at longer wavelengths and ii) deeper supporting optical/UV imaging with *HST* (potentially prior to *JWST* launch) in maximising the power and robustness of a major extragalactic NIRCam survey. I show that MIRI parallel 7.7-μm imaging is of most value for better constraining the redshifts and stellar masses of the dustiest ($A_V > 3$) galaxies, while deep *B*-band imaging (reaching $m_{AB} \simeq 28.5$ mag) with ACS on *HST* is vital for determining the redshifts of the large numbers of faint/low-mass, $z < 5$ galaxies that will be detected in a deep *JWST* NIRCam survey.

Finally, I attempt to assess the prevalence of the dusty subset of galaxies that MIRI will observe, utilising the current deepest UV/optical/near-IR and far-IR/sub-mm observations. The data collected from numerous telescopes covers a total of 1.8 deg^2 in the UDS and COSMOS fields. Combining the UV and IR data, I assess the total number density as a function of cosmic time and compare the methods of detecting/selecting high-redshift, high mass dusty galaxies. I calculate the total star-formation rate (SFR) as a function of redshift and compare the

contribution from sub-mm galaxies and UV/optically-selected dusty galaxies. I also calculate the star-formation rate density (SFRD) across cosmic history in an attempt to extend the Madau & Dickinson (2014) plot to higher redshifts for obscured star-formation. I show that both the UV/optical and (sub)-mm approach to detecting high-redshift dusty galaxies both produce a consistent estimation of their evolving comoving number density at high redshift. I find clear evidence of a rapid decline in the total comoving number density of these objects beyond $z > 3$, which results in a similarly steep decline in the SFRD of the Universe contributed by obscured star-formation. Comparing to recent work through in the literature, my results strengthen the existing evidence for a transition between unobscured & obscured star formation as the dominant mode of star-formation activity at $z \simeq 2{-}3$.

Declaration

I declare that this thesis was composed by myself, that the work contained herein is my own except where explicitly stated otherwise in the text, and that this work has not been submitted for any other degree or professional qualification except as specified.

Parts of this work have been published in Kemp et al. (2019).

(*T. W. Kemp, October 2019*)

Acknowledgements

Firstly, thank you very much to my supervisors Jim Dunlop and Ross McLure for taking me on as a PhD student and for supporting me throughout the full four years of my project. The opportunities to present work at various conferences have provided some of the best experiences I have had over the past few years. I would like to thank Andy Lawrence and Beth Biller who were my 3rd and 4th supervisors and have provided helpful feedback for all of the end of year assesments. I would also like to thank everybody else at the Royal Observatory and the Institute for Astronomy, whom many have become great friends. In particular, the help of Fergus Cullen, Owen Turner and Derek McLeod has been immense, making my time at the Observatory far more enjoyable. I'd also like to single out the pleasure of meeting and spending time with Paula Wilkie, who has been a massive help during both my Masters and PhD. I'd also like to thank the UKATC, specifically Pamela Klaassen, Gillian Wright and Alistair Glasse who supported me throughout the first 12 months of my PhD, while working on MIRI.

Finally, my work over the past four years would not have been possible without the continued support from my family; my partner Christine (Stijn), my pa (Big Bill), my mum (Ingrid), Saskia, Samantha, Zoe, Charlie, Sagal, the 'Dutchies' and of course the 'Academicals'. To you all, I dedicate this thesis.

Contents

List of Figures

List of Tables

1

Introduction

To understand how galaxies formed and evolved from the very first stars into the Universe we see today, we must observe galaxies in all phases of their lifetime. Various theoretical and observational studies have been performed in an attempt to do this, resulting in a wealth of information about galaxy luminosity functions, stellar mass functions and star-formation rates across cosmic time. In doing so, we have revealed an impressively complex and diverse pattern of structure on almost every scale in the Universe. However, when observing the large-scale structure at the very earliest stages of the Universe, it appears extremely homogenous and isotropic. In short, it turns out that the bulk of star formation occurred during a 4 billion year window between redshifts $z \simeq 1$ and $z \simeq 3$. My PhD focuses on understanding the growth of galaxies across the history of the Universe, specifically with the upcoming James Webb Space Telescope (*JWST*). In this introduction, I present a brief background of the astrophysics that relates to the work accomplished during my PhD before summarising the current observations utilised to study galaxy formation and evolution in the form of the Star Formation History of the Universe. I start with a general introduction to the current picture of the history of the Universe.

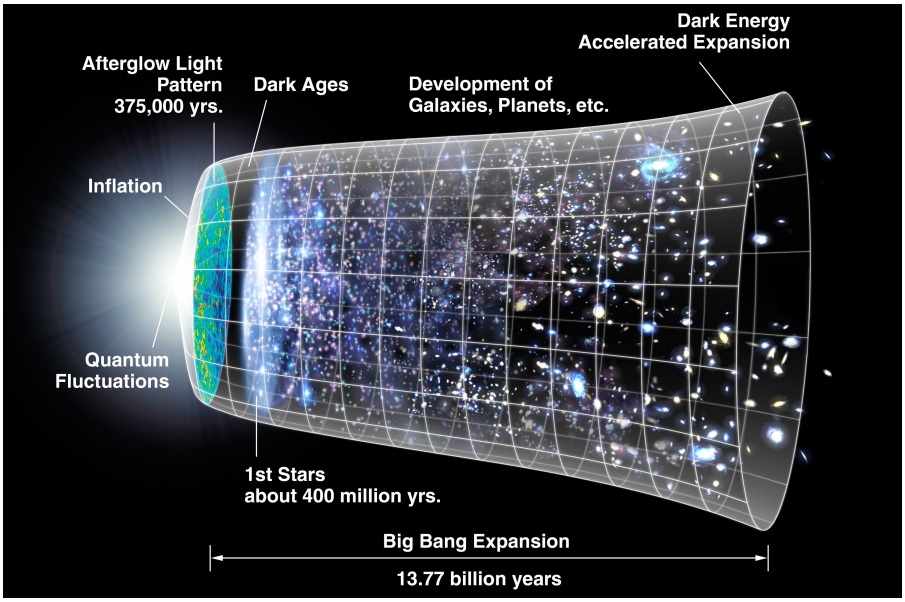

Figure 1.1 *A schematic diagram of the history of the Universe take from the NASA / WMAP Science Team (`https://map.gsfc.nasa.gov/media/060915/index.html`). Time runs from left to right showing the history of the Universe from the Big Bang to the current observable Universe.*

1.1 Cosmology and History of the Universe

1.1.1 Before First Light

The beginning of the Universe consists of a rapid and complicated sequence of events culminating in the birth of the very first stars and galaxies. In the early 1920s, Georges Lemaître and Alexander Friedmann theoretically proposed that the Universe is expanding and has been since a singularity, now known to be 13.7 billion years ago. Observationally Vesto Slipher had been measuring the spectra of nebulae within our own galaxy (e.g. Slipher 1912, 1915, 1917, 1921) as well as the spectrum of the Andromeda Galaxy (M31) for several years. Slipher discovered that M31 was blueshifted towards us, travelling at around $\simeq 200$ kms^{-1}, Slipher (1913, 1914)). Slipher had also measured several other galaxy spectra by the mid-1920s (e.g. Slipher 1922, 1924), calculating the Doppler shifts of some that were travelling away from us (redshifted). It was not until Edwin Hubble in 1929 calculated the distances to several Cepheids, young massive core helium-burning stars with immense luminosities that pulsate for 2-100 days that Hubble confirmed this expanding Universe theory finding that the distances (d) to galaxies strongly

correlated with their redshifts (z), yielding Hubble's Law (Hubble 1929):

$$v = Hd \tag{1.1}$$

where H is known to be $\simeq 70 \mathrm{kms}^{-1}\mathrm{Mpc}^{-1}$. This expansion theory tells us that the Universe was a much hotter and denser place in the past. In the first few moments (10^{-37} seconds) after the Big Bang, it is thought that a phase of rapid expansion occurred called 'Cosmic Inflation', as illustrated in the left hand side of Fig. 1.1. This expansion decreased the density and cooled the Universe during which time, quantum-scale density fluctuations were amplified, which ultimately created the seeds of the large-scale structure that we see today.

The next phase of the Universe is less speculative as we have re-created these conditions in particle accelerators (e.g. CERN). Quarks and Gluons began to combine and create Baryons (protons and neutrons) and subsequently, these particles combined to create the nuclei of hydrogen and helium atoms. It was not until 380,000 years after the Big Bang that the free-roaming electrons began to combine with the nuclei to create the first stable atoms in the Universe. This resulted in the release of radiation; however, it was only now that the surrounding hot plasma was sufficiently cooled and the number density of free electrons dropped, allowing these photons to propagate freely through the Universe. This process is known as recombination, and we can observe the resulting emitted radiation today, the Cosmic Microwave Background (CMB; $T = 2.73K$), see LHS ('Afterglow Light Patterns') of Fig. 1.1 or Fig. 1.2. Upon completion of this process, the Universe was now neutral, but still rapidly expanding and cooling, stuck in a period known as the 'Dark Ages'. In this period the majority of the matter in the Universe was comprised of hydrogen, helium and trace elements of metals. This material then began to infall into the overdense regions of the Universe, creating the first stars and galaxies while the underdense regions evolved into what we call 'voids'. The neutral Universe then underwent a process of re-ionisation, where high-energy photons from these young objects ionised the surrounding Inter-Galactic Medium (IGM).

This type of 'visible' matter only makes up around 4% of the total mass-energy distribution in the entire Universe. A considerable fraction is made up of 'dark matter', comprising around 26% of all the energy density in the Universe while an even less understood quantity 'Dark Energy' constitutes the remaining 70%. Both dark matter and dark energy play a significant role in how the Universe expands in

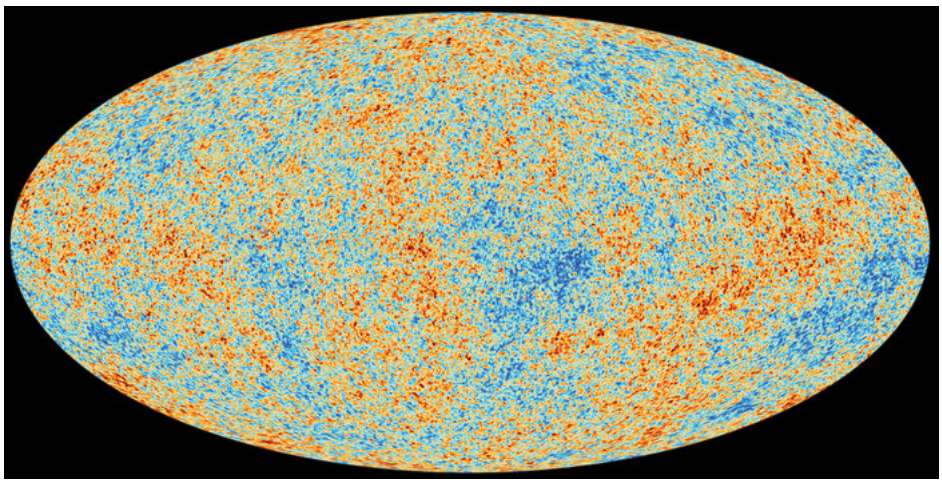

Figure 1.2 *Planck's view of the cosmic microwave background (CMB). A snapshot of the CMB highlighting the cool (blue/green) and warm (orange/red) temperature fluctuations which correspond to density fluctuations throughout the Universe. The overdensities and underdensities became the seeds for the galaxies and voids we see today, respectively. (Planck Collaboration et al. 2018;*`https://www.esa.int/spaceinimages/Images/2018/07/Planck_s_view_of_the_cosmic_microwave_background`*).*

the manner it does. The best model we currently have that describes this immense expansion from the Big Bang is the Lambda Cold Dark Matter (ΛCDM)model. Measurements from the Wilkinson Microwave Anisotropy Probe (WMAP; Spergel et al. 2003) and the more recent Planck spacecraft Planck Collaboration et al. (2018), showed that the temperature fluctuations in the CMB are consistent with what can be explained by the ΛCDM model.

Redshift

The most common way to explore large astronomical distances is through Redshift, z. As light travels through the expanding space from very distant receding objects to the observer, the light is effectively 'stretched'. Observationally, we see that the light detected appears to be redder than the expected light from the source. Redshift is, therefore, a straightforward way to quantify the ratio of observed wavelength ($\lambda_{observed}$) to the emitted wavelength ($\lambda_{emitted}$) of light:

$$\lambda_{observed} = (1 + z)\lambda_{emitted} \tag{1.2}$$

or:

$$z = \frac{\lambda_{observed} - \lambda_{emitted}}{\lambda_{emitted}} \tag{1.3}$$

It is important to recognise that this is an effect of the overall expansion of the Universe and for an assumed isotropic Universe we can associate the redshift to a time at which the source/galaxy is being observed and a time at which the light was emitted:

$$1 + z = \frac{a(t_{observed})}{a(t_{emitted})} \tag{1.4}$$

where $a(t_{observed})$ and $a(t_{emitted})$ are the size of the Universe at the time the light from the object is observed and emitted, respectively.

Distances and Areas

Measuring the redshift of an object opens the door to understanding the distances and volumes in play between the objects emitting and the observer receiving the light. Several distance measures are essential when studying distant galaxies; the comoving distance, angular diameter distance and the luminosity distance. Accurate astronomical distances are fundamental in astronomy in order to infer the physical properties of systems (luminosity, size and mass). Light needs time to travel to the observer from the source and one can, therefore, define a distance between the two at a given cosmological time. This is known as the proper distance, and if you were to evaluate this quantity at the present day, it is called the comoving distance. Consider a beam of light emitted at a time ($t_{emitted}$) from a source along the line of sight (LOS) to the observer at time $t = t_{observed}$. The beam travels a distance $c \times dt$ while being stretched by the expanding Universe and thus integrating over the entire travelling time provides the LOS comoving distance D_C:

$$D_C = \int_{t_{observed}}^{t_e} c \frac{a_{t_0}}{a(t)} dt \tag{1.5}$$

where $a(t)$ and $a(t_0)$ represents the scale factor at a time, t where $t = t_0$ for present day. In terms of redshift, we can integrate over the contribution between nearby events along the radial ray from z=0 to the object:

$$D_C = D_H \int_0^z c \frac{dz'}{E(z')} \tag{1.6}$$

where the function $E(z)$ is:

$$E(z) = \sqrt{\Omega_M (1+z)^3 + \Omega_k (1+z)^2 + \Omega_\Lambda} \tag{1.7}$$

and D_H is the Hubble Distance ($D_H = c/H_0 = 3000 h^{-1} Mpc = 9.26{\times}10^{25} h^{-1}$m). $dz'/E(z')$ is proportional to the time of flight of the light beam travelling across the redshift interval dz' divided by the scale factor at that time.

The co-moving distance between two events at the same redshift (separated on-sky by some angle dθ) is D_M dθ, where D_M is the transverse comoving distance; equivalent to the comoving distance D_C in the flat Universe. The angular diameter distance (D_A) relates the object's observed angular diameter on the sky (θ) in radians, with the physical transverse size at that redshift. It is related to the transverse comoving distance by:

$$D_A = \frac{D_C}{(1+z)} \tag{1.8}$$

One might intuitively think that the angular size of an object will increase indefinitely as we increase the redshift; however, it appears to turn over at z $\simeq$ 1 where objects beyond this point appear larger in angular size.

The luminosity distance (D_L) relates the intrinsic luminosity (L) and the observed flux (S) of an astronomical object:

$$D_L = \sqrt{\frac{L}{4\pi S}} \tag{1.9}$$

or calculated using the comoving distance and angular diameter distance:

$$D_L = (1+z) D_M = (1+z)^2 D_A \tag{1.10}$$

Magnitudes and Fluxes

The luminosity distance (D_L) is a quantity required to calculate the absolute magnitude (M) from the observed apparent magnitude (m). The apparent magnitude is defined to be the ratio of the observed apparent flux of that source to the apparent flux of Vega (a bright star sitting 25 light years away). The absolute magnitude is the measurement of the intrinsic luminosity of the object and therefore is equal to the apparent magnitude the object would have if it were 10 pc away. The equation that allows one to convert between the two using the luminosity distance is:

$$M = m - 5.0 \log_{10} \left(\frac{D_L}{10\text{pc}} \right) + K \tag{1.11}$$

K represents the K-correction, a factor that takes into account some of the additional effects of redshift, specifically, the fact that the observed frequency range/filter is measuring a different frequency range of the spectrum than in the rest-frame of the galaxy. K therefore depends on the SED of the object being observed and therefore the differential luminosity L_ν or L_λ.

$$K = -2.5 \log_{10} \left[(1+z) \frac{L_{(1+z)\nu}}{L_\nu} \right] = -2.5 \log_{10} \left[\frac{1}{(1+z)} \frac{L_{\lambda/(1+z)}}{L_\lambda} \right] \tag{1.12}$$

When considering the differential flux (S_ν or S_λ) and luminosity (L_ν or L_λ) of an astronomical object, redshift also changes the total width of the bandpass we use to observe the object. Putting everything together we define the flux per unit wavelength and per unit frequency resepectively:

$$S_\nu = (1+z) \frac{L_{(1+z)\nu}}{L_\nu} \frac{L_\nu}{4\pi D_L^2} \tag{1.13}$$

and:

$$S_\lambda = \frac{1}{(1+z)} \frac{L_{\lambda/(1+z)}}{L_\lambda} \frac{L_\lambda}{4\pi D_L^2} \tag{1.14}$$

In summary, the redshift of an object affects the flux density in four ways. Firstly, photon energies are redshifted, so the flux density reduces by a factor of $1 + z$.

Secondly, the arrival rate of photons is time dilated reducing the flux density by another factor of $1+z$. Thirdly, the observed photons have a frequency of $(1+z)$ times that of the emitted frequency. Finally, the bandwidth (d_ν) is reduced by a factor of $1+z$, which increases the energy flux per bandwidth by a power of $1+z$.

Comoving Volume and Lookback Time

Another quantity that is vital for studying high-redshift galaxies is the comoving volume, V_C. In order to calculate comoving number densities, luminosity functions and mass functions across cosmic history we need to be able to calculate the comoving volume of a defined redshift bin. The comoving volume element in a solid angle dω within the redshift interval dz is:

$$dV_C = \frac{c}{H_0}\frac{(1+z)^2 D_A^2}{E(z)} d\omega dz \tag{1.15}$$

where $E(z)$ is defined by Equation 1.7 and D_A is the angular diameter distance at redshift z. If we were to integrate the comoving volume element to the present day from a redshift z, and assume a flat universe the total comoving volume would be equivalent to:

$$V_C = \frac{4\pi}{3} D_M^3 \tag{1.16}$$

Finally, the lookback time (t_L) is a quantity that allows astronomers to study the evolution of galaxies across multiple epochs. t_L is defined as the difference between the age of the Universe at the time of observation ($t_{observed}$) and the age of the Universe when the photons were emitted from the observed source ($t_{emitted}$). t_L is given by:

$$t_L = t_H \int_0^z c\frac{dz'}{(1+z')E(z')} \tag{1.17}$$

1.1.2 The First Stars and Galaxies

It is thought that at around 50 - 200 Myrs after the Big Bang ($z \simeq 20$ - 50) the very first stars and galaxies were formed (e.g. Bromm et al. 1999; Abel et al.

2002). During the 'Dark Ages', the majority of the Universe was comprised of neutral hydrogen and helium, with trace amounts of heavier metals. This neutral gas began collapsing into structures with a distribution dictated by the shape of the dark matter distribution (observed as the fluctuations of the CMB, see Fig. 1.2). To form stars, the gas is required to fall into these potential wells and cool enough to form a core of sufficient density to begin nuclear fusion. This 'pristine' gas falls into the mini-haloes creating the first Population III stars, consisting of only really hydrogen and helium (e.g. Bromm & Yoshida 2011; Stacy & Bromm 2014). The actual process of how gas cools and forms stars is still the focus of active research. In present-day galaxies, star-forming regions are accompanied by dust which prevents substantial amounts of optical/UV light from escaping, impeding our view. Observationally we have never been able to see the very first stars and galaxies directly, therefore, Much of the work in the very early Universe is based entirely on numerical simulations and semi-analytic modelling (SAM).

These first stars formed under very different circumstances to the star-formation we see in the present day. The lack of metals made the cooling mechanisms very ineffective resulting in stars with masses of 10-1000 $M_\odot$ as thermal pressure and gravity battled against one another. . These first stars then explode as supernovae fueling the surrounding medium with heavier metals and gas. This gas, however, is far too hot and diffuse for it to be able to form more stars instantaneously. The gas needs time to cool and increase in density; it is therefore thought that star-formation in the very early stages of the Universe is somewhat intermittent. Some simulations have shown that this can take up to 100 million years to cool sufficiently matching relatively well to the timescale for the first dwarf galaxy halos to be properly formed. This allows for eventual dwarf galaxies to be formed in low mass halos populated with Population II stars (more metal-rich).

The massive size of Pop III stars subsequently means that they are likely to be remarkably luminous, emitting an extreme number of ionising photons. The Epoch of Reionisation (EoR) is an area of extragalactic astrophysics still under extensive study. However, it is thought that these early stars contributed significantly to the reionisation of the IGM (Robertson et al., 2013). This epoch is a significant phase transition of the Universe, marking the first generation of galaxies that we have currently observed. Gunn Peterson trough measurements (absorption of light from the prescence on neautral hydrogen in the IGM) of high-redshift quasars suggest that the reionisation of the Universe took place at $z \simeq 6$

(Fan et al., 2006). While CMB polarisation anisotropies from WMAP and Planck initially suggested a reionisation redshift of $z \simeq 11$ (e.g. Spergel et al. 2003; Planck Collaboration et al. 2014), more recent Planck results indicate an instantaneous reionisation redshift of $z \simeq 7.7$ Planck Collaboration et al. (2018). Additionally, an apparent decline in the number of Lyman-α emitters (LAEs; Section 1.2.1) indicates a large neutral fraction at $z > 7$ as the Lyman-α emission is being absorbed by the IGM and thus not reaching us (e.g. Mesinger & Furlanetto 2008; Curtis-Lake et al. 2012; Stark 2016; Pentericci et al. 2018; Mason et al. 2018, 2019; Hoag et al. 2019).

1.2 Selecting and Observing High-Redshift Galaxies

The vast majority of galaxies discovered in the Universe have been found through photometric surveys across multiple different wavelength ranges. Effectively, a telescope observes across different regions of the sky and observes in multiple different photometric filters detecting photons within each bandpass. The total flux detected per unit frequency (F_ν) is related to the apparent magnitude (m) of that object in a specific bandpass ($d\nu$):

$$m = -2.5 \log_{10} \left[\int F_\nu e(\nu) d\nu \right] + C \tag{1.18}$$

where $e(\nu)$ represents the response function of the filter/bandpass and C represents the zero-point. The zero-point in a photometric system is a way to calibrate to a standard magnitude system and is defined as the detector count when the apparent magnitude is zero. For example, throughout this work I use the AB magnitude system (Oke 1974; Oke & Gunn 1983) which is defined relative to a flat spectrum source with a zero point $F_\nu = 3631$ Jy [1].

$$m_{AB} = -2.5 \ \log_{10} \left(\frac{\int F_\nu e(\nu) d\nu}{\int 3631 \text{ Jy } e(\nu) d\nu} \right) \tag{1.19}$$

or assuming for a specific bandpass:

[1] 1 Jy = 10^{-26} W Hz^{-1} = 10^{-23} erg s^{-1} Hz^{-1} cm^{-2}

$$m_{AB} = -2.5 \log_{10} \left(\frac{F_\nu}{3631 \text{ Jy}} \right) \tag{1.20}$$

There are several techniques for selecting and detecting galaxies out to the highest redshifts. Below, I provide a brief overview of the most commonly used techniques.

1.2.1 Rest-frame UV Selection

Lyman Break Galaxies (LBGs)

Young star-forming galaxies that are not entirely suppressed by dust emit extreme amounts of UV continuum light. UV bright objects display an intrinsic drop in their spectra produced from the absorption of UV photons by neutral hydrogen present within the galaxy itself (Inter Stellar Medium: ISM). This feautrue is known as the Lyman Limit at λ= 912Å. As you increase in redshift ($z > 5$), the increasingly dense neutral hydrogen clouds (in the interveing IGM) also absorb the strong Lyman-α emission creating what is known as the Lyman-α forest, affecting the region of the spectrum between the λ_{rest} = 912 - 1216 Å. The combination of these two effects produces an often powerful spectral feature for UV bright galaxies at increasing redshifts know as the 'Lyman-break'.

Therefore, one of the most common methods of selecting and detecting high-redshift galaxies is exploiting this feature and utilising broadband photometry to detect the location of this sudden drop in flux. Galaxies that show this feature are known as Lyman-break Galaxies (LGBs) or Lyman-dropouts, because, with photometric data across a wide range of filters, one can identify in which shorter-wavelength filter the object disappears while remaining fairly bright in the longer-wavelength filters. This technique was first used for redshift $z \simeq 3$ galaxies where the rest-frame UV emission and the Lyman Limit at 912Å is observed in the U-B filters ($\lambda \simeq 3600$Å) (e.g. Guhathakurta et al. 1990; Steidel & Hamilton 1992; Steidel et al. 2004). They presented distinctive colours in the UGR filters system, where they have a relatively flat $G - R$ colour along with extremely red $U - G$. Using longer-wavelength filter sets this 'color cut' technique has been done out to increasingly higher redshifts, $z \simeq 3$ - 7 (e.g. Steidel et al. 1996; Steidel, Giavalisco, Pettini, Dickinson & Adelberger Ste; Ouchi et al. 2004; Bouwens et al. 2007, 2010; Oesch et al. 2010; Finkelstein et al. 2010; Bowler et al. 2012). An

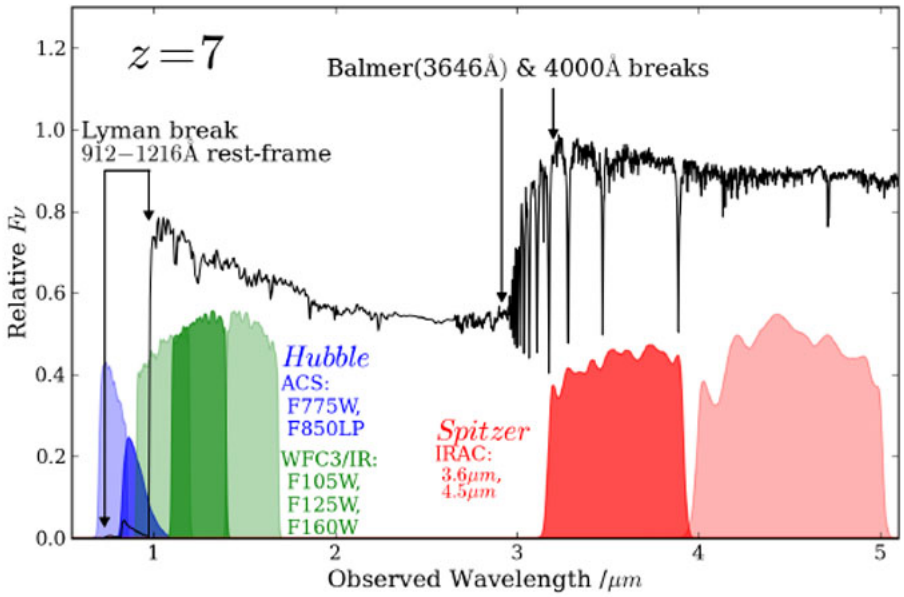

Figure 1.3 *An illustration of the rest-frame UV SED for a young star-forming galaxy at redshift $z = 7$. Along with the SED, important filters from HST(ACS andWFC3/IR) and Spitzer(IRAC) are highlighted in order to show the region of the spectrum probed by each observatory. Both the Lyman-break at $\lambda_{rest} < 1216$Å and the Balmer/4000Å break can be seen, redshifted into the optical/near-IR filters, from (Dunlop et al., 2013).*

alternative method in selecting high redshift LBGs is through spectral energy distribution fitting (SED-fitting), which I go into more detail in section 1.3.1. This process is used to estimate the photometric redshifts, based on features in the SED, like the break seen in an LBG.

There are, of course, difficulties when using the rest-frame UV in selecting galaxies at high redshift. By definition, this technique is only sensitive to young galaxies with on-going star formation and thus cannot be used to select quiescent galaxies. There are also several types of objects in the Universe that can contaminate a sample of LBGs by mimicking the shape of the SED. The first of which, is very dusty galaxies and/or AGN sitting at low redshifts ($z \simeq$ 1-3). This class of objects can reproduce a rapid drop in flux over a short wavelength range at different wavelengths depending on their redshift. This can be accounted for by placing a set of criteria for the final sample of LBGs. For example, a minimum Lyman-break strength, ensuring deep enough broadband imaging beyond the suspected break and confining the objects to young star-forming only objects. This type of contaminant can be a problem when SED-fitting the photometric data, mainly if the dust content parameter space is limited to $A_V < 5$ (Dunlop et al. 2007). A similar problem is encountered with potential cool galactic star contamination, specifically from M, L and T dwarf stars. This is a particular issue for ground-based surveys because a large portion of LBGs galaxies ($z > 5$) detected from the ground are unresolved. Deep multi-band IR photometry can help distinguish between the two as these dwarf stars have redder $Y-J$ colours (by $\simeq$ 1 mag). Also, there is potential confusion between the detection of a Lyman break and a Balmer (3650Å) or 4000Å break, an issue probed in much more detail in Chapter 4.

Lyman-α Emitters

Lyman Alpha Emitters (LAEs) selection is a method in identifying high redshift galaxies using narrow-band photometry rather than broad-band photometry as discussed above for LBGs. There is some overlap between the samples of LAEs and LBGs, as Lyman-α is expected to be extremely strong in star-forming galaxies. The majority of Lyman-α emission is thought to be produced by the recombination of interstellar hydrogen that is ionised through on-going star-formation. LAEs are selected directly from the strength of their emission line. This is calculated using narrow-band selection, where a filter configuration is created to calculate the excess of flux within the narrow band in comparison to

that of the surrounding filters created when the Lyman alpha line passes through the narrow filter. To prevent contamination by other emission lines at alternate redshifts, there needs to be evidence of some break (i.e. Lyman-break) to ensure the emission line selected is, in fact, Lyman-α. Careful filter selection is therefore required, and consequently, the redshift range probed by a survey designed for LAEs is usually limited.

Since the 1990s LAE surveys have played an essential role in our understanding of early star formation, and the contribution galaxies make to the re-ionisation of the neutral Universe. The enormous equivalent widths (EW) of Lyman-α made it possible to study LAEs out to redshifts $z > 5$, even in the late 1990s and early 2000s (e.g. Dey et al. 1998; Hu et al. 1998, 2002). Selecting LAEs out to the highest redshifts has largely been made possible due to the dramatic increase in sensitivity capabilities of optical/near-IR cameras through narrow-band imaging. In particular, the NB816 narrow-band filter on the Subaru/SuprimeCam, allowed studies to extend out to $z \simeq 6$ (e.g. Ouchi et al. 2005; Shimasaku et al. 2006; Ajiki et al. 2006). The installation of still redder filters (NB921 and NB973) allowed analogous surveys to reach redshifts of $z \simeq 6$ -7 (e.g. Taniguchi et al. 2005; Kashikawa et al. 2006; Iye et al. 2006; Ouchi et al. 2010). Again, this boundary was further extended with the addition of the NB1006 filter yielding LAEs out to beyond redshifts $z \geq 7$ (e.g. Iye et al. 2008; Shibuya et al. 2012; Konno et al. 2014).

LAEs selected through narrow-band imaging surveys require spectroscopic follow-up to remove potential contamination. Due to the nature of a narrow-band survey, it is challenging to distinguish between the Ly-α line from any other emission line that happens to mimic the Ly-α line.As previously stated, this can be somewhat overcome by setting selection criteria requiring a break blueward of the emission line. Therefore broad-band photometry blueward of the narrow-band is very important.

1.2.2 Rest-frame optical/IR selection

Photometrically selecting galaxies based on their rest-frame optical or near-IR spectra is only really possible through the detection of the Balmer (3650Å) or 4000Å break. The Balmer break forms due to the dominance of A-type stars, whose presence and limited lifetime indicate activity within the previous $\simeq 100$ Myr. Often, therefore, a Balmer break is also present in an LBG, as shown by

the spectrum of a redshift $z \simeq 7$, star-forming galaxy in Fig. 1.3. A Balmer Break can also still be present within the spectrum of a galaxy if star-formation has recently been turned off, up to a post-starburst age of approximately 1 Gyr. This means that the strength/depth of the Balmer Break provides a probe of galaxies' age. The 4000Å break is produced by the absorption of high energy radiation from metals within the stellar atmospheres and the lack of hot blue stars. The 4000Å break is therefore fairly strong in massive stellar populations, where the star-formation ceased at least 1 Gyr prior to observation. To select galaxies at higher redshifts based on their rest-frame optical breaks, we require very deep imaging in the near-IR. A similar analysis to that of the LBGs of colours can then be done to identify massive, evolved galaxies.

As already stated, the UV is very sensitive to dust extinction, where the corrections to the UV can reach $\simeq$ 3 - 10 mag. Much of the absorbed UV light is re-radiated by the warmed dust grains in the sub-mm/far-IR wavelength region (Section 1.2.3 and Chapter 5). Here, however, we are more interested in the recombination/nebular emission lines (e.g. Hα, Hβ and O[II]). These emission lines are produced when the ionising flux from young stars ionises the surrounding neutral hydrogen. The subsequent recombination of the hydrogen atoms produces an abundance of different emission lines. Hα provides a direct indicator of recent star-formation; however, it can still be somewhat affected by dust extinction. These effects can be accounted for using the matching Hβ emission line, if visible (the equivalent width is far smaller). It has been shown that Hα EW evolves with redshift, suggesting that not only is it visible out to very high redshift (with sufficient imaging depth) but also that these obbjects could contaminate broad-band filters affecting our ability to SED-fit data that cover the rest-frame optical. I go into more detail about using Hα as a probe of SFR at high redshift in Section 1.4.1. Galaxies have also been selected based on their Hα emission in a similar manner to that of LAEs. A customised filter selection can be used to narrow-band select galaxies that emit Hα with extreme equivalent widths.

1.2.3 Rest-frame mid-infrared to sub-mm selection

Some of the most extreme star-forming galaxies in the Universe emit the bulk of their radiation in the sub-mm and mid/far-IR region of the spectrum. The emission is the result of recent star formation and therefore, young stars emitting large amounts of UV radiation, which is then absorbed and scattered by the

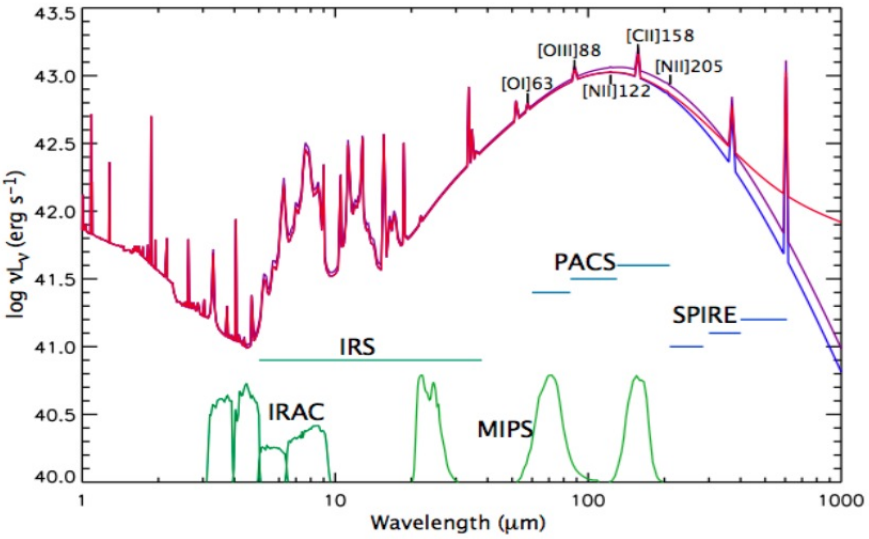

Figure 1.4 *The SED of a typical star-forming galaxy (`https://www.ast.cam.ac.uk/research/galaxies.and.active.galactic.nuclei/kingfish/science`). The interstellar dust absorbs the UV/optical light at $\lambda < 0.5\mu$m from young stars and re-radiates it in the mid-IR to sub-mm ($5 < \lambda < 1000\mu$m). Some filter curves for instruments that observe in the far-IR to sub-mm are shown. (I discuss IR and sub-mm surveys in more detail in Section 1.5)*

.

surrounding dust. These warmed dust grains then re-radiate in the far-IR and sub-mm. The effects of dust extinction are thought to be negligible in this region of the spectrum (certainly most dust emission is optically thin at $\lambda > 100\mu$m), and hence the IR luminosity calculated from these systems is directly proportional to the level of star-forming activity.

Fig. 1.5 shows the SED of a typical simulated star-forming galaxy. The IR region of the spectrum is broken down into three sections; the near-IR (2-5μm), the mid-IR (5 - 30μm) and the far-IR (30-300μm). The sub-mm wavelength range can be defined as $\lambda \simeq 200\mu$m to 1000μm. The mid-IR region of the spectrum in star-forming galaxies is dominated by hot dust, heated to a temperature >100K by young stars. There is an accompanying set of emission features called the Polycyclic Aromatic Hydrocarbons (PAH) that can be very difficult to account for when observing as they can be the same width as some broad-band filters and in-turn contribute up to 30% of the entire IR luminosity. The far-IR region of the spectrum is dominated by the reprocessed light from stars by surrounding dust grains. The emission has a characteristic blackbody shape peaking between 60 - 200μm depending on the physical properties of the dust causing the emission. The 'warm' dust component surrounding the star-forming region peaks at around

60μm while a cooler dust component, emitting at a longer wavelength ($\lambda >$ 100 μm), heated from interstellar radiation. The sub-mm is thought to represent this cooler component emission, where the dust temperature is thought to be < 30K.

Sub-mm and far-IR instrumentation, therefore, probe different dust temperatures, the cool and hot dust respectively. Both, however, have allowed for the detection of the very brightest IR galaxies to the highest redshifts, Ultra-luminous Infrared Galaxies (ULIRGs). Surveys carried out using the James Clerk Maxwell Telescope (JCMT: Scott et al. 2002, 2006; Geach et al. 2013) in particular the Sub-millimetre Common-user Bolometer Array (SCUBA: Mortier et al. 2005) and the Atacama Large Millimetre/sub-millimetre Array (ALMA) and have uncovered a significant population of ULIRGS and sub-mm bright galaxies (SMGs - e.g. Smail et al. 1997; Hughes et al. 1998; Barger et al. 1998).

For high-redshift science, sub-mm galaxies have always been relatively easy to detect, in comparison to their low-redshift counterparts, due to the powerful negative K-correction. Effectively, this means distant galaxies are observed at a rest-frame wavelength very close to the peak of their spectral energy distribution (SED). At wavelengths beyond $\lambda > 250\mu$m, the flux density of galaxies above redshift $z > 1$ no longer decreases at a rate of the inverse square of the distance to the object, and in-fact remains relatively constant as the redshift increases beyond $z > 1$. However, probing this wavelength range has disadvantages, specifically both the high-background and poor angular resolution, limiting our ability only to observe the brightest and most star-forming galaxies, which subsequently means the rarest.

1.3 Galaxy Properties

1.3.1 SED-Fitting

Over the past few decades, there has been a rapid increase in the photometric data available, both in terms of the sky area and wavelength ranges. This plethora of information has made spectral energy distribution (SED) analysis vital for understanding galaxy formation and evolution. SEDs, particularly from the UV-IR, contain a large amount of information about the star-formation history (SFH), the stellar mass, metallicity and the dust content of galaxies. To estimate these

properties from broad-band photometry, one must match the data to a synthetic SED. This synthetic SED, in general, is based on a set of simple stellar populations (SSPs) that represent 'bursts' of star-formation. A composite stellar population (CSP), is the result of combining a number of the SSPs and evolving them with an assumed SFH. The finalised synthetic SED is produced when the effects of dust attenuation, IGM attenuation and nebular emission are taken into account. Fig. 1.5 shows a schematic diagram of the process of building a composite stellar population. The upper panels highlight the necessary ingredients for constructing SSPs: an IMF, isochrones for a range of ages and metallicities, and stellar spectra spanning a range of T_{eff}, L_{bol}, and metallicity. The middle panels highlight the ingredients necessary for constructing CSPs: star formation histories and chemical evolution, SSPs, and a model for dust attenuation and emission. The bottom row shows the final CSPs both before and after a dust model is applied.

The most important parameter for producing accurate physical property estimations is the redshift. Calculating the redshift accurately (whether derived through photometry or spectroscopy) fixes the SED to a specific emitted wavelength and cosmic time, from which the other properties (intrinsic) that are redshift-dependent can then be accurately derived. The stellar mass, dust attenuation and SFR are all highly-dependent on accurate redshift estimations. Much work has therefore been done in order to quantify the accuracy with which SED-fitting codes estimate the redshift of a galaxy. A good way of testing this is to fit the photometry of a galaxy for which a high SNR spectroscopic observation exists (and hence a robust redshift). If one has a high SNR spectroscopic observations of an object, the redshift of that object can be calculated using the measurement of multiple emission lines.

1.3.2 Properties

It is crucial to consider the multiple components that are brought together to create a synthetic SED. The process begins with the Initial Mass Function (IMF) which effectively determines the ratio of low-mass to high-mass stars created for each burst of star-formation and hence ultimately determine the total stellar mass of the resulting galaxy SED. There are three standard IMFs assumed when SED-fitting. The first is the Salpeter IMF (Salpeter 1955), derived in 1955 focusing on the stars with a stellar mass greater than our sun, represented by the solid pink line in Fig. 1.6 ($\alpha = 2.35$ across all masses). The functional form of the Salpeter

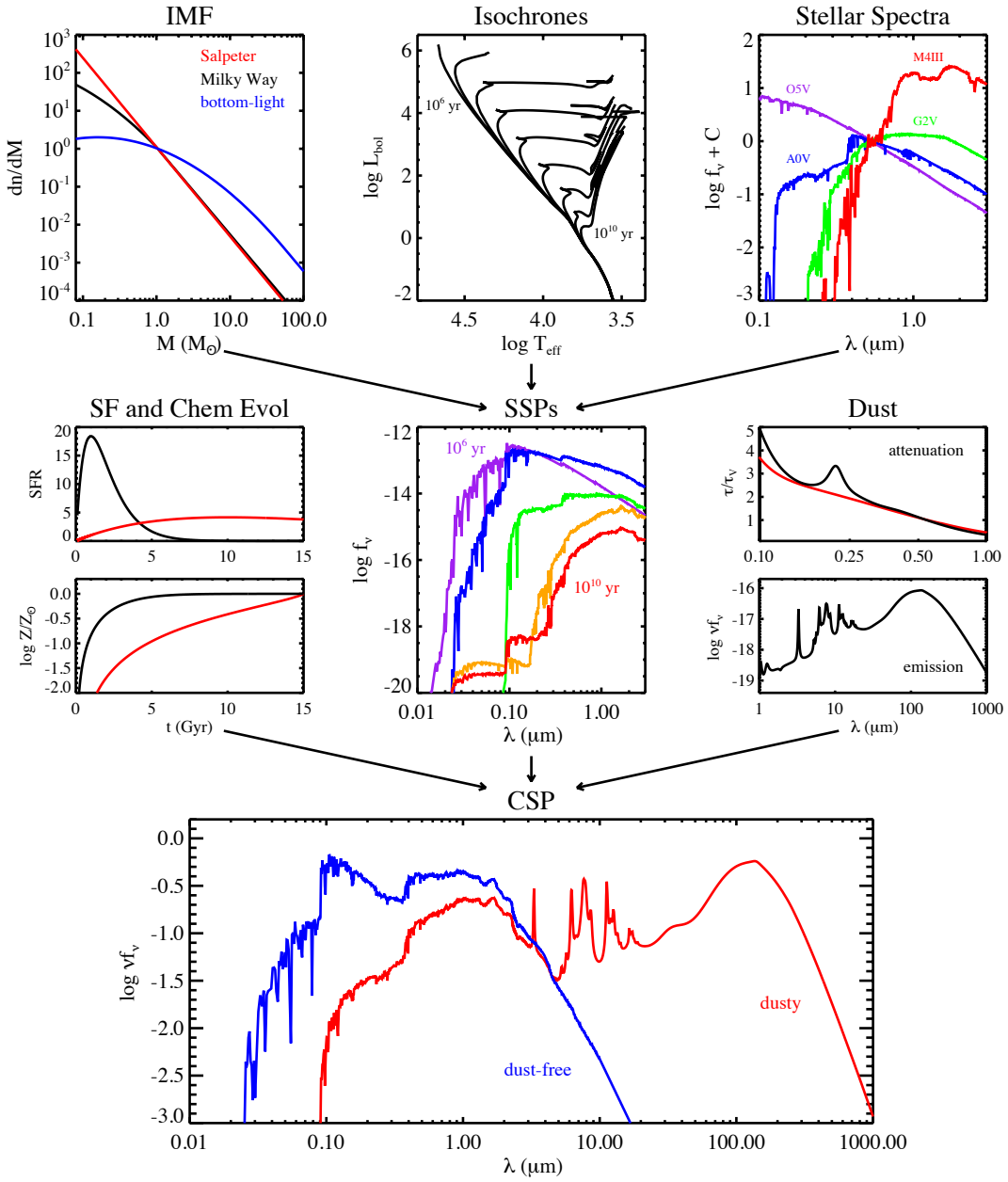

Figure 1.5 *Overview of the construction of building CSP used in the SED-fitting process (Conroy 2013). The upper panels highlight the necessary ingredients for constructing SSPs: an IMF, isochrones for a range of ages and metallicities, and stellar spectra spanning a range of T_{eff}, L_{bol}, and metallicity. The middle panels highlight the ingredients necessary for constructing composite stellar populations (CSPs): star formation histories and chemical evolution, SSPs, and a model for dust attenuation and emission. The bottom row shows the final CSPs both before and after a dust model is applied.*

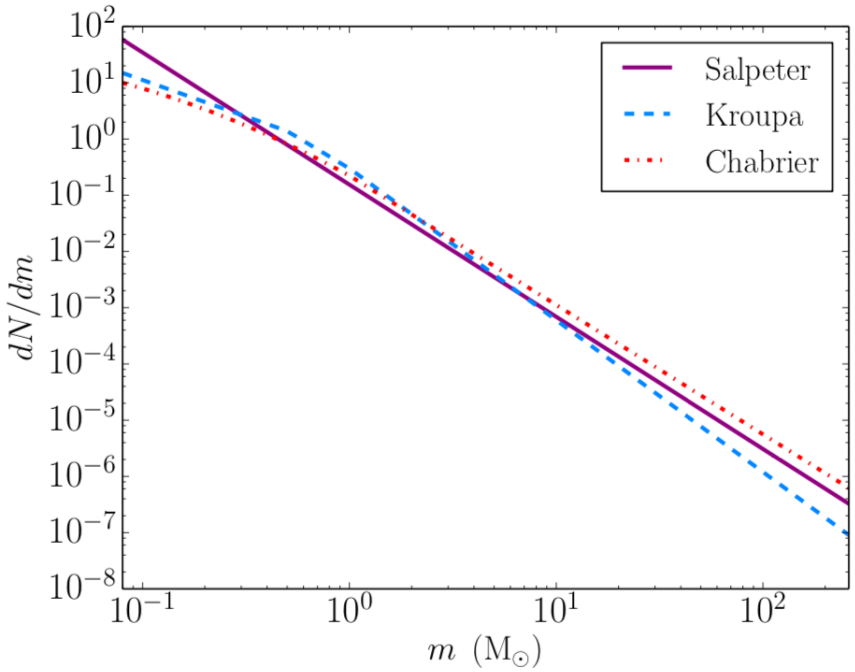

Figure 1.6 *The three IMFs considered in this work are Salpeter (violet, solid line; Salpeter 1955), Kroupa (blue, dashed line; (Kroupa 2001), and Chabrier (red, dot-dashed line; Chabrier 2003), over a mass range of 0.08 $M_\odot$ to 260 $M_\odot$. The integrated area under each of the curves is the same. The Salpeter IMF emphasises low-mass stars, the Kroupa IMF emphasises intermediate-mass stars, and the Chabrier IMF is the most top-heavy of the three, emphasising high-mass stars (Crosby et al. 2016).*

IMF is:

$$\xi(m)\Delta m = \xi_0 \left(\frac{m}{M_\odot}\right)^{-2.35} \left(\frac{m}{M_\odot}\right) \tag{1.21}$$

The final two IMFs are the Kroupa (Kroupa 2001) and Chabrier (Chabrier 2003), which considers various power laws in different mass regimes. Both are somewhat similar as can be seen in Fig. 1.6. The former is split up into three mass ranges with an α for each:

$$\begin{aligned} &\xi(m) = m^{-\alpha} \\ &\alpha = 0.3 \text{ for } m < 0.08 \\ &\alpha = 1.3 \text{ for } 0.08 < m < 0.5 \\ &\alpha = 2.3 \text{ for } m > 0.5 \end{aligned} \tag{1.22}$$

Chabrier has a more complex form, basically resembling that of Kroupa. Fig. 1.6 plots a comparison of the three most commonly used IMFs with Salpeter, Kroupa and Chabrier represented by the solid pink, dashed blue and dotted red lines respectively. In general, The Salpeter IMF emphasises low-mass stars, the Kroupa IMF emphasises intermediate-mass stars, and the Chabrier IMF is the most top-heavy of the three, emphasising high-mass stars.

The star-formation history of a galaxy describes the manner in which stars form over time and space. Usually, it is given as the total mass of stars formed per year as a function of redshift or time. There are many prescriptions of a galaxy's star-formation history describing when the main build-up stellar mass occurred. Unfortunately, it is most likely that galaxies form stars in a more complicated manner (intermittently) to that of a simple parameterisation. The main parameterisations of star formation histories are the exponentially increasing or decreasing, constant, log-normal and double power law. An excellent summary of the different types of SFHs used for fitting the SEDs of galaxies is given by Carnall et al. (2018b).

Extinction and Attenuation

Attenuation and extinction from multiple sources dramatically affects the SED shape of galaxies. The first is the absorption and/or scattering of UV/optical photons from dust grains encompassing star-forming regions within galaxies. The absorption by dust is dependent on the energy of the photons, increasingly more impactful on the shorter wavelength end of the spectrum. This makes the SED appear redder hence this process is also known as reddening. Much of the absorbed energy is re-radiated in the far-IR region of the spectrum, producing what we know as sub-mm galaxies (SMGs) or dusty star-forming galaxies (DSFGs). It is essential to recognise the difference in the definition of extinction and attenuation. Extinction quantifies the absorption of photons and scattering of photons out of the line of sight. Attenuation includes the scattering of photons back into the line of sight and thus is more relevant for an extended system such as a galaxy

Like SFHs, a lot of work has gone into parameterising the effects of extinction and attenuation on an SED. As previously stated, light at shorter wavelengths is more strongly affected by dust. This wavelength dependence can be parameterised by A_λ, which represents the total extinction at a wavelength λ. This can be used to

find the relation between the intrinsic flux of a galaxy $f_{int}(\lambda)$ and the observed flux $f_{obs}(\lambda)$ by:

$$f_{obs}(\lambda) = f_{int}(\lambda)10^{-0.4A_\lambda} \tag{1.23}$$

where A_λ is often expressed relative to the total extinction in the V-band ($\lambda \simeq$ 5500Å), A_V:

$$A_\lambda = k(\lambda)E(B-V) = \frac{k(\lambda)A_V}{R_V} \tag{1.24}$$

where $k(\lambda)$ is the extinction or attenuation curve, describing the amount of extinction or attenuation as a function of wavelength. R_V is a constant that depends on the reddening law used. The $E(B-V)$ term is defined as the colour excess or the difference in $B-V$ colour before and after the reddening.

Several different studies have attempted to determine a law which governs dust extinction and attenuation accurately. Initially, in the 1980s interstellar extinction was studied using the Small Magellanic Cloud (SMC; Prevot et al. 1984), Large Magellanic Cloud (SMC; Fitzpatrick 1986) and the Milky Way (MW; Cardelli et al. 1989). This work on resolved stellar populations gave rise to the three extinction laws known as the SMC, LMC and MW extinction laws. These three laws are largely similar at longer wavelengths between 0.3 and 1 μ m, but display slightly different features at the blue end. When attempting to extend this work to distant galaxies where we cannot resolve the stellar population, we are studying a slightly different geometry of dust extinction. For resolved stellar populations we measure the dust between the source and observer, whereas when observing distant galaxies, the stars and dust are mixed, giving rise to attenuation rather than extinction. Calzetti et al. (1996, 2000) observed star-forming galaxies in the local Universe, providing the first robust attenuation curve, known as the Calzetti Law. For high redshift science and in this Thesis, the Calzetti law is generally used, where $R_V = 4.05 \pm 0.80$.

The second form of attenuation is the absorption of UV radiation along the line of sight by the intergalactic medium (IGM) between the observer and a distant source. The neutral gas clouds that lie intermittently between the observer and the source absorbs the ionising flux from young stars. This is the cause of the Lyman break, as the majority of ionising photons at rest-frame $\lambda < 1216$ Å

are absorbed or scattered. This results in a spectrum blueward of the Lyman-α emission line showing a dramatic decrease in flux (or 'break'). The amount of flux decrement is dependent on the physical properties of the gas clouds along with the redshift of the object. The most common method of applying these decrements to an SED is using Madau (1995) and Inoue et al. (2014) prescriptions.

1.4 Star Formation

Star formation is a critical process that drives galaxy formation and evolution. Many different techniques are available for deriving the star-formation rate of a galaxy. The details, advantages and disadvantages of each technique are detailed by Kennicutt (1998) and Kennicutt & Evans (2012).

The Hubble sequence was the first real step in quantifying star-formation rates in different galactic populations. Work on galaxy colours, young stellar content and spectra aided Roberts in 1963 in understanding how the content and properties of galaxies affect the evolutionary processes and hence allowed him to outline a galactic sequence (Roberts 1963). It took another six years and evolutionary synthesis models of galaxy colours to quantify star-formation rates fully, followed by predictions of how these rates changed with a cosmic look back time (Tinsley 1968). It was not until the early 1980s that more precise methods, such as integrated line fluxes, near Ultraviolet (UV) and Infrared (IR) continuum fluxes, provided the foundation for a more complete picture of star-formation rates in a larger sample of nearby galaxies (e.g. Rieke & Lebofsky 1978; Gallagher et al. 1980; Telesco & Harper 1980; Kennicutt & Kent 1983).

The first spaced-based IR telescope, The Infrared Astronomical Satellite (IRAS) soon discovered a population of Ultraluminous InfraRed Galaxies (ULIRGs). These violent starburst galaxies were known to exist from ground-based research, but in-depth studies were only readily available now, propelling the field forward (e.g. Clements et al. 1996 and Soifer et al. 2000). Towards the end of the century, star-forming galaxies were being detected at higher redshifts. This coincided with well-calibrated techniques for measuring star-formation in the local universe, thus providing the opportunity to directly trace star-formation rates/densities along an evolutionary path with cosmic lookback time.

Lilly et al. (1996) used the comoving luminosity density calculated using data

from the Canada-France redshift survey to put a constraint on the star-formation rates of galaxies with $z < 1$. Madau et al. (1996) then looked at the redshift distribution of faint galaxies in the Hubble deep field ($2 < z < 4.5$) using colour selection criteria derived from evolutionary synthesis models (Bruzual A. & Charlot, 1993) of star-forming galaxies. This work constrained the global history of star and structure formation of galaxies up to $z \simeq 5$. A decade later, this work was calibrated and expanded by Hopkins & Beacom (2006) using updated ultraviolet and far-infrared measurements up to $z \simeq 6$. It was shown that the key to finding the star-formation rates of galaxies entirely depends on the properties of the population being studied, including the IMF. Madau & Dickinson (2014) detail the contributions made in deducing the cosmic star formation history of the universe.

1.4.1 Measuring Star Formation

Theoretically, the most effective way of measuring the star-formation rate in a galaxy is to count the number of young stars. However, as we cannot spatially resolve stars in most systems, integrated measurements of light at different wavelengths are required. This, matched with earlier work on the evolutionary synthesis models of colours allows for a good quantitative measurement of the SFR. Different tracers of star formation are sensitive to different physical properties of the galaxy. Stellar age, the IMF and stellar masses affect the region of the spectrum where the star formation dominates emission and need to be accounted for when making SFR calculations.

Looking at the spectra of galaxies, clear differences and fundamental trends are found in distinguishing star-forming galaxies from non-star forming. The former has an increase in relative blue continuum and nebular emission lines, such as Hα, along with absorption features changing from K-giant to A-star dominated. At visible wavelength ranges, main-sequence stars dominate the integrated luminosities and thus provide a method of estimating the star-formation rate using observed broadband colours. Assuming a linear relationship between the SFR and continuum luminosity is a valid method only appropriate for a galaxy dominated by young stars. The approximation, therefore, breaks down for most normal galaxies and evolutionary synthesis models are required (Bruzual A. & Charlot 1993; Bruzual & Charlot 2003).

1.4.2 UV Emission and the Luminosity Function

The UV continuum emission in most galaxies, except the oldest population, is dominated by massive and short-lived stars. For a given IMF and dust content, we can easily deduce a star-formation rate, and by limiting observations to the UV, we focus on the integrated light from young stars. Fortunately, SFR scales nearly linearly with the luminosity across the wavelength range of $1250 - 2500$ Å (Kennicutt 1998). The conversion between SFR and UV luminosity can be derived using evolutionary synthesis models and, over the years, as the models have improved the calibration of this relationship has also improved. It is always essential to use the specific conversion factor for the type of stellar population under observation. The Galaxy Evolution Explorer (GALEX; Martin et al. 2005) revolutionised this method by studying a large area of the sky across a range of UV wavelengths and gaining integrated UV fluxes for a vast number of galaxies.

The Luminosity function (LF) is a way to effectively parameterise the abundance of objects as a function of luminosity while also able to provide information about the luminosity density of objects over the entire Universe. The LF describes how many galaxies of a given luminosity are present within a defined volume of space. In order to parameterise it across cosmic time, one must assume the volume is the comoving volume, introduced in section 1.1.1. This means the LF is usually given in units of the number of objects mag^{-1} Mpc^{-3}, denoted as ϕ. The UV LF is also important in studying the high redshift Universe as it can tell us about the amount of ionising radiation at each epoch, enabling us to decide whether or not certain objects can re-ionise the Universe. The LF is often fitted with a Schechter function (Schechter 1976):

$$\phi(L) = \phi^* \left(\frac{L}{L^*}\right)^{\alpha} \mathrm{e}^{-L/L^*} \tag{1.25}$$

and in terms of magnitudes:

$$\phi(M) = 0.4 \ \ln 10 \ \phi^* [10^{0.4(M^*-M)}]^{\alpha+1} \exp[-10^{0.4(M^*-M)}] \ \mathrm{d}M. \tag{1.26}$$

It can also be used a proxy for the SFR, as the UV radiation is very closely linked to the star formation of a galaxy. This technique has been used widely in order

to estimate the SFRD of the Universe (e.g. Lilly et al. 1996; Madau et al. 1996; Madau & Dickinson 2014). The SFR can be estimated directly from the UV luminosity using the Madau et al. (1996) relation:

$$SFR(\mathrm{M}_{\odot}\mathrm{year}^{-1}) = 1.4 \times 10^{-28} L_{UV}(\mathrm{erg\ s}^{-1}\mathrm{Hz}^{-1}) \tag{1.27}$$

which assumes no dust attenuation. However, it should be noted that the UV is incredibly sensitive to extinction: the absorption and scattering due to gas and dust in the cosmos can dim sources by up to more than five magnitudes. It is clear then that using appropriate dust and extinction models is vital in order to estimate star-formation rates of galaxies using the UV luminosity accurately. It has become the normal convention to parametrise the ultraviolet (UV) continuum slopes of galaxies in terms of a power-law index, β, where $f_{\lambda} \propto \lambda^{\beta}$. The β slope is often used to estimate the attenuation from dust. Over the past decade much work has been accomplished to minimise the systematic error of this quantity. However, these calibrations rely heavily on the natural colour, the shape of the dust extinction curve and the physical properties of the system being studied.

1.4.3 Infrared

Equation 1.27 excludes any effects of extinction, which will effectively reduce the SFR calculated as the total luminosity with be underestimated. In order to accurately estimate the total SFRD from the UV light, one must correct for this loss of light from dust. As previously stated, the UV is often re-processed through to IR wavelengths meaning that to study the SFRD of the Universe effectively, we need to correct for dust or directly measure the IR emission.

To measure the IR emission from galaxies, we require space-based telescopes. The Earth's atmosphere and general thermal emission from the Earth itself inhibit our view of the IR Universe. The total IR emission of galaxies covers a vast range of wavelengths, making it more challenging to observe directly from one instrument or telescope. In fact, to ensure all re-processed light from UV absorbed photons is taken into account, one must integrate from $8 - 1000\,\mu$m. However, in practice, the majority of the IR emission will sit in the $10 - 120\,\mu$m region. The reason why the dust emits over an extended wavelength range is because of the different physical properties of the dust grains. In any case, if one were to have an accurate measurement IR luminosity (L_{IR}) over the full wavelength range, then the relation

between the L_{IR} and SFR is:

$$SFR(\mathrm{M_{\odot}year^{-1}}) = 4.5 \times 10^{-44} L_{IR}(\mathrm{erg\ s^{-1}Hz^{-1}}) \tag{1.28}$$

from Kennicutt (1998).

1.4.4 Emission Lines

One distinguishing feature between non-star-forming and star-forming galaxies is the significant increase in the number and/or flux of nebular emission lines. These signatures effectively reprocess the integrated stellar luminosity of the young stars (UV emission) within star-forming regions. Observing and measuring the flux from the emission, therefore, probes the star-formation rate and the number of young stars in a system directly. The strength of the Hα is often measured as it has a very short lifetime after star formation occurs (<20 Myr); therefore, effectively an instantaneous tracer. Again, the synthesis models have provided the conversion between ionising flux and SFR, calibrated mostly over the past 20 years (Madau et al. 1998 and (Kennicutt, 1998)) where they yield

$$SFR(\mathrm{M_{\odot}year^{-1}}) = 7.9 \times 10^{42} L(H\alpha)(\mathrm{erg\ s^{-1}Hz^{-1}}) \tag{1.29}$$

assuming a Salpeter IMF (Salpeter 1955). The limitations of this method are the sensitivity to extinction (significantly less than the UV), IMF and the assumption that most star formation is traced by ionised radiation. HII regions also release ionising radiation, and it is still unknown as to the escape fraction of the diffuse Hα emission. Constraining this would allow a tighter calibration of the conversion between Hα flux and SFR. The most recent calibrations are in Table 1.1. These were taken from Kennicutt & Evans (2012).

The age range (Column 2) is a simple indication as to the age of the stellar population that is most contributing to the emission. Columns 3 and 4 indicate the SFR conversion factor from the relevant luminosity is used in conjunction with Equation 1.30 with these values, the UV, nebular emission lines and FIR can be used to determine the star-formation rates of a galaxy.

Data	Age Range (Myr)	L_x **Units**	**log** C_x	**References**
FUV	0- 10 - 100	ergs s^{-1} νL_ν	43.35	1, 2
NUV	0- 10 - 200	ergs s^{-1} νL_ν	43.17	1, 2
Hα	0 - 3 - 10	ergs s^{-1}	41.27	1, 2
24μm	0- 5 - 100	ergs s^{-1} νL_ν	42.69	3
70μm	0- 5 - 100	ergs s^{-1} νL_ν	42.23	4
1.4 GHz	0 - 100	ergs s^{-1} Hz^{-1}	28.20	1
1 - 10 keV	0 - 100	ergs s^{-1}	39.77	5

Table 1.1 *Star-Formation Rate Calibrations from Kennicutt & Evans (2012): References (1; Murphy et al. 2011) (2; Hao et al. 2011) (3; Rieke et al. 2009) (4; Calzetti et al. 2010 (5; Ranalli et al. 2003)*

$$\log\dot{M}(\mathrm{M}_\odot \mathrm{year}^{-1}) = \log L_x - \log C_x \tag{1.30}$$

Lyman-α has been used widely over the past decade as a tracer for star formation, largely due to its sensitivity to low mass star-forming galaxies, along with it being approximately 8.7 times stronger than the Hα line. It is predominantly utilised as a means for identifying a star-forming region rather than calculating the star-formation rate itself. The trapping and absorption of photons from dust provides relatively inaccurate SFRs, and at higher redshifts, the rise of the Lyman-α forest inhibits our observations further. Lyman alpha photons resonantly scatter off neutral hydrogen, so an accurate escape fraction is also required to account for this discrepancy in calculating the SFR (e.g. Atek et al. 2009; Hayes et al. 2011).

1.5 Galaxy Surveys

Galaxy imaging surveys have provided the primary database for extragalactic astronomy. The community uses data from galaxy surveys in many different ways, such as identifying new objects and contextualising galaxy properties across cosmic time. In this section, I provide a brief overview of the major telescopes used to conduct both space-based and ground-based galaxy surveys.

1.5.1 Spaced Based Surveys

The Hubble Space Telescope (*HST* or *Hubble*) is a space telescope in a low Earth orbit, launched in 1990 [2]. It has a 2.5m mirror with four instruments studying the UV, Optical and near-IR region of the EM spectrum. The two main imaging instruments on-board *HST* are Advanced Camera for Surveys (ACS) and the Wide Field Camera 3 (WFC3). The ACS is capable of imaging from near-UV to near-IR (115 nm $< \lambda <$ 1050 nm). WFC3 operates in two channels, the UVIS which observes the UV/optical ($\lambda = 200 - 1000\,\mathrm{nm}$) and the IR channel observing the near-IR ($\lambda = 900 - 1700\,\mathrm{nm}$).

Several programmes and surveys have been conducted using HST, some entirely using HST's instruments alone while other used in conjunction with other space-based or ground-based telescopes. There have also been a number of surveys from different telescopes accepted and conducted based on the use of ancillary *HST* data. The James Webb Space Telescope (*JWST* or Webb) is an IR optimised telescope expected to be the successor of Hubble, however, to ensure the full efficiency and effectiveness of *JWST* data, ancillary *HST* will be required. In this section, I will provide a review the current surveys conducted with *HST* and other instruments.

HDF and UDF

One of the first deep fields observed by *HST* was the Hubble Deep Field (HDF), covering about $\simeq 5$ arcmin^2 in the early 90s using the Wide Field and Planetary Camera 2 (WFPC2). A total of four broadband filters were used covering the near-UV to near-IR (300−814 nm) with approximately $\simeq$ 35−45 hours of total exposure time in each filter. The small region of observations meant that there were very few foreground stars contaminating the image, meaning the $\simeq$ 3000 objects detected were galaxies, including the most distant observed at that time. This wealth of data enabled the extensive study galaxies across a range of epochs, allowing astronomers to initially estimate the SFH of the Universe to $z \simeq 4$ (Madau et al. 1996). Using the Lyman-break technique galaxies were observed out to the highest redshifts probed so far where UV LF was constrained out to $z \simeq 4$ with additional ground-based spectroscopic data from Keck (Steidel et al. 1999, 2000). The success of the HDF observations then led to additional coverage

[2] `http://www.stsci.edu/hst/HST_overview`

called the Hubble Deep Field South (HDF-S) following a very similar strategy.

It was not until 2002, when one of the most important instruments on-board *HST* was installed, the ACS. It unveiled a statistical sample of galaxies beyond $z > 5$. Primarily because of the improvement in sensitivity at the red end of the optical spectrum and which pushed our ability to observe the Lyman-break of LBGs to higher redshifts. Not only was this because of the now extended wavelength coverage, but the increase in depth enabled the discovery of an increasing number of faint galaxies. A single pointing of 11 arcmin^2 was conducted with HST/ACS in a similar set of filters to that of the HDF, called the UDF. Subsequently, the HDF became the centre of the Great Observatories Origins Deep Survey (GOODS) field, a shallower but broader survey. This UDF which became the centre of the GOODS-South (GOODS-S) field while the original GOODS field became known as the GOODS-North (GOODS-N) field. The increase in the area enabled the discovery of brighter but rarer LBGs at redshifts up to $z \simeq 6$ (e.g. Bouwens et al. 2006; Beckwith et al. 2006), which in turn constrained the evolution of the number densities in this new redshift regime for galaxies.

Additional observations in the HUDF were made possible with the installation of the Wide Field Camera 3 (WFC3) in 2009. The IR channel of WFC3 was used to obtain images from 1−1.6 μm in three filters. Subsequently, this opened the door to extending LBG selection beyond $z > 7$. Specifically, the UDF09 observing programme obtained deep Y_{105}, J_{125} and H_{160} over 4.5 arcmin^2 enabling LBG selection out $z \simeq 8$ producing the first LF at these extreme redshifts (e.g. Oesch et al. 2010; Bouwens et al. 2010; McLure et al. 2010). The number of galaxies detectable at $z > 7$ was increased with additional *HST* data in the UDF in 2012 (UDF12) pushing the limit to $z \simeq 8$ (e.g. Ellis et al. 2013; Schenker et al. 2013; McLure et al. 2013b; Bouwens et al. 2014).

CANDELS and HFF

The Cosmic Assembly Near-infrared Deep Extragalactic Legacy Survey (CANDELS: Grogin et al. 2011; Koekemoer et al. 2011; Fig. 1.7) is a programme using both the ACS and WFC3 cameras on-board *HST* aiming to study the evolution of galaxies in the early Universe from $z = 1$−8. There are five fields in total; the Ultra Deep Survey (UDS), the Extended Growth Strip (EGS), GOODS-N, GOODS-S and the Cosmic Evolution Survey (COSMOS). Initially, it was planned that *HST* would study these five fields using the WFC3/IR and ACS cameras for

more than 250,00 galaxies in order to detect bright galaxies across a much wider area than the Hubble fields.

CANDELS was used in conjunction with the The 2012 Hubble Ultra Deep Field (UDF12) pushing the LF boundary out to $z \simeq 8$ (e.g. Schenker et al. 2013; McLure et al. 2013b; Bouwens et al. 2014). However, the huge increase in area coverage meant that the statistical sample of high-redshift galaxies significantly increased. This wider area allows the bright end of the LF to be better sampled, detecting the more luminous (and therefore rare) galaxies.

The Hubble Frontier Fields (HFF; Lotz et al. 2017) is an *HST* programme centred on galaxy clusters utilising the magnification from gravitational lensing to observe very faint high redshift galaxies, potentially too faint to be detected through traditional observations ($m_{AB} \simeq 29.0$ mag). HFF used *HST* to observe six cluster fields(Abell 2744, MACSJ0416.1-2403, MACSJ0717.5+3745, MACSJ1149.5+2223) lying between redshift $z \simeq 0.2 - 0.33$ with analogous parallel blank-field observations in both the HST/ACS and HST/WFC3 instruments. Additional *Spitzer* data in the 3.6 and 4.5 μm bands was taken to complement the UV/optical to near-IR *HST* observations. HFF also has complementary data from a previous lensing survey Cluster Lensing And Supernova survey with Hubble (CLASH; Postman et al. 2012). The increased depth through lensing has produced some LBGs out to redshift $z \simeq 9 - 11$ (e.g. Coe et al. 2013; Zitrin et al. 2014; McLeod et al. 2015) with substantial numbers of $z > 6$ galaxies (e.g. Atek et al. 2014; Livermore et al. 2017).

Fig. 1.8 shows the UV LF derived by McLeod et al. (2016) along with comparative studies from Oesch et al. (2014). The evolution of the UV LF is shown by the solid blue lines from Bowler et al. (2015), a Schechter function fit to data from the ground-based near-IR UltraVista survey. The UV LF derived from McLure et al. (2013b) is also shown, represented by the solid pink line. McLure et al. (2013b) used objects selected in the HUDF to SED-fit ACS, WFC3/IR, *Spitzer* (3.6μm and 4.5μm), Subaru (z′), VLT (Y) and UKIRT (K) photometry, and shows a steeper fall off in the UV LF at $z \geq 8$. This plot nicely summarises the work that has been done in constraining the shape of the UV LF out to the highest redshift using the data and techniques described in Section 1.2 and 1.5.

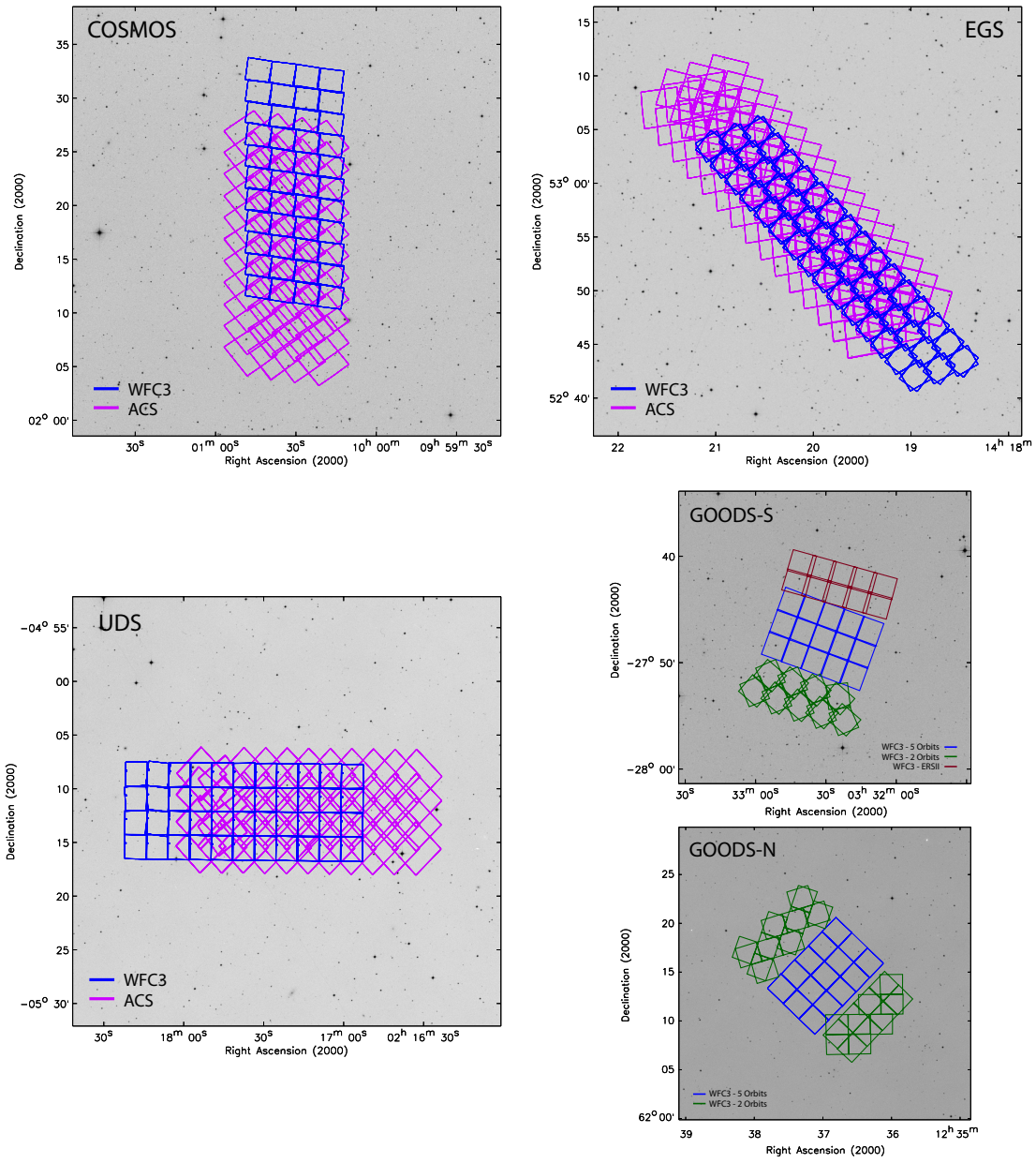

Figure 1.7 *Maps of the deep HST WFC3 and ACS pointings in the five CANDELS (Grogin et al. 2011; Koekemoer et al. 2011) survey fields* `http://arcoiris.ucolick.org/candels/survey/field_maps/All_Fields.wlegends.pdf`

IR

Extension to longer near/mid-infrared wavelengths has proven more difficult, as it is virtually impossible to achieve imaging of sufficient depth from the ground at $\lambda > 2.3\,\mu$m for the study of distant galaxies. The first space-based surveys in the

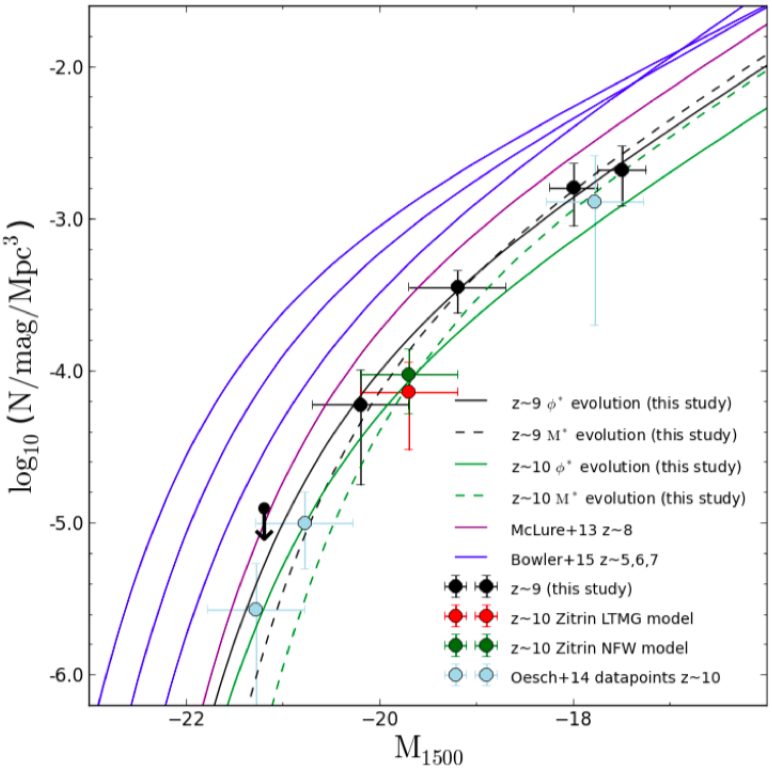

Figure 1.8 *The $z \simeq 8$–9 UV LF calculated by McLeod et al. (2016) based on data from the HFF and CLASH surveys (Black points, solid/dashed lines and Green solid/dashed lines). McLeod et al. (2016) compared their results with other $z > 8$ UV LF work from Oesch et al. (2014), represented by the light blue point. The evoltuion of the UV LF from Bowler et al. (2015) is also plotted (solid blue lines) along with the $z \simeq 8$ UV LF from McLure et al. (2013b).*

IR were conducted by The Infrared Astronomical Satellite (IRAS) in 1983 aiding the first measurements of the far-IR luminosity function (FIRLF) (e.g. Lawrence et al. 1986; Soifer et al. 1987; Sanders 2003). IRAS covered a small fraction of the IR spectrum from 12 to 100 μm, but AKARI extended this to 160μm which probed the bolometric luminosity more accurately.

The provision of useful data at $\lambda \simeq 3 - 30\,\mu$m has had to rely on the much smaller *Spitzer Space Telescope*. *Spitzer* was equipped with three instruments: Infrared Array Camera (IRAC), Infrared Spectrograph (IRS) and Multiband Imaging Photometer for *Spitzer* (MIPS). IRAC has four filters covering 3.6 - 8 μm which complimented the *HST* imaging surveys very nicely by extending the wavelength range of much of the data. MIPS had three detector arrays centred on 24μm, 70μm and 160μm. The data produced by deep surveys with the IRAC and MIPS instruments on-board *Spitzer* have been undeniably impressive (e.g. Sanders et al. 2007; Damen et al. 2011; Ashby et al. 2013, 2015, 2018; Labbé et al. 2013, 2015), and have demonstrated the power of such longer-wavelength imaging for rest-frame optical/near-infrared studies to the very earliest times (e.g. Dunlop 2013; Stark 2016), but nonetheless they are ultimately limited in angular resolution (> 1.5 arcsec) and depth (to $m_{AB} \simeq 25$ mag) by the small (85-cm) aperture of *Spitzer*.

The *Herschel Space Observatory* improved the sensitivity capabilities for FIR observations (70−500 μm) observing with three instruments; Photodetecting Array Camera and Spectrometer (PACS), Spectral and Photometric Imaging Receiver (SPIRE) and Heterodyne Instrument for the Far Infrared (HIFI). PACS is an imaging camera and spectrograph covering 55 - 210μm, while SPIRE extended the total wavelength coverage from 192−672μm. Several surveys were conducted over the most well-studied regions of the sky (GOODS-S, GOODS-N and COSMOS). *Herschel* did not reach the depths of the deepest *Spitzer* 24 μm imaging but the extended wavelength range allowed for direct access to the re-radiated UV emission from dusty galaxies enabling excellent estimation of the star-formation rates. This was particularly valuable therefore in constraining the SFH out to the highest redshift contributed from obscured star-formation (e.g. Gruppioni et al. 2010, 2013; Rowan-Robinson et al. 2016).

The work on the IRLF produces two primary results. Firstly, the IRLFs cut off less steeply at high luminosities in comparison to the UVLF. Secondly, the IRLF extending to much higher luminosities than the UVLFs at similar redshifts. This is due to the immense SFR exhibited by star-forming galaxies that are enshrouded

by dust.

1.5.2 Ground-based surveys

UV to near-IR

Simultaneously, as the Hubble fields were being used to observe the highest redshift LBGs to date, ground-based telescopes were making observations in the UV/optical and near-IR over much larger scales. Subaru and The United Kingdom Infra-Red Telescope (UKIRT) were at the forefront of ground-based observations collecting data in the UV/optical and near-IR over degree scales. In particular, the Subaru Deep Field (SDF) and the UKIRT Infrared Deep Sky Survey (UKIDSS) Ultra Deep Survey (UDS), also known as the Subaru/XMM-Newton Deep Field (SXDF) provided substantial datasets. These wide-area, but relatively shallow surveys, detected brighter and rarer objects to a depth of $z' \simeq 26$ mag (e.g. Shimasaku et al. 2005 and McLure et al. 2006, 2009). For comparison, the combined UDF, two parallel fields and GOODS-N/S fields have a total area of $\simeq 300$ arcmin^2 but extend to depths of $z_{850} \simeq 27.5{-}29$ mag.

The Visible and Infrared Survey Telescope for Astronomy (VISTA) is a 4-m ground-based telescope built to study wide-area surveys in the Optical and near-IR region of the EM spectrum. It has the ability to study in 5 separate filters; Z, Y, J, H, K_s and $NB118$. Numerous wide-field surveys have been conducted using VISTA; however, for this Thesis, the most important one is UltraVISTA (UVISTA: McCracken et al. 2012; Bowler et al. 2014). UltraVISTA is an ultra-deep near-IR survey with the European Southern Observatory (ESO) VISTA survey telescope. Over the course of 10 years, UltraVISTA has repeatedly imaged the COSMOS field in four broad-bands and one narrow- band (Y, J, H, Ks and NB188, respectively) split into the separate surveys. The first is an ultra-deep broad-band (Y, J, H and Ks) set of strips covering 0.73 deg^2 (1408hr), the second is a contiguous shallower but wider broad-band survey (Y, J, H and Ks) covering 1.5 deg^2 (212hr) while the third is a narrow-band imaging survey covering the entire ultra-deep area. The resulting data has been used to study the high-redshift Universe, selecting some of the brightest and rarest objects detected at $z > 6$, Bowler et al. 2012, 2014, 2015. Another important survey conducted with VISTA was the VISTA Deep Extragalactic Observations (VIDEO; Jarvis et al. 2013) survey which provided near-IR data covering the entire UDS field (> 4.5

deg^2).

Another important ground-based telescope is the Canada France Hawaii Telescope (CFHT) located near the summit of Mauna Kea in Hawaii. The CFHT obtains observations using a 3.6m mirror with a total of four instruments in current use; MegaCam, WIRCam, ESPaDOnS and SITELLE. The MegaCam (Boulade et al. 2003) is a wide-field imager with a square deg field of view housing five filters covering 0.3−1μm (u, g, r, i, z). The CFHT Legacy Survey (CFHTLS; `http://www.cfht.hawaii.edu/Science/CFHLS/`) was a wide-field survey conducted with the CFHT MegaCam covering the COSMOS field. It provided complimentary optical data to the UltraVISTA survey of COSMOS.

Sub-mm

The near-IR and mid-IR are very difficult to observe from the ground, as the thermal emission from the Earth's atmosphere and the Earth itself inhibits our view of the sky. The sub-mm, however, is visible from the ground making this region of the spectrum readily accessible over large areas of the sky. In particular, the two most critical sub-mm telescopes are the James Clerk Maxwell Telescope (JCMT) and the Atacama Large Millimetre/sub-millimetre Array (ALMA).

The JCMT is a sub-mm telescope based at the at Mauna Kea Observatory in Hawaii that house the Submillimetre Common-User Bolometer Array (SCUBA; Mortier et al. 2005). SCUBA operated at 450 and 850mm wavelengths simultaneously between 1997 and 2003. Subsequently, SCUBA was replaced by the next generation instrument, SCUBA-2, in 2011. SCUBA-2 operated at the same wavelengths as SCUBA.

Surveys carried out using SCUBA in the HUDF uncovered a significant population of sub-mm bright galaxies (SMGs - e.g. Smail et al. 1997; Hughes et al. 1998; Barger et al. 1998) where it was concluded that these galaxies show the most extreme levels of star-formation (100-2000 $M_{\odot}yr^{-1}$) in the entire Universe. This was a significant breakthrough, as approximately half of the star-formation activity in the Universe is undetected by the traditional UV/optical studies of high-redshift galaxies. Since then, the role of SMGs in galaxy evolution and formation has been studied extensively in an attempt to understand what drives the immense star-formation rates (SFR) observed (see reviews; Blain et al. 2002 and Casey et al. 2014).

ALMA is an astronomical sub-mm/mm interferometer, comprised of 66 radio telescopes in the Atacama Desert of northern Chile. ALMA covers the wavelength range of 300μm to 9.6mm. More recent SCUBA-2 and ALMA surveys covering the most well-studied fields (COSMOS, UKIDSS-UDS, GOODS and EGS) have provided multi-wavelength data from the UV to mm (e.g. Geach et al. 2016; Dunlop et al. 2017). These data enabled direct comparisons between star-forming galaxies selected by UV and IR emission sparking a debate as to the contribution to the total SFRD in cosmic time from obscured to unobscured SF (e.g. Koprowski et al. 2017; Dunlop et al. 2017; Bourne et al. 2017; Wang et al. 2019). This topic is explored in more detail in the next Section and Chapter 5.

1.6 Star Formation History of the Universe

One of the most common ways to probe galaxy evolution across cosmic time is through the cosmic star formation history. This is done by calculating the volume-averaged star-formation rate as a function of epoch (ψ) in units of $M_{\odot}yr^{-1}Mpc^{-3}$. Often this is accomplished by calculating the SFR of a galaxy using one of the methods outlined in Section 1.4.1 and placing it in terms of cosmic time using the estimated redshift.One method not fully discussed in Section 1.4.1 is the use of the LF in determining the SFR. Once the LF at a certain redshift has been determined, one can calculate the UV luminosity density (often denoted as ρ_{UV} through a luminosity weighted integration of the Schecter function (see Section 1.4.2 and Equation 1.4.2. This ρ_{UV} is, therefore, an observational proxy for the cosmic star formation rate density at a given epoch (ψ).

Work done by Lilly et al. (1996) showed the star-formation rate density (SFRD) rises from the present day to redshift $z \simeq 1$ as $(1+z)^4$. Subsequent observations and measurements of the UV emission (e.g. Hogg et al. 1998; Wyder et al. 2005; Schiminovich et al. 2005; Robotham & Driver 2011) and IR emission (e.g. Sanders 2003; Takeuchi et al. 2003) supported this steep rise in SFRD. This indicates that the majority of the stars in galaxies today formed at $z > 1$. It is therefore clear that the peak of star formation in the Universe is lying at $z > 1$, but exactly when is still under scrutiny.

This analysis was extended out to redshift $z \simeq 4.5$ which shows the SFRD flatten at $z \simeq 2$ with a slightly drop in the SFRD beyond this point (e.g. Madau et al. 1996, 1998; Hopkins & Beacom 2006). Multiple observations over the course of

the following decade were made which constrained the shape of the SFRD to $z \simeq 6$ by using both the UV emission (e.g. Dahlen et al. 2007; Reddy & Steidel 2009; Cucciati et al. 2012; Bouwens et al. 2012) and IR emission (e.g. Magnelli et al. 2011, 2013; Gruppioni et al. 2013). The work is summarised in Madau & Dickinson (2014), where the efforts are combined into a consensus best-fitting SFRD function $\psi(z)$:

$$\psi(z) = 0.015 \frac{(1+z)^{2.7}}{1 + \left[\frac{(1+z)}{2.9}\right]^{5.6}} \, \mathrm{M_\odot \ yr^{-1} \ Mpc^{-3}} \tag{1.31}$$

which is represented by the solid black line in Fig. 1.9.

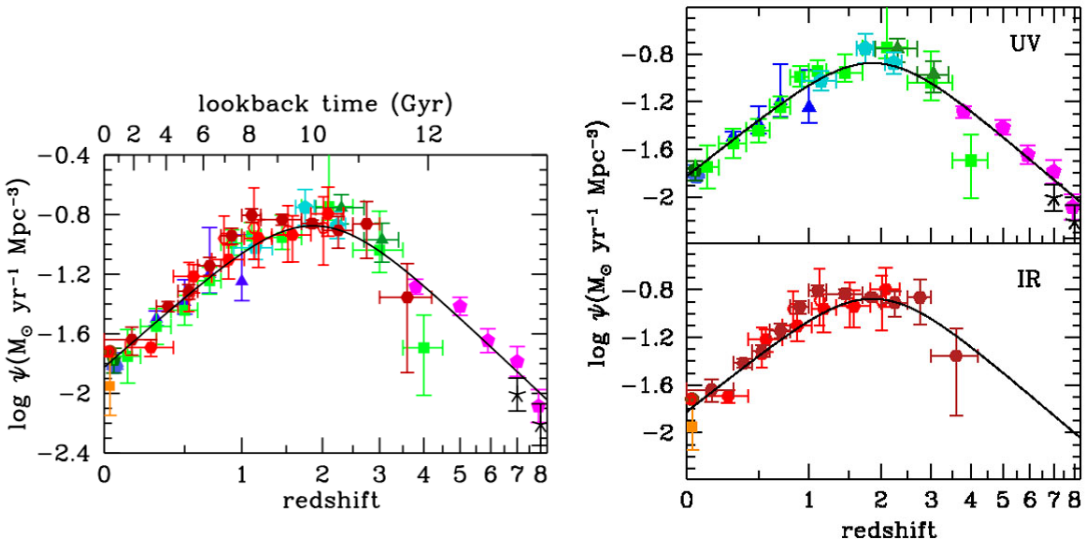

Figure 1.9 *The Star Formation History of the Universe using the FUV+IR (left panel) data described in Madau & Dickinson (2014). The right panel highlights the two FUV (top right) and IR (bottom right) samples used to create the combined SFHU. All the SFR were calculated using the methods described in Section 1.4.1 valid for a Salpeter IMF. Notice the lack of IR data beyond $z \simeq 3$.*

The peak of star formation in the Universe lies in the redshift range $1 < z < 3$ with a decline from redshift $z \simeq 1$ - 3 to present day after what appears to be a rapid early rise from the Big Bang. The exact location of this peak is under some scrutiny with more recent studies based on UV and IR emission, suggesting it could sit at a slightly earlier time. Madau & Dickinson (2014) and Behroozi et al. (2013) suggest it sits approximately at $1.5 < z < 2$, while more recent studies have reported peaks at $2.0 < z < 2.5$ (e.g. Koprowski et al. 2017; Dunlop et al.

2017; Wang et al. 2019). However, arguably the complete census of obscured star formation at $z > 3$ has yet to be completed. This is because most obscured star formation seems to be concentrated in the rare, high mass objects and therefore large area surveys, with good redshift information are required. A lot of work in recent years has gone into understanding the shape of obscured SFRD beyond $z \simeq 3$; notice the lack of IR data beyond $z \simeq 3$ in Fig. 1.9. Gruppioni et al. (2013), Rowan-Robinson et al. (2016) and Wang et al. (2019) report a shallower/ non-existent decline in dust-obscured SFRD from $z \simeq 3$ to $z \simeq 6$. However, work by Dunlop et al. (2017); Bourne et al. (2017) and Koprowski et al. (2017) using SCUBA-2 and ALMA data suggest that there is a dramatic decrease at high-redshift in the SFRD from dust-obscured star formation, driven by the decline in the number of dusty star-forming galaxies in the early Universe with increasing lookback time.

Another contentious issue is the relative contribution to the SFRD of the Universe from obscured and unobscured star-formation. The nature and prevalence of obscured star formation at high redshift is still uncertain. There is evidence suggesting that at lower redshifts ($z < 3$) the evolution of SFRD is dominated by obscured star formation, while at high redshift ($z > 4$) unobscured UV luminous sources are the dominant contributors (e.g. Burgarella et al. 2013;Gruppioni et al. 2013; Dunlop et al. 2017; Bourne et al. 2017; Koprowski et al. 2017; Wang et al. 2019). In Chapter 5, I cover this in much more detail and attempt to add to the current literature.

1.7 Thesis Outline

The structure of the remainder of this Thesis is as follows. In Chapter 2, I first present an overview of the James Webb Space Telescope (*JWST*), providing an outline of the instruments onboard, including a detailed description of the Mid-Infrared Instrument (MIRI). I then introduce a piece of software that I have built to simulate observations that will be made using MIRI onboard *JWST*. This software, developed in part as an independent check on the performance of the official MIRI simulator (MIRISim), is capable of simulating all of MIRI's available observing modes: MIRI Imager, Low-Resolution Spectrograph (LRS), Medium Resolution Spectrometer (MRS). I also present an analysis of a set of simulations of a star-forming galaxy at high-redshift and our ability to observe such an object with the MIRI MRS. I conclude Chapter 2 with a description of a set of tests

conducted to assess how accurately my simulator reproduces simulations made with the official Exposure Time Calculator (ETC) and the official MIRI test team simulator (MIRISim).

In Chapter 3, I provide an overview of a deep extragalactic imaging proposal submitted for the Director's Discretionary Early Release Science (DD-ERS or ERS) programme, Public Release Imaging for Extragalactic Research (PRIMER). I also include a detailed overview of the currently accepted programmes that aim to study high-redshift galaxies with either NIRCam or MIRI imaging. In Chapter 4, I present the work completed in Kemp et al. (2019), which utilised an observing strategy similar to our ERS proposal, in order to analyse the effectiveness of NIRCam and MIRI observations, in particular for studying dusty star-forming galaxies at high redshift. Then in Chapter 5 I attempt to quantify the prevalence of dusty star-forming galaxies and their contribution to the total star formation in the Universe as a function of redshift using available ground-based data from UV/optical/near-IR and sub-mm telescopes. In doing so, I attempt to quantify the potential impact of MIRI parallel observations. Finally, in Chapter 6, I provide a brief overview of the entire Thesis and discuss avenues for future research, in particular looking forward to the launch of *JWST*.

2

Simulating observations of high-redshift galaxies with *JWST*+MIRI

This Chapter provides a detailed introduction to the James Webb Space Telescope (*JWST*), focusing on the Mid-Infrared Instrument (MIRI), and then introduces a piece of software I have built to simulate observations that will be made using MIRI. This piece of software is capable of simulating all of MIRI's available observing modes: MIRI Imager, Low-Resolution Spectrograph (LRS), Medium Resolution Spectrometer (MRS). This software is then used to show the potential of measurements of the Hα emission line in high-redshift star-forming galaxies using the MRS IFU, while also outlining the tests undertaken to quantify the accuracy with which the independent simulator makes observations. I show that with approximately $\simeq$ 6-hour integration time with the MIRI MRS, the Hα emission line can be detected in a $m_{AB} \simeq 25$ mag, $z \simeq 7$ galaxy with a SNR of approximately $\simeq 11$. Therefore, I conclude that the MIRI MRS could be an impressive tool for determining the star-formation rates of $z > 7$ galaxies.

There are a large number of acronyms I will be using throughout this chapter and so, for ease of following the text, I present a list of the most common ones below:

CSA - Canadian Space Agency
ESA - European Space Agency
FOV - Field of View
FGS - Fine Guidance Sensor
FQPM - Four Quadrant Phase Methods
HST - Hubble Space Telescope
IFU - Integral Field Unit
IOC - Input optical Calibration
ISIM - Integrated Science Instrument Module
LRS - Low Resolution Spectrometer
LW - Long-Wavelength
MIR - Mid-InfraRed
MIRI - Mid-Infrared Instrument
MRS - Medium Resolution Spectrometer
NASA - National Aeronautics and Space Administration
NIR - Near-InfraRed
NIRCam - Near-Infrared Camera
NIRISS - Near-Infrared and Slitless Spectrograph
NIRSpec - Near-Infrared Spectrograph
PTC - Pulse Tube Cooler
SMO - Spectrometer Main Optics
SOC - Science and Operation Center
SPO - Spectrometer Pre Optics
STScI - Space Telescope Science Institute
SW - Short-Wavelength
TESS- Transiting Exoplanet Survey Satellite

2.1 *JWST*

The James Webb Space Telescope (*JWST* or *Webb*) is a large infrared (IR)-optimised space laboratory, depicted in Fig. 2.1. *JWST* is the result of a collaboration between NASA, ESA and CSA based on an idea in 1996 that the Hubble Space Telescope (*HST*) would eventually require a successor. In fact *JWST* has now become the larger successor to both *HST* and *Spitzer*. *JWST* has a 6.5m diameter primary mirror providing a total area of approximately $\simeq 25\text{m}^2$, dwarfing the *HST* 2.4m and *Spitzer* 0.85m mirrors. *JWST* was initially expected to launch at some point between 2008 and 2013; however, a series of delays caused by the sheer complexity of the mission have now pushed back the launch date to at least 2021. *JWST* will be launched using an Ariane 5 rocket, one of the most reliable rockets ever built (80 successful launches), provided by the European Space Agency (ESA). The launch site for the Ariane 5 is the Ariane space's ELA-3 launch complex at the European Spaceport located near Kourou in the French Guiana. In general, it is beneficial for rockets to be launched from close to the equator, as the spin from the Earth (1670km/hr) provides an additional push, reducing the total fuel required for launch. The extra push is even more import for *JWST* as the size of the instruments puts a tremendous amount of strain on the payload mass regulations.

The Ariane 5 rocket will propel *JWST* to 1.5×10^6 km anti-sunward from Earth to Lagrangian point two (L2). At a Lagrangian point, the gravitational system between Earth, the Sun and *JWST* itself, creates a situation where these three bodies can stably orbit one another while staying in the same position, relative to each other (i.e. *JWST* will orbit the Sun with the Earth). This position has many benefits, such as an uninterrupted view of the surrounding Universe with no worry of orbiting in and out of the Earth and Moon shadow while also allowing direct communication with *JWST* throughout its operations. Unlike *HST* in a low-earth orbit, at L2, *JWST* will benefit significantly from the lack of thermal emission produced by the Earth. This excellent location means that several satellites have been placed at L2 previously: the *Herschel* Space Observatory, *Planck*, the Deep Space Climate Observatory (*DSCOVR*; formerly known as Triana), the Global Geospace Science *(GGS)* Wind satellite and the Advanced Composition Explorer *(ACE)*. Interestingly, the orbit at L2 is only metastable, meaning that an object sitting at L2 will gradually drift away. This forces *JWST* to constantly use small amounts of fuel to orbit L2 with a radius similar to that of the Moons orbit around Earth. The Ariane 5 rocket itself only has a small compartment (4.57×16.19m)

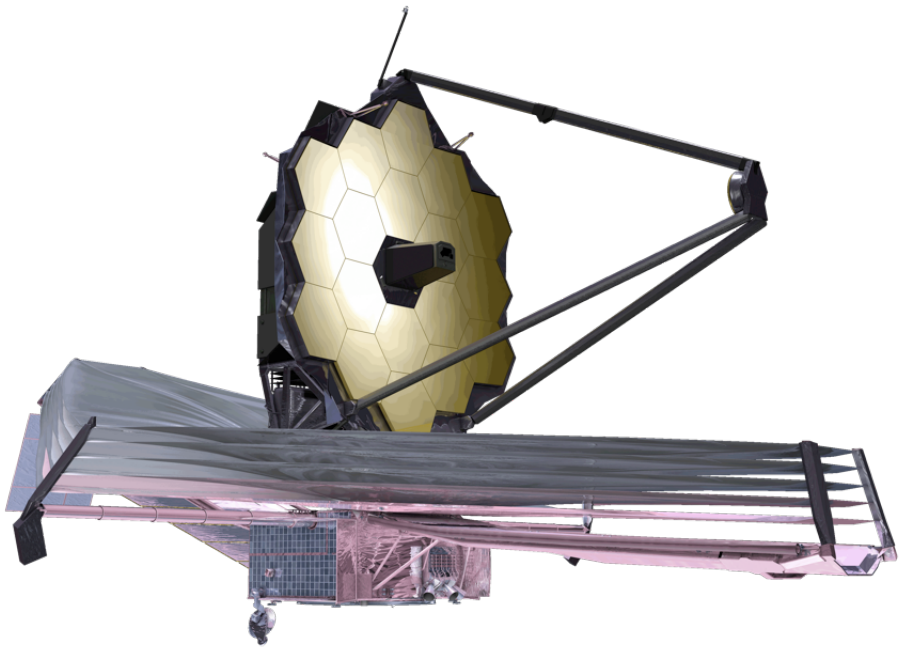

Figure 2.1 *A simulated image of the James Webb Space Telescope (JWST) showing the gold mirror (6.5m) and the six-layered silver sunshield (22m). The spacecraft bus lies beneath the mirror, while the instruments sit in the heart of the observatory, between the primary mirror and the spacecraft bus.*

in which to fit the large *JWST* mirror (6.5×6.5m) and sunshield (15×22m). For *JWST* to fit, it must fold up and be packed inside the compartment. Therefore during the journey from Earth, the telescope must be unfolded to its original state to be ready to observe the Universe when it arrives at L2.

JWST is equipped with four main instruments: NIRSpec (Near Infrared Spectrograph), MIRI (Mid-Infrared Instrument), NIRCam (Near-Infrared Camera), and FGS/NIRISS (Fine Guidance System/Near-InfraRed Imager and Slitless Spectrograph). NIRCam, NIRSpec and NIRISS will operate in the near-IR part of the EM spectrum, $0.6 < \lambda < 5\mu$m, while MIRI will cover the mid-IR, $5 < \lambda < 30\mu$m. Each instrument provides both imaging and spectroscopic observations at a range of resolutions in several different observing modes. The Integrated Science Instrument Module (ISIM) contains all of the instruments and the respective subsystems as one payload. Looking at Fig. 2.1, the ISIM sits directly behind the primary 6.5m mirror at the heart of *JWST*.

The headline scientific goals for *JWST* have been split into four broad categories/themes;

1. ***First Light and Reionisation***
2. ***The Assembly of Galaxies***
3. ***The Birth of Stars and Protoplanetary Systems***
4. ***Planetary and the Origins of Life***

Details of the scientific cases can be found at `https://jwst.nasa.gov/content/science/index.html`.

2.2 *JWST* Instruments

An overview of the four *JWST* instruments (NIRSpec, NIRCam, MIRI and FGS/NIRISS) is provided in Fig. 2.2, along with their respective positions in the *JWST* focal plane.

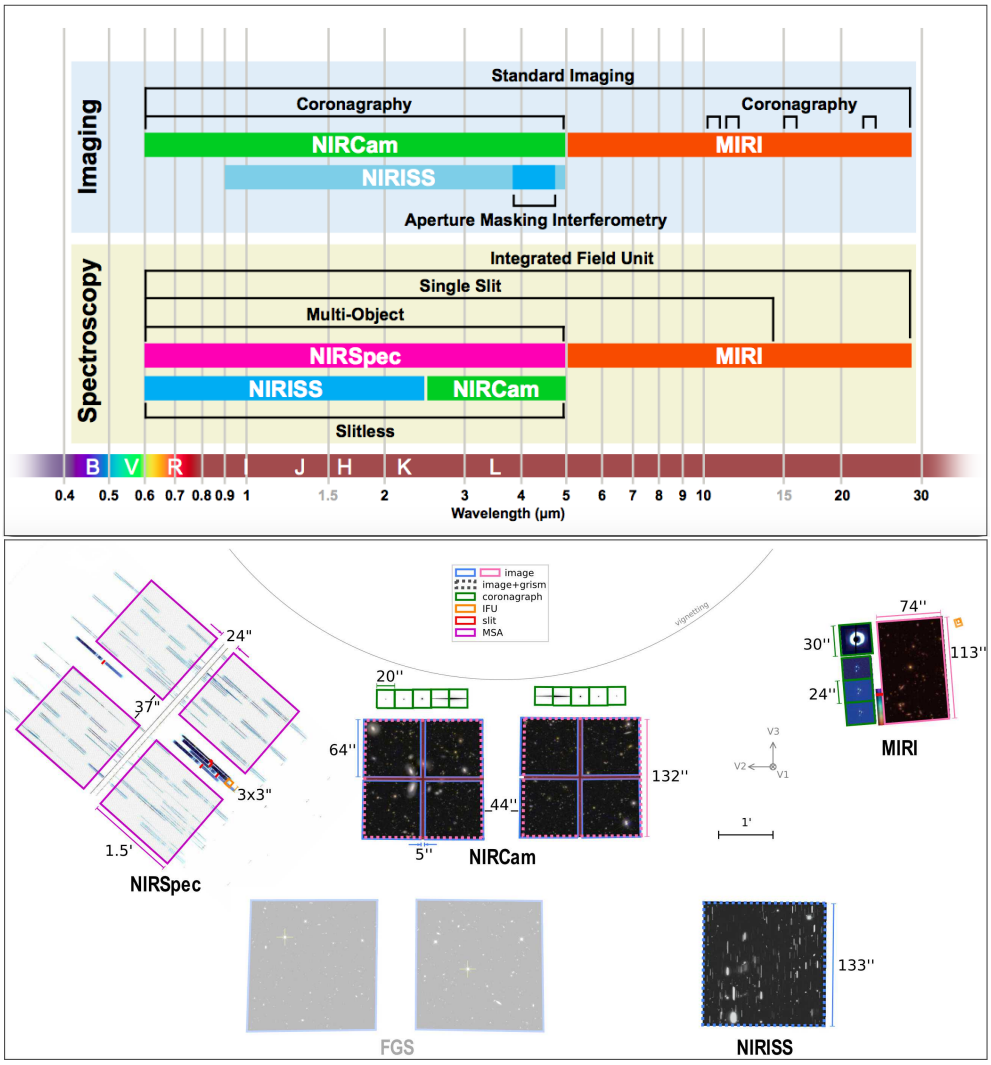

Figure 2.2 *Upper Panel: An overview of the JWST instruments and the region of the IR spectrum to which each observing mode will provide access. The wavelength in microns is plotted on the x-axis with MIRI, NIRCam, NIRISS and NIRSpec represented by red, green, pink and blue respectively. Lower Panel: The JWST focal plane showing the relative positions of all the instruments on the sky.* `https://jwst-docs.stsci.edu`

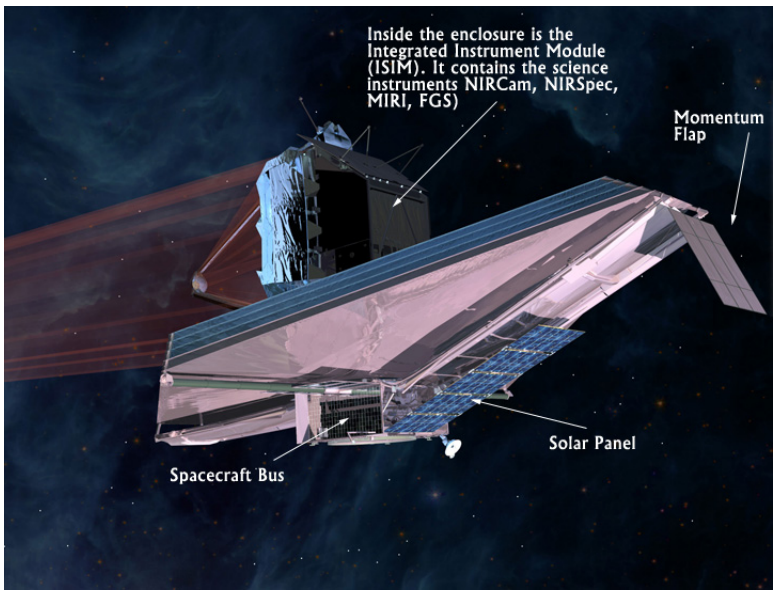

Figure 2.3 *A simulated image of the rear-view of JWST, highlighting where the ISIM sits with respect to the rest of the telescope. Also shown are the locations of the spacecraft bus, solar panels and momentum flap.* `https://jwst.nasa.gov/content/observatory/instruments/index.html`

2.2.1 Integrated Science Instrument Module (ISIM)

The Integrated Science and Instrument Module is a cage-like structure surrounding and protecting the four cameras and instruments on-board *JWST*. The ISIM itself can be split into many self-contained structures; ISIM Subsystem, ISIM Thermal Control Subsystem, ISIM Control and Data Handling Subsystem, ISIM Flight Software and the ISIM Harness Assemblies. Fig. 2.3 show the rear-view of *JWST* indicating the location of the ISIM and its contents. The ISIM sits right in the heart of *JWST* just behind the primary mirror where it is completely protected by the sunshield [1].

The ISIM is made up of three components; *i*) the cage containing NIRCam, MIRI NIRSpec and NIRISS/FGS protected with a radiated observatory enclosure (cryogenic instrument module) *ii*) the ISIM Electronic Compartment (IEC) containing the electronic equipment for all the instruments contained in a thermally controlled environment and *iii*) the ISIM Command and Data Handling (ICDH), cryo-cooler compressor and cryo-cool electronics. Component 1 chills the detectors to an initial operating temperature of ~40K, preventing contamination

[1] `https://jwst.nasa.gov/isim.html`

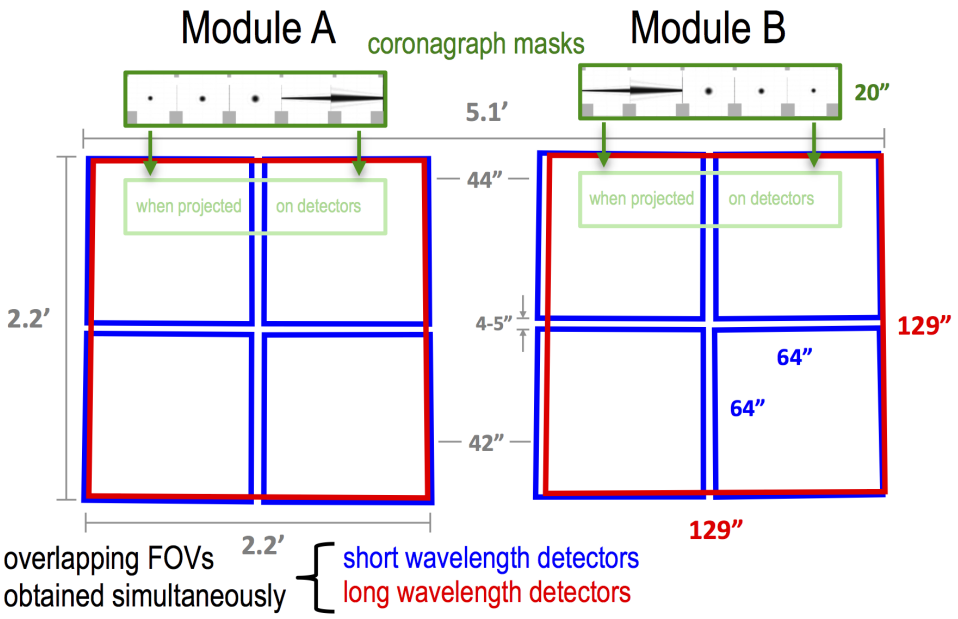

Figure 2.4 *The NIRCam FOV, highlighting the two modules, A (left) and B (right). Each module simultaneously observes a parallel region of the sky, separated by a* $\simeq 44''$ *gap. NIRCam can observe in both the short-wavelength (SW) and long-wavelength (LW) channel concurrently, represented by the blue and red solid lines respectively. The SW channel has four detector arrays creating smaller detector gaps, while the LW channel is a single detector array.* `https://jwst-docs.stsci.edu/near-infrared-camera`

from the instruments themselves when observing IR light. Component 2 houses the electronics for all instruments while component 3, located in the spacecraft bus, contains the ICDH along with the integral ISIM flight Software, and the MIRI cryo-cooler compressor and control electronics. Fig. 2.3 shows the location of the ISIM and instruments on-board *JWST*, sitting directly behind the primary mirror.

2.2.2 Near-Infrared Camera (NIRCam)

The Near-Infrared Camera (NIRCam) is the primary imager on-board *JWST*, observing near-IR light over the wavelength range $0.6 < \lambda < 5\mu$m, offering imaging, coronagraphy, and grism slitless spectroscopy. A single pointing with the NIRCam imager observes a 9.7 arcmin^2 field split between two identical modules, A and B. Fig. 2.4 shows the NIRCam FOV and the two modules whilst also highlighting the short ($0.6 < \lambda < 2.3\mu$m) and long ($2.4 < \lambda < 5.0\mu$m) wavelength

channels represented by the blue and red solid lines, respectively. NIRCam is capable of observing in both modules and wavelength channels simultaneously. The two modules point in adjacent FOVs each covering an area 2.2′×2.2′ split by a 44″ detector gap.

The short-wavelength (SW) channel covers a wavelength range of 0.6 μm to 2.3μm, where the FOV is arranged in a set of 2×2 detector arrays (2040″ × 2040″ pixels) with pixel scales of 0.032″. In Fig. 2.4, this is highlighted by the solid blue lines overlayed on both module A and B. As the detector array is split into four quadrants, there are additional detector gaps of 4″-5″ that form a cross in both modules. Without dithering during observations, these would form gaps in the image. The long-wavelength (LW) channel covers 2.4 μm to 5μm with only one detector array (2040″ × 2040″ pixels) with a pixel scale of 0.065″ per pixel. The SW channel has twelve filters in total; five wide-band (R ∼ 4), four medium-band (R ∼ 10), and three narrow-band (R ∼ 100). The LW channel consists of three broad-band, eight medium-band, and four narrow-band filters. All of the NIRCam filters are plotted in the upper panel Fig. 2.5 while the sensitivity capabilities for the broad-band photometric bands are plotted in the lower panel [2].

Along with imaging, NIRCam also provides the opportunity to conduct wide-field slitless spectroscopy (WFSS) using the NIRCam Grisms with spectral resolution of R = $\lambda/\Delta\lambda \simeq$ 1,600. Each Grism is used in conjunction with one of the medium or wide filters from the LW channel (2.4-5.0 μm) across both modules (9.7 arcmin^2). However, for the work in this Thesis, only the NIRCam imager is of real importance.

2.2.3 Near-Infrared Spectrograph (NIRSpec)

NIRSpec enables spectroscopy at resolving powers of R ∼ 100, R ∼ 1000 and R ∼ 2700 in four different observing modes covering the entire near-IR region of the spectrum (0.6 < λ < 5.3μm). The four observing modes on NIRSpec are: Multi-object spectroscopy (MOS) with the Micro-Shutter Assembly (MSA), Imaging spectroscopy with the Integral Field Unit (IFU), high-contrast single-object spectroscopy with the Fixed Slits (FSs) and high throughput Bright Object Time-Series (BOTS) spectroscopy with the NIRSpec wide aperture.

[2] `https://jwst-docs.stsci.edu/near-infrared-camera/nircam-overview`

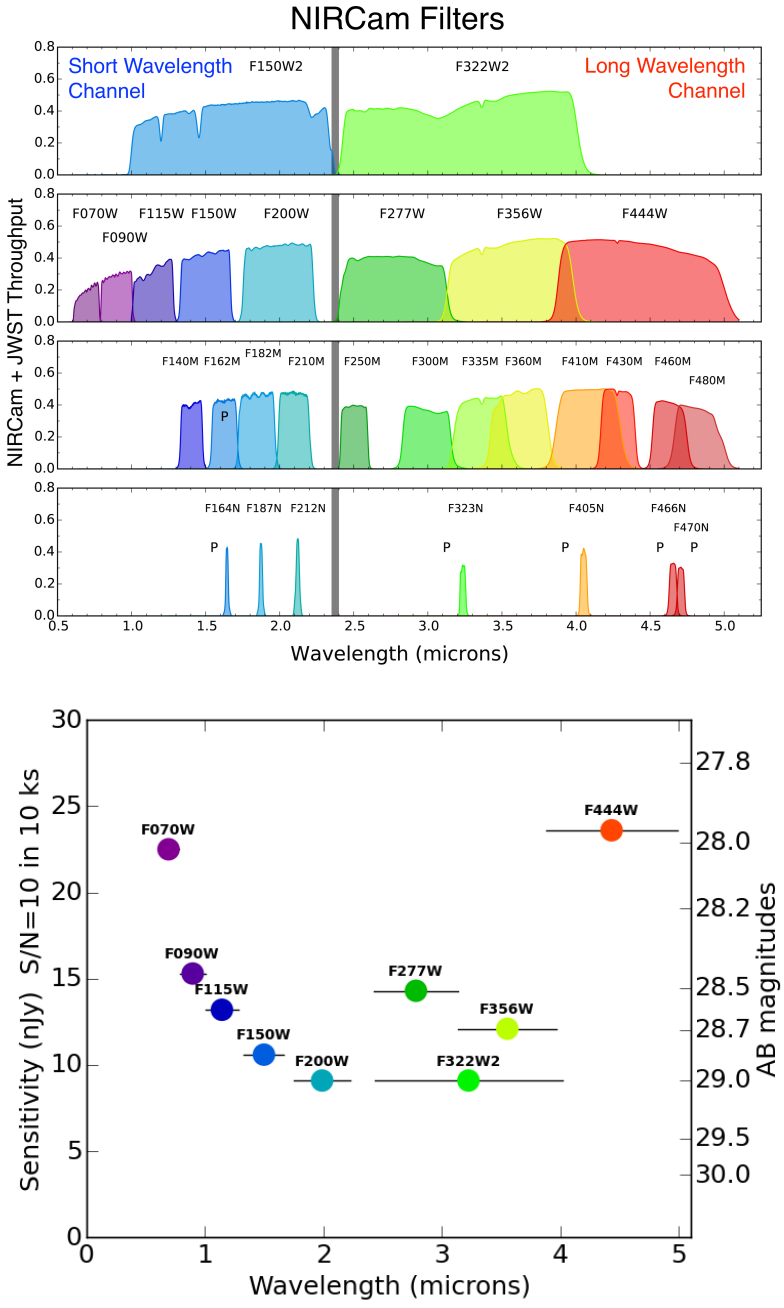

Figure 2.5 *Upper Panel: NIRCam and JWST Optical Telescope Element (OTE) filter throughputs (version 4.0: April 22, 2016). The vertical grey bar marks the approximate dichroic cutoff between the short and long-wavelength channels. Filters marked 'P' are located in the pupil wheel, requiring transmission through a second filter in the filter wheel, either F150W2, F322W2, or F444W. In those cases, the combined transmissions are plotted. Lower Panel: the NIRCam broad-band filter sensitivities, assuming a 10-σ SNR and a 10,000s integration.* `https://jwst-docs.stsci.edu/near-infrared-camera/nircam-overview`

Disperser-Filter Config.	Nominal resolving power	Wavelength Range (μm)
G140M/F070LP	(R ~ 1000)	0.9 - 1.27
G140M/F100LP		0.97 - 1.89
G235M/F170LP		1.66 - 3.17
G395M/F290LP		2.87 - 5.27
G140M/F070LP	(R ~ 2700)	0.9 - 1.27
G140M/F100LP		0.97 - 1.89
G235M/F170LP		1.66 - 3.17
G395M/F290LP		2.87 - 5.27
PRISM/CLEAR	(R ~ 100)	0.6 - 5.3

Table 2.1 *Instrument configurations, spectral resolutions, and wavelength ranges for the NIRSpec IFU* `https://jwst-docs.stsci.edu/near-infrared-spectrograph/nirspec-observing-modes/`

The MOS uses the MSA, a set of 250,000 shutters that can be configured to potentially observe over one hundred sources at any given moment. The MSA consists of four quadrants (Fig. 2.2, lower panel, top left), each housing 171 rows of shutters. Each shutter has a FOV of $0.24'' \times 0.46''$, but a series of shutters can be opened to create a spectral slit. The MSA opens its shutters by initially sweeping across the MSA with a magnet, opening all $\simeq$ 250,000 shutters, then the magnet moves back across the quadrants to close unused shutters and leave open those configured to observe specific science sources. This configuration process takes about 90 seconds.

THE MOS MSA has a total of nine filter/disperser combinations covering the entire near-IR wavelength range ($0.6 < \lambda < 5.3\mu$m). There are four medium-resolution (R ~ 1000) disperser/filters and four high-resolution (R ~ 2700) disperser/filters, with a low-resolution (R ~ 100) prism covering the entire spectral range of NIRSpec (see Table 2.1). The IFU has a much smaller FOV, covering approximately $0.1'' \times 0.1''$, with the ability to observe in the same set of filter/disperser combinations as the MOS MSA. The Fixed Slits (FSs) option is for observations of single objects, where high sensitivity is required. The NIRSpec bright object time-series (BOTS) mode is for observations of bright sources that require high throughput and stable time-resolved spectroscopy. More information about the NIRSpec instruments, and a more comprehensive breakdown of each type of spectroscopy available with NIRSpec is accessible at `https://jwst-docs.`

stsci.edu/near-infrared-spectrograph/nirspec-overview.

2.2.4 Fine Guidance Sensor/Near Infrared and Slitless Spectrograph (FGS/NIRISS)

The Fine Guidance Sensor (FGS) is an instrument that allows the telescope to precisely point at selected targets. It ensures that the objects at vast distances are the objects we want to study. The Near-Infrared Imager and Slitless Spectrograph (NIRISS) has a wide range of scientific objectives; first light detection, exoplanet analysis and exoplanet transit spectroscopy. The instrument has three main observing modes: wide-field slitless spectroscopy, single-object cross-dispersed slitless grism spectroscopy and aperture masking interferometry. The wide-field slitless spectroscopy produces spectra with a resolution of 150 in the wavelength range of 1.0 to 2.5 μm. Single-object slitless spectroscopy aims to achieve a resolution of 700 over the broader wavelength range of 0.6 to 2.6 μm while the interferometry covers the range between 2.6 and 4.8 μm

2.3 Mid Infrared Instrument (MIRI)

Over the past 50 years, near-IR observations from the ground have improved in detection limits and sensitivity more than any other region of the infrared spectrum. The mid-IR has been relatively untouched, simply because of the thermal background produced by the atmosphere rendering these instruments effectively useless for deep imaging and spectroscopy. Mid-IR telescopes, therefore, require to be space-based and even then have to be cooled constantly to minimise the background. Examples include *IRAS*, *Spitzer*, *Akari* and *WISE* (e.g Steidel et al. 1996; Ellis 1997; Sanders et al. 2007; Damen et al. 2011; Ashby et al. 2013, 2015, 2018; Labbé et al. 2013, 2015). The problem of having to propel these telescopes into space limits the apertures of these systems (to typically all less than one meter), restricting the angular resolution. One simple comparison with an 8-m ground-based telescope of similar angular resolution can summarise the technological advance offered by *JWST*; we expect *JWST* to produce a ×3000 increase in sensitivity for imaging and × 1000 for spectroscopy.

The Mid-Infra-Red Instrument (MIRI, Figure 2.6) on-board *JWST* is, in fact, a combination of NIRCam and NIRSpec in one instrument covering the mid-

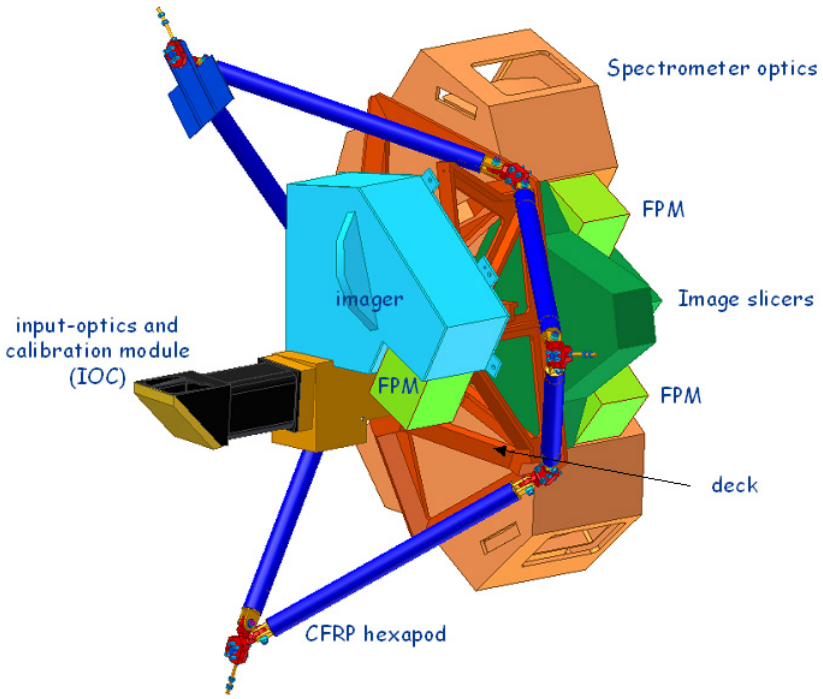

Figure 2.6 *Schematic Diagram of MIRI. Each colour represents a different instrument or region within an instrument. The blue region highlights the MIRI imager (aswell as LRS and coronograph), while the orange shows the location of the MIRI MRS. The light green regions highlight the Focal Plane Modules (FPM) for each instrument. These are detailed in the text.* `https://jwst.nasa.gov/miri.html`

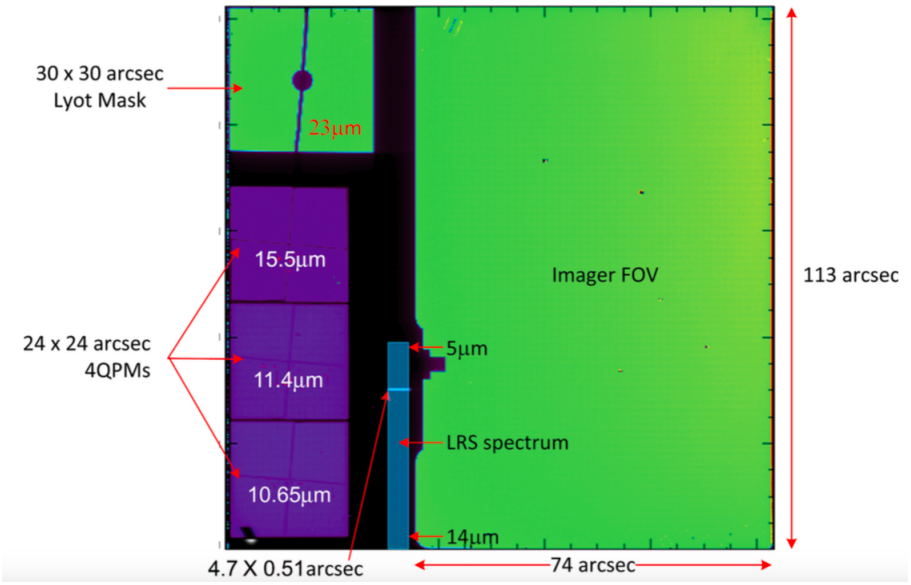

Figure 2.7 *A diagram depicting the key aspects of the MIRI Imager Module, outlining the FOV of each component and the configuration within the module itself.* `https://jwst-docs.stsci.edu/mid-infrared-instrument/miri-observing-modes/miri-imaging`

infrared region (5 to 28 μm, nine photometric bands). The camera provides the ability to take wide-field and broad-band imaging, ensuring a detailed first look analysis of a variety of objects. The spectrograph will allow for mid-IR spectroscopy of objects further away than ever before. With the combined powers of the spectrograph and camera, MIRI can produce a well rounded and in-depth study of high-redshift objects.

MIRI provides four main necessary capabilities: imaging, low-resolution spectroscopy, high-resolution spectroscopy and coronography. The collection of instruments is known as the optical module (OM) and is protected by the Integrated Science Instrument Module (ISIM: Section 2.2.1) with a surrounding operating temperature of ~40K, reducing the effects of thermal emission.

2.3.1 Imager and Low Resolution Spectrometer (LRS)

The Mid Infrared Imager Module (MIRIM; Bouchet et al. 2015) is an instrument providing broad-band imaging, low-resolution spectroscopy (LRS: Kendrew et al. 2015) and coronography. The total FOV of MIRIM is 113″×113″, shown in Fig. 2.6. The MIRI imager makes up a total of 74″ × 113″ of MIRIM with nine

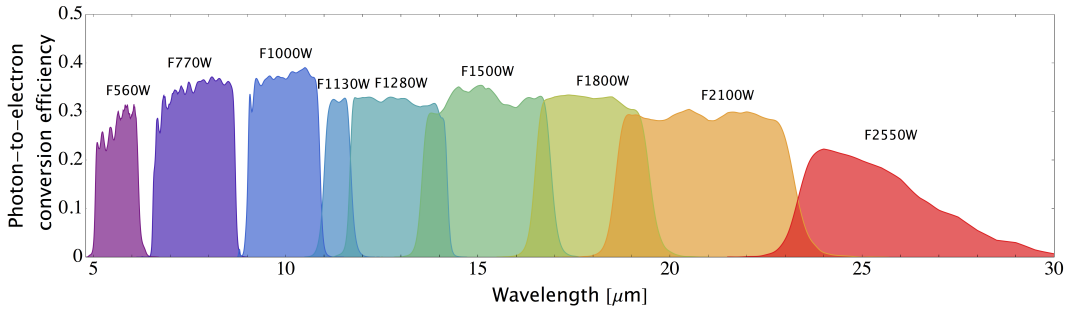

Figure 2.8 *The photomertic bands on-board MIRI. Eight of the nine photometric bands are broad-band (F560W, F770W, F1000W, F1280W, F1500W, F1800W, F2100W and F2550W) with the remaining F1130W band being slightly narrower to study the 11.3 μm PAH feature effectively.* ***https://jwst-docs.stsci.edu/mid-infrared-instrument/miri-observing-modes/miri-imaging***

photometric bands covering the mid-IR region of the spectrum (5 to 28 μm). Eight of the nine photometric bands are broad-band (F560W, F770W, F1000W, F1280W, F1500W, F1800W, F2100W and F2550W) with the remaining F1130W band being slightly narrower to enable the effective study of the 11.3μm PAH feature at $z \simeq 0$. Fig. 2.8 shows all of the photometric filters provided by MIRI. MIRI is diffraction-limited in all filters and background limited at all wavelengths blueward of $\lambda < 15\mu$m. Beyond this point, *JWST's* instruments themselves dominate the noise. I go into more detail about the MIRI background and the details of read-out modes and dither patterns in Section 2.4.

The LRS offers both slit and slitless spectroscopy from 5 -12 μm at a resolution of 40 at 5 μm, and 160 at 10 μm. The LRS is a part of the MIRIM (thin blue strip in Figue 2.7, where spectra are imaged onto the imager detector array. The design is relatively simple; it is a double prism housed in the imager filter wheel which is used for a single long-slit or slitless spectroscopy. The former is preferable to obtain spectra from relatively faint objects due to the diffraction losses seen from a bright source, while the latter is primarily for planetary transit measurements.

2.3.2 MIRI Mid Resolution Spectrometer (MRS)

The Mid Resolution Spectrometer (MRS; Wells et al. 2015) on-board the MIRI is a mid-infrared (5 - 28 μm) integral field unit (IFU) spectrometer; specifically an image slicer. It has the capability to produce spectral images with a resolution

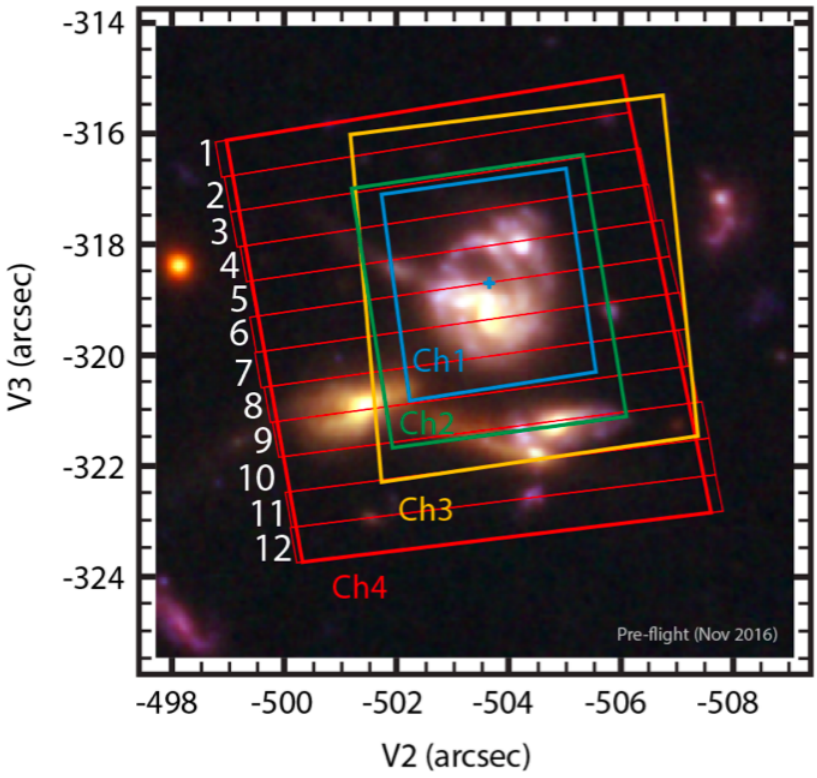

Figure 2.9 *The transformed MRS on-sky FOV in JWST. Colours highlight each channel: channel 1 (blue), 2 (green), 3 (yellow) and 4 (red). The solid lines represent the field borders for each channel along with the slices created from the image slicer. For comparison, the total FOV of the MRS is the small orange square top right of the MIRI FOV in the bottom panel in Fig. 2.2. The units in the above figure are the offset from the centre of the MIRIM.* `https://jwst-docs.stsci.edu/display/latest/MIRI+Medium+Resolution+Spectroscopy`

ranging from 1300 to 3500 (wavelength dependent) with a field of view of up 7.7″ × 7.7″. It has two separate detectors that measure the light from short and long wavelength channels; however the long-wavelength set of detectors are relatively useless for high-redshift observations due to the order-of-magnitude increase in the thermal background (noise) at these wavelengths (see Section 2.4.1, Figure 2.12).

The MRS is made up of four channels with overlapping fields of view (Fig. 2.9). The channels have limited wavelength ranges allowing the user to focus on a specific part of a spectrum without contamination from a region with increased noise. Light from *JWST* is directed to the MRS FOV in the Input Optics Calibration (IOC), and the incident beam of all wavelengths between 5 and

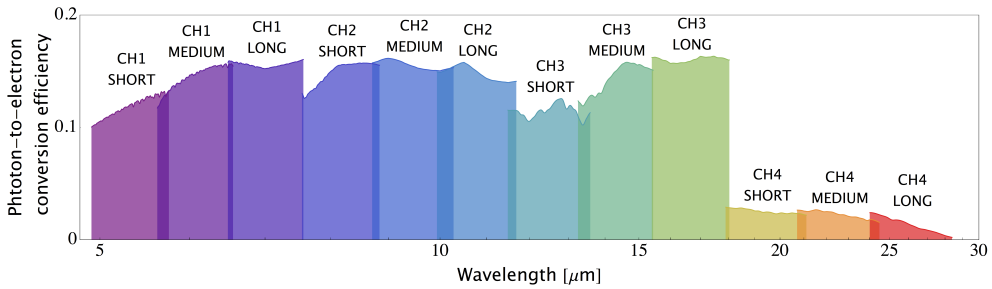

Figure 2.10 *The filter profiles for the MRS.*

28 μm is split into these four channels based on the spectral wavelengths in the Spectrometer Pre-Optics (SPO). There is an independent IFU for each channel in the SPO which also reformats the FOV and aligns them for the Spectrometer Main Optics (SMO). The SMO collimates the light for the diffraction gratings, and then re-image the diffracted dispersed light into a readable spectrum.

Input optics and Calibration (IOC) and MRS Spectral Pre-Optics (SPO)

The sky and pupil image of *JWST* needs to be reformatted, ensuring there is adequate information for the SPO input. The IOC undertakes this operation, converting the input beam from *JWST* (F/20) into a format acceptable for the SPO (F/39.37). It is important to remember that MIRI is only one of four instruments on-board *JWST* and therefore, the IOC is an incredibly important component for MIRI.

The SPO divides the incoming light spatially and spectrally, re-shaping it into a pre-determined form for the SMO. This is the region where spectrally, the FOV is split into four channels of equal width. This happens in the dichroic level, where a set of dichroic filters are used to pass through light of different wavelength ranges selectively. Spatially, the image is divided into slices using an image slicer for each channel. The image slicers are housed within the IFUs of the MRS (discussed in more detail in Section 2.3.2). The dichroic level is a necessity when the image is sliced. The diffraction of light is wavelength dependent and thus, to ensure the full range (5–28 μm) is diffracted appropriately, the FOV is split into these channels. Each channel requires three sub-spectra observations to obtain complete wavelength coverage, and consequently, three more dichroics split the channels further (Short - A, Medium - B and Long - C). Fig. 2.10 and Table 2.2

Channel	**Wavelength** (μm)	**Pixel Size** (arcsec)	**Slice Width** (arcsec)	**No. Slices**	**FOV** (arcsec^2)	**Resolving Power**
1 - A	4.87 - 5.82					
1 - B	5.62 - 6.73	0.196	0.176	21	3.00 × 3.87	2450 - 3710
1 - C	6.49 - 7.71					
2 - A	7.45 - 8.90					
2 - B	8.61 - 10.28	0.196	0.277	17	3.50 × 4.42	2480 - 3690
2 - C	9.94 - 11.87					
3 - A	11.47 - 13.67					
3 - B	13.25 - 15.80	0.245	0.387	16	5.20 × 6.19	2400 - 3600
3 - C	15.30 - 18.24					
4 - A	17.54 - 21.10					
4 - B	20.44 - 24.72	0.273	0.645	12	6.70 × 7.73	2000 - 2400
4 - C	23.84 - 28.82					

Table 2.2 *The fundamental spectral properties of the four channels provided by the MRS IFU.*

presents the different filter configurations provided by MIRI-MRS.

Integral Field Unit (IFU)

An integral field unit is an instrument used for a specific method of imaging and spectroscopy, dividing the FOV of the incoming light into separate segments to provide spatially resolved spectra of astrophysical sources. The MRS is specifically an image slicer, where the observation is dissected in the plane of the image and rearranged end to end, so the image falls on a 'slit'. This method was chosen for two reasons. Firstly, there is no need to accurately centre point sources on a narrow slit, and therefore, when studying point sources, there are no slit losses (loss of light) at the slices. In a long slit spectrometer, these losses can rise to approximately 50% of the light which can only be resolved by increasing the width of the slit. In the mid-IR, the signal to noise would drop dramatically due to the rise in the thermal background. Secondly, the vast wavelength range of MIRI consequently detects multiple mechanisms of emission. These mechanisms may dominate at different regions of the MIRI wavelength coverage, and an IFU provides spatially resolved spectroscopy over the entire field.

Each IFU is equipped with anamorphic pre-optics, an image slicer, re-imaging mirrors (2) and slit masks, optimised for its spectral bandwidth (Fig. 2.11). The number of spectral pixels in each channel has been chosen so that the average spectral resolution is the same. The sub-bands (A, B, C) then have a slightly larger bandwidth to ensure an approximate 15% overlap in the spectral range. The design ensures that each channel will cover half of a 1024×1024 detector, the largest possible FOV and that the long and short arms of the spectrometer are identical.

The anamorphic pre-optics re-format the square input field onto the rectangular image plane, by differential magnification in two axes. This process allows full spectrum sampling at the detector with the required dimensions at the image slicer. The square input field is accepted by four toroidal mirrors which directs the light to a flat output mirror. This produces an output beam which has a pupil image and a field image for the pupil mask and image slicer respectively. Implementing this magnification before the image slicing is convenient because the technique is applied to a single unit rather than several different slices.

Image slicing allows simultaneous spectroscopy of an entire field of view. The

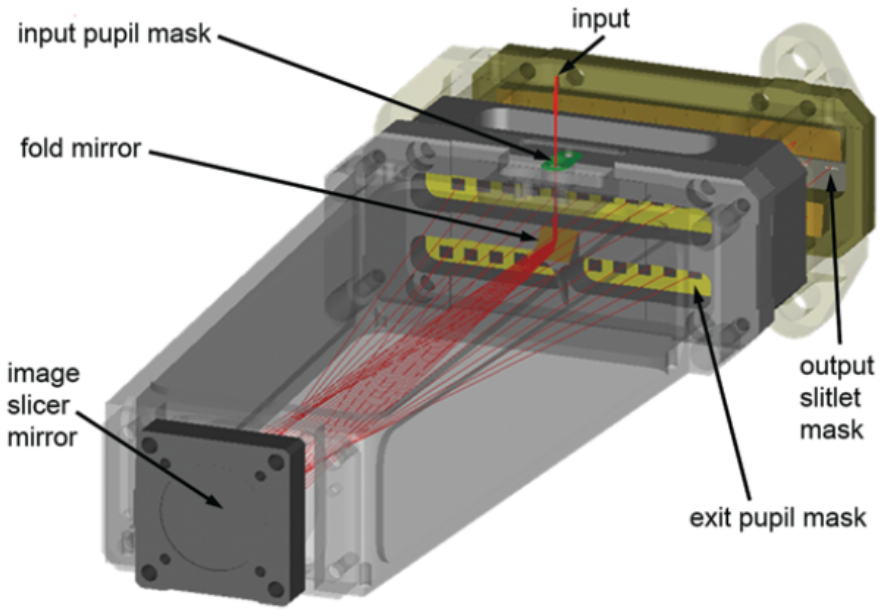

Figure 2.11 *A three-dimensional view of the Channel 3 Integral Field Unit (IFU). This is where the input image is sliced and then reformatted.* `https://jwst-docs.stsci.edu/display/latest/MIRI+Medium+Resolution+Spectroscopy`

widths of the slices represent the entrance slit size, and the image width defines the spectral sample width. To gain full Nyquist sampling of the telescope PSF, each IFU should have a slice width (W) equal to the half-width at half-maximum intensity of the minimum wavelength (λ_{min}), in that passband (Equation 2.1)

$$W = \frac{\lambda_{min}}{D} \tag{2.1}$$

where D is the diameter of the *JWST* primary telescope mirror, with the diffraction losses across the respective wavelengths minimised. The image slicing is achieved using a stack of angled mirrors that splits the image along the dispersion direction of the spectrometer. The sliced light needs to be magnified in order to match the plate scale at the detector before it exits the IFU through individual pupil masks and slitlets for each beam (1A,1B...). The image slicers are made from a single unit of aluminium to avoid alteration under the vibration pressure during launch. Each slicer also has a specific number of angled mirrors (i.e slices) which increase with each channel accounting for the more extensive spectral coverage.

Behind the slitlets, two re-imaging mirrors (for each side of the image slicers) direct the beams to their corresponding spectrometer. Specifically, they direct light towards a flat mirror (roof mirror), which outputs the sliced images at the output slit masks of each pupil created. Effectively the re-imaging mirror forms an image of the slicing mirrors that are used as inputs for the spectrometer with the now rectangular FOV (in the direction along the slices) defined by this output slit mask. This mask is designed to reduce the scattered light between the slices as well as avoiding overlap between them and preventing saturation of the image. In summary, the IFU takes a rectangular FOV and produces an arrangement of slitlets allowing accessibility to the grating spectrometer in the Spectrometer Main Optics (SMO). The SMO controls the optical path from the IFUs to the detectors using four grating spectrometers. Each spectrometer collimates the output from the SPO, dispersing these beams and imaging the output spectra to the correct magnification on one-half of the two detector arrays. The diffraction gratings are housed in two spectrometer arms including two for the short-wavelength channels (one and two) and two for the long-wavelength channels (three and four).

2.4 MIRI Simulator

The ATC has conducted a large amount of work in testing and calculating the sensitivity of the operating systems on MIRI (Glasse et al. 2015). Assessment of the imager, MRS and LRS has put boundaries on their capabilities. We have measured the efficiency of converting photons emitted from an astronomical target to the detectors within the MIRI instrument.

The design of MIRI is driven by the optimisation of signal from a target collected at the *JWST* primary aperture and minimising the effects of noise as these photons travel through the optical train to the detector. These effects are not only from the thermal background but also the optoelectronic subsystems used when dealing with the input field. This has been modelled by component-level testing along with cryogenic testing of the module as a whole. Swinyard et al. (2004) initially created a set of sensitivity models, however constant tracking of developments and tinkering of the models have allowed for a set of accurate and up-to-date on-orbit performance models for all of MIRI's observing modes.

2.4.1 Background

The 25-m^2 collecting mirror of *JWST* provides the potential for huge gains in sensitivity for a mid-infrared telescope. This, coupled with the cold radiative environment ($\simeq 40$ K) of *JWST* will allow MIRI to excel in a relatively unexplored region of the electromagnetic spectrum for extra-galactic science. As MIRI covers a broad spectral range, care must be taken to track the change in dominating background factors as a function of wavelength. At short wavelengths, the Zodiacal dust concentrated in the ecliptic plane of our solar system dominates the background noise. However, as one moves to longer wavelengths, the general thermal background increases by a few orders of magnitude. A model of the thermal background is the sum of the six thermal emission sources expected when observing with MIRI (Equation 2.2) where each background source has a different effective temperature and emissivity (ϵ, quantifying the efficiency of emission/absorption relative to a perfect black-body):

$$B_\nu = \epsilon \frac{2h\nu^3}{c^2} \frac{1}{e^{h\nu/kT} - 1} \tag{2.2}$$

Table 2.3 presents a breakdown of the different contributions to the thermal background emission that MIRI will be exposed to when operating. Components A and B take into account the scattered and emissive components of the Zodiacal dust spectrum, while C to F account for stray light in the telescope. Component G is representative of a 'high background', simulating double that currently expected in the optical system. The grey-body profiles are plotted in Fig. 2.12, where the problems encountered when venturing into the longer wavelengths accessible with MIRI are clear. The thermal background increases by several orders of magnitude, reducing the observational abilities of the instrument. At $\lambda > 14\,\mu$m, the background noise is dominated by the *JWST* components and the thermal emission they produce when the telescope is in operation (e.g. the sunshield, primary mirror etc.). At shorter wavelengths ($\lambda < 15\mu$m) the background is dominated by the Zodiacal dust spectrum. The Zodiacal dust spectrum represents the light that is scattered and absorbed by dust within the Solar System, which dominates in the ecliptic plane. For *JWST*, the target location on the sky, therefore plays a significant role in the total background expected when observing at wavelengths $\lambda < 15\mu$m with MIRI and NIRCam.

To quantify the background noise, an analytical integration can be performed

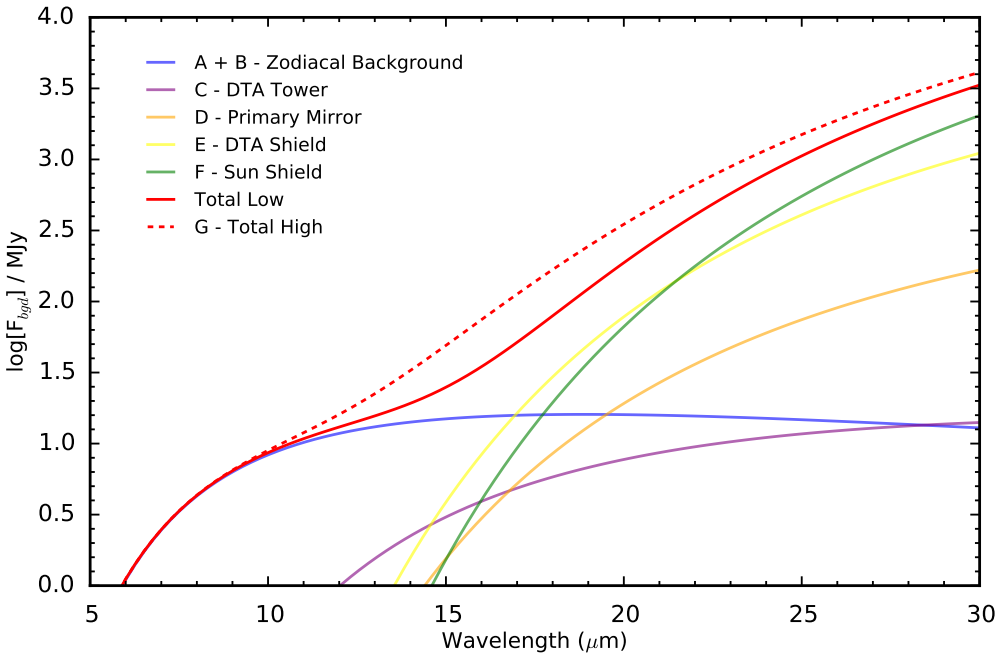

Figure 2.12 *The thermal background MIRI will detect during observations. The grey-body profiles represent the total flux in MJy as a function of wavelength. As we go from short to long wavelengths (5 - 30 μm) the photon background increases by three orders of magnitude, highlighting the difficulty of observing in the mid-IR. At $\lambda < 15\mu$m the background is dominated by the zodiacal light (red lines) while beyond $\lambda > 15\mu$m the JWST components dominate the background.*

Table 2.3 *Specific JWST background contributions. Used in conjunction with Equation 2.2, this information can be used to produce a set of profiles describing the wavelength-dependent thermal background emission which will be observed with MIRI.*

Component	Emmisivity (ϵ)	Temperature / K
A - Zodiacal	4.20×10^{-14}	5500
B - Zodiacal	4.30×10^{-8}	270
C - DTA Tower	3.35×10^{-7}	134
D - Primary Mirror	9.70×10^{-5}	71
E - DTA Shield	1.72×10^{-3}	62
F - Sun Shield	1.48×10^{-2}	52
G - High Background	1.31×10^{-4}	87

over the grey-body profiles across the specified wavelength range, for example, the range of photometric bands for MIRI imaging, or the separate MRS bands and channels when undertaking spectroscopic observations. It is crucial to integrate across these channels separately, as various variables depend on the wavelength. The quantum efficiency, τ_λ, and optical transmission, η_λ, vary on small scales, and therefore we can use the mean values rather than integrating a designated profile. The Photon Conversion Efficiency (PCE: the number of detected electrons per incident photon) is the product of τ_λ and η_λ. The PCE stays relatively constant over small wavelength ranges, varying by about 3% within the separate passbands. To accurately calculate the background in each channel, one must integrate each grey body profile individually:

$$i_{bgd} = \Omega_{pix}\tau_{tel}\tau_{EOL}\int_{\lambda_1}^{\lambda_2} P_{bgd}(\lambda)\tau_\lambda\eta_\lambda d\lambda \tag{2.3}$$

Ω_{pix}, τ_{tel} and τ_{EOL} represent the solid angle field-of-view from each pixel and two forms of transmission efficiency respectively. Specifically, $\tau_{tel}(0.88)$ describes the transmission of the clean optics at the start of the mission while $\tau_{EOL}(0.8)$ accounts for the 'end of life' transmission where we see losses in the optical train. These transmission coefficients were derived by the manufacturer's cryogenic measurements in an operational environment. P_λ can be found using:

$$P_\lambda = S_{bgd}(\lambda)\frac{A_{tel}}{h\lambda} \tag{2.4}$$

where S_{bgd} defines the background source flux density, Equation 2.4 also guarantees proper unit conversion, providing variables ready to be integrated using Equation 2.3.

2.4.2 Target

A key component in measuring the sensitivity and SNR of MIRI is to consider the target flux. Not all the light from an astronomical target will contribute to the photo-electric currents produced within MIRI as the signal is distributed over a range of pixels. This is due to the many optical systems implemented throughout the telescope scattering the light, from the input pupil to the detector array. This broadening effect is known as the Point Spread Function (PSF), and it perturbs

the result from point-source objects, primarily for the imager on-board MIRI. We do, however, see a knock-on effect to the MRS and thus it is a quantity that needs to be accounted for in the MRS calculations.

The mean photon flux density can be found using Equation 2.5. It uses flux (F_{tgt}) from an astronomical target (in Jy) and converts it to the number of photons/sec/m/arcsec^2 that contribute to the measured signal in the telescope:

$$P_{tgt}(\lambda) = \frac{F_{tgt(\lambda)} f_{phot}}{\Omega_{pix} N_{phot}} \frac{A_{Tel}}{h\lambda} \tag{2.5}$$

where f_{phot}, Ω_{pix} and N_{phot} represent the fraction of signal falling within the appropriate aperture, solid angle subtended and the number of pixels the light falls on respectively. f_{phot} accounts for the misalignment in the image due to light broadening along with the lost light out with the photometric aperture. f_{phot} is dependent on the wavelength and therefore channel in which the MIRI instrument is operating, as does the number of pixels (N_{phot}). The next step is to turn this flux density into a photocurrent via integrating over the selected separate passbands in the requested observing mode, as we did for the background signal.

For the MRS, the detector pixels sample the photometric aperture in one direction parallel to the integral field slices. The above scattering takes place in the imager and is therefore only applicable along the slice direction. In the dispersion direction, the scattered light is diffracted out with the resolution element. In short, the impact of this scattering on the sensitivity of the MRS depends entirely on the size of the photometric aperture and the spectral resolution. The FOV for a single MRS pixel is approximately 0.20 arcsec in the shorter-wavelength channels, in comparison with the 0.11 arcsec for the imager. Across the spectral range, the element is about 0.9 pixels wide, which is smaller than the photometric aperture of the imager. This explains the drop in signal between the two instruments due to this detector scattering. This has also been taken into account for the sensitivity models within the f_{phot} term (Equation 2.5).

Once the mean photon flux density is found, the photocurrent can be calculated using Equation 2.6:

$$i_{tgt} = \tau_{tel}\tau_{EOL} \int_{\lambda_1}^{\lambda_2} P_{tgt}(\lambda)\tau_\lambda \eta_\lambda \frac{\lambda}{R_{sp}(\lambda)} \tag{2.6}$$

To integrate over the individual spectral ranges, $d\lambda$ is required, a quantity defined by the resolution and wavelength values within each passband, represented by the last term in Equation 2.6, $\frac{\lambda}{R_{sp}(\lambda)}$. The other terms in the equations have the same meaning and values used in calculating the background flux. The units of the photocurrent are still per second and to turn this into a quantitive value for a signal, we need to multiply the photocurrent with the time taken for one integration resulting in a signal per pixel per integration (Equation 2.7):

$$S_{int} = i_{tgt} t_{int} \tag{2.7}$$

To then determine the total integrated signal from a source with respect to an exposure time, this term needs to be multiplied by the number of integrations per exposure and then the total number of exposures.

2.4.3 Noise

Once the background and target signal have been quantified, the noise can be calculated using Equation 2.8:

$$N_{int}^2 = K_1(i_{sig} + i_{bgd})t_{int} + K_2 i_{dark} t_{int} + K_3 R_N^2 \tag{2.8}$$

The total noise expected to be detected by MIRI consists of three terms, each representing a different background source. The first accounts for the total incident photon flux from the target and background. The second accounts for an induced current detected in each pixel in the absence of illumination (i.e. dark current). The third, read noise (R_N^2), describes the fluctuations associated with the electronic equipment within the optical systems.

Equation 2.9 defines the factor by which the noise measured within the system exceeds the theoretical shot noise limit:

$$K_1 = K_{exc} \frac{6}{5} \frac{n_{read}^2 + 1}{n_{read}^2 - 1} \tag{2.9}$$

The shot noise describes the random arrival of photons to the telescope pupil and therefore affects increasingly weaker sources. Here, it is specifically defined under

the conditions that the astronomical target or background is the dominating source of photons. K_{exc} accounts for gain and gain dispersion in the detectors from the signal. The noise associated with the dark current in term two of Equation 2.8 follows a Poisson form, effectively behaving like shot noise. This allows us to set the coefficient K_2 to unity, with the dark current (i_{dark}) taking a value depending on the observing mode in use (Imager, Low Resolution Spectrometer (LRS), Medium Resolution Spectrometer (MRS), Short Wavelength (SW) or Long Wavelength (LW) Channels). The final term is n_{read} which simply determines the number of equispaced pixel reads per integration.

As discussed above, R_N defines the noise picked up from electrical components with a coefficient given by Equation 2.10:

$$K_3 = K_{RNobs}^2 \frac{12 n_{read}}{n_{read}^2 - 1} \tag{2.10}$$

where R_N is equal to 32.6 electrons or 11.53 electrons depending on whether the instrument is working in 'FAST' or 'SLOW' readout mode, respectively. The type of science goal and instrument selected determines which readout mode is required. 'SLOW' mode is used for observing faint objects with MRS spectroscopy, whereas 'FAST' mode is sufficient for almost all other observing scenarios. The additional term, K_{RNobs}, reflects the factor by which the system noise does not reach the 'ideal' behaviour.

Once a target object has been defined in terms of flux, these equations allow the calculation of the signal and noise expected in each integration. Depending on the instrument (Imager, MRS and LRS) and the observing mode is chosen, specific values for all factors are required. The user can select the readout mode, the number of groups/frames, the number of integrations and the number of exposures for each observation in each photometric band giving a total exposure time. With the selected background, the user can determine a signal to noise ratio for the simulated observation of a user-defined astronomical target.

2.5 Hα with MIRI-MRS

A combination of theory and observations have allowed the community to build a consistent picture of the early Universe. The Big Bang produced dark energy,

dark matter, hydrogen, helium, the Cosmic Microwave Background (CMB) and traces of heavier elements. Initially, there were no stars or galaxies, a mix of particles such as protons, neutrons, and electrons that were yet to combine and form hydrogen and helium nuclei. As the Universe began to cool and expand, the protons and neutron fuse into hydrogen and helium nuclei, the electrons were attracted to the positively charged ionised particle combining to create neutral hydrogen and helium. The majority of which was hydrogen by about a factor of three, this is known as the epoch of recombination. As electrons were now not free, the light was free to travel throughout the Universe, forming the CMB

Population III (pop III) stars are the first objects that formed in the Universe producing consistent light. Although they are enormous (30−300 $M_{\odot}$), *JWST* will not be able to detect these directly; however, *JWST* will be able to detect massive star clusters/galaxies containing the pop III stars. To observe these objects, *JWST* will require extremely deep imaging surveys across several broad-band filters with NIRCam. MIRI imaging will be able to help identify true pop II stars, using the colors in conjunction with NIRCam imaging to study the rest-frame UV.

Studying the UV emission from galaxies can also provide a huge amount of information about star formation. However, much of the UV is subject to dust extinction inhibiting our view of star-forming regions. This UV emission is also absorbed by neutral hydrogen, which subsequently is ionised. The resulting recombination of hydrogen atoms produces emission lines, like Hα. Only relatively young stars from a star-forming region contribute significantly to the integrated ionising flux, and therefore these emission lines provide a nearly instantaneous measure of the SFR. Work by Madau et al. (1998) and Kennicutt (1998) (summarised in Kennicutt & Evans 2012) has provided the conversion between ionising flux and SFR yielding:

$$SFR(\mathrm{M_{\odot}year^{-1}}) = 7.9 \times 10^{42} L(H\alpha)(\mathrm{ergss^{-1}}) \tag{2.11}$$

For observing Hα, MIRI becomes an increasingly important instrument at higher redshifts ($z > 6.7$). The Hα line moves beyond the near-IR region of the spectrum at this redshift, rendering NIRCam and NIRSpec useless for this specific science. Recent work has also suggested that bright high-redshift galaxies produce nebular emission lines of large equivalent widths (Hα $\mathrm{EW}_{RF} > 300$Å; Bowler et al. 2017). It is also essential to consider that, in the early Universe, we see galaxy metallicity

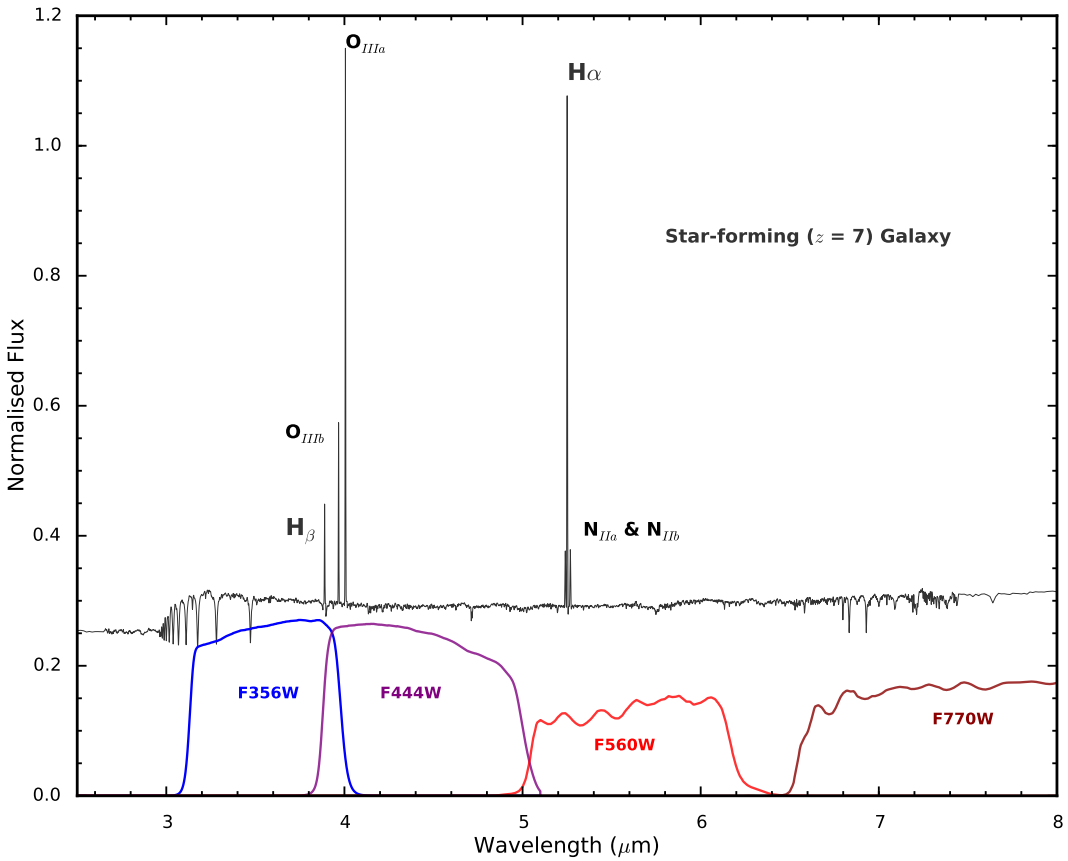

Figure 2.13 *The spectrum of a typical star-forming galaxy, set at a redshift of 7 ($z = 7$) and normalised to $m_{AB} \simeq 25$ at $5\,\mu m$ (Bowler et al. 2017). We see that Hα lies beyond the NIRSpec wavelength range and falls within MIRI's coverage. Several nebular emission and forbidden lines have also been added with an appropriate equivalent width for Hα (200Å).*

drop, which can potentially inhibit observing other emission lines in the rest frame UV and optical. However, if we do obtain emission lines of shorter wavelength, we can utilise NIRSpec and MIRI to determine important line ratios, a proxy for various galaxy properties.

Using the independent simulator (Section 2.4) we have assessed the capabilities of using the MIRI Medium Resolution Spectrometer (MRS) for observations of high redshift star-forming galaxies, specifically looking at the ***Hα*** emission line present in a $z = 7$ galaxy. We have simulated the background signal expected during observations and have applied it to a chosen input spectrum. Based on the sensitivity models (Section 2.4.1; Glasse et al. 2015), every potential source of background noise has been taken into account from cosmic rays emitting photons to dark currents, producing the most up to date programme simulating the on-

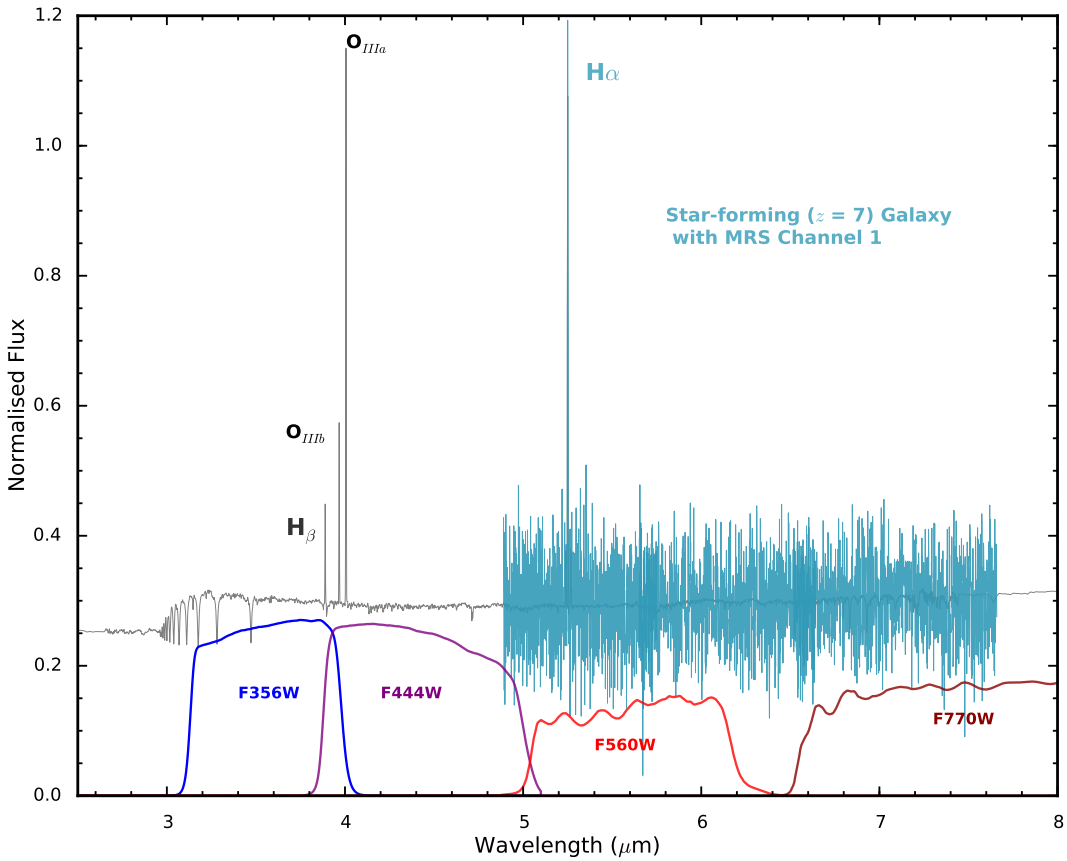

Figure 2.14 *The simulated observation through MRS overplotted with the original input spectrum and the same respective NIRCam and MIRI filters. The SNR is 10.6 after an exposure time of 6 hours. The noise swallows the two nitrogen lines, yet the Hα emission line remains visible.*

orbit performance of the MRS.

Using the SSP BC03 templates (Bruzual & Charlot, 2003), we extracted a star-forming galaxy and applied a series of nebular emission lines, including an Hα line with an equivalent width of 200Å and velocity dispersion of 100 kms^{-1}. We also included Hβ, O[III] and N[II] lines based on appropriate line ratios, in order to test if they can also be resolved with the MRS at high redshift. We normalised the spectrum to $m_{ab} \simeq 25$ mag at a wavelength of 5μm. The input spectrum is plotted in Fig. 2.13, where the emission lines are highlighted. This plot shows that the Hα emission line lies beyond the wavelength limit of NIRcam NIRSpec. This input spectrum was put into our independent simulator, with a specified set of observing criteria optimised to high-redshift science with the MRS IFU.

With a SNR profile calculated for the first channel of the MIRI MRS, we want

to simulate the spectra that would be observed. This can be done by perturbing each point in the spectra by a Gaussian distribution where the standard deviation is equivalent to the flux value divided by the SNR. We only observe with the first channels of the MIRI MRS because the order-of-magnitude increase in noise beyond the first channel (1A, 1B and 1C), forces the disposal of the final three channels (2-4). This, in turn, limits the wavelength range when observing high redshift galaxies with MIRI MRS to 4.87−7.72 μm.

The resulting spectrum of our star-forming galaxy at redshift $z = 7$ is plotted in the Fig. 2.14. The blue SED highlights the region of the spectrum observed with the MIRI MRS. Assuming a 6-hour integration in each sub-band of channel 1, we get an emission-line SNR of 10.6. We can see the N_{II} lines completely disappear from the spectrum in comparison to Figure 2.13; however, the Hα line is resolved rather clearly.

Studying objects in the mid-IR poses several problems. Thermal background noise from the atmospheres makes ground-based research very difficult. When trying to resolve this by sending a MIR instrument into space, only small apertures and therefore lower angular resolution is possible. The *JWST* MIRI instrument manages to find an equilibrium with a 6.5m primary mirror and a mid-IR instrument that reaches out to 30 μm. Hα is a direct probe of recent star formation, and it has a close relation to the photoionisation rates due to the UV emission from young stars. Observing and studying high-redshift star-forming galaxies is a primary goal of *JWST* and measuring Hα is a relatively accurate way of doing so. While NIRSpec and NIRCam may accomplish this up to $z \approx 6.7$, it is only MIRI which has the capabilities of exceeding $z > 7$. Using the sensitivity models, I have shown that in fact, the MRS on-board MIRI is capable of doing so. A 6-hour exposure time can produce a spectrum, that measures Hα, with a SNR of ≈ 10.

2.5.1 Testing

In order to ensure our independent simulator accurately simulates *JWST* observations, we ran a series of tests against the official Exposure Time Calculator (ETC) and the official test team MIRI simulator (MIRISim). In this sub-section, I describe the testing of the MIRI imager and MRS observing modes against the ETC and MIRISim, respectively.

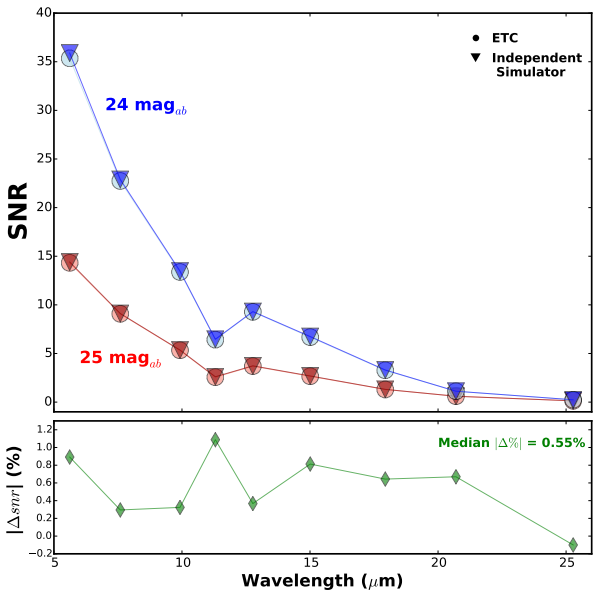

Figure 2.15 *The upper panel presents the average SNR in each MIRI imaging band calculated by both the ETC (filled circles) and our independent simulator (downward triangles). The red and blue points represent a $m_{AB} \simeq 25$ mag and $m_{AB} \simeq 24$ mag galaxy respectively. The lower panel shows the average SNR percentage offset calculated in each filter (green diamonds), and we also print the median percentage offset for all MIRI bands.*

Fig. 2.15 presents tests completed in order to assess the accuracy of our independent simulator used to calculate and simulate the MIRI observations in this work. In the upper panel, we show the average SNR calculated for two test runs, the first was a $m_{AB} \simeq 25$ mag object (red points), while the second was a $m_{AB} \simeq 24$ mag object (blue points). The filled downward triangles represent the SNR calculated in a 5550s exposure by our independent simulator, whereas the filled circles represent the SNR calculated using the official ETC[3]. The lower panel of Fig. 2.15 presents the median SNR percentage offset ($|\Delta snr|$) in each band (green filled diamonds). We assume the same target source, background models and specific observing strategy in all cases. We also appropriately reduce the number of groups/integrations for both the ETC and our independent simulator to avoid background saturation in the longer-wavelength MIRI filters. In general, our independent simulator tends to overestimate the SNR capabilities of MIRI imaging marginally; however, this effect is almost negligible, producing an average SNR offset of 0.55%.

MIRISim is a programme that intends to replicate MIRI observations. It

[3] `https://jwst.etc.stsci.edu`

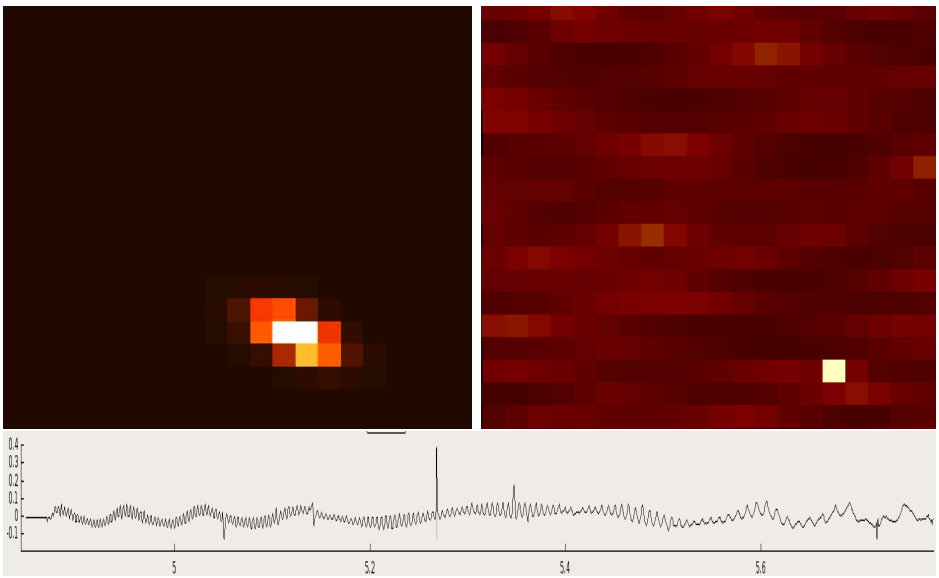

Figure 2.16 *(Top Left) - High-redshift target galaxy simulated by MIRISim with an effective radius of 0.094″ (0.07 kpc at z = 7) The spectral data cube image slice (Top Right) centred on 5.25μm with the spectrum of the object (bottom) showing the clear Hα emission line with no nitrogen emission. The SNR is approximately 10, agreeing with the results from our independent simulator (Fig. 2.14)*

simulates the raw data expected from the Imager, LRS and MRS ready to be put into the data reduction pipeline. MIRISim is consistent with the MIRI sensitivity models; however, the programme is not yet finished. I have undertaken the opportunity to address the progress made with the MRS aspect, 'Specsim', and have created a simulator based on these sensitivity models for MIRI. This independent simulator is presented in Section 2.4 while we use it to assess the capabilities for MIRI-MRS to observe the Hα emission line in Section 2.5. We input the same star-forming spectrum shown in Fig. 2.13 into MIRISim, with an identical observing strategy described in Section 2.5.

The results showed that both of the simulators determine the SNR to be approximately 10, suggesting the background noise is being modelled appropriately. The only caveat is that DHAS subtracts the fringing component of the MIRI observations. This is not yet fully integrated within MIRISim itself, i.e. the data reduction subtracts a noise component where there is none. This oscillatory profile dominates the noise in the spectrum, and therefore, further testing is required. In addition, we see comparisons between the simulated emission lines. Hα is visible, yet the noise swallows the other two Nitrogen lines. This is also the case with the independent simulator, shown in Fig. 2.14. The final part of the

analysis is calculating the relative flux values of MIRISim and our independent simulator. We do this for various stages through the optical train of both simulators. MIRISim's output flux units are in detected electrons per second, and careful care is taken when changing the units. We see a small discrepancy in flux value by a factor of 1.9. The explanation is still somewhat unclear but could be due to assumptions made in either case.

2.6 Summary

In this chapter, we introduced *JWST*, a large (6.5m primary mirror) infrared ($0.6 < \lambda < 30\mu$m) telescope. *JWST* provides imaging and spectroscopy with four main instruments protected by the ISIM: NIRSpec, MIRI, NIRCam, and FGS/NIRISS. While NIRCam and NIRSpec provide the primary imaging and spectroscopy observations for *JWST*, respectively, MIRI will impressively extend the wavelength capabilities of the telescope out to $\lambda \simeq 30\mu$m. MIRI provides four key capabilities: imaging, low-resolution spectroscopy, high-resolution spectroscopy and coronography. Studying objects in the mid-IR poses several problems. In particular, thermal background noise from the atmospheres makes ground-based extragalactic research very difficult. When trying to resolve this issue by sending a mid-IR instrument into space, only small apertures and therefore lower angular resolution is possible.

I introduced a piece of software that I built to realistically simulate *JWST* MIRI observations and in doing so, have tested MIRIs ability to observe a bright ($m_{ab} \simeq 25$ mag) high-redshift ($z \simeq 7$) star-forming galaxy. Specifically, I tested the MRS's ability to detect the Hα emission line, a sensitive star-formation indicator, providing a direct probe of the photoionisation rates produced by UV emission from young stars. This is a particularly important simulation for MIRI, because the Hα emission line is redshifted beyond the NIRSpec and NIRCam wavelength range at $z \simeq 6.7$.

I initially constructed a z= 7 star-forming galaxy based on the BC03 SSPs (Bruzual & Charlot 2003) and normalised the galaxy spectrum to $m_{ab} \simeq 25$ mag. I then introduced an Hα line with an equivalent width of 200Å and a velocity dispersion of 100 kms^{-1} with additional nebular emission lines (Hβ, O[III] and N[II]) based on appropriate line ratios. Assuming a realistic observing strategy and a 6-hour integration time, I reclaimed Hα with a SNR of $\simeq 11$. I also presented

a series of tests undertaken in order to compare independently developed software to that of the official ETC and MIRI Test team's MIRISim.

3

A deep extragalactic survey with *JWST*

In this Chapter, I first present a brief description of the *JWST* launch, orbit logistics, and the science timeline, before providing a detailed overview of the Public Release Imaging for Extragalactic Research (PRIMER) proposal developed and submitted as part of the Director's Discretionary Early Release Science (DD-ERS) programme for Cycle-1 of *JWST*. I then conclude this chapter with a new overview of the *JWST* ERS and GTO programmes that focus on observations of high-redshift galaxies, to place PRIMER in the context of currently-accepted future *JWST* observing programmes.

3.1 *JWST* Timeline

3.1.1 *JWST* Launch and Orbit Timeline

JWST is expected to launch in the near future, with current estimations suggesting sometime in 2021. *JWST* will be launched from the French Guiana on an Ariane 5 rocket. Post-launch, *JWST* is propelled towards Lagrangian Point

2 (L2), 1.5×10^6km anti-sunward from Earth. L2 was explicitly chosen to allow the telescope to stay in line with Earth as it moves around the Sun. This, in turn, allows the sun-shield to block out all thermal energy from the Sun, Earth and the Moon simultaneously. The six-month orbit around L2 prevents *JWST* from entering into the Earth and Moon shadow. This is unlike the Hubble Space Telescope (*HST*), which falls in and out the Earth's shadow every 90 minutes making it more complex to schedule observations. Consequently, *JWST* will have an uninterrupted view of the sky throughout the year (depending on target sky position). *JWST* will use propellant to ensure stabilisations while constantly orbiting L2. This limits the lifetime capable of *JWST* to a minimum of 5 years, with a goal of potentially reaching an extended lifetime of up to 10 years.

During the 30-day journey out to L2, the rocket and *JWST* will gradually unpack itself automatically, disposing of components not required for the assembly process. The Ariane 5 rocket will initially provide thrust for less than 10 minutes, propelling *JWST* out of Earths orbit. Once detached from the rocket, the *JWST* spacecraft bus will deploy a solar array to provide electricity for small thrusters, altering the trajectory of *JWST* when required. Within the first day, *JWST* will have passed the Moon's orbit. In the following week, *JWST* will begin the sequence of deployment, initially with the sunshield pallet arms extending appropriately. The spacecraft bus will move approximately two metres away from the telescope itself, allowing for the deployment tower assembly to be fully extended. This is followed by the full deployment of the entire sunshield and momentum management flap. The final sequence before *JWST* reaches L2 is the deployment of the primary and secondary mirrors. Initially, the secondary mirror scaffolding and the mirror itself is extended into position, followed by the wings of the primary mirror.

During the final days of the journey to L2, the telescope needs to gradually cool down, making use of the deployed sunshield while the electronics and flight software are powered up. Upon reaching L2, the telescope will be at the scientific operational temperature. However, to prevent condensation from building up on the instruments, the ISIM is warmed slightly by electric heaters. It is at this time that the Fine Guidance Sensor, NIRCam and NIRSpec will be switched on. NIRCam will take the first images of a crowded star field, ensuring light can pass through the optical train of *JWST*. At this point, *JWST's* primary and secondary mirror will not be aligned, and thus, it is expected that the images will be out of focus. Work will be undertaken for a couple of weeks to ensure the mirrors and

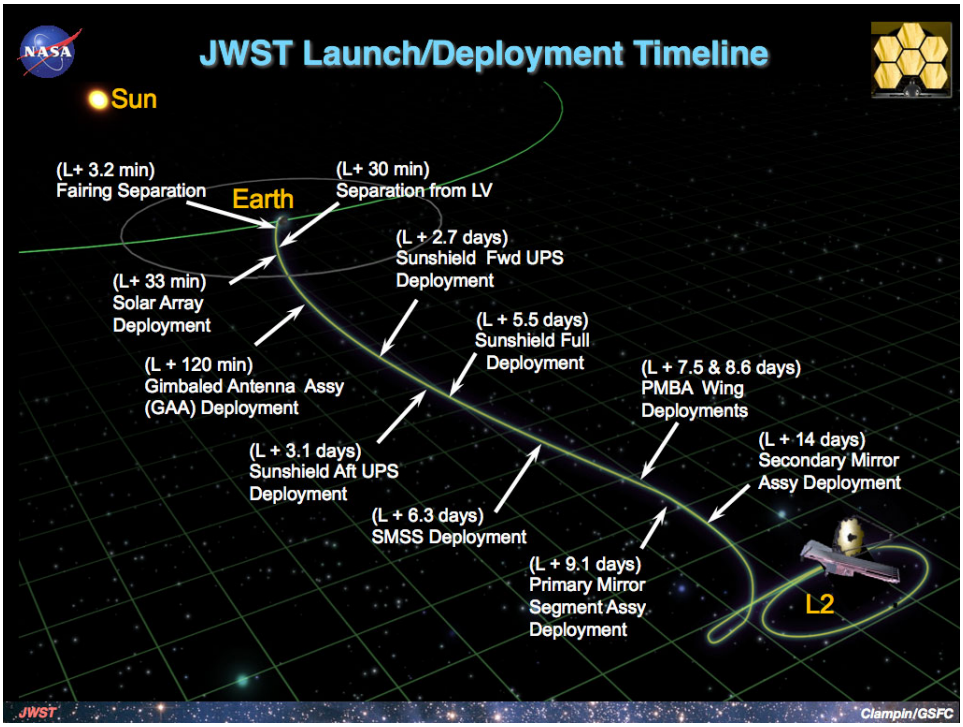

Figure 3.1 *The JWST deployment timeline from launch to the very first light being detected by JWST. L in the diagram indicates the initially launch with the sequence of deployments taking 14 days (L+14 days). A video of the entire launch process can be found at* `https://jwst.nasa.gov/launch.html`

the primary mirror segments are calibrated and aligned. Three months into the mission, MIRI will be turned on, and the first scientifically accurate images can be taken with NIRCam. In the following weeks, the other instruments will be tested and optimised by observing representative scientific targets. Six months after the initial launch from the French Guiana, *JWST* should be fully operational with the start of the first cycle of scientific observations underway.

3.1.2 *JWST* Science Timeline and Observations

With only a 5-10 year operational window for *JWST*, efficiency is the key to making the telescope a success. The *JWST* science observations timeline is split into separate 'Cycles' running each year, with Cycle 1 commencing upon completion of the 6-month commissioning phase described above in Section 3.1.1. There are three types of observational programmes, Guest Observer (GO) programmes, Guaranteed Time Observer (GTO) programmes and Director Discretionary (DD) programmes. GO programmes are open for the entire community to propose and make up $\approx 80\%$ of the total allocated time through the first 5 Cycles. For Cycle-1 this is equivalent to approximately 6000 hours of observing time. These programmes are categorised as either small, medium or large, depending on total charged time ($<$ 25 hrs, 25 - 75 hrs and $>$ 75 hrs, respectively), as well as being classified as Calibration, Long-Term, Treasury, and Survey programmes. Each category has to meet specific criteria to be a successful proposal and ultimately, a successful *JWST* observation. GTO programmes are awarded to scientists that have provided an essential service or component for the design of progression of *JWST*. For example, each instrument team has a certain number of allocated hours in which they are allowed to design *JWST* observations. At least 2000 hours will be allocated for GTO programmes in the first cycle with a total of 4020 hours in the first 30 months (cycles 1-3). The GTO programmes hold precedence over many other observations, so careful planning is required so as not to 'duplicate' observations currently being made by an accepted GTO programme (see Section 3.3). The final type of observations is the DD, with an allocation of approximately 10% of the time in each cycle ($<$ 877 hours). This tends to be for rapid response observations or very targeted science programmes.

Currently, Cycle 1 is expected to begin late 2021 with the Directors Discretionary Early Release Science Programme (DD-ERS or ERS). The DD-ERS programme was driven by the limited lifetime of *JWST* and, in an attempt to maximise the

efficiency of the first *JWST* data, all ERS data is open access. This should allow the entire community to familiarise themselves with *JWST* capabilities and the data analysis tools on offer. In total, 500 hours have been made available for ERS proposals, taken from the total Cycle-1 time allocation.

Initially *JWST* was only planned to take primary observations, i.e. using one instrument at a time. However, due to the limited lifetime, *JWST* operations have now been redesigned to allow simultaneous use of multiple instruments. These types of observations are known as parallel observations and allow for increased efficiency and science return from *JWST*. There are two types of parallel observations utilised by *JWST*, co-ordinated parallels and pure parallels. A co-ordinated parallel observation is a single proposed programme with complementary observations requesting the use of two instruments at once. In doing so, the primary and parallel observations should be planned together for a single programme to accomplish the science goals. In contrast, pure parallel observations are two separate programmes with prime observations only that align in such a manner that allows two instruments to be used simultaneously. Mainly these end up being calibration testing rather than two separate science programmes; however, either is possible. For Cycle-1, only a limited number of instruments are compatible with co-ordinated and pure parallel observations.

3.1.3 Proposal Tools

A *JWST* observing proposal requires a detailed analysis of the scientific potential and technical difficulties of the observing programme. We need to make predictions about the scientific significance while ensuring we maximise the efficiency of *JWST's* limited lifetime. Several tools have been created to aid the community; the Exposure Time Calculator (ETC), The Astronomers Proposal Tool (APT) and the *JWST* User Documentation. For *JWST*, all proposal can be submitted using a single stream process where only a single form is required for submission. This is useful because *JWST* is an event-driven facility (as compare to *HST's* orbit-driven process) and so, *JWST* will continuously observe different visits during each cycle. This means more information needs to be detailed in the proposal process so that total time and efficiency can be made available to the *JWST* Telescope Allocation Committee (TAC) and other review panels.

APT

The Astronomers Proposal Tool is a powerful software package used to create, modify and submit detailed *JWST* and *HST* observing proposals. The APT requires the user to specify the general-purpose information and proposed target fields. From there, the user can then detail the chosen instruments, observing modes, mosaicing strategies and a vast range of special requirements (V3PA constraint etc.). The APT can then build the observations on-sky allowing the user to visualise the observing programme, while also checking the schedulability of the observations based on roll-angle constraints and guide-star availability. The APT will also calculate the total overheads expected from the programme, allowing the user to calculate efficiency for each observation. Moreover, the APT also allows the user to check for duplications among currently accepted *JWST* programmes, such as in the GTO and ERS series.

There are three major types of observing *JWST* overheads: direct, indirect and instrument overheads. A direct overhead is an additional time associated with a given programme: major slews, mechanism motion times, guide-star acquisition times, small-angle manoeuvres and target acquisition. Slews, in general, are the most significant source of overheads. A slew is a change in pointing for the observatory either to change target, build a mosaic, or to dither. The reason slews dominate the total overheads of observations is because a slew requires three operations: time to move the observatory, time to let the observatory settle and the acquisition of a guide star. Indirect overheads are related to activities performed for the general support of science observations. Instrument overheads constitute the additional time required for each instrument to change filters, detector readout modes, integrations and exposure. It is vital, therefore, to take all potential overheads into account, and the APT is very helpful in calculating these.

ETC

Pandeia calculates 2-D pixel-by-pixel signal-to-noise ratios for all observing modes on-board *JWST*. The *JWST* Exposure Time Calculator (ETC) web interface is based on this same PYTHON engine. However, for large numbers of objects and simulations, the web interface is not sufficient. Pandeia allows the user to define an astrophysical scene with an external input SED, and then to 'observe' the

synthesised objects using observational parameters defined by the user. The input SEDs can be normalised at any wavelength, across all *JWST* and *HST* filters.

The astronomical scene comprises a set of sources and associated SEDs independent of the observing strategy and instrument mode chosen. This, in turn, maximises the efficiency of Pandeia, as multiple calculations across several independent observing modes can share this scene. This scene is projected onto a realised scene, that is initially spatially sub-sampled, avoiding under-sampling of the PSF. The realised scene cube is then projected onto an appropriate detector plane, dictated by the chosen instrument and the observing mode defined by the user. The details of how this is done are described in Pontoppidan et al. (2016). The intermediate step of tracking the photons through the optical train to the detector is done in a similar manner to our independent MIRI simulator (see Chapter 2, Section 2.4). Once the SNR has been found in each photometric band for our chosen integration times, we assign an error and scatter the data accordingly (assuming a Gaussian distribution). The result is the best estimate of the anticipated NIRCam photometry (and uncertainty) for each of our simulated galaxies, after processing with the NIRCam data-reduction pipeline.

The *JWST* Exposure Time Calculator (ETC) is based on the same Pandeia python script described above. However, the ETC also utilises a modern online web interface to ensure simplicity when building synthetic observations. All observing modes and instruments on-board *JWST* are fully supported: NIRCam (Spectroscopy, Imaging), NIRSpec (Spectroscopy), MIRI(Spectroscopy, Imaging, Coronography), NIRISS (Imaging and Spectroscopy). The web interface allows the user to construct numerous unique sources with individually assigned Spectral Energy Distributions (SEDs), either SEDs uploaded by the user or SEDs built using the ETC itself. Redshifts, specific emission lines and normalisation can be added/performed on the input SED in real-time. These objects can then be projected and visualised onto a scene, where the shape, offset, and separation distance can all be adjusted by the user. The ETC produces a 'realistic' on-sky image of the astrophysical scene with the associated SEDs of each source on the observing plane.

The background model utilised in the ETC follows a similar set of background thermal emission models as described in Chapter 2, Section 2.4.1. For every synthetic observation made, the ETC will calculate the appropriate background noise expected during the observations based on details provided by the user. The user can define a sky location along with an observation date in order to simulate

the most accurate background noise expected when observing with *JWST*. For more general purposes, the user can decide between a low (10th percentile), medium (50th percentile) and high (90th percentile) background located in the celestial position defined.

Upon completion of the scene and background definition, the user is required to perform a SNR calculation based on a set of prescribed observing conditions. Several different parameters are defined for a calculation; background models, instrument mode, detector setup and extraction strategy. The instrument mode includes the filter or grating choices for the imaging and spectroscopy observations, respectively. The detector setup governs the readout mode along with the number of groups per integrations, the number of integrations per exposure and the total number of exposures for each instrument. Combining these parameters provides the user with a total exposure time for the specified observations in each selected filter.

3.2 ERS Proposal - PRIMER

Public Release Imaging for Extragalactic Research (PRIMER), is a large (52hr), deep, fully-sampled NIRCam and MIRI imaging programme proposed for the ERS programme for *JWST* Cycle-1. PRIMER was designed to efficiently ($\approx 75\%$ observing efficiency) observe the faintest galaxies in the best-studied available (non-GTO Covered) equatorial *HST* CANDELS field, COSMOS. We planned to efficiently utilise both NIRCam and MIRI Prime and Parallel observations to adequately cover the majority of the COSMOS CANDELS field in multiple photometric bands with both instruments. We proposed to observe a total of 25 arcmin^2 with NIRCam, to a maximum depth of $m_{ab} \simeq 30.2$ mag (F200W), and a total of 9.0 arcmin^2 with MIRI, to a limiting sensitivity of $m_{ab} \simeq 27.21$ mag (F560W).

We aimed for the resulting dataset to be able to revolutionise our knowledge of galaxy and black-hole formation/evolution to the high-redshifts currently probed, while also catering for the wider extragalactic community. PRIMER would have delivered the deepest public *JWST* NIRCam+MIRI imaging to inform the community for Cycle-2 guaranteed observing (GO) proposal preparation, specifically the deepest public imaging *JWST* would have produced for the first 18 months of the mission. The wavelength coverage ($0.6 < \lambda < 10\mu$m) of PRIMER

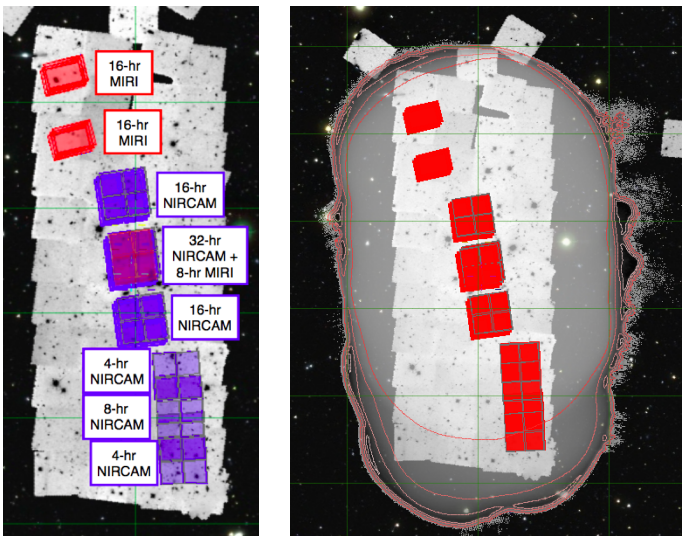

Figure 3.2 *The left-hand side of Fig. 3.2 shows the layout of our observing in the COSMOS CANDELS field built using the APT (Section 3.1.3). We show the HST current coverage with ACS in V_{606} and i_{814}, along with WFC3 F125W. The red tiles represent the MIRI FOV coverage, while the blue tiles represent NIRCam. The right-hand side shows the addition of SCUBA-2 coverage in the COSMOS field, with the same ERS PRIMER observing strategy represented by the red tiles.*

enables the detection and redshift determinations of galaxies beyond $z > 10$, with an improved angular resolution, breaking through existing confusion limits and enabling spatially resolved studies out to the highest redshifts. MIRI parallel observations would have provided the first deep, unconfused mid-IR imaging across a vast wavelength range (5–20 μm), where we could explore the dust-obscured star formation to over an order of magnitude deeper than achieved with *Spitzer's*. This wavelength range is currently not being utilised by any Cycle-1 GTO program. The vast number of objects with the deepest near/mid-IR imaging achievable within the ERS constraints will provide hundreds of new high-redshift galaxy targets that are sufficiently bright enough for NIRSpec follow up in later *JWST* Cycles. The locations of the observations also allows potential follow up and exploitation of current observations with other instruments, such as ALMA, SCUBA-2 and *HST*.

3.2.1 Observing Description Overview

We proposed two NIRCam imaging prime pointings in eight filters (F090W, F115W, F150WW, F200W, in the NIRCam SW channel, andF277W, F356W, F444W, F410M in the NIRCam LW channel), with associated MIRI parallel

imaging in four MIRI filters (F560W, F770W, F1280W, F1800W). This would then be followed by two MIRI prime pointings in the F770W filter, with associated NIRCam parallel imaging in the same eight NIRCam filters selected in the previous section of our observing strategy. The MIRI Primes are located on top of the NIRCam primes to ensure a multi-wavelength set of contiguous observations with both NIRCam and MIRI ($0.60 < \lambda < 10\mu$m). The desire to open up galaxy discovery space beyond redshift $z > 10$ leads to required detection limits of $m_{ab} \simeq 30.2$ mag in the NIRCam F200W filter. This requires a baseline plan of 4hr integration in each of the eight NIRCam filters while also stepping with a module size NIRCam step. This ensures that module A for pointing two will lie on-top of modules B's initial pointing for the second set of integrations. This in-turn doubles the total number of exposures and integrations, resulting in a 4.5 arcmin^2 region with a total exposure time of 8hrs for every NIRCam filter. This forms the deepest component of our NIRcam observations and also increases the area and dynamic range of our MIRI parallel observations. An invaluable further increase in area at somewhat shallower depths (2hr and 1hr/filter), is provided by the NIRCam parallel imaging taken in parallel to our two MIRI prime pointings. In total, this provides a total NIRCam coverage, at a range of depths, of 25 arcmin^2.

The MIRI prime pointings consist of two 4-hr pointings in the F770W filter covering the same 4.5 arcmin^2 deepest region of our NIRCam prime pointings, within the COSMOS CANDELS Field. This band provides a crucial long-wavelength extension to the NIRCam imaging, improving our ability to reclaim redshifts and stellar masses of extremely high-redshift galaxies. These MIRI pointings reach a 5σ detection limit of $m_{ab} \simeq 26.4$ mag, providing the deepest mid-IR photometry currently achievable. Along with the NIRCam Prime pointings, we observe with MIRI in parallel. The deep four-band MIRI imaging in parallel covers a separate 4.5 arcmin^2 region lying within the COSMOS CANDELS field. The integration times are solely driven by the prime NIRCam observations providing 4-hour integrations in each filter (F560W, F770W, F280W, F1800W). This filter mix was designed to best constrain the spectral energy distributions of intermediate redshift ($1 < z < 3$), low-mass, dusty star-forming galaxies. This difference in total integration time between NIRCam and MIRI is mostly down to NIRCam's ability to observe in both a SW and LW filter simultaneously, effectively doubling the integration time per filter.

The left-hand side of Fig. 3.2 shows the layout of our observing in the COSMOS CANDELS field built using the APT (Section 3.1.3). We show the current *HST*

coverage with ACS in V_{606} and i_{814}, along with WFC3 F125W. The red tiles represent the MIRI FOV coverage, while the blue tiles represent NIRCam. The right-hand side shows the addition of SCUBA-2 coverage in the COSMOS field, with the same ERS PRIMER observing strategy represented by the red tiles.

3.2.2 Scientific Rationale

The advances offered by *JWST* for the study of galaxies in the young Universe are spectacular. Most uniquely transformative are its capabilities at wavelengths $\lambda > 2\,\mu$m, in terms of depth and angular resolution.

Early Galaxy Evolution and Re-ionisation

A key goal of the proposal was to produce the deepest possible NIRCam+MIRI imaging survey (consistent with the constraints of the ERS program), in order to extend our knowledge of galaxies to both higher redshifts, and fainter magnitudes than is currently achievable with *HST*. This work is fully motivated by that fact that, beyond $z \simeq 9$ (where only $\simeq 10$ galaxies are currently confirmed: Ellis et al. 2013; Oesch et al. 2014, 2016; McLeod et al. 2016; Ishigaki et al. 2018) the prevalence and/or evolution of galaxies is essentially unknown. Theoretical and observational constraints on reionisation suggest that galaxy evolution extends to $z > 15$ (e.g. Robertson et al. 2015). In addition, even at $z \simeq 7$–8, virtually all theoretical arguments suggest that the bulk of the UV luminosity density and mass density lies below the current detection limits of the deepest *HST* imaging (e.g. Dayal et al. 2014; Mason et al. 2015), motivating surveys capable of detecting lower-luminosity galaxies, down to $M_{UV} \simeq -15$. At the same time we need to remove the bias against the selection of temporarily quiescent/quenched galaxies to complete the high-redshift galaxy census (via Balmer-break selection), and for the first time constrain the dusty star-forming cycle at early times.

JWST provides enormous potential for advancing our knowledge of early galaxy formation, and for this to be realised, we need very deep imaging while also gaining as much area coverage as possible. The wider area allows detection of the very brightest objects in the Universe, providing candidates for appropriate follow-up (e.g. NIRSpec) while also reducing the effects of cosmic variance. My simulations (see Chapter 4) also indicate that eight-band NIRCam imaging is required to yield secure photometric redshifts, explicitly including the NIRCam

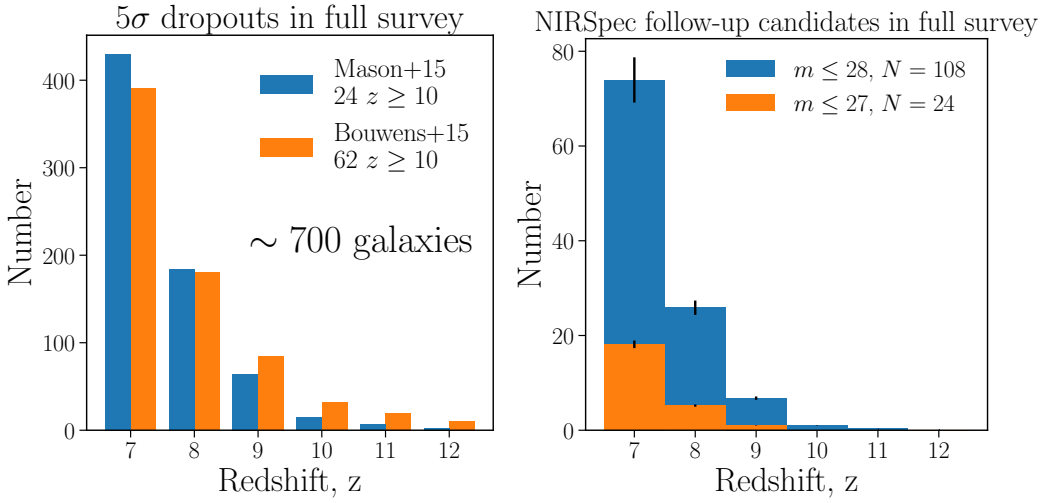

Figure 3.3 **Left**: *Predicted redshift distribution of galaxies at $z > 7$ calculated for the PRIMER proposal, based on the observing strategy outlined in 3.2.3. We plot two alternative predictions for all galaxies beyond $z > 7$ detected with at least 5σ confidence from both Mason et al. (2015) and Bouwens et al. (2015). It shows that a programme like PRIMER would detect approximately 700 galaxies beyond $z > 7$ and therefore, for the first time measure the (currently unknown) prevalence of galaxies beyond $z > 10$.* **Right**: *Predicted number counts for all galaxies beyond $z > 7$ expected to be detected by a JWST program, similar to that of PRIMER. We predict the number of galaxies that are of the correct brightness to be followed up by NIRSpec spectroscopy to be larger than 100 (Mason, private communication).*

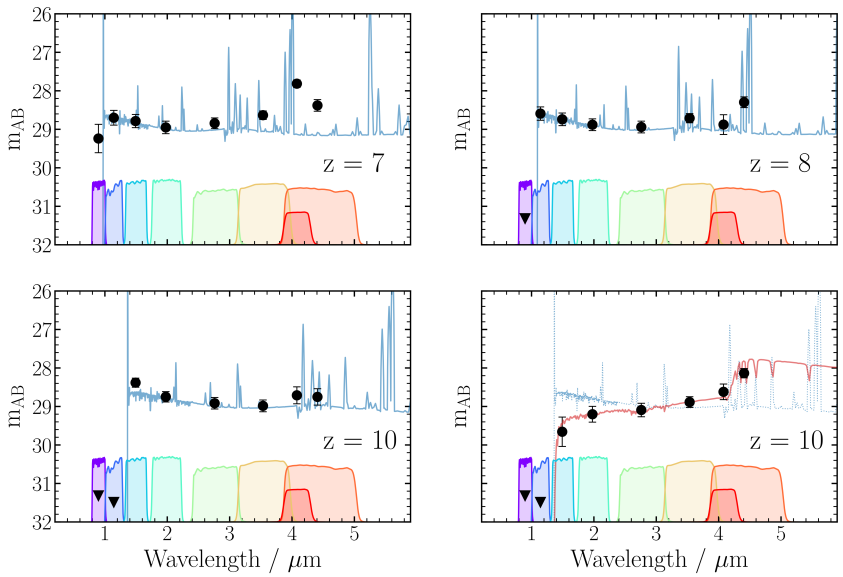

Figure 3.4 *The power of multi-band NIRCam + MIRI imaging for the discovery and study of high-redshift galaxies. The blue SED shown at* $z = 7, 8, 10$ *is that of a FiBY (Paardekooper et al. 2013; Cullen et al. 2017) simulated star-forming galaxy with* $Z/Z_{\odot} \simeq 1/3$*, normalised to* $m_{3\mu m} = 29$ *mag, with the data-points showing the simulated photometry (and associated uncertainty) assuming 1-hr exposures per NIRCam filter. As well as a clear delineation of the Lyman-break, the impact of the strong rest-frame optical emission lines (produced by sub-solar metallicity galaxies) on the photometry is clear; F444W−F410M colour is invaluable for redshift refinement and provides estimates of emission-line equivalent widths, and resulting corrections to stellar mass. The 4th panel shows an alternative (red) SED at* $z \simeq 10$*, produced by a starburst at* $z \simeq 15$ *(*$\simeq 200$ *Myr old), demonstrating that NIRCam + MIRI imaging can also provide key information on earlier star-formation activity.*

filters with a $\lambda_{effective} < 2.0\mu$m, as these filters are vital in identifying the Lyman-break at $z \geq 7$. Within the $\simeq$ 50 hrs limit of the largest of ERS programmes, the optimal approach involves two overlapping NIRCam prime-pointings, with additional area/dynamic-range provided by NIRCam parallel observations (taken in parallel with MIRI prime imaging, detailed in Section 3.2.3 and 3.2.3). In Fig. 3.3 I show predictions of the sample-size/redshift distribution of galaxies at $z \geq 7$, which should be revealed by this survey design. We anticipate $\geq$ 700 galaxies at $\simeq$, of which between approximately $\simeq$ 25 and $\simeq$ 60 will lie within the previously uncharted territory at $z > 10$. Moreover, because our approach covers a total area of $\simeq$ 25 arcmin^2, a programme like PRIMER would deliver a substantial sample (>100) of $z \geq 7$ galaxies of sufficient brightness for appropriate NIRSpec follow-up in Cycle-2 of *JWST* science timeline (see Chapter 2).

Although WFC3/IR enabled *HST* to probe beyond the $z \simeq 6$ Universe and into the first Gyr of cosmic time, the isolation of secure samples of galaxies beyond redshift $z > 7$ has been severely hampered by the curtailment of *HST* wavelength coverage, which is limited to $\lambda < 1.6\mu m$. Robust redshift information benefits greatly not only from the identification of the Lyman-break at $\lambda_{rest} = 1216$Å, but also from the extended/high-quality wavelength coverage above the break which allows us to exclude lower-redshift red and dusty interlopers. Here, *JWST* is again transformative. As we show in Fig. 3.4, our eight-filter NIRCam approach can not only securely identify the Lyman-break galaxies out to the highest redshifts, but can also provide robust SED information such as; revealing the presence of rest-frame optical emission lines or a Balmer-break, with the combination of F444W and the medium-band 410M filter being particularly influential. This is explored further in the next chapter (see Chapter 4) It is now well-established that [OIII] lines of extreme equivalent widths (EW_0) become more prevalent with increasing redshifts and/or decreasing metallicity (Nakajima et al. 2016), and, for brighter objects, have already proved detectable in broad-band *Spitzer* IRAC photometry (Smit et al. 2015). Not only can such emission-line signatures provide invaluable additional redshift information, but they also offer one of the few ways of estimating the escape fraction of ionising photons from young galaxies in the reionisation epoch (Stark 2016).

Primaeval Galaxies

The shape of the rest-frame UV continuum emission from a galaxy, or more simply the UV continuum slope β (where $f_\lambda \propto \lambda^\beta$) is a powerful probe of the physical properties of a star-forming galaxy. In particular, while present-day star-forming galaxies typically display a $\beta \simeq -2$, it is clear that a measurement of $\beta \simeq -3$ would unambiguously indicate the presence of a young, low-metallicity, stellar population along with a high ionising escape fraction (Robertson et al. 2015) with measured values $\beta < -3$ potentially leading to the first discovery of genuinely metal free (i.e POP-III, see Chapter 1) stars. The initial excitement that this had been achieved with WFC3/IR at $z \simeq 7$ (Bouwens et al. 2010) was subsequently tempered by a full understanding of the uncertainties and biases. In fact, it was concluded that the critical problem was not only the depth of *HST* imaging but also the lack of accessible wavelength baseline red-ward of the Lyman-break. This resulted in an average β calculated for galaxies at such redshift of around $\beta = -2 \pm 0.3$. However, there is intrinsic scatter in the galaxy β distribution (Rogers

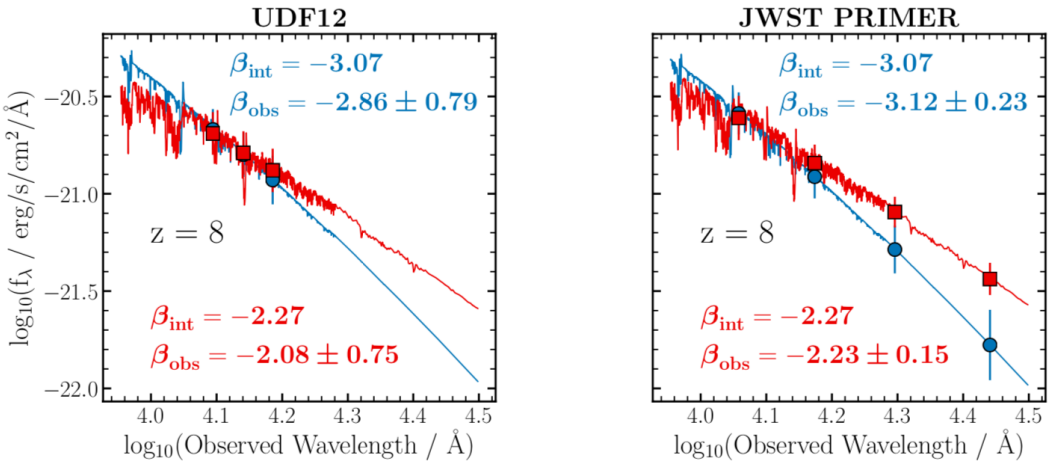

Figure 3.5 *The accuracy with which UV continuum slope, β (where $f_\lambda \propto \lambda^\beta$) can be measured with PRIMER, as compared to current state-of-the-art HST measurements. The red curve shows a 300 Myr BPASSv2-100bin constant star-formation model with solar metallicity ($Z/Z_\odot$ = 1), while the blue curve shows a 1 Myr BPASSv2-100bin starburst model with $Z/Z_\odot$ = 0.05, both at $z \simeq 8$, and normalized to m_{F125W} = 29 mag. Assuming no dust attenuation, the intrinsic UV slopes are β_{int}=−2.3 and β_{int}=−3.1, respectively. In the left panel we show the (very poor) accuracy with which these UV slopes can be recovered with the deepest existing HST near-IR photometry from the UDF12 campaign (F125W, F140W, F160W). In the right panel both SEDs are now sampled by the four NIRCam filters covering the rest-frame UV at $z \simeq 8$ (F115W, F150W, F200W, F227W). With the improved depth ($\simeq$ 10-σ and wavelength baseline, the β values are recovered to $\simeq$ 5% accuracy, enabling these SEDs to be clearly distinguished, and hence potentially exotic, dust-free, low-metallicity systems to be cleanly isolated for subsequent study.*

et al. 2014) and incredibly blue objects could still be found in the high-z galaxy population.

JWST and PRIMER offer the depth and wavelength coverage that has been lacking in order to transform this situation (see Fig. 3.5). Of the $\simeq$ 700 $z > 7$ galaxies we expect to uncover in the imaging, we predict that $\simeq$ 400 will be detected at the 10-σ level, which will result in approximately 5% accuracy in the β measurement for individual galaxies. A programme like PRIMER would revolutionise our knowledge of the SEDs and hence the physical properties of galaxies in the reionisation era, and is therefore capable of revealing the first genuinely primaeval galaxies.

The Early Growth of Stellar Mass

For comparison with theory, it is vital to determine accurate stellar masses for high-redshift galaxies to establish the evolving galaxy stellar mass function (SMF). Because rest-frame UV emission is so sensitive to recent star-formation activity and dust obscuration, this requires observations sampling long-ward of the 4000Å/Balmer break, and ideally imaging at $\lambda \simeq 1\mu m$. Consequently, due to the rest-frame UV bias of *HST* imaging at high-z, and the limited sensitivity of *Spitzer*, it has not been possible to measure the accurate stellar masses for all but the brightest galaxies at $z > 4$ (Grazian et al. 2015); indeed our current knowledge of the evolving galaxy mass function at $z > 4$ is primarily based on bootstrapping from the UV luminosity function. In addition, it is currently impossible to accurately quantify the contribution of red, quiescent galaxies at $z > 4$, which cannot be detected by the Lyman-break technique.

A program, like PRIMER, will be able to overcome these problems. In Figure 3.6, we show that the 9-band NIRCam+MIRI imaging strategy is not only capable of completing the mass census at high-z by uncovering previously undetectable quiescent red galaxies at $z \simeq 4$, but also demonstrates the crucial importance of our deep 7.7μm MIRI imaging for distinguishing genuinely quiescent galaxies from the dusty star-forming objects (Glazebrook et al. 2017; Simpson et al. 2017). This is a key step in establishing reliable galaxy masses for red sources, and hence completing the census of global mass density at early times.

These *JWST* programmes will transform the accuracy with which stellar masses can be measured at all redshifts. Stellar mass estimates will now be reliable up to $z \simeq 12$, down to stellar masses as low as $M_* \simeq 10^8 M_\odot$. With PRIMER we would be able to accurately delineate the evolution of the stellar mass function up to $z \simeq 12$, with direct, assumption-free measurements, and a mass-complete sample. Crucially, since the stellar mass is an integral product of earlier star formation, accurate measurements at $z \simeq 10$ will provide the first indication on when 'first light' occurred.

A complete census of dust-enshrouded star formation

Although a multi-band deep NIRCam and MIRI imaging programme, like PRIMER, will discover galaxies at extreme redshifts, the vast majority of galaxies observed will be at intermediate redshift. These galaxies themselves extend a

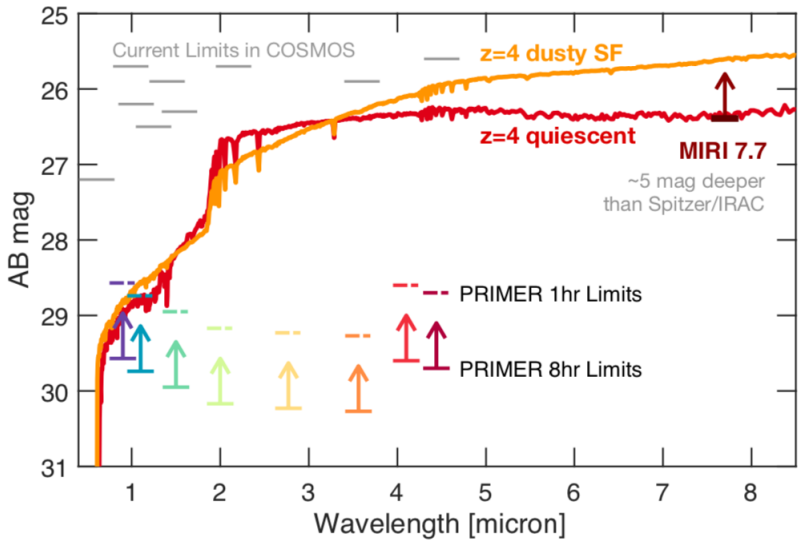

Figure 3.6 *A demonstration of the ability of PRIMER to reveal red quiescent high-redshift galaxies (here, a 1-Gyr old galaxy at $z \simeq 4$) which lie well below the detection thresholds of HST and Spitzer imaging. The plot also shows the crucial role of our planned deep MIRI 7.7-μm photometry in enabling genuinely quiescent galaxies to be distinguished from dusty star-forming objects.*

different frontier: that of low stellar mass and low SFR, a parameter space not previously accessible at $z \simeq 1$–3. Our strategy employes MIRI parallel observations in four filters over 4.55 arcmin^2 to achieve a deeper understanding of this regime. With predicted depths ($m_{ab} \simeq 24$ mag in F1800W) and extrapolating the 24 μm source counts from Béthermin et al. (2010), we would expect to detect approximately 200 sources at 18 μm. Not only is this approximately thirty times deeper than achieved in the deepest *Spitzer* surveys (Papovich et al. 2004), it also represents approximately ×100 improvement in SFR sensitivity over the deepest radio surveys.

Deep contiguous imaging with MIRI, like our parallel imaging, will therefore open a new window on obscured star formation rate in numerous low-mass galaxies ($M_* \simeq 10^9 - 10^{10}$ $M_\odot$ between redshifts $z \simeq 1$–2, which cannot be selected with any other facility including ALMA (Dunlop et al. 2017). Among many legacy capabilities, this will reveal the prevalence of transient starbursts at $M_* \simeq 10^9$ $M_\odot$, relative to the quasi-stable growth known to dominate at $M_* > 10^{11} M_\odot$. (Schreiber et al. 2017), as well as transition systems as in the 'green valley' and their role in assembling the red sequence (Rowlands et al. 2018). It is essential to select depth capabilities at least matching the current *Spitzer* IRAC and *HST* imaging in UV-NIR (CANDELS, S-CANDELS), thus directly connecting

the MIR excess to a well-sampled UV SED for direct constraints on the dust extinction curve (e.g. Salmon et al. 2016). In PRIMER, we utilised the 5.6μm, 7.7μm and 12.8μm bands to maximise the number of galaxies with multi-colour photometry (detecting N $\simeq$ 600, 500, 200 respectively in each band, based on EGG; Schreiber et al. 2017). This will (i) provide emission-line-free stellar masses and photometric redshifts which is especially crucial for red galaxies beyond redshift $z > 2$; (ii) determine the incidence and relative strength of AGN/SFR composite MIR SEDs in low-mass galaxies lying below $z < 2$; (iii) characterise the PAH emission line features and strengths enabling the leverage of single MIRI-band SFR calibrations (applicable to the 7.7 μm MIRI prime observations) Finally, the full MIRI catalogue will provide valuable priors for stacking in the deep SCUBA-2 imaging (Bourne et al. 2017), as well as potential targets for ALMA and MIRI (MRS, LRS) follow-up spectroscopy.

Galaxy Morphologies

As already discussed, the massively improved angular resolution offered by *JWST* will break through the confusion limit of previous *Spitzer* observations at $\lambda \simeq 3 - 24$ μm , but the quality of the NIRCam and MIRI imaging delivered by a *JWST* programme like PRIMER will also transform our understanding of the structure and assembly history of galaxies, along with their super-massive black holes in the young Universe.

First, the approximately ×3 improvement in spatial resolution over *HST* WFC3/IR imaging offered by the NIRCam SW channel will enable the rest-frame UV sizes/structures of high-z galaxies to be traced out to $z \simeq 11 - 12$. This, coupled with the new larger samples of galaxies beyond $z > 6$ should resolve the current controversy over the redshift/luminosity dependence of galaxy sizes (e.g. Oesch et al. 2010; Oesch et al. 2013; Curtis-Lake et al. 2016). Moreover, armed with the first reliable stellar masses at high-z, we will be able to perform the first investigation of the size-mass relation at these extreme redshifts, for comparison with theoretical predictions.

Second, imaging from a programme like PRIMER would provide the very first robust information on the rest-frame optical/IR morphologies of galaxies over a more extensive range of redshifts. This can be crucial for tracing the distribution of stellar mass, and for removing (and quantifying) the UV morphological distortions introduced by the dust obscuration. At intermediate

redshifts, NIRCam SW imaging can provide near-IR imaging resolution-matched to deep *HST* ACS imaging, enabling detailed pixel-by-pixel SED analysis, and the investigation of the stellar masses of star-forming clumps (e.g. Wuyts et al. 2012), studies of the UV-optical morphologies of dusty star-forming galaxies (Targett et al. 2012) well matched to what is now being delivered by the sub-mm observations in ALMA, and new information on the evolution of structure crucial to our understanding of quenching mechanisms (e.g. van Dokkum et al. 2015; Whitaker et al. 2017; Almaini et al. 2017). At the highest redshifts, deep *JWST* imaging, as proposed through PRIMER, will provide the first insight into the spatial distribution of stellar mass in galaxies, where our current completely UV-biased view can even leave ambiguity over what constitutes an individual galaxy (Bowler et al. 2017).

3.2.3 Technical Description

Target Field and Layout

Our proposed PRIMER observing strategy is summarised in Fig. 3.2, which shows the overall observing layout of our NIRCam and MIRI pointings within the COSMOS CANDELS field, along with the estimated area and depth calculations per filter for each subregion. The chosen target field was driven by the importance of pre-existing *HST* imaging over the relevant scales, naturally leading to a CANDELS field. A number of the GTO programmes comprehensively cover the GOODS-S and GOODS-N CANDELS fields (see JADES; Section 3.3.2, CEERS; Section 3.3.1 MIRI-UDF; Section 3.3.2 and Section 3.3.2) making them unavailable for an ERS proposal given the constraints on duplications and the available time. The UDS and COSMOS are equatorial fields, where we are constrained by roll angle and limited visibility to introduce some complexity in designing an efficient programme. The COSMOS and UDS fields are only visible for approximately ≈ 30 days, twice a year. *JWST* also has a minimal V3 position angle, fixing the orientation (≈ 90-100 degrees) of the *JWST* focal plane on the sky. However, in our case, this aligns perfectly with current COSMOS CANDELS observations enabling both NIRCam and MIRI prime and parallel observations to fit within the *HST* COSMOS observing region as well as lying within current deep SCUBA-2 observations (Fig. 3.2).

Fig. 3.7 shows a plot of the various V3 position angles and dates throughout the

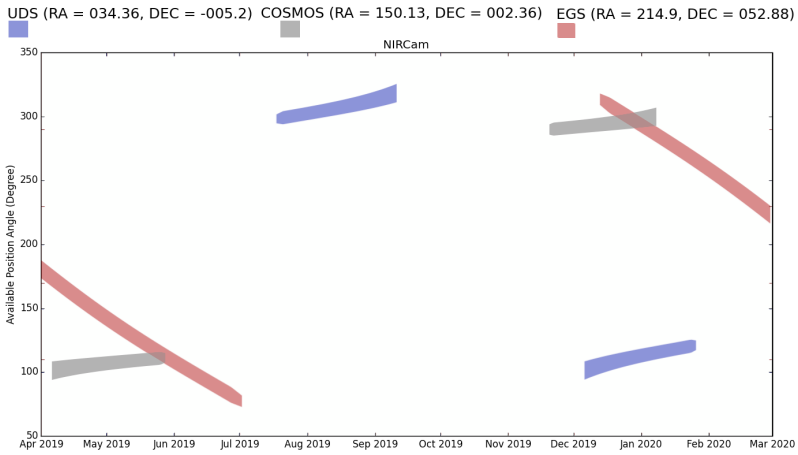

Figure 3.7 *This plots shows the observing windows and telescope V3 position angles for the COSMOS, UDS and EGS CANDELS fields. COSMOS is the preferred field for PRIMER as it is ideally placed in the original ERS schedule. It also sits at an excellent, effectively stationary angle of ≃ 100 degrees (see 3.2 for visualisation). The EGS is also an option; however, it is far more rapidly rotating, and the PA is only consistent with the HST CANDELS data for a small amount of time. The EGS is also unobservable with ALMA.*

year for three of the CANDELS fields, COSMOS, UDS and EGS. COSMOS is the most preferred target field for our observing strategy, as it sits nicely at the correct V3PA for an extended amount of time. The EGS sits at one V3PA for a minimal amount of time meaning the FOV needs to be rotated continuously. This not only adds overheads but also prevents any efficient contiguous and homogenous mosaicing.

NIRCam depths, filters, integration times and pointings

We proposed two sets of observations with NIRCam, a prime pointing with MIRI parallels and a parallel pointing with MIRI Primes. The former provides us with the deepest region of our observational programme, while the latter allows for a MIRI overlap in the same region. Initially, we would observe with NIRCam for 4 hours in one pointing while rotating through four sets of filters. NIRCam can observe in both a short-wavelength and long-wavelength channel at the same time, allowing us to observe in eight filters each with 4 hours of integration, leading to a total expenditure of 16 hours. We would then step module A onto module B and repeat the same set of observations providing a total exposure time of 8 hours for each filter in a small region equating to approximately 1 module NIRCam FOV ($\approx$ 4.5 arcmin^2). This, of course, leaves two extra pointings either

side of the deepest region with half the total exposure time of our deepest region equating to 4 hours per filter with a total area of approximately 9.0 arcmin^2. In total we observe in eight NIRCam photometric bands, through four short-wavelength filters (F090W, F115W, F150W and F200W), while simultaneously observing with four filters in the long-wavelength channel (F277W, F356W, F410M, F444W). The filter selection was chosen to provide a contiguous set of photometric bands enabling an extensive wavelength coverage of the spectral energy distributions of galaxies across a wide range of redshifts and stellar masses. There are also two NIRCam parallel pointings associated with the MIRI prime pointings south of our deepest NIRCam prime pointings. This provides a valuable increase in NIRCam area coverage at a shallower depth of approximately 1/2hr integration times per filter. This increases the total area coverage of NIRCam in PRIMER to $\approx$ 25 arcmin^2. The total number of galaxies expected to be detected is $\approx$ 15,000, with around 80% of these currently undetectable by *HST* and *Spitzer*.

All NIRCam prime pointings, in all filters, use an intra-module three-point primary dither pattern. This ensures full coverage within each NIRCam module covering the gaps between the detector quadrants. For a small mosaicing imaging strategy with NIRCam, this is the most efficient method of primary dithering providing minimal movement between each dither and integration. Large primary dithers are far more beneficial for substantial mosaicing strategies because the continuous large movement of the NIRCAm FOV has an increasingly less significant effect on the total overheads. These larger dither patterns also remove the need to step into the inter-module gap between both module A and module B of the NIRCam focal plane. The intra-module dither pattern ensures we maximise the efficiency of the NIRCam prime pointing while also ensuring a contiguous image in each module.

Along with the intra-module dither pattern, we require a sub-pixel dither pattern to ensure we fully sample the PSF in all filters with NIRCam. As we observe with a parallel observation with MIRI we require a dither pattern compatible for both MIRI and NIRCam. The sub-pixel dithering is therefore set to a 2-point pattern for most filter configurations, maximising efficiency yet ensuring we appropriately sample the PSF in all filters for both NIRCam and MIRI. This is not a possible option for MIRI's shortest filter F560W, which in our case is accompanied by the prime NIRCam observations in F090W (SW channel) and F277W (LW channel). For simplicity, we choose the 4-point sub-pixel dither pattern (rather than the 3-point dither pattern) in order to keep the integration times comparable across

all filters by halving the number of integrations.

Detector readout modes also require careful consideration when building an observing programme. As charge accumulates on a detector pixel from interacting with incoming photons during a NIRCam integration, the detectors are read out multiple times without destructively interfering with the charge in each pixel itself. This effectively allows us to sample the data without interrupting the integration. Readout modes differ by changing the number of times a charge is read out before the end of the integration. Each readout pattern contains a group of up to 20 detector reads, with each group yielding a separate saved image obtained by averaging over a certain number of groups. Depending on the type of science and length of integrations, different types of readout modes perform to higher quality and efficiency. In general, averaging over more frames yields a slightly higher signal to noise ratio for a given group length and integration time but increases vulnerability to cosmic rays. The readout modes chosen for our NIRCam prime observations is DEEP8 with a number of groups between 5-7; this was suggested by the NIRCam test team to maximise the efficiency of observation. In this case, we use six groups. The readout mode and number of groups determine the total time per integration time per pointing for each pixel. So, in this case, a DEEP8 readout mode with six groups has a total time of 1160s per integration. Then one chooses the number of integrations to determine the total integration time; in this case, we chose four integrations per pointing. Including the 3-point intra-module dither pattern, this strategy produces a total of 12 integration; this equates to a total integration time of 4 hours per integration for each filter. The NIRCam Parallel observation assumes the same readout patterns and number of groups for a small number of integrations. We assume a similar dither pattern in all cases ensuring full coverage of the intra-module gap.

MIRI depths, filters, integration times and pointings

Our MIRI prime observations consist of two 4hr pointings in only the F770W filter situated on top of the deepest NIRCam prime imaging region. The F770W filter was chosen mainly due to its excellent sensitivity, while also providing a much more useful longer wavelength extension to our NIRCam imaging than F560W. This imaging is key to the successful extension of stellar mass measurements out to the highest redshifts, specifically for high-mass dusty galaxy populations. It can provide direct detections of any galaxies with $M_* > 10^9 M_\odot$ out to

$z \approx 8$ and average masses via stacking for fainter galaxy populations detected in the NIRCam imaging. We split each of the two MIRI pointings into four separate observations to allow for the appropriate filter changing in the NIRCam parallels, matching the NIRCam primes. This ensures full survey coherence between the NIRCam primes and parallels; this adds almost no overheads to the programme as the procedure is fully contiguous. The MIRI primes utilise the 'FAST' readout mode, which is suggested for almost all scientific purposes. The 'FAST' readout mode minimises the thermal noise from an observation where the background-dominated regimes. We select a number of groups and integrations that maximises the efficiency of the observation reaching the best SNR while limiting the overheads and total exposure time. Each observation and filter configuration again utilises a 3-point dither pattern with sub-pixel dither to ensure appropriate sampling of the PSF across all wavelengths, and to also cover the intra-module gap between the detector quadrants of the NIRCam parallels. As the MIRI primes have one MIRI-sized step to cover the full deepest region of the NIRCam primes observations, this covers the inter-module gap between module A and module B in the NIRCam parallels, providing a contiguous region of observed sky.

We also include deep 4-band (F560W, F770W, F1280W, F1800W) MIRI parallel imaging over ≈ 4.5 arcmin^2 associated with the previously described NIRCam prime observations. This utilises the resolution and sensitivity of *JWST* MIRI to break through the confusion limit of *Spitzer* and transform our understanding of the dust-obscured star formation at intermediate redshifts and low stellar masses. The integration times are driven by the NIRCam prime observations with the scientific rationale for the filter choices described in Section 3.2.2. The technical configuration of the MIRI parallel's is somewhat dictated by the NIRCam primaries, specifically the dither patterns, alluded to previously. As stated, the number of integrations in the F560W filter is halved to account for the extra sub-pixel dithering prescribed by the NIRCam primes. The total number of integrations is, therefore, the same for the first two MIRI filters, as well as having the same number of groups. The longer wavelength filters require a smaller number of groups per integration to avoid saturating the pixels in the detector. This is trivially done by halving the number of groups and doubling the number of integrations giving us the same exposure time across all MIRI filters. We see this affects the efficiency of the total observing charged times to a very small factor. The readout mode is 'Fast' for all MIRI exposures as this is the default for imaging; this mode minimises noise from the background-dominated regimes.

3.3 Accepted *JWST* Proposals

3.3.1 DD-ERS Proposals

In this section, I overview the accepted *JWST* DD-ERS proposals that study galaxies and the IGM at high redshift. Further information about more local Universe programmes currently accepted for the *JWST* ERS programme can be found at `http://www.stsci.edu/jwst/observing-programs/approved-ers-programs`. I only cover the programmes with some form of imaging from either NIRCam or MIRI. The DD-ERS programme is a set of observations designed as a showpiece for *JWST's* science capabilities and instruments and will allow the scientific community to get up to speed in terms of data reduction. These observations will take place during the first five months of *JWST* scientific operations, following completion of the 6-month commissioning period.

The Cosmic Evolution Early Release Science (CEERS) Survey - 1345

The Cosmic Evolution Early Release Science (CEERS) Survey is a *JWST* imaging and spectroscopy survey covering a total of 100 arcmin^2 targeting the majority of the Extended Growth Strip (EGS) *HST* legacy field. CEERS will observe using three instruments in a number of different observing modes to create a mosaicing imaging strategy including 10 NIRCam pointings with approximately 37 hours of science integration time at a total cost of $\simeq$ 63 hours. Six of these NIRCam pointings will be accompanied with parallel NIRSpec MSA observations, while the remaining four pointings will include MIRI parallel imaging. In addition to the prime NIRCam pointings, CEERS will utilise the NIRCam grism spectrograph to cover an area equivalent to $\simeq$ 4 NIRCam pointings. The placement of the mosaic lies nicely on the EGS aligning with the current *HST*/WFC3 region. A V3PA roll angle of 130 degrees is necessary to maximise the total crossover between CEERS and current *HST*/WFC3 region; however, this is, fortunately, the limiting roll-angle constraint when observing in this region of the sky. The EGS is, therefore, the preferred target; however, there is flexibility in being able to change to either the COSMOS or UDS CANDELS field, albeit with detriment to the total observing efficiency and crossover between the instruments being used in CEERS.

CEERS will observe in a total of six filters across the entirety of the NIRCam

pointings in both the SW and LW channels simultaneously; F115W+F356W, F150W+F277W and F200W+F444W. Similarly to ERS PRIMER, each exposure consists of between 4-8 groups in the DEEP8 readout mode with three integrations resulting in a total exposure time of 2867 seconds when using five groups per integration for every filter. With the shortest wavelength filter lying at an effective wavelength of $\lambda \simeq 1.15\mu$m, Lyman-break selection can only be used to find the very highest redshift galaxies ($z > 9$). This also means that CEERS requires another set of integrations across the NIRCam imaging region in the F115W band; this is done in parallel with the NIRCam grism spectroscopy. Consequently, when in parallel, a different recipe of groups and integrations are needed as Grism spectroscopy requires dithering to ensure a fully sampled SED. This effectively increases the required number of integrations, decreasing the total number of groups and in turn, reducing the total efficiency of the NIRCam F115W imaging.

CEERS enables immediate community science into both extragalactic *JWST* science drivers 'First Light and Reionisation' and 'The Assembly of Galaxies', including 1) The discovery of 20-80 galaxies at $z \simeq 9{-}13$, constraining their abundance and physical nature; 2) Deep spectra of > 400 galaxies at $z > 3$, including 40 known candidates at $6 < z < 9$, enabling redshifts and constraints on the physical conditions of star-formation and black hole growth via line diagnostics; 3) Quantifying the first bulge and disk structures at $z > 3$; and 4) Characterising galaxy mid-IR emission to study dust- obscured star-formation and supermassive black hole growth at $z \simeq 1{-}3$. As previously stated, the shortest wavelength filter used in CEERS is the NIRCam F115W band which places the Lyman break at around $z \simeq 9$. Therefore, by design, CEERS will heavily rely on sufficient *HST* data to maximise the scientific output of the resulting NIRCam dataset.

Through the Looking GLASS: A *JWST* Exploration of Galaxy Formation and Evolution from Cosmic Dawn to Present Day - 1324

Through the Looking GLASS is an ERS programme primarily utilising NIRSpec and NIRISS with NIRCam parallel imaging of the Frontier Field Cluster, Abell 2744 [1]. In doing so, the aim is to study the intrinsically faint magnified galaxies over the redshift range $z \simeq 1{-}6$. The main scientific questions this programme will attempt to answer are: i) when did reionisation happen?, ii) what were the sources

[1] `http://glass.astro.ucla.edu/ers/`

of reionising photons?, and iii) how do baryons cycle in and out of galaxies?

There are two sets of primary observations, one with NIRISS: Wide Field Slitless Spectroscopy and the second with the NIRSpec MOS. Both sets of observations are accompanied by multi-wavelength NIRCam parallel imaging. The deepest NIRCam imaging will be obtained in seven filters in parallel with NIRSpec MSA primary observations. These seven filters are again observed simultaneously in the short and long wavelength channels: F090W + F444W, F115W + F444W, F150W + F277W and F200W+F356W. This multi-band photometry will require a DEEP8 readout mode with seven groups and only one integration. In this case, there will be no dithering, resulting in an undersampled PSF for the short-wavelength photometric bands. However, the imaging will reach impressive depths with a total of 4.6, 2.3 and 9.2 hours in the first two (F090W and F115W), middle four (F150W, F200W, F277W and F356W) and the final (F444W) filters respectively. This will result in an average AB magnitude of approximately m_{ab} $\simeq$ 29.5 mag in each filter. The primary NIRSpec observations utilise the multi-shutter array to a resolution of R $\sim$ 2700 in three gratings: G140H/F100LP, G235H/F170LP, and G395H/F290LP (see Chapter 2, Section 2.2.3). Each grating requires a total exposure time of 5 hours, including a three shutter dither pattern.

The primary NIRISS wide-field spectroscopy also observes in three direct imaging broad-band filters, F115W, F150W, F200W, to a total observing time of 35ks per filter at a resolution of R $\sim$ 150. The total exposure time per filter per grism is divided into six exposures of 900s each with small dithers between them, totalling 2.9 hours per filter. The grism continuum depth capability for 3σ per pixel is m_{ab}=26.3, 26.0 and 25.5 mag in the F115W, F150W and F200W filters, respectively. The direct imaging sensitivity capabilities are m_{ab} 27.5 mag in F115W, m_{ab} 27.6 mag in F150W, and m_{ab} 27.8 mag in F200W to a 10σ limit. In parallel with these observations, NIRCam short-wavelength and long-wavelength imaging will be obtained in the same filter sets as the NIRSpec parallel observation described above (F090W, F115W, F150W, F277W, F200W, F356W, F444W). As the NIRISS observations are not quite as long as the NIRSpec observations, here the NIRCam imaging is somewhat shallower, only imaging F090W and F115W for a total of 2.8 hours, and in F150W, F200W, F277W and F356W for 1.4 hours each. 5.6 hours of imaging will also be obtained in the F444W filter resulting in a flat depth capability of approximately $m_{ab} \simeq$ 29.0 mag per filter (5-σ).

TEMPLATES: Targeting Extremely Magnified Panchromatic Lensed Arcs and Their Extended Star Formation - 1355

Targeting Extremely Magnified Panchromatic Lensed Arcs and Their Extended Star Formation (TEMPLATES) is a 55-hour MIRI, NIRSpec and NIRCam imaging and spectroscopic programme studying four gravitationally-lensed galaxies (SGAS1723, SGAS1226, SPT2134 and SPT2147) in the redshift range $1 < z < 4$. The effect of lensing pushes *JWST's* ability to spatial resolve the star-forming region in galaxies beyond the peak era of cosmic star-formation activity. In order to achieve this, TEMPLATES make use not only of multiple instruments, but also multiple instrument modes onboard *JWST*, utilising NIRCam imaging, NIRSpec IFU spectroscopy, MIRI imaging, and MIRI MRS IFU spectroscopy. TEMPLATES targets the brightest and most-well characterised (by ancillary data) lensed sources currently detected, spanning a wide range of physical properties such as redshifts, specific star-formation rates, dust extinction and luminosity. The resulting dataset will be used to **i)** demonstrate extinction-robust star formation rate diagnostics for distant galaxies; **ii)** determine the physical scales of star-formation in distant galaxies, in an extinction-robust way; **iii)** measure specific star-formation rates and compare the spatial distribution of the young and old stars and **iv)** measure the physical conditions of star formation and their spatial variation.

Each object will be observed in all four observing modes (NIRCam imaging, NIRSpec IFU spectroscopy, MIRI imaging, and MIRI MRS IFU spectroscopy). The NIRCam imaging objective is to obtain broad-band photometry in multiple bands in order to resolve the SEDs for each object and create maps of stellar mass. TEMPLATES conducts NIRCam imaging in a total of 6 photometric broad-band filters, again observing in both the SW channel and LW channel simultaneously (F115W+277W, F150W+F356W, F200W+F444W). In total, each object will be observed with between 0.8 - 1-hour exposure for all filters combined, while the team has taken the precautionary measure of using a readout mode that will prevent saturation from neighbouring sources. The MIRI imaging obtained will allow for detailed analysis of the SED through the near-IR and mid-IR, explicitly mapping the PAH features through SED fitting. In total, TEMPLATES uses 7 out of the 9 possible broad-band filters available in MIRI: F560W, F770W, F1000W, F1280W, F1500W, F1800W and F2100W. Each object will be observed in these MIRI bands for a total exposure time of between 0.8 and 1.8 hours.

3.3.2 GTO

In this final sub-section, I provide an overview of the accepted GTO proposals that will study galaxies and the Intergalactic Medium at high redshift focusing only on the more extensive imaging surveys that contain either MIRI or NIRCam imaging. The *JWST* Guaranteed Time Observations (GTO) programme is designed to reward scientists who helped develop the critical hardware and software components or technical and inter-disciplinary knowledge for the observatory. The programme provides a total of about 16% use of the observatory over the first three cycles of operation. The relevant approved GTO programmes are briefly described below, organised by science topic.

JADES

The *JWST* Advanced Deep Extragalactic Survey (JADES) program[23] is a collaborative NIRCam and NIRSpec team GTO programme accepted as part of *JWST* Cycle-1. The main science goal is to study the formation and evolution of galaxies across a wide range of redshifts ($2 < z < 12$). Utilising the three main instruments on-board *JWST*, NIRCam, MIRI and NIRSpec, JADES is designed to maximise the crossover with current *HST*,*Chandra*, ALMA, and JVLA data, to produce an unprecedented view of high-redshift galaxies. This ancillary data will provide complimentary studies in the UV/optical/radio/sub-mm/X-ray. Targeting the well studied CANDELS fields, in particular, GOODS-North and GOODS-South (which includes the Hubble Ultra Deep Field, *HUDF*), JADES will provide a two-tier survey with 'Deep' NIRCam imaging in the GOODS-S field and a 'Medium' depth survey in both GOODS-S and GOODS-N. A total of nine NIRCam broad-band and medium-band filters will be used in addition to NIRSpec spectroscopy covering 0.7 - 5.2 μm. There will also be MIRI imaging taken in parallel to these primary observations spanning the wavelength range 7.7 - 12.8μm.

The 'Deep' survey will cover a total of 46 arcmin^2, centred on the HUDF/GOODS-S, with 10-σ NIRCam imaging to $m_{AB} \simeq 29.8$ mag with a peak exposure time of 120ks in the F115W filter. The nine broad-band and medium-band filters used in JADES are as follows: F070W, F090W, F115W, F150W, F277W, F200W, F356W, F410M, F444W. In addition to the NIRCam imaging, two

[2] `https://www.cosmos.esa.int/web/jwst-nirspec-gto`
[3] `https://issues.cosmos.esa.int/jwst-nirspecwiki/display/PUBLIC/Overview`

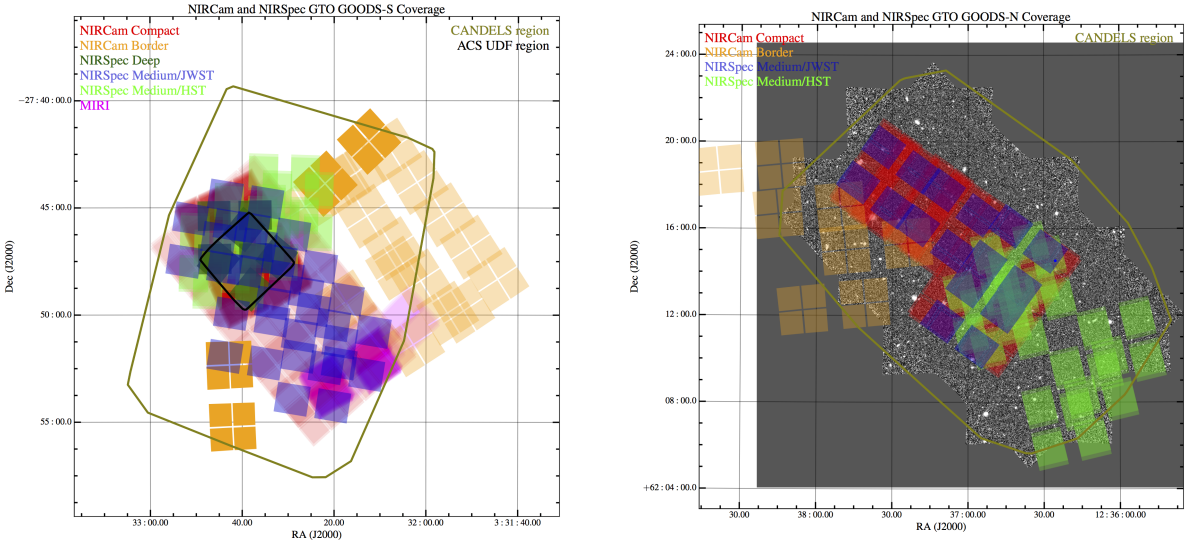

Figure 3.8 **Left Panel**: *The potential observing layout for JADES in the GOODS-S field. The underlying HST CANDELS coverage is represented by the gold border with the ACS HUDF highlighted by the black border. Different coloured panels represent the respective FOV for all observations. The light-green and dark-green panels represent the medium and deep NIRSpec pointings, respectively, with the dark-red and orange panels representing the medium and deep NIRCam observations, respectively. Finally, the MIRI observations are depicted by the pink panels.* **Right Panel**: *The potential observing layout for JADES in the GOODS-N field. The underlying grey image shows the current ACS/WFC3 coverage in the GOODS-N field with the entire CANDELS field shown by the gold border. The NIRCam and NIRSpec pointings are depicted by both the orange/red and blue/green panels, respectively. This image was taken from* `https://issues.cosmos.esa.int/jwst-nirspecwiki/display/PUBLIC/Overview`

NIRSpec pointings, each with a total integration time of 200ks, will be observed, one centred on the HUDF and the other centred on the forthcoming NIRCam imaging. These NIRSpec observations concentrate on studying $z > 6$ galaxies spectroscopically. It is important to note that there is no overlapping MIRI imaging in this region of the survey.

The 'Medium' survey comprises a much wider but shallower set of observations, covering a total of 190 arcmin^2 in both GOODS-S and GOODS-N to a depth of $m_{ab} \simeq 28.8$ mag. In this case, there will be a two-tier overlapping set of MIRI observations covering a total of 14 arcmin^2 with a deeper region reaching a depth of $m_{ab} \simeq 28.8$ mag in the 7.7μm broad-band MIRI filter only covering 8 arcmin^2. An additional set of 12 NIRSpec pointings will be conducted in JADES; expecting to collect >5,000 faint galaxy spectra, with a substantial number observed within the deep *JWST* imaging survey.

The resulting dataset will provide multi-wavelength data enabling comprehensive study through multiple methods of analysis to gain an understanding of vital galaxy properties such as stellar mass, luminosity, star-formation rate, stellar ages, sizes, metallicity, nuclear activity, gas kinematics, and outflows, over a wide range of redshifts. The potential field layouts are presented in Fig. 3.8, where the left panel shows the configuration for the GOODS-S field and the right panel shows the configuration for the GOODS-N field. It is clear that the layout is far from homogenous and, specifically for MIRI, there is very little overlapping coverage. Like CEERS, however, the dataset produced will require sufficiently deep *HST* optical data to robustly select Lyman-break galaxies at $z < 7$.

The MIRI HUDF Deep Imaging Survey

The MIRI HUDF Deep Imaging Survey is a GTO programme proposed by part of the MIRI GTO team, specifically the European Consortium MIRI (EC-MIRI) team lead by Dr Norgaard Nielsen and Professor Pablo Gonzalez. In effect, this is a joint project with the NIRSpec and NIRCam test team studying the Hubble Ultra Deep Field in the GOODS-S. Again utilising 3 of the 4 main science instruments onboard JWST, the EC-MIRI team propose a single co-ordinated parallel observation with a prime MIRI pointing for 60 hours in the most sensitive MIRI broad-band filter, F560W. This will therefore only cover the area of a single MIRI FOV, approximately $\simeq 2.3$ arcmin^2. During this total exposure time of 60 hours with MIRI prime observations, the EC-MIRI team will also acquire 40 hours

of co-ordinated parallel observations with NIRCam and 20 hours of spectroscopic observations using NIRISS.

MIRI's sensitivity capabilities just beyond 5.0μm will play a significant role in studying the epoch of reionisation. Specifically, these observations will enable reasonable estimations of the total stellar masses of objects not only at $z > 4$ and will also provide a significant detection of the Balmer break allowing for detailed calculations of the stellar masses and ages of objects beyond $z > 8.5$. This, in turn, will allow estimations of star formation rates and thus the contribution of ionising photons in the EoR. In addition, this deep MIRI imaging will be conducted in a region where there already exists deep observations with both ALMA and MUSE. The estimated detection limit of $m_{AB} \simeq 28.3$ (4σ) in the F560W filter should reveal a limited number of the brightest sources at $z > 9$.

While the EC-MIRI team will only observe in the F560W MIRI filter, the co-ordinated parallel imaging with NIRCam will cycle through three filters. Observing in both the LW channel and SW channel simultaneously, the EC-MIRI team will observe in F115W+F2777W and F115W+F356W. In both cases, they will use the DEEP8 readout mode with a total of 32 integrations, including the 4-point dither pattern required to fully sample the PSF in the MIRI F560W band and all the NIRCam filters. This results in a total of 40 hours exposure time in the F115W filter and 20 hours in the final 2 NIRCam filters (F277W and F356W) covering 1 NIRCam dual-module FOV, equivalent to approximately 2 x 2.2 x 2.2 arcmin^2 (9.5 arcmin^2). This will provide supplementary observations for the NIRCam survey (JADES), detailed in Section 3.3.2, particularly in optimising the detection of $z > 10$ galaxies using the Lyman break technique with deeper F115W observations. The co-ordinated final 20 hours of parallel observations will be conducted with NIRISS, providing deep wide-field slitless low-resolution spectroscopy of all high-z sources in a field of 2.2 $\times$ 2.2 arcmin^2 around the HUDF. This again will provide supplementary observations for the JADES NIRSpec survey (WIDE MOS), by providing deeper spectroscopy of non-pre-selected targets in the HUDF.

As discussed in Section 3.3.2, the JADES programme will produce very deep NIRCam imaging to a depth of $m_{AB} \simeq 29.8$ mag across all NIRCam broad-band filters. As MIRI sits so close to the end of the wavelength range of NIRCam, it does seem somewhat wasteful to observe in one single MIRI FOV in the first MIRI filter (F560W). Indeed, when observing high-redshift galaxies and SED-fitting the photometric data, there is a balance between extending the wavelength coverage

and the sensitivity to which the photometric data is obtained. We discuss the pro and cons of such a programme in Chapter 4 and show that F770W is far more desirable when assessing the photometric and stellar mass estimations made when SED-fitting NIRCam +MIRI photometry, as it provides a more extended wavelength base in detecting the shape of the SED in the mid-IR wavelength range. Moreover, as a result of the lack of area coverage, only a small number of high-redshift objects will in-fact be detected due to the rarity of such sources. The selection of the MIRI filter F560W does make sense in isolation, as the F560W filter offers the best sensitivity and resolution for MIRI imaging; however, NIRCam has significant superior sensitivity capabilities that will produce far deeper imaging than any observations made by MIRI.

MIRI in the Hubble Ultra-Deep Field

Like the MIRI HUDF Deep Imaging Survey, the MIRI in the HUDF programme is a MIRI GTO team program, but in this case designed by the American counterpart of the MIRI GTO team (US-MIRI), led by George Rieke, based at the University of Arizona. US-MIRI designed a multi-band imaging survey with MIRI covering approximately $\simeq$ 30 arcmin^2 in the HUDF. The US-MIRI team will also observe selected galaxies with NIRSpec at a resolution of R $\sim$ 1000 across the wavelength range of 1.2-5.2μm. This results in a total programme time of 85 hours.

In theory, this programme is split into two parts, the first being the multi-band imaging with MIRI across all eight photometric broad-band filters: F560W, F770W, F1000W, F1280W, F1500W, F1800W, F2100W and F2550W. This will be obtained using a set of pointings creating a 3x5 mosaic (total $\simeq$ 30 arcmin^2) in the HUDF/GOODS-S field. Each filter has a specific set of observing criteria (i.e. number of groups/integrations and dither patterns). This is mostly due to the different sensitivity capabilities in each filter, and how the mid-IR background impacts on each band. The majority of the filters require a minimum of a 4-point dither pattern to ensure the PSF is fully sampled in every filter. Each filter also requires a number of groups per integration and number of total integrations per exposure. This changes depending on which wavelength range is being probed since, at longer wavelengths, a larger number of groups per integration will cause a saturation of the image. Therefore, for F2100W and F2550W a larger number of integrations per exposure is required to balance the reduction in the number of

groups. The mosaic is placed in an optimal position to overlap with the NIRCam GTO NIRCam survey (JADES), maximising the total area coverage with both multi-band NIRCam and multi-band MIRI photometry. These two datasets can be combined, to enable the selection of targets for NIRSpec MOS follow-up, which constitutes the second part of the programme. In total, three pointings will be made with NIRSpec to obtain the spectra of the pre-selected targets.

Selections will be made based on colour selection and detections of AGN. Currently the US-MIRI team are working on techniques that will allow for careful selection of AGN using the MIRI photometry. Relative flux densities between certain MIRI bands is a potential method to highlight AGN and separate them from star-forming galaxies. It is thought that MIRI photometry will be able to help select an appropriate spectral template by comparing the behaviour of the SED at 6−13 μm (aromatic bands) and the emission/scattering from dust grains at MIRI wavelengths beyond $\lambda > 13\mu$m. It is expected that a survey of this scale and depth will be able to detect around 30−40 AGN while also detecting $\simeq$ 2000 star-forming galaxies with relatively high SNR (10σ).

3.4 Summary

I have presented a brief overview of the logistics and timeline for the launch, orbit and science for *JWST*. In doing so, I detailed the key steps and techniques required to build a *JWST* proposal, in particular, the basics of the ETC and APT. These pieces of software were extensively used to build the Public Release Imaging for Extragalactic Research (PRIMER), a large (52hr), deep, fully-sampled NIRCam and MIRI imaging programme proposed for the ERS. We designed PRIMER to efficiently ($\approx$ 75% efficiency) observe the faintest galaxies in the best-studied available (non-GTO Covered) equatorial *HST* CANDELS field, COSMOS.

After detailing the science goals and observational design of PRIMER, I placed the programme into context by providing a new description of the currently accepted ERS and GTO *JWST* programmes that study galaxies at high-redshift. While these programmes impressively showcase the capabilities of *JWST*, they fail to produce a comprehensive wide-area dataset of deep, full-sampled contiguous NIRCam and MIRI imaging. Therefore, in the next chapter, I present a new analysis of the potential power of a NIRCam+MIRI imaging survey with *JWST* to improve our knowledge of galaxy evolution.

4

Maximizing the power of deep extragalactic imaging surveys with the James Webb Space Telescope

In this Chapter, we analyse the effectiveness of a NIRCam and MIRI imaging programme under realistic observing circumstances. We build a suite of more than > 20,000 BC03 models and simulate NIRCam and MIRI observations before analysing the robustness of photometric redshift and stellar mass estimations across a wide redshift range ($3 < z < 9$). We focus on quantifying the significance of MIRI's contribution in a number of different observing scenarios with an aim to determine the type of galaxy where MIRI's contribution is most significant. We find the addition of MIRI filters reduces the catastrophic outlier rate by a factor of 2 for our highlighted galaxy sample across all SFH's. We show the importance in reclaiming redshifts with MIRI is strongly dependent on the stellar mass and dust content of the galaxy. Using the Empirical Galaxy Generator (EGG) simulations, we determine the prevalence of the highlighted objects across an even wider redshift range ($0.05 < z < 12$). We observe the EGG galaxy sample under a realistic *JWST* observing strategy providing a mock galaxy catalog expected

from a Cycle I imaging survey with and without the addition of *HST* ancillary data. We predict the effectiveness of these different filter combinations and weigh up the value of added MIRI F770W or *HST* B_{435} data. We show that although only a small number of high mass dusty galaxies exist, a population of weakly dust-obscured galaxies can be helped with the addition MIRI F770W. We show that, in general, the improvement in current *HST* B_{435} ancillary data is far more transformative for reclaiming the physical properties of high-redshift galaxies than MIRI will be.

4.1 Introduction

In recent years, deep, multi-band imaging surveys have played a key role in advancing our understanding of galaxy evolution. Deep optical surveys have been conducted with wide-format CCD cameras on ground-based telescopes such as Subaru (e.g. Taniguchi et al. 2007, Furusawa et al. 2008, Furusawa et al. 2016), and with the Advanced Camera for Surveys (ACS) on the *Hubble Space Telescope HST* (e.g. Giavalisco et al. 2004; Beckwith et al. 2006; Scoville et al. 2007). Over the past decade these studies have been extended into the near infrared with ground-based imagers such as WFCAM on UKIRT (Lawrence et al. 2007; Hartley et al. 2013), VIRCAM on VISTA (McCracken et al. 2012; Jarvis et al. 2013) and HAWK-I on ESO's Very Large Telescope (VLT) (Fontana et al. 2014; Brammer et al. 2016), and with Wide Field Camera 3 (WFC3) on *HST* (e.g. Grogin et al. 2011; Ellis et al. 2013; Illingworth et al. 2013; Lotz et al. 2017). This extension in wavelength coverage to $\lambda \simeq 2\,\mu$m (or $\lambda \simeq 1.6\,\mu$m in the case of *HST*) has been crucial in pushing back our knowledge of galaxy luminosity functions (e.g. McLure et al. 2010, 2013b; Bouwens et al. 2011, 2015, 2017; Bowler et al. 2014, 2015; Finkelstein 2016; McLeod et al. 2015, 2016; Ishigaki et al. 2018; Oesch et al. 2018) and stellar mass functions (e.g. Fontana et al. 2006; Muzzin et al. 2013; Tomczak et al. 2014; Davidzon et al. 2017) to earlier times, facilitating the study of red dust-obscured objects and passive galaxies at redshifts $z > 1$ (e.g. Dunlop et al. 2007, 2017; Fontana et al. 2009; Bourne et al. 2017; Glazebrook et al. 2017; Koprowski et al. 2018; Merlin et al. 2018), and improving the quality of photometric redshift information at all redshifts (e.g. Cirasuolo et al. 2010; Ilbert et al. 2013; Dahlen et al. 2013; Simpson et al. 2014; Santini et al. 2015; Parsa et al. 2016; Laigle et al. 2016; McLure et al. 2018b). Extension to longer near/mid-infrared wavelengths has proven more difficult, as it is essentially impossible to

achieve imaging of sufficient depth from the ground at $\lambda > 2.3\,\mu$m for the study of distant galaxies. As a result the provision of useful data at $\lambda \simeq 3 - 30\,\mu$m has had to rely on the much smaller *Spitzer Space Telescope*. The data produced by deep surveys with the IRAC and MIPS instruments on-board *Spitzer* have been undeniably impressive (e.g. Sanders et al. 2007; Damen et al. 2011; Ashby et al. 2013, 2015, 2018; Labbé et al. 2013, 2015), and have certainly demonstrated the power of such longer-wavelength imaging for rest-frame optical/near-infrared studies to the very earliest times (e.g. Dunlop 2013; Stark 2016), but nonetheless they are ultimately limited in angular resolution (> 1.5 arcsec) and depth (to $m_{AB} \simeq 25$ mag) by the small (85-cm) aperture of *Spitzer*.

Both the resolution and depth of near/mid-infrared imaging will be revolutionized by the *James Webb Space Telescope* (*JWST*; Gardner et al. 2006). There are four main instruments on-board *JWST*: NIRSpec (Near Infrared Spectrograph, Posselt et al. 2004), MIRI (Mid-Infrared Instrument, Rieke et al. 2015), NIRCam (Near-Infrared Camera, Horner & Rieke 2004), and FGS/NIRISS (Fine Guidance System/Near-InfraRed Imager and Slitless Spectrograph, Doyon et al. 2012). While the spectroscopic capabilities of *JWST* clearly promise enormous advances in our understanding of the physical properties of galaxies (especially at high redshifts), the focus of the work presented here is on planned deep imaging surveys, primarily with NIRCam, but also potentially involving MIRI.

Modest programmes of NIRCam and MIRI imaging have already been approved as part of the *JWST* Early Release Science (ERS) programme (e.g the Cosmic Evolution Early Realease Science (CEERS) survey; Finkelstein et al. 2017) with more ambitious imaging also planned as part of the guaranteed time programmes in Cycle-1 (e.g. as part of the *JWST* Advanced Deep Extragalactic Survey (JADES) program[12]). CEERS plans to provide 100 arcmin^2 of *JWST* imaging and spectroscopy across the majority of the Extended Growth Strip *HST* legacy field with approximately 37 hours of science integration time at a total cost of $\simeq$ 63 hours. CEERS utilises 10 NIRCam prime imaging pointings with 6 parallel NIRSpec spectroscopy observations and 4 MIRI imaging parallels.This results in an estimated depth capability of $m_{AB} \simeq 28{-}29$ mag for NIRCam and $m_{AB} \simeq 25{-}26$ mag in MIRI F770W. Therefore, CEERS NIRCam imaging should enable the detection of $\simeq 50$ galaxies between $z \simeq 9 - 13$. However, the shortest wavelength filter used in CEERS is the NIRCam F115W band which places the Lyman break

[1] `https://www.cosmos.esa.int/web/jwst-nirspec-gto`

[2] `https://issues.cosmos.esa.int/jwst-nirspecwiki/display/PUBLIC/Overview`

at around $z \simeq 9$. Therefore, by design, CEERS will heavily rely on sufficient *HST* data to maximise the scientific output of the resulting NIRCam dataset.

JADES is a *JWST* Cycle-1 programme designed by the NIRSpec and NIRCam GTO team, aiming to observe in both the CANDELS GOODS-N and GOODS-S fields with a two-tier exposure strategy consisting of a 'Deep' and 'Medium' imaging survey. The 'Deep' survey, centred on GOODS-S/HUDF, will reach depths of $m_{AB} \simeq 29.8$ mag across 46 arcmin^2 with no MIRI imaging parallels. The shallower 'Medium' survey will cover a wider area of $\simeq 190\,\mathrm{arcmin}^2$ to a limiting magnitude of $m_{AB} \simeq 28.8$. Here, there will be a total of $\simeq 14$ arcmin^2 of parallel MIRI imaging in the F770W filter, with approximately 8 arcmin^2 reaching a limiting magnitude of $m_{AB} \simeq 26.7$ mag. Like CEEERS, the dataset produced will require sufficient *HST* optical data to robustly select Lyman break galaxies at $z < 7$. However, as outlined in Finkelstein et al. (2015), the community has ambitions to go beyond these programmes and to engage in more ambitious NIRCam+MIRI surveys increasing the contiguous area coverage and depth across all the CANDELS fields (COSMOS and UDS) in the early years of *JWST* operations. This will enable the community to discover and study hitherto undetected populations of galaxies (at extreme redshifts, low masses and/or extreme dust obscurations), to better constrain the redshifts, stellar masses, and rest-frame optical morphologies of known high-redshift galaxies, and also to select future targets for *JWST*. spectroscopic follow-up within the lifetime of the mission. One attractive feature of larger area ($> 100\,\mathrm{arcmin}^2$) NIRCam mapping is that parallel-mode *JWST* observing can be used to drag MIRI (which lies $\simeq 6\,\mathrm{arcmin}$ distant from NIRCam in the telescope focal plane) over regions already mapped with NIRCam, to produce homogeneous imaging of consistent depth across the full wavelength range $0.8 < \lambda < 20\,\mu\mathrm{m}$, exploiting to the full *JWST's* near-to-mid infrared imaging capabilities.

Such *JWST* imaging surveys promise huge advances in our understanding of cosmic history, but, given the substantial investment in observing time required for large area mapping with *JWST*, and the range of possible observing strategies, their detailed design demands to be based on careful analysis. Notwithstanding the obvious fact that deep *JWST* imaging will open up new discovery space, enough is now known about the expected performance of the telescope and instrumentation, and the properties of the known galaxy population, to merit a proper quantitative evaluation of the trade-offs between different choices of NIRCam filter combinations, and survey depth versus area. There are two key

related aspects to consider, which are the primary focus of this chapter, namely i) the added value of MIRI parallel observations (which while nominally 'for free' can set significant constraints on survey layout, scheduling etc) and, ii) the depth/quality of *optical* data in the chosen survey fields required to maximise the power of the investment planned with *JWST*.

The approach taken here, considering fully realistic photometry, and deriving full posterior probability distributions for derived galaxy physical parameters under different observational strategies differs somewhat from that of other published studies aimed at providing extragalactic predictions for *JWST*. In recent years, a number of such '*JWST* prediction' papers have appeared, typically analysing mock *JWST* catalogues built using semi-analytic models, or numerical cosmological hydrodynamical simulations of galaxy formation and evolution (e.g. FiBY Paardekooper et al. 2013, BlueTides Feng et al. 2016; Wilkins et al. 2017, GALFORM Lacey et al. 2016, Barrow et al. 2017, Lovell et al. 2018, Yung et al. 2019).

As a recent example, Cowley et al. (2018) built a mock galaxy catalogue based on the GALFORM semi-analytic model, and used this to predict galaxy number counts, redshift distributions and luminosity functions in all broadband filters available for NIRCam and MIRI. They predict that assuming a 10^4s exposure, very few galaxies will be detectable per field-of-view beyond $z > 10$ and $z > 6$ with NIRCam and MIRI, respectively. They also estimate the size of the galaxies in each photometric band in order to understand the resolving capabilities of NIRCam and MIRI at high redshift. Williams et al. (2018) made similar predictions for NIRCam only, assuming the observational prescriptions of the *JWST* Advanced Deep Extragalactic Survey (JADES) GTO program. They show that they expect to detect thousands of galaxies at $z > 6$ with tens at $z > 10$ across the entirety of the JADES NIRCam imaging (236 arcmin^2) as well as constraining the evolution of the galaxy UV luminosity function at $z > 8$. However, the goal of these studies was not to investigate the accuracy and reliability with which the *JWST* data would enable simple galaxy properties, such as redshift and stellar mass to be robustly reclaimed. This means that the predicted results are inevitably somewhat unrealistic, and also precludes quantitative comparison of the power of alternative observing strategies, and the importance of supporting data outside the wavelength range of NIRCam.

One study which tested how reliably galaxy properties can be reclaimed under different filter combinations of *JWST* photometry is that of Bisigello et al.

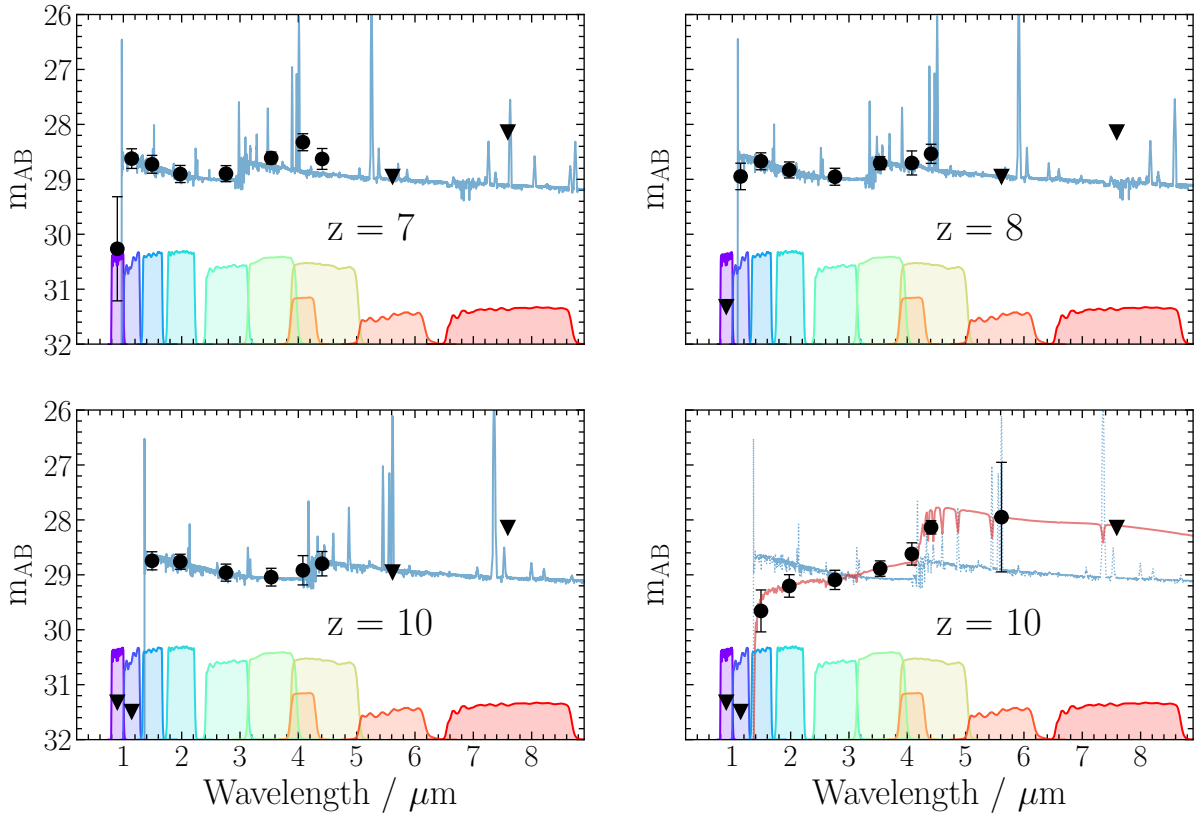

Figure 4.1 *The power of multi-band NIRCam + MIRI imaging for the discovery and study of high-redshift galaxies. The blue SED shown at* $z = 7, 8, 10$ *is that of a FiBY (Paardekooper et al. 2013; Cullen et al. 2017) simulated star-forming galaxy with* $Z/Z_{\odot} \simeq 1/3$*, normalised to* $m_{3\mu m} = 29$ *mag, with the data-points showing the simulated photometry (and associated uncertainty) assuming 1-hr exposures per NIRCam filter. As well as clear delineation of the Lyman-break, the impact of the strong rest-frame optical emission lines (produced by sub-solar metallicity galaxies) on the photometry is clear; F444W−F410M colour is invaluable for redshift refinement, and provides estimates of emission-line equivalent widths, and resulting corrections to stellar mass. The 4th panel shows an alternative (red) SED at* $z \simeq 10$*, produced by a starburst at* $z \simeq 15$ *(*$\simeq 200$ *Myr old), demonstrating that NIRCam + MIRI imaging can also provide key information on earlier star-formation activity.*

(2016, 2017). First focussing on photometric redshifts, Bisigello et al. (2016) created a mock galaxy catalogue, added appropriate observational noise, and then used spectral energy distribution (SED) fitting in order to estimate the physical properties of each 'observed' galaxy. They concluded that, in isolation, NIRCam data struggle to deliver acceptable photometric redshifts in certain redshift ranges, and they attempted to explore which filter combinations offered the best prospect of overcoming (or at least ameliorating) this problem. Their main conclusion is that, while deep optical data at $\lambda < 0.6\,\mu$m from *HST* is desirable, the lack of such short-wavelength information can be mitigated somewhat by the use of MIRI photometric observations in the F560W and F770W filters. In particular, they reported that the addition of such MIRI imaging to a NIRCam survey can reduce the photometric redshift Catastrophic Outlier Rate (COR, defined as $|\Delta z| > 0.15$, where $|\Delta z| = |(z_{phot} - z_{input})/(1 + z_{input})|$, by a significant fraction both with and without the addition of *HST* data. However, in coming to this conclusion, the authors assumed that a MIRI detection at 28 AB mag would have a comparable S/N as a NIRCam detection at 29 AB mag in the F150W filter. This is an optimistic (and, in practice, unrealistic) assumption for an imaging survey, since it requires MIRI integrations $\simeq 50$ times longer than the NIRCam integrations in this scenario. Therefore, this is not appropriate to the anticipated real-world case described above for MIRI imaging being obtained in parallel to NIRCam imaging, and would require a NIRCam+MIRI survey design that committed > 95% of the available integration time to MIRI imaging. In a second paper, Bisigello et al. (2017) then focussed on exploring the optimum combination of NIRCam and MIRI filters for reclaiming the physical properties of a sample of 1542 simulated galaxies in the high redshift range, $z = 7 - 10$. Again they reported that the addition of MIRI data was very valuable, especially for improving stellar mass and specific star-formation rate (sSFR) estimation at $z \simeq 10$. However, again these calculations are not really realistic for a *JWST* imaging survey, as a signal:noise ratio of $S/N = 10$ is assumed for a galaxy with $m_{AB} \simeq 28$ mag in the F560W filter which, even with a low background level, requires $\simeq 200$ hr of integration per MIRI pointing.

The aim of the study presented here was therefore to: i) consider a set of fully schedulable and realistic observing scenarios, ii) explore a wide range of assumed input galaxy types (> 20,000 alternative model galaxies), iii) perform detailed signal:noise calculations to perturb the resulting predicted photometry, and iv) use state-of-the-art Bayesian methods to assess the precision and accuracy with which basic galaxy physical parameters can be reclaimed. Armed with

such machinery we are able to accurately assess the power of alternative observing strategies (both for the galaxy population in general, and for special galaxy subclasses of potential interest) and, specifically, the importance of complementing NIRCam imaging with MIRI observations and/or additional *HST* optical imaging than already exists in the likely target *JWST* survey fields.

The structure of this chapter is as follows. In Section 4.2 we summarize the key properties of the NIRCam and MIRI imagers, and explain the rationale behind our adopted NIRCam filter combination and observing strategy for the discovery and study of high-redshift galaxies. Next, in Section 4.3, we describe the methods used to produce simulated galaxies. Here we aimed both to sample a wide range of possible galaxy properties (using the models of Bruzual & Charlot (2003), with star-formation histories informed by the First Billion Years (FiBY) simulations; Paardekooper et al. 2013; Cullen et al. 2017), and to consider realistic models of the evolving galaxy population (based on current data, using The Empirical Galaxy Generator (EGG; Schreiber et al. 2017). Then, in Section 4.4, we describe the process by which we synthesized the predicted *JWST* photometry for the simulated galaxies, considering realistic NIRCam+MIRI observing strategies. In Section 4.5, we explain how we utilised the Bayesian SED-fitting code Bagpipes (Carnall et al., 2018b) to reclaim the physical parameters of the simulated galaxies from the *JWST* photometry, and explore the accuracy with which this can be achieved both with and without the addition of MIRI and deeper *HST* photometry to the core NIRCam dataset. Finally, in Section 4.6, we give a summary of our main conclusions. Throughout the chapter magnitudes are quoted in the AB system (Oke 1974; Oke & Gunn 1983) and we assume a flat cosmology with $\Omega_M = 0.3$, $\Omega_\Lambda = 0.7$, and $H_0 = 70\,\mathrm{km\,s^{-1}\,Mpc^{-1}}$.

4.2 Imaging high-redshift galaxies with *JWST*

4.2.1 The *JWST* imagers

Full details of the *JWST* instrumentation are publicly available online[3],[4],[5]. The key features of NIRCam and MIRI can be summarized as follows.

[3] https://jwst.stsci.edu/instrumentation
[4] https://www.nasa.gov/mission_pages/webb/instruments/index.html
[5] https://jwst-docs.stsci.edu/display/JTI

The Near-Infrared Camera (NIRCam, Horner & Rieke 2004) is the primary imager onboard *JWST* with a wavelength range of $0.6 < \lambda < 5\mu$m. There are two identical modules, A and B, where the field of view (FOV) is split into a short-wavelength channel and a long-wavelength channel with co-aligned FOV's (2.2 × 2.2 arcmin). The short-wavelength channel has twelve filters in total; five wide-band (R ∼ 4) filters, four medium-band (R ∼ 10) filters, and three narrow-band (R ∼ 100) filters. The long-wavelength channel consists of three wide-band, eight medium-band, and four narrow-band filters. In total, there are therefore 8 available broad-band filters: F070W, F090W, F115W, F150W, F200W, F277W, F356W and F444W. With such filters, the key spectral feature of extreme redshift galaxies, the Lyman break at $\lambda_{rest} = 1216$Å, can in principle be detected over the redshift range $4.2 < z < 40$, while the 4000Å/Balmer break feature is identifiable over the redshift range $0.6 < z < 11.3$.

The Mid Infrared Imager (MIRI, Bouchet et al. 2015) is a combination of multiple instruments providing observing capabilities over a vast range of MIR wavelengths ($\lambda = 5 - 27\,\mu$m). In broad-band imaging mode, nine photometric broad bands are available, with resolution capabilities of R ∼ 5 (F560W, F770W, F1000W, F1130W, F1280W, F1500W, F1800W, F2100W, F2550W). Along with broad-band imaging, this module contains instruments that perform coronography and low-resolution spectroscopy (LRS, Kendrew et al. 2015). MIRI's sensitivity, combined with its long wavelength baseline, will provide unrivalled mid-infrared data. The wavelength range accessible with MIRI becomes very important for high-redshift galaxies (especially at $z > 6$), where the rest-frame optical continuum and several of the key nebular emission lines become redshifted longward of $\lambda \simeq 5\,\mu$m. MIRI's first two bands are by far the most sensitive, with the F560W band sitting very close to the end of the NIRCam wavelength range.

4.2.2 *JWST* imaging strategy for high-redshift galaxy surveys

Although WFC3/IR enabled *HST* to probe beyond $z \simeq 7$ into the first ≃ Gyr of cosmic time, the isolation of secure samples of $z > 7$ galaxies has been severely hampered by the curtailment of *HST* wavelength coverage at $\lambda_{\rm obs} < 1.7\,\mu$m. Robust redshift information benefits greatly not only from identification of the Lyman-break at $\lambda_{\rm rest} = 1216$ Å, but also from extended/high-quality wavelength

coverage redward of the break to exclude lower-redshift red/dusty interlopers. Here, *JWST* will be transformative; as we show in Fig. 4.1, an 8-filter NIRCam approach can not only securely identify Lyman-break galaxies out to the highest redshifts, but can also provide powerful SED information (e.g. revealing the presence of rest-frame optical emission-lines or a Balmer break).

As can be seen from Fig. 4.1, 7 NIRCam broad-band filters (F090W, F115W, F150W, F200W, F277W, F356W, F444W) provide complete (and independent) coverage of the observed spectral range $\lambda = 0.8 - 5\,\mu$m. We have decided to adopt this as our baseline NIRCam filter set for the simulations presented here, with inclusion of the F090W filter (excluded in the CEERS ERS program) vital for delivering samples of galaxies at $z = 7 - 8$. We do not include imaging in the F070W filter, because i) this is the least sensitive short-wavelength channel broad-band filter for NIRCam imaging, ii) this wavelength range is least unique to *JWST*, and iii) the image quality in this filter is not expected to be significantly better than achieved with *HST* at comparable wavelengths.

We also assume equal exposure times in all 7 of these broad bands. There are two reasons for this. First, since imaging is performed simultaneously in a short-wavelength channel filter and a long-wavelength channel filter, it is not straightforward/practical to fine-tune the relative exposure times (e.g. increasing systematically with wavelength). Second, the imaging sensitivity expected in each of these filters (in terms of AB mag or μJy) is comparable (to within 0.5 mag, with the exception of F444W[6]), and thus already well matched to the consistent detection of high-redshift star-forming galaxies, which are known to have a fairly 'flat' (i.e. $\beta = -2$, where $f_\lambda \propto \lambda^\beta$) rest-frame UV continuum above the Lyman-break, as shown in Fig. 4.1.

Having decided on a combination of 4 broad-band filters in the short-wavelength NIRCam channel, and all 3 available broad-band filters in the long-wavelength channel, it only remains to decide on the choice of a fourth long-wavelength channel filter. The obvious options are additional integration in one of the broad-band filters already included (i.e. F277W, F356W, F444W) or inclusion of imaging in a different long-wavelength channel filter. In practice, this becomes a choice between more integration in F444W (given it is the least sensitive of the broad bands in the long-wavelength channel) or inclusion of a long-wavelength channel medium-band filter in a comparable wavelength regime. For constraining

[6] `https://jwst-docs.stsci.edu/display/JTI/NIRCam+Imaging`

continuum SEDs, experiments indicate that this choice is unimportant as the relative sensitivity capabilities and effective wavelengths are somewhat similar for the F444W and F410M NIRCam filters [7]. However, here we choose to utilise the medium-band F410M filter (as again shown in Fig. 4.1) because of its potential to help distinguish between a spectral break at the red end of the NIRCam imaging, or the presence of strong emission lines within the broad band (similar baseline filter set in the JADES program). In this regard, the combination of F444W and the medium-band F410M filter can be particularly powerful. It is now well-established that [OIII] lines of extreme equivalent widths (EW_0) become more prevalent with increasing redshift and/or decreasing metallicity (Nakajima et al. 2016), and, for brighter objects, have already proved detectable in broad-band *Spitzer* IRAC photometry (Smit et al. 2015). Not only can such emission-line signatures provide invaluable additional redshift information, but they also offer one of the few ways of estimating the escape fraction of ionizing photons from young galaxies in the reionization epoch (Stark 2016).

Given this NIRCam imaging strategy, one of the key issues we aim to explore in this work is the added value of MIRI imaging for high-redshift galaxy studies. In principle this would appear to be extremely valuable. The wavelength coverage of NIRCam and MIRI compliment each other nicely, and while surveys with NIRCam alone will effectively encompass the 4000Å/Balmer break displayed by galaxies across the broad redshift range $1 < z < 10$, at $z > 4$, the wavelength range sampled by MIRI better samples the light from the evolved stellar populations which dominate the stellar masses of galaxies. Moreover, the enhanced wavelength baseline offered by the addition of MIRI imaging can be of value for distinguishing between quiescent and dusty star-forming galaxies, and hence establishing reliable galaxy masses for red sources and completing our census of the stellar-mass density at early times.

The appeal of adding MIRI imaging is, at first sight, further enhanced by the fact that it can be obtained in parallel with NIRCam imaging. MIRI lies $\simeq 6$ arcmin from NIRCam in the *JWST* focal plane, and thus images a different part of the

[7] Although the F444W band is slightly more sensitive than F410M band for most observations, the background is steeply rising between 4 and 5 μm (this is the Wien tail of the thermal zodiacal dust spectrum). The F444W filter goes out to almost 5 μm, so it takes the brunt of this rise. This significantly counteracts the sensitivity gains that would otherwise be obtained from the wider bandpass. Because F444W is more sensitive to the background than F410M, any observation with long exposure time becomes background-dominated in F444W, and thus the flat-field residual noise on the background becomes significant for background-dominated calculations.

sky. However, for moderately wide-area surveys (e.g. of GOODS/CANDELS fields $> 100\,\mathrm{arcmin}^2$) the observations can be designed to drag the MIRI parallel imaging over the majority of the area imaged with NIRCam, and thus the MIRI imaging can be obtained 'for free'. However, such a strategy means that the MIRI integration times are, necessarily, limited to be comparable to the NIRCam integration times. One could of course choose to keep observing in a single MIRI filter while the observations at a given location cycle through all of the NIRCam filters described above, but that still sets a maximum MIRI integration time of $\simeq 4\times$ the NIRCam integration time per filter. This is then potentially problematic when trying to close the gap between the detection limits of NIRCam and MIRI. Even the two most sensitive MIRI filters at wavelengths immediately longward of those probed by NIRCam, F560W and F770W, are $\simeq 10\times$ less sensitive than NIRCam F444W imaging. The sensitivity rapidly degrades further with increasing wavelength in the MIRI channels, largely due to the increased background noise from the *JWST* insturments themselves[8]. This means that realistic calculations need to be performed to assess the true added value of MIRI photometry to deep multi-band NIRCam imaging, including a full simulation of the accuracy with which the physical parameters of galaxies over a range of masses, redshifts and spectral types can be reclaimed with and without the addition of MIRI parallel imaging.

In the simulations presented here we assume that all the available parallel imaging integration time is devoted to 7.7-μm MIRI imaging (i.e. F770W) because i) the sensitivites offered by F560W and F770W imaging are comparable, and ii) 7.7-μm imaging most significantly extends the wavelength baseline covered by NIRCam. We stress that important extragalactic science can undoubtedly be undertaken using the longer-wavelength MIRI filters, but the aim here is to test the extent to which MIRI imaging in the most sensitive MIRI channels, taken in parallel with deep NIRCam imaging, can really contribute to our knowledge of the tens of thousands of previously undiscovered galaxies which will be revealed by deep NIRCam imaging surveys.

Finally, while Fig. 4.1 shows that at redshifts $z > 7$ essentially all of the transmitted galaxy SED lies longward of $\lambda \simeq 1\,\mu$m, and is thus fully sampled by *JWST*, it remains the case that the vast majority of the new galaxies which will be discovered in deep *JWST* surveys will lie at more modest redshifts. This means that shorter-wavelength (optical) observations can still be of value in constraining

[8] `https://jwst-docs.stsci.edu/display/JTI/MIRI+Sensitivity`

Table 4.1 *Physical parameter values used to build the suite of model galaxies based on the BC03 templates for our simulated galaxies at $z = 3 - 9$. These values were used for all of the SFH prescriptions detailed in Table 4.2.*

Property	**Parameter**	**Value(s)**
Stellar mass	$log_{10}(M_*/\mathrm{M}_\odot)$	8, 9, 10
Metallicity	Z / $\mathrm{Z}_\odot$	0.2, 1
Redshift	z	3, 3.5, 4 ... 8, 8.5, 9
Dust obscuration	A_V / mag	0, 0.2, 0.4, 0.8 ... 6.4
Ionisation parameter	$\log_{10} U$	-3
Age of the Birth Cloud	T_{bc} / Gyr	0.01

the galaxy SEDs, and raises the question of whether the exisiting optical (e.g. *HST* ACS) imaging in likely target *JWST* survey fields is adequate to enable full exploitation of deep *JWST* imaging data. This is the second key strategic issue that we explore here through our galaxy simulation work.

4.3 Simulated Galaxies

In this section, we describe the two suites of galaxy models we constructed to explore the potential power of *JWST* imaging surveys. First we constructed an extensive (deliberately not necessarily representative) range of galaxy SEDs utilising the models of Bruzual & Charlot (2003) (BC03). As described in detail below (subsection 4.3.1), we explored the impact of a wide range of physical properties, in part to enable a search for those types of (possibly extreme) galaxies for which MIRI data could have the most significant effect on reclaimed galaxy parameter estimates. Second, as described in subsection 4.3.2, we constructed a more representative (at least given current knowledge) distribution of galaxy SEDs using the Empirical Galaxy Generator (EGG) simulations (Schreiber et al. 2017), in an attempt to quantify the actual number/redshift-distribution of galaxies which will be uncovered by deep NIRCam surveys, and assess the relative prevalence of the likely subsets of galaxies for which additional MIRI or *HST* photometry is predicted to be of most value.

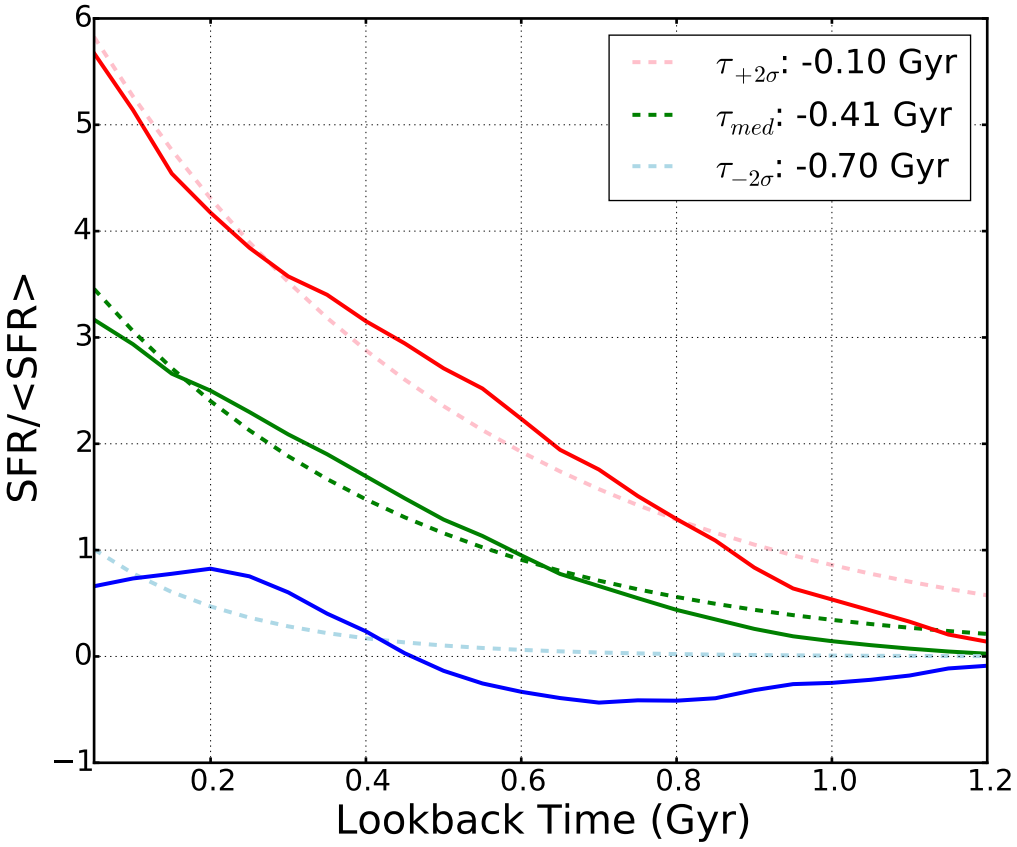

Figure 4.2 *Polynomial fits to the median* FiBY *SFHs for $z = 4$ galaxies. The solid coloured lines represent the median (green) and $\pm 2\sigma$ (blue and red) normalised SFHs across the mass range $10^8 - 10^{10}\,\mathrm{M}_\odot$. The dashed lines show the minimum-χ^2 polynomial fits to the solid lines. The resulting extracted rising star-formation τ values are displayed in the top-right corner. These are the τ values adopted to build our suite of exponentially-increasing BC03 galaxies*

4.3.1 BC03 Models

Using the population synthesis models of Bruzual & Charlot (2003), we created a set of 21,216 galaxy SEDs covering a vast range of specified physical parameters. We built this suite of galaxies using the model generation component of the spectral fitting code Bayesian Analysis of Galaxies for Physical Inference and Parameter Estimation (Bagpipes; Carnall et al. 2018b). We spread the BC03 templates across 13 evenly-spaced redshift bins (z = 3, 3.5, 4 ... 8, 8.5, 9), and, at each redshift, constructed galaxies at three stellar masses of potential interest ($M_* = 10^8, 10^9, 10^{10}\,\mathrm{M}_\odot$). At each redshift and stellar mass, we created model galaxies with both solar or 1/5 solar metallicity, explored 34 alternative star-formation histories (SFH) (16 exponentially-declining models, 12 exponentially-increasing models, 3 burst+constant star-formation models, and 3 constant+burst models), and considered a range of dust obscuration extending up to $A_V \simeq 6$, applying dust attenuation using the Calzetti reddening law (Calzetti et al. 1994; Calzetti et al. 2000). The effect of the intergalactic medium (IGM) attenuation is also included in these models, following the prescription of Inoue et al. (2014). The BC03 templates do not include nebular emission, however, Bagpipes has fully integrated the latest version of the cloudy photoionization code (Ferland et al., 2017). The logarithm of the ionisation parameter (U, defined as the ratio of ionising photons to neutral particles) combined with the input metallicity determines the level of nebular emission applied to the BC03 templates. In this work, we fix the logarithm of the ionization parameter to $\log_{10}(U) = -3$. More information on the implementation of these processes is detailed in Carnall et al. (2018b).

At all redshifts the maximum galaxy age is limited by the age of the Universe at that redshift. The burst+constant SFH models represent galaxies with an initial burst of star-formation activity at the epoch of formation, followed by a constant build-up of additional stellar mass over the remaining period of time governed by the defined age of the galaxy. In contrast, the constant+burst models are defined by an intitial extended period of constant star formation, followed by a short, sharp burst immediately before the epoch corresponding to the redshift of the observed galaxy. Each of these models is split into 3 separate mass prescriptions, with either 1/3, 1/2 or 2/3 of the total stellar mass built up in either the burst or constant component of the SFH. The exponentially-declining (τ) models are, as is standard practice, defined by a range of e-folding timescales. and ages (four of each). However, while such models may be appropriate for

Form of SFH	Parameter	Value(s)
Exponentially Decreasing		
Timescale	τ / Gyr	0.05, 0.25, 1.25, 6.25
Age of SFH	T / Gyr	0.02, 0.1, 0.4, z-lim Age
Exponentially Increasing		
Timescale	τ / Gyr	-0.1, -0.4, -0.7
Age of SFH	T / Gyr	0.02, 0.1, 0.4, z-lim Age
Burst then Constant		
Fractional mass in SF burst	M_b / M_c	1/3, 1/2, 2/3
Constant then Burst		
Fractional mass in const. SF	M_c/M_b	1/3, 1/2, 2/3

Table 4.2 *SFH parameter values used to create the suite of SEDs based on the BC03 templates and applied to galaxies with the chosen physical parameters summarized in Table 4.1.*

relatively mature galaxies in the late-time Universe, a range of observations and simulations suggest that rising star-formation histories are more plausible for growing galaxies in the young high-redshift Universe. In an attempt to ensure physically-realistic rising star-formation histories, we estimated appropriate τ values for exponentially-rising models via fits to the SFHs of typical young galaxies in the First Billion Years (FIBY) simulations (Paardekooper et al. 2013; Khochfar et al. in preparation), as shown in Fig. 4.2. The FIBY simulation suite is a set of high-resolution cosmological hydrodynamics simulations using a modified version of the GADGET code utilised in the Overwhelmingly Large Simulations (OWLS) project (Schaye et al., 2010). These simulations reproduce the stellar-mass function and star-formation rate of galaxies at $z > 6$ and at the same time also recover the trends in the metallicity evolution of galaxies. We extracted the median SFH of all galaxies within the stellar mass range, 10^8–$10^{10}\,\mathrm{M}_\odot$, and performed a simple polynomial (minimum-χ^2) fit to the median and $\pm2\sigma$ SFH for each redshift bin in the FIBY simulations. Fig. 4.2, shows these fits along with the calculated τ values for the $z = 4$ galaxies. The solid coloured lines represent the median and $\pm2\sigma$ normalised SFHs extracted from the FIBY simulations, with the dashed lines showing the polynomial fits. We found that the median (green line) and $\pm2\sigma$ (red and blue, respectively) τ values ($\tau = -0.1, -0.4, -0.7\,\mathrm{Gyr}$) encompass all calculated τ values up to redshifts $z > 9$ in the FIBY simulations. They are also consistent with the values reported by

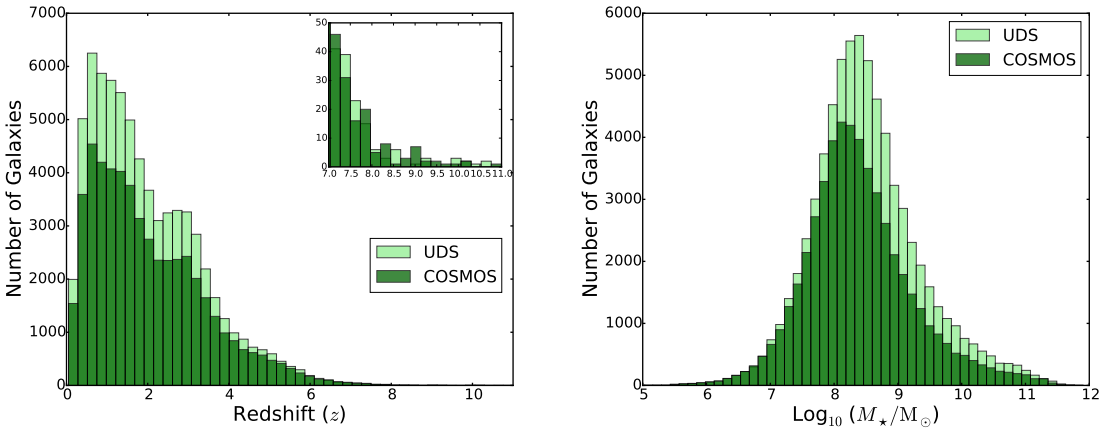

Figure 4.3 *The redshift and stellar-mass distributions of our finalised EGG mock galaxy catalogues of JWST-detected galaxies in the COSMOS-CANDELS and UDS-CANDELS survey fields, observed under a realistic observing strategy for JWST (see Section 4.4.3). The inset in the first panel provides a zoom-in of the anticipated detectable galaxy samples at $z > 7$.*

Finlator et al. (2011), who found that τ should vary over the range $50 - 350\,\mathrm{Myr}$ within the redshift range $6 < z < 12$.

The complete list of adopted values is summarized in Tables 4.1 and 4.2, where Table 4.2 summarizes the SFH parameters. Our simulated galaxy sample contains 9,984 exponentially-decreasing, 7,488 exponentially-increasing, 1,872 burst+constant and 1,872 constant+burst model SEDs distributed equally across the redshift range $3 < z < 9$ and the stellar-mass range $10^8, 10^9, 10^{10}\,\mathrm{M}_\odot$.

4.3.2 EGG

The Empirical Galaxy Generator (EGG v.1.1.0; Schreiber et al. 2017), is a tool that can generate large mock galaxy catalogues with realistic flux densities. These catalogues are built using empirical prescriptions rather than deriving galaxy properties from physical first principles or simulations, and seek to provide the most accurate match to current observational data for galaxies in the redshift range $0 < z < 7$. EGG takes the approach of assuming that the galaxy population can be simply segregated into star-forming galaxies and quiescent galaxies, and assumes that redshift, z, and stellar mass, M_*, are the fundamental properties from which all of the other observables can be statistically derived. In essence, drawing z and M_* from the observed stellar-mass functions for star-forming and

Table 4.3 *A summary of the key features of the galaxy samples predicted (by EGG) to be detected with JWST in the the COSMOS-CANDELS and UDS-CANDELS fields, assuming a JWST observing time committment of* $\simeq 100\,hr$ *to each field (see Section 4.4.3)*

Field	Area /arcmin^2	Mass Range $\log_{10}(M_\star/\mathrm{M}_\odot)$	Median Mass $\log_{10}(M_\star/\mathrm{M}_\odot)$	Redshift range	Median z	SFG-QG Ratio	No. of Galaxies
COSMOS	$\simeq$150	5.02 – 11.90	8.45	$0.050 < z < 11.69$	2.019	11.10	51,879
UDS	$\simeq$250	5.11 – 11.86	8.48	$0.050 < z < 10.92$	1.969	10.97	69,766

Table 4.4 *Calculated typical JWST 5σ point-source depths in each filter for our strawman NIRCam+MIRI survey observing strategy.*

Survey Field	F090W	F115W	F150W	F200W	F277W	F356W	F410M	F444W	F770W
COSMOS-CANDELS	28.96	29.23	29.43	29.51	29.47	29.42	28.65	28.93	25.91
UDS-CANDELS	28.58	28.84	29.05	29.09	29.08	29.01	28.20	28.44	25.96

quiescent galaxies, EGG uses the SFR–M_* 'main sequence' displayed by star-forming galaxies to assign a SFR to each galaxy drawn for the star-forming mass function, and then utilises empirical relations (established from the *HST*, *Spitzer* and *Herschel* observations of the CANDELS fields) to derive dust attenuation, optical colours and disk/bulge morphologies for the galaxies. Dust attenuation is applied using the Calzetti law (Calzetti et al. 1994; Calzetti et al. 2000) while the redshift-dependent impact of the Inter-Galactic Medium (IGM) is calculated using the prescription of Madau (1995).

After random scatter is introduced (to reflect the observed distributions of each parameter), Schreiber et al. (2017) assign each galaxy a best-fitting SED and also calculate synthetic photometry by integrating the redshifted SED through any chosen set of filters as specified by the user. Effectively, Schreiber et al. (2017) create a mock galaxy catalogue calibrated to the highest-quality existing data, with the ability to produce either SEDs or perfect (noise-free) multi-wavelength photometry.

For the current investigation we initially used EGG to create a sample of 3,908,096 galaxies across a sky area of $1.2\,\mathrm{deg}^2$, complete to a magnitude limit of 29.5 mag in the F440W NIRCam filter. The resulting synthetic galaxy population spans the redshift range $0 < z < 15$, and hence has a wide range of stellar masses ($5 < \log_{10}(M_*/\mathrm{M}_\odot) < 12$). From this large-area sample we then constructed two galaxy sub-samples satisfying the area/depth of the two $\simeq 150 - 250\,\mathrm{arcmin}^2$ regions produced by our observing strategy in the COSMOS and UDS CANDELS fields, which are the two most obvious equatorial extragalactic survey fields for a major public NIRCam+MIRI survey, beyond CEERS and JADES (see section 4.4.3 and Fig. 4.4 for a more detailed description). The shapes of these two survey fields were defined using the existing *HST* mosaics, but with realistic NIRCam+MIRI mosaicing strategies, taking into account *JWST* roll-angle and minimum background constraints.

Having defined these two survey fields, we adopted a straw-man approach to observing time, and calculated what could be achieved if we committed $\simeq 100\,\mathrm{hr}$ of *JWST* observing time to each field. The calculation of the resulting noise levels for each passband is described in detail in Section 4.4, but taking into account the achievable sensitivities, we trimmed our EGG galaxy samples by removing any non-detected objects (defined as < 4-σ detections in more than 4 filters according to our proposed 8-filter NIRCam observing strategy).

The final redshift and mass distributions for the predicted *JWST* COSMOS-CANDELS and UDS-CANDELS galaxy samples are shown in Fig. 4.3. The predicted number of detected galaxies is 69,766 and 51,879 in the UDS and COSMOS, respectively, and the sample properties are summarised in Table 4.3. The slightly different galaxy numbers and redshift/mass distributions shown in Fig. 4.3 result from the necessarily slightly different observing strategies adopted for each field (due to field geometry and allowed telescope roll angle); the proposed UDS survey is approximately 2× wider and therefore shallower than the COSMOS survey. Nevertheless, the predicted galaxy populations are broadly very similar. The anticipated galaxy redshift distribution in both fields peaks at $z \simeq 0.5$, with median $z \simeq 2$, and extends to $z > 10$, while the stellar-mass distribution is predicted to peak at $\log_{10}(\boldsymbol{M}_*/\mathrm{M}_\odot) \simeq 8.5$ and extend to $\log_{10}(\boldsymbol{M}_*/\mathrm{M}_\odot) > 11$. The UDS appears to yield far more lower-redshift galaxies than our deeper COSMOS observations, yet a similar number of high-redshift objects are detected in both fields. This is largely caused by the increased detection of higher-mass galaxies found at lower-redshift, while the COSMOS imaging is better suited to detecting the higher-redshift objects and/or lower-mass objects in our deep field.

In the next section we explain how we added noise to the photometry of the simulated galaxies, and summarize the realistically achievable depths given our adopted strawman observing strategy.

4.4 Simulating Observations

In this section we describe the processes by which we simulated the *JWST* NIRCam and MIRI data for our model galaxies, and then outline the strawman observing strategy which leads on to the typical depths anticipated in each NIRCam and MIRI filter.

4.4.1 NIRCam Simulations

The NIRCam observations were simulated using the simulation-hybrid PYTHON engine, Pandeia (Pontoppidan et al., 2016). Pandeia calculates 2-D pixel-by-pixel signal-to-noise ratios for all observing modes onboard *JWST*. The *JWST* Exposure Time Calculator (ETC) web interface is based on this same PYTHON engine. However, for large numbers of objects and simulations, the web interface

is not sufficient. Pandeia allows the user to define an astrophysical scene with an external input SED, and then to 'observe' the synthesized objects using observational parameters defined by the user. The input SEDs can be normalized at any wavelength, across all *JWST* and *HST* filters.

The astronomical scene comprises a set of sources and associated SEDs independent of the observing instrument. This scene is projected onto a realised scene, that is initially spatially sub-sampled, avoiding under-sampling of the PSF. The realized scene cube is then projected onto an appropriate detector plane, dictated by the chosen instrument and the observing mode defined by the user. The details of how this is done are described in Pontoppidan et al. (2016).

In our case, we define our observing strategy using background models, an instrument mode and a specified detector setup. The background models are chosen based on the region of the sky where *JWST* is pointing at a user-defined time of year. The detector setup governs the specified read-out mode along with the number of groups per integration, number of integrations per exposure and the total number of exposures. Combining these parameters provides a total exposure time for our observations in each selected filter. These values were selected based on the average exposure times calculated from our APT-designed observing strategy described in section 4.4.3. We note that we assume the objects are point sources.

The intermediate step of tracking the photons through the optical train to the detector is done in a similar manner to our independent MIRI simulator (described next in section 4.4.2). Once the SNR has been found in each photometric band for our chosen integration times, we assign an error and scatter the data accordingly (assuming a Gaussian distribution). The result is a best estimate of the anticipated NIRCam photometry (and uncertainty) for each of our simulated galaxies, after processing with the NIRCam data-reduction pipeline.

4.4.2 Independent MIRI Simulator

We calculated the MIRI photometry using an independent code which we had already created prior to this work based on a set of sensitivity models used in the official MIRI Team simulator, MIRISim (Glasse et al., 2015). We could of course have used the Pandeia software to perform SNR calculations in the MIRI bands, but it transpires to be far less efficient than our own simulator; for a

few objects this would not be important, however, as we wished to run more than 20,000 galaxies through our pipeline under different observing scenarios, Pandeia can become very computationally expensive. Our own MIRI simulator quickly produces very accurate synthetic observations to within a ~1% accuracy of that predicted by the official ETC for all observing modes with MIRI. We show the results of a simple test run to asses the quality and accuracy with which our own independent simulator compares to that of the ETC in the appendix (Fig. 2.15). After calculating the expected photometric errors for our chosen observing configuration, we again scattered the predicted photometry using a Gaussian distribution to provide the raw observational data expected from our MIRI imaging of the simulated (BC03 and EGG) galaxies. Full details of our MIRI simulator are published in Kemp et al. (in preparation), but for the interested reader we provide a brief summary of its key elements (and the underlying physics) in Appendix A.

4.4.3 Observing Strategies

Clearly the final observing strategy of any large-scale public extragalactic survey with *JWST* cannot be known until *JWST* is operational, and open-time programmes are selected for the early observing cycles. However, our aim here is to provide predictions which are both generic and realistic. We have therefore explored in detail possible NIRCam+MIRI imaging strategies for the UDS-CANDELS and COSMOS-CANDELS covering the survey areas outlined in Table 4.3. As a result we have produced a fully-realistic, schedulable,'strawman' observing strategy which devotes $\simeq$ 100 hr of *JWST* observing time to each of these two fields, while striving to maintain > 50% efficiency: specifically our proposed observing scenario devotes 101.9 hr of observing yielding 53.4 hr of science time in the UDS-CANDELS field, and 90.6 hr of observing time yielding 47.5 hr of science time in the COSMOS-CANDELS field. The mosaic footprint for our COSMOS CANDELS field imaging strategy is shown in Fig. 4.4. We overlay the proposed observing strategy for our MIRI (red tiles) and NIRCam (blue tiles) pointings on the current *HST* and UVISTA COSMOS coverage. The UDS observing strategy follows a different format due to more difficult V3PA constraints (perpendicular to COSMOS). Both the UDS and COSMOS strategies were built using the APT to ensure a fully realistic and schedulable set of observations.

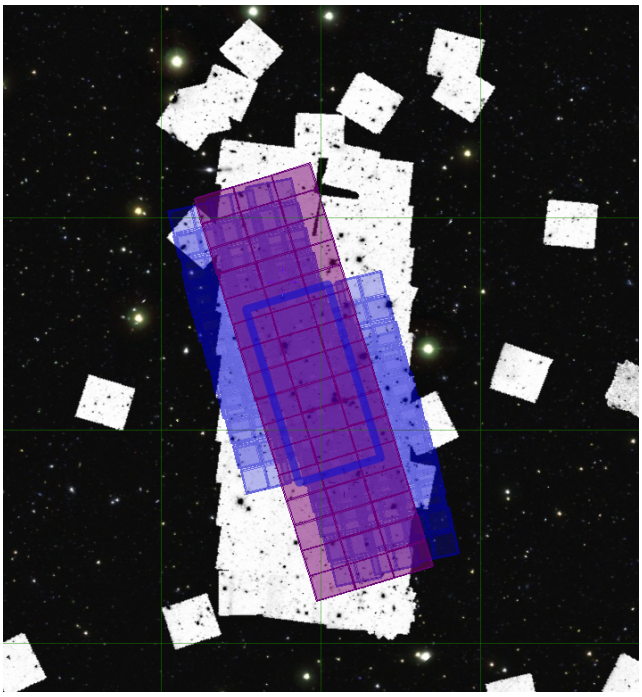

Figure 4.4 *The layout for our prescribed COSMOS observing strategy described in section 4.4.3. The red tiles represent the dithered MIRI coverage in the F770W filter, while the blue tiles represent the dithered NIRCam pointings with the deepest region (due to multiple exposures) highlighted by the dark blue box. We overlay this mosaicing strategy onto the current HST ancillary data available in COSMOS CANDELS along with the UVISTA colour composite image.*

As explained above, the proposed observing plan involves equal integration times in 8 NIRCam filters (F090W, F115W, F150W, F200W, F277W, F356W, F410M, F444W), with MIRI observations obtained in parallel over as much of the NIRCam area as possible given the constraints of survey field size/shape and the fairly limited permitted *JWST* roll angles for equatorial target fields. For this strawman survey we devote all of the parallel MIRI integration time to F770W imaging since, as already explained, the focus of this chapter is on the value of the added 7.7 μm MIRI photometry to the NIRCam photometric dataset. The anticipated 5-σ point-source depths (for all 10 NIRCam+MIRI filters) predicted by our noise simulations for the deepest region of contiguous area coverage in each field under our prescribed observing strategy are summarized in Table 4.4. The typical depths are somewhat lower in the UDS-CANDELS field because, as already explained above, the field geometry leads naturally to a somewhat wider-area, shallower survey (assuming comparable intergation time in each field) if substantial MIRI+NIRCam overlap is to be achieved. We stress, however, that the main results of this work, described in the next section, apply to any similar NIRCam multi-band survey with MIRI parallel observations, and in that sense our conclusions can be regarded as generic, even if based on a specific strawman observing strategy to ensure realism.

Given these depths (summarized in Table 4.4), as previously mentioned in relation to Table 4.3 and Fig. 4.3, in the interests of efficiency and meaningful analysis, we removed any galaxies from the simulations that did not match certain criteria as judged from the simulated photometry. Specifically 'non-detections' were removed, as judged by synthesised photometry which yielded less than 4-σ detections in more than four *JWST* wavebands.

Finally, we assumed that we can utilise ancillary homogeneous *HST* optical imaging coverage of our survey fields at the depths/filters of the current public ACS data. For the UDS-CANDELS and COSMOS-CANDELS fields, this consists of V_{606} and i_{814} imaging which, in both bands and in both fields reaches a 5-σ point-source detection limit of 28.4 mag. As with the *JWST* photometry, we simulated and scattered the predicted photometry in the *HST*/ACS bands given the known depths, and assuming Gaussian errors.

4.5 Reclaiming Galaxy Properties

In this section we introduce the SED-fitting code Bagpipes and explain the process of reclaiming the physical properties of the simulated galaxies from the synthesized *JWST* photometry. We also present and analyse the results for our BC03 and EGG simulations, exploring the impact of the addition of both MIRI and *HST* photometry to the core NIRCam 8-filter data.

4.5.1 SED Fitting Code - Bagpipes

Bayesian Analysis of Galaxies for Physical Inference and Parameter Estimation (Bagpipes, Carnall et al. 2018b) is a Bayesian spectral-fitting code, capable of fitting galaxy SEDs to photometric and/or spectroscopic data simultaneously in a statistically robust manner. Bagpipes can also be used to also generate model galaxy spectra based on set physical parameters described via python dictionaries; all of our simulated galaxy SEDs based on the Bruzual & Charlot (2003) spectrophotometric models were generated using Bagpipes, with the specified physical parameters summarized in Tables 1 and 2.

Bagpipes requires defined multiple-model parameterisation to fit against the submitted observational data, including the uncertainties of the observations. The user is required to define a prior probability distribution, describing the free parameters and limits for the fitting process. For this work we varied galaxy redshift ($0 < z < 15$), stellar mass ($0 < \log(M_*/\mathrm{M}_\odot) < 13$), metallicity ($0 < (Z/\mathrm{Z}_\odot) < 3$) and dust obscuration ($0 < (A_V/\mathrm{mag}) < 7$). All galaxies are fitted against two separate SFHs, exponentially decreasing/increasing and Log-Normal (see Section 2.3 in Carnall et al. 2018a) . We allow the exponential prescription to vary in both decay timescale ($-10 < \tau < 10$) and age ($0.001 < T/\mathrm{Gyr}) < 10$), thus allowing SFHs to be exponentially increasing or decreasing, and spanning a very large region of parameter space. For the Log-Normal SFH, we allow a wide range in Full Width Half-Maximum ($0 < (FWHM/\mathrm{Gyr}) < 10$) and maximum age ($0.001 < (t_{max}/\mathrm{Gyr}) < 10$). Through attempting to fit this range of models to the simulated photometry, Bagpipes produces a posterior distribution for each free parameter, and hence calculates the posterior median along with the ± 1-σ confidence intervals for each parameter value.The free parameters and their allowed ranges are summarized in Table 4.5.

Table 4.5 *The free parameters, and their allowed ranges, used to build the SED library within* BAGPIPES *for fitting to our simulated galaxy photometry.*

Parameter	Description	Range
M_*	Stellar Mass	$0 < \log_{10}(M_*/\mathrm{M}_\odot) < 13$
Z	Metallicity	$0 < (Z/\mathrm{Z}_\odot) < 3$
z	Redshift	$0 < z < 15$
A_V	Dust Obscuration	$0 < (A_V/\mathrm{mag}) < 7$
	Exponential SFH	
τ	Timescale	$-10 < (\tau/\mathrm{Gyr}) < 10$
T	Age of SFH	$0.001 < (T/\mathrm{Gyr}) < 15$
	Log-Normal SFH	
$FWHM$	SFH width	$0 < (FWHM/\mathrm{Gyr}) < 10$
t_{max}	Age of SFH	$0.001 < (t_{max}/\mathrm{Gyr}) < 15$

4.5.2 Results for the BC03 simulated galaxy sample

In Fig. 4.5 and Fig. 4.6 we show an example of using BAGPIPES to fit the simulated photometry of a $z = 5$, $M_* = 10^{10}\,\mathrm{M}_\odot$, dusty ($A_V = 3.2\,\mathrm{mag}$) galaxy, fitting to *HST*+NIRCam and then *HST*+NIRCam+MIRI F770W photometry respectively. In each case, we show the posterior distributions and contour plots for all the fitted free parameters described in Table 4.5, including also the inferred SFH (top right). We present the median and ±1-σ best-fit SEDs to our scattered photometric data in the lower panel of each figure.

In the first example (Fig. 4.5), the redshift posterior distributions and contours plots are dual-peaked, with the majority of the distribution lying within the low-redshift peak at $z \simeq 2$. As a result, the posterior median (middle dashed line) lies within the incorrect, low-redshift peak of the solution. A separate peak in the redshift distribution can be seen close to the correct (simulated) redshift at $z \simeq 5$, however the dominance of the low-redshift solution means that this is only just included within the $+1\sigma$ confidence region.

Incorrectly inferring the redshift has an obvious detrimental impact on the estimation of galaxy mass, especially given this type of bi-modal posterior distribution. The stellar-mass distribution and contour plots also therefore show two potential solutions, peaking at approximately $M_* \simeq 10^9\,\mathrm{M}_\odot$ and $M_* \simeq 10^{10}\,\mathrm{M}_\odot$. The width of the distribution lying around the incorrect (lower) stellar-mass estimate at $M_* \simeq 10^9\,\mathrm{M}_\odot$, draws the posterior median to lie at

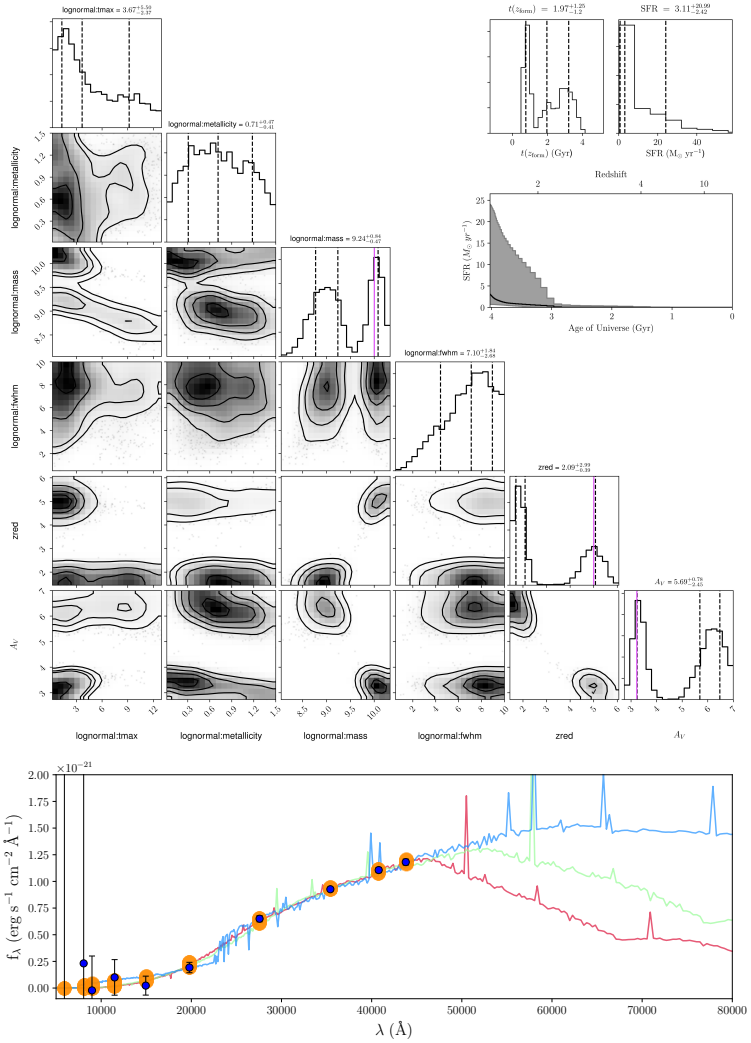

Figure 4.5 *An example of a* Bagpipes *fit to a dusty (A_V = 3.2 mag), z = 5 galaxy without any MIRI photometry (i.e. fitting only to the photometry from the 8 NIRCam filters). The upper panel presents a corner-plot of the resulting posterior distributions of all 6 free parameters described in Table 4.5. We also show the inferred age, SFR and SFH. The dashed lines in each panel represent the posterior median along with the ±1-σ solutions. The solid purple line marks the true input values for the stellar mass, redshift and dust obscuration. The lower panel shows our simulated galaxy photometry (blue points with error-bars), along with the* Bagpipes *SED fits to these data. The green line represents the SED extracted from the posterior medians of each distribution, in this case, at redshift $z \simeq 2.09$. The red and blue lines show the corresponding −1-σ and +1-σ SEDs respectively. In this case, the blue line corresponds to a high-redshift solution (at $z \simeq 5$, close to the true value), while the red line corresponds to a low-redshift solution (at $z \simeq 1.8$, close to the stronger low-redshift peak seen in the redshift corner plot). Most parameter distributions appear to be dual-peaked, with a larger proportion of the redshift distribution lying in the low redshift solution ($z \simeq 2$, red SED).*

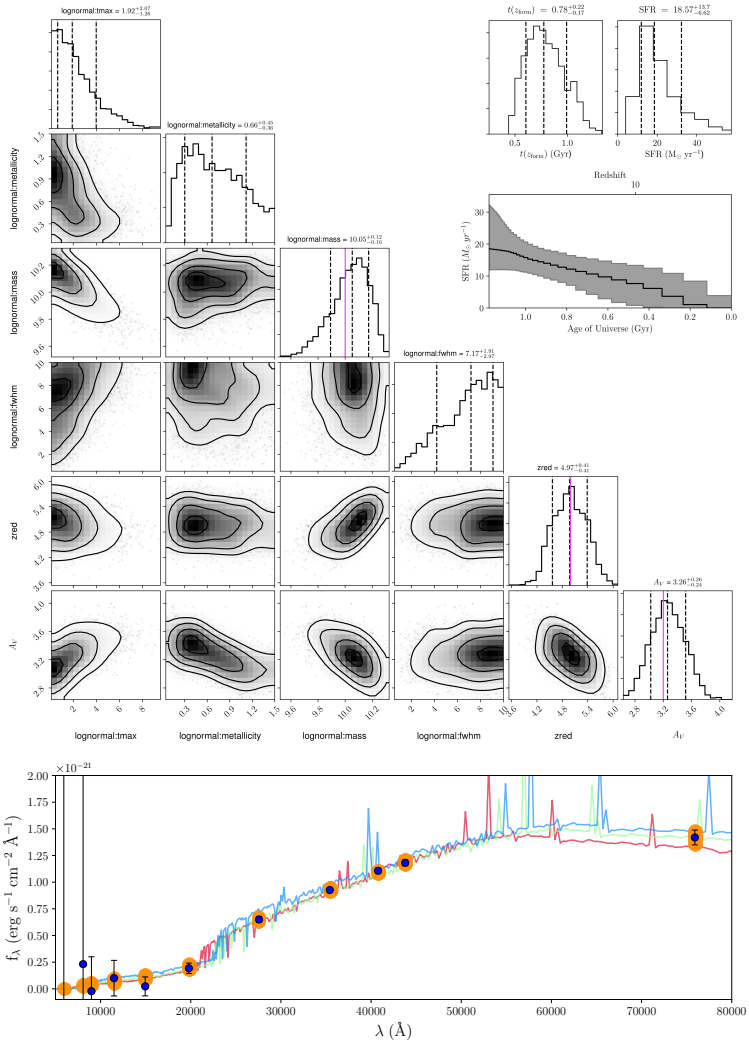

Figure 4.6 *The* Bagpipes *fit to the same $z = 5$ galaxy as in Fig. 4.5, but this time also fitting to the simulated MIRI F770W photometry. Again, the upper panel presents a corner-plot of the resulting posterior distributions of all 6 free parameters described in Table 4.5, and we also show the inferred age, SFR and SFH. As before, the dashed lines in each panel represent the posterior median along with the ± 1-σ solutions, but this time it can be seen that the parameter distributions are no longer dual-peaked and sit close to the true input values represented by the solid purple line. The lower panel shows our simulated galaxy photometry (blue points with error-bars, this time including the MIRI 7.7-μm photometry), along with the* Bagpipes *SED fits to these data. The green line represents the SED extracted from the posterior medians of each distribution, this time at redshift $z \simeq 4.97$ (only $\Delta z = 0.03$ from the true value). The red and blue lines show the corresponding -1-σ and $+1$-σ SEDs respectively; these now quantify the width of the single peak close to $z = 5$ ($z = 4.56$ and $z = 5.38$) due to the fact that the addition of the MIRI photometry has removed the bimodality in the distributions.*

approximately $10^{9.25}\,M_\odot$. This type of serious mass under-estimate (clearly linked to the bi-modal distribution of redshift) can introduce substantial errors in the determination of the galaxy stellar-mass function, and its inferred evolution with cosmic time.

The best-fitting SEDs are shown alongside the galaxy photometry in the bottom panel of Fig. 4.5. The blue points represent the raw photometry (with black error bars), while the orange 'points' show the photometric posterior distribution. Three SEDs are shown, with the red, green and blue SEDs showing the best fitting SEDs for the posterior median (green) and ±1-σ (blue and red, respectively). These can be matched to the dashed lines on the posterior distributions found in the corner plots: the blue line is a $z \simeq 5$, $M_* \simeq 10^{10}\,M_\odot$, $A_V = 3.2$ mag galaxy, while the green line represents the median $z = 2.09$, $M_* = 10^{9.25}\,M_\odot$, $A_V = 5.7$ mag SED fit, and the red line is a $z = 1.7$, $M_* = 10^{8.77}\,M_\odot$, $A_V = 6.5$ mag galaxy.

In Fig. 4.6 we show the results of fitting the same simulated galaxy, but this time including MIRI F770W photometry in the simulated dataset. It can be seen that the posterior distributions are very different, and in particular no longer dual-peaked. The distributions for redshift, stellar mass and dust obscuration all take the form of a single sharp peak lying very close to the correct values. This results in much tighter ±1-σ confidence intervals with a relatively narrow range of allowed parameter values. We also reclaim the shape of the SFH relatively well, with the fitting producing a SFR that grows slowly with time, matching very well the input fiducial $\tau = -0.1$ SFH shown in Fig. 4.2.

The scatter seen in the fitted SEDs also reduces dramatically with the addition of the F770W filter. This time the SED extracted from the posterior medians (green line) lies at redshift $z \simeq 4.97$ (only $\Delta z = 0.03$ from the true value), and the red and blue lines (showing the corresponding -1-σ and $+1$-σ SEDs respectively) now simply quantify the width of the single peak close to $z = 5$ ($z = 4.56$ and $z = 5.38$) due to the fact that the addition of the MIRI photometry has removed the bimodality in the distributions.

For this type of dusty, red, high-redshift galaxy the impact of adding MIRI photometry is thus clear. It is also clear that the *HST* ACS optical data (in this case V_{606} and i_{814}) has very little impact: the red colour of this galaxy combined with the depth of available ACS imaging in the CANDELS fields means that the errors on the ACS photometry are too large (in comparison with the *JWST* photometry) to significantly affect the fit.

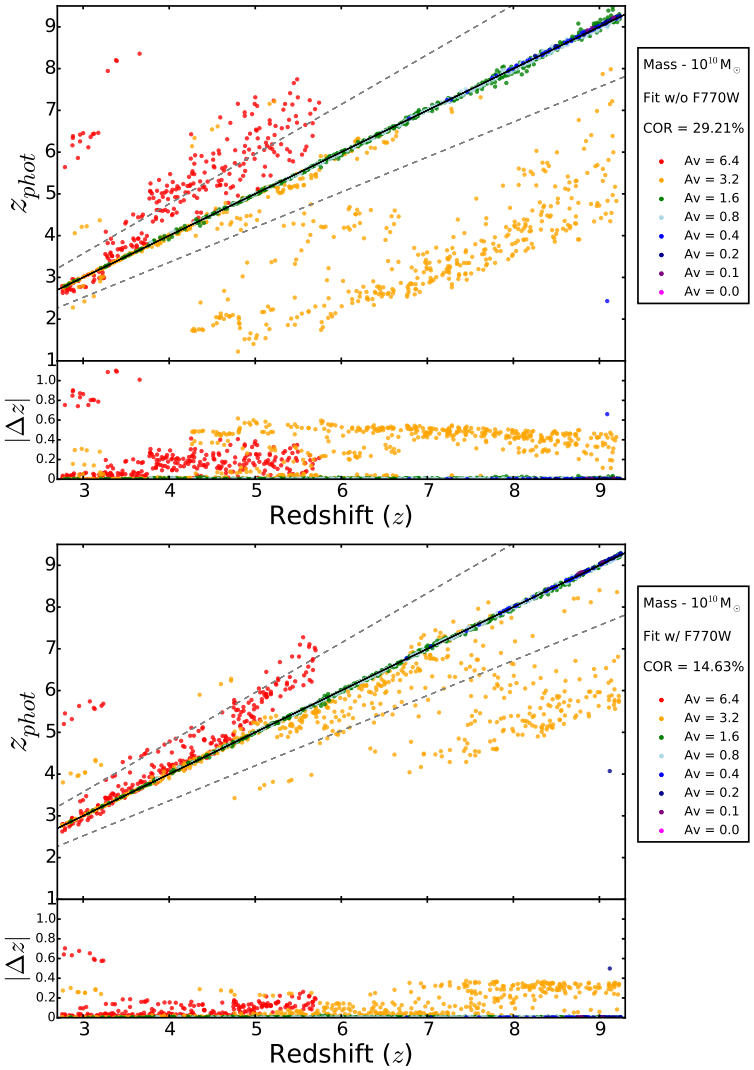

Figure 4.7 *Photometric versus input redshifts (with* $|\Delta z| = |(z_{phot} - z_{input})/(1 + z_{input})|$ *sub-plotted below each panel) for the* $10^{10}\,\mathrm{M}_\odot$ *exponentially-increasing SFH BC03 simulated galaxies. As indicated in the legend, the data points are coloured according to 8 bins in simulated dust obscuration (*A_V *=0, 0.1, 0.2, 0.4, 0.8, 1.6, 3.2, 6.4 mag). The upper panel shows the results when the galaxies are fitted without including the MIRI F770W photometry in the simulated dataset, while the lower panel shows the impact of including the MIRI photometry. The legend on the right-hand side of both panels gives the catastrophic outlier rates (COR), where the COR is defined by the percentage of galaxies for which* $|\Delta z| > 0.15$*. It can be seen that the photometric redshifts are of excellent quality for all but the dustiest galaxies (*$A_V >$ 3 *mag) and that the addition of the MIRI data improves the results for a significant subset of these, particularly at intermediate redshifts (as illustrated by the example shown in Fig. 4.5 and Fig. 4.6).*

Having highlighted an example of an object for which MIRI photometry clearly matters, in Fig. 4.7, we plot derived photometric redshift versus true input galaxy redshift for our sample of $M_* \simeq 10^{10}\,M_\odot$ BC03-simulated galaxies over the redshift range $3 < z < 9$, in this case (for clarity) focussing on the subset of such galaxies simulated with exponentially-rising SFHs. These plots show the results of attempting to determine photometric redshifts without (upper panel) and then with (lower panel) inclusion of the MIRI data. Both the $z - z$ plot and the normalised redshift distribution ($|\Delta z| = |(z_{phot} - z_{input})/(1 + z_{input})|$) are plotted in each case, and the galaxies are colour-coded by (input) dust obscuration. It is important to note that although we have 13 discrete redshift bins, we scatter the true input redshift values on the x-axis randomly by up to $\pm 0.25\ \delta z$. We subsequently apply the same offset to the fitted photometric redshifts on the y-axis to effectively project the redshift onto smaller, equally sized redshift bins making the plot itself far more digestable. Fig. 4.7 confirms that the galaxy discussed above (Fig. 4.6 and Fig. 4.5) is indeed typical of the sort of object for which the addition of MIRI 7.7-μm photometry is important. The addition of the MIRI data has no real impact on the (already excellent) photometric redshifts for the vast majority of objects with $A_V < 2$ mag, but clearly impacts on the (often much poorer) results for the galaxies in the two highest bins of obscuration (essentially $A_V > 2$ mag). The catastrophic outlier rate (COR, defined as $|\Delta z| > 0.15$) is reduced by a factor of two (from COR = 29.2% to COR = 14.6%) by the inclusion of the MIRI photometry, with the improvement most dramatic at intermediate redshifts ($z \simeq 4-6$). At very high redshifts the improvement is much less dramatic, primarily because dusty galaxies of this mass yield relatively poor-quality detections at $z > 7$ in the F770W filter (given our chosen exposure times). In general, the scatter is extremely large for the dusty subset of objects due to the severe suppression of the UV emission in the NIRCam filters. For the objects with better detection in the NIRCam bands, there is a bimodal distribution favouring neither the high redshift nor low redshift solution. This effectively means the posterior median is being drawn almost randomly across a wide redshift range. Interestingly, we tend to overestimate the redshift for the dustiest subset of galaxies ($A_V \simeq 6.4$, red points), while we predominantly underestimate the redshift for the $A_V \simeq 3.2$ sub-sample. We overestimate the redshift of the dustiest set of galaxies because the most extreme amount of UV suppression mimics a more likely fit to a high-redshift Lyman and/or Balmer break. The less extreme dust-obscured objects that sit at high-redshift are more likely to fit more extreme dust obscuration at lower redshift, hence the general underestimation in redshift

for the orange points, (see Dunlop et al. 2007). Finally, we note here that while the results shown in Fig. 4.7 include *HST* ACS photometry, the effect of excluding any *HST* ancillary data only degrades the COR by a very small amount ($\simeq 2\%$) but, as we discuss further in the next section, this is largely because **i)** the impact of *HST* optical data is most important at redshifts $z < 3$, and **ii)** the BC03 simulated galaxy sample analysed here contains a (deliberately) unrealistically-large proportion of dusty galaxies with extreme values of A_V. The approach taken here has therefore enabled us to isolate the *type of galaxy* for which MIRI parallel-mode imaging is of real value in contraining model parameters.

How important such dusty high-redshift galaxies actually are obviously depends on their prevalence/distribution in the general galaxy population, and the science question to be addressed. We note that, while we have assumed that such objects exist in all three mass bins of our BC03 simulated galaxy sample ($M_* = 10^{10}, 10^9, 10^8\,M_\odot$), it transpires that, in the two lower mass bins, very few such objects survive our S/N cuts due to the combination of low mass, high redshift, and extreme dust attenuation. Thus, even if such objects exist at such masses, they do not feature in our simulated *JWST* samples. In summary, given realistic exposure times, it is only at stellar masses $M_* \geq 10^{10}\,M_\odot$ that MIRI data can have a significant impact on the accuracy with which the physical properties of dusty high-redshift galaxies are reclaimed. However, there is in any case a growing body of evidence that dust content is strongly correlated with galaxy stellar mass, and hence that such objects are indeed largely confined to the stellar mass range $M_* \geq 10^{10}\,M_\odot$ in the real Universe (Dunlop et al. 2017; McLure et al. 2018a).

4.5.3 Results for the EGG simulated galaxy sample

Finally, we used Bagpipes to reclaim the properties of the galaxies in the simulated EGG galaxy samples in the COSMOS and UDS simulated surveys as summarized in Table 4.3. Again we explored the impact of adding the MIRI photometry to the *HST*-ACS + *JWST*-NIRCam dataset, and this time found that the addition of parallel MIRI F770W photometry had very little impact on the accuracy of the reclaimed photometric redshift estimation. In fact, the photometric redshifts improved for only $\simeq$1% of the EGG-simulated *JWST*-detected galaxy population, which is of course intended to produce a more realistic distribution of galaxy properties than explored in the BC03 simulations. There

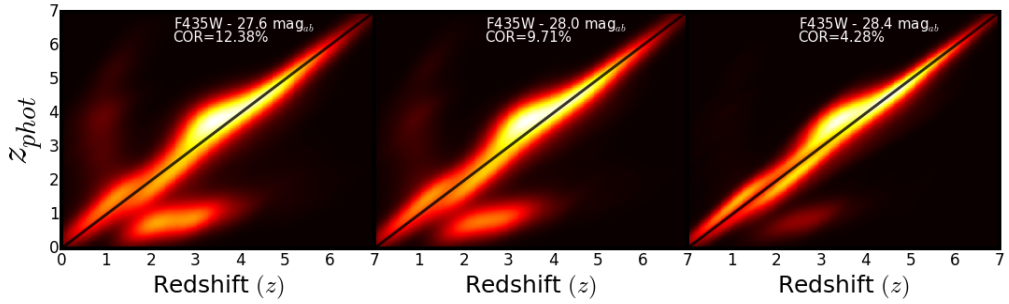

Figure 4.8 *Density maps showing reclaimed photometric redshift as a function of simulated galaxy redshift for our sample of EGG galaxies, exploring the impact of increasingly deep HST ACS B_{435} imaging as indicated in each panel. Left: Photometric redshifts reclaimed using the 8 NIRCam Bands with existing HST V_{606}, i_{814} and B_{435} imaging (reaching 27.6 mag, 5-σ). Centre: The results of the same procedure, but assuming the B_{435} imaging is 0.4 mag deeper. Right: The results when it is assumed that the B_{435} imaging is 0.4 mag deeper still. The catastrophic outlier rate (COR) in each case is also given, defined as the percentage of galaxies with $|\Delta z| > 0.15$, where $|\Delta z| = |(z_{phot} - z_{input})/(1 + z_{input})|$.*

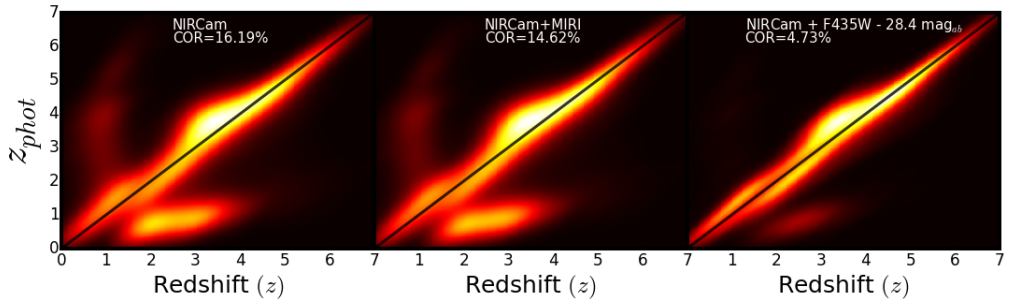

Figure 4.9 *Density maps showing reclaimed photometric redshift as a function of simulated galaxy redshift for our sample of EGG galaxies in multiple filter combinations. Left: Photometric redshifts reclaimed using the 8 NIRcam Bands with existing HST V_{606} and i_{814} imaging. Centre: Photometric redshifts reclaimed using the 8 NIRcam Bands with existing HST V_{606} and i_{814} + MIRI F770W photometry. Right: Photometric redshifts reclaimed using the 8 NIRcam Bands with HST V_{606} and i_{814} + B_{435} (28.4 mag) imaging. The catastrophic outlier rate (COR) in each case is also given, defined as the percentage of galaxies with $|\Delta z| > 0.15$, where $|\Delta z| = |(z_{phot} - z_{input})/(1 + z_{input})|$.*

are two reasons for the relatively low impact of MIRI. First, the EGG simulations extend down to essentially $z \simeq 0$, and the redshift distributions are dominated by galaxies at $z < 3$. Such objects, which were deliberately not included in the BC03 simulations (which were aimed at exploring the high-z galaxy population) have redshifts that are already well-constrained by multiple detections in the ACS+NIRCam filters, or if not are too faint for MIRI to help. Second, binning the EGG sample by dust obscuration, we found that the EGG simulations contained only a tiny number of dusty galaxies with $A_V > 3.0$ mag in the simulated *JWST* survey galaxy samples. This may reflect a problem with EGG which requires further exploration/refinement, since such objects are certainly known to exist in the CANDELS fields (Dunlop et al. 2007), but at least it explains the virtually negligible impact of MIRI on the photometric redshifts (and hence stellar masses etc).

In fact, we found that where MIRI was making its very modest impact on the EGG photometric redshifts was for a small sample of relatively dust-free galaxies which happened to have two alternative peaks in their posterior redshift distributions, and the addition of the MIRI F770W photometry just happened to tip the probability balance slightly in favour of the correct peak. However, for these objects, the impact of MIRI was still too modest to modify the posterior distributions to the extent that the incorrect solutions could be excluded, and on close examination of this subset of objects we discovered that the real problem was the lack of *HST* data at wavelengths shortward of the existing V_{606} data. We therefore decided to explore whether the addition of ACS B_{435} imaging in these fields would actually have more impact on this subset of objects than the addition of the MIRI photometry. To explore the impact of adding B_{435} imaging of increasing depth, we decided to perform a series of re-runs using differing B_{435} depths of 27.6, 28.0 and 28.4 mag. The first of these depths was chosen to represent what could be achieved in a Medium-sized *HST* programme, the second effectively matches the depth of the available B_{435} imaging in the GOODS fields, while the final deepest depth was chosen to match (in terms of AB magnitudes) the depth of the existing V_{606} and i_{814} imaging in the UDS-CANDELS and COSMOS-CANDELS fields.

The impact of this simulated progressive increase in B_{435} imaging depth on the photometric redshifts delivered by BAGPIPES for the EGG *JWST* galaxy sample is shown in Fig. 4.8. There is a major impact on the number of incorrect redshifts at $z < 3.5$, and as a result the COR is predicted to decline from $\simeq 12\%$ to $\simeq 4\%$

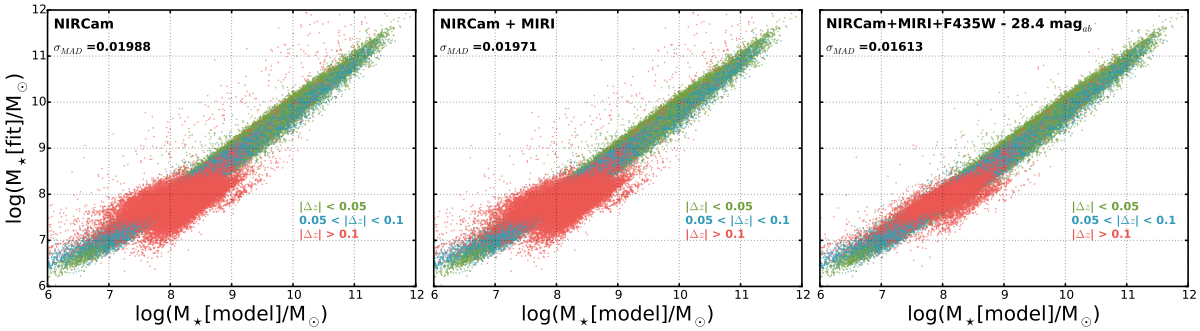

Figure 4.10 *Reclaimed galaxy stellar mass versus input fiducial model mass for the galaxies in our JWST-detected EGG Sample, with NIRCam alone (Left), NIRCam with added MIRI F770W (Centre) and with the addition of deep HST ACS B_{435} photometry reaching 28.4 mag (5-σ) (Right). We colour code by photometric redshift offset ($|\Delta z|$) in three separate bins. The green points represent galaxies fitted with well-constrained photometric redshifts ($|\Delta z| < 0.05$), the blue points represent galaxies that have reasonably good fits to redshift ($0.05 < |\Delta z| < 0.1$) while the red points represent galaxies with poor photometric redshift estimations ($|\Delta z| > 0.1$). We also give the mean $|\Delta m|$ in each case, where $|\Delta m|$ is defined as* $\log(M_*[model]/\mathrm{M}_\odot) - \log(M_*[fit]/\mathrm{M}_\odot)$.

simply by deepening the ACS B_{435} imaging by a factor of $\simeq 2$ in limiting flux density. The vertical arm feature representing $z \simeq 1$ galaxies with seriously over-estimated photometric redshifts almost completely disappears as we now have a good enough detection of the flux blueward of 0.6μm. Previously, the poor detection allows for an incorrect confirmation of the Lyman-break pushing the posterior median of the photometric redshift distribution to higher redshifts. We also see a substantial number of genuine $z \simeq 2-3.5$ galaxies have their previously under-estimated redshifts corrected by better confirmation of the Lyman-break feature due to the deeper B_{435} imaging. We see no real improvement beyond $z > 5$ as, for many of these galaxies, a more secure non-detection in the B-band adds little to the information provided by the existing V_{606} imaging given the location of the Lyman break.

The relative added value of either MIRI F770W or *HST* B_{435} imaging is compared in Fig. 4.9. Here we show the inferred photometric redshift versus the fiducial input redshift for 3 separate filter combinations of photometric data. In producing the results shown in the left-hand panel we used *HST* V_{606}, *HST* i_{814} and the 8 *JWST* NIRCam bands, in the middle panel we added MIRI F770W photometry, and for the right-hand panel we instead added deep (28.4 mag.) *HST* B_{435} photometry. Consistent with the above results, we see a small improvement when

we add the MIRI F770W parallel photometry, with COR reduced by ∼2.3%, while the addition of deep *HST* B_{435} imaging decreases the COR by ∼10%.

As already demonstrated for the example galaxy highlighted in Fig. 4.5 and Fig. 4.6, an error in photometric redshift is one of the key sources of systematic error in reclaimed galaxy stellar mass. Consequently, catastrophic redshift errors of the type seen in Fig. 4.8 and Fig. 4.9 can have a serious impact on the determination of galaxy mass functions. For example, a galaxy in the vertical arm feature focused at a true redshift of $z \simeq 1$ in Fig. 4.8 and Fig. 4.9 could have its redshift over-estimated up to a value of $z_{phot} \simeq 5.3$. This alters the inferred galaxy stellar mass from $M_* = 10^{6.4}\,\mathrm{M}_\odot$ to $M_* = 10^{9.1}\,\mathrm{M}_\odot$. Fig. 4.10 shows reclaimed stellar mass versus the fiducial model stellar mass for the galaxies in our EGG sample first with NIRCam only, then NIRCam with the addition of MIRI F770W imaging and finally with the proposed deeper *HST* B_{435} imaging data (reaching 28.4 mag, 5-σ). We colour code each panel with 3 photometric redshift offsets bins: the green points represent galaxies with a good photometric redshift ($|\Delta z| < 0.05$), the blue points represent galaxies with reasonably well fitted photometric redshifts ($0.05 < |\Delta z| < 0.1$), while the red points represent galaxies with a poorly inferred photometric redshift ($|\Delta z| > 0.1$). The relationship is significantly tightened only with the addition of the deep B-band data where a large number of galaxies with true stellar masses in the range $M_* = 10^7 - 10^{10}\,\mathrm{M}_\odot$ have their reclaimed masses restored to their true (i.e. input) values. This is primarily as a result of the reduction in catastrophic redshifts, where not only do we see a dramatic decrease in scatter as we add the B_{435} imaging, but also the vast reduction in the number of galaxies with poor photometric redshift constraints (*i.e* reduction in the number of red points). The normalised change in stellar mass $|\Delta m|$ (where $|\Delta m| = \log(M_*[\mathrm{model}]/\mathrm{M}_\odot) - \log(M_*[\mathrm{fit}]/\mathrm{M}_\odot)$ drops by 0.0336, reflecting the accuracy with which the stellar masses are reclaimed with the addition of the deep B_{435} imaging. Clearly an accurate determination of galaxy stellar masses is key to an effective confrontation between the results from *JWST* galaxy surveys and the predictions of theoretical models and simulations. These results indicate that deep B_{435} *HST* optical imaging in the CANDELS fields is crucial for minimising systematic errors in the stellar masses of the galaxies that will be uncovered in deep *JWST* surveys.

4.6 Summary and Conclusions

We have undertaken an analysis of simulated *JWST*+*HST* photometry for a wide range of model galaxies, in order to explore the ability with which the redshifts and physical properties of galaxies can be reclaimed from different multi-band combinations of photometry. In particular we have explored the potential value of extending the wavelength baseline of *JWST* NIRCam photometry to longer wavelengths with *JWST* MIRI, and/or to shorter wavelengths with additional *HST* ACS imaging. The former is of interest because, for moderate size NIRCam surveys, MIRI data can be obtained in parallel, while the latter is of interest because we still have the opportunity to utilise *HST* to improve the available optical imaging in likely *JWST* extragalactic survey fields.

In this chapter we ensure our results are fully realistic, because **i)** they are based on fully-developed observing strategies which are achievable with *JWST* in the selected survey fields; **ii)** we assume MIRI integration times that are achievable in parallel-mode observing, and **iii)** we use the latest information on available *HST* imaging in the survey fields, while also exploring what improvements can be achieved with feasible future *HST* large programmes.

We created two different simulated galaxy samples, one (based on the models of Bruzual & Charlot 2003) designed to explore a wide range of possible galaxy properties including very dust-obscured objects, and a second (based on the Empirical Galaxy Generator: EGG) that is designed to be representative of the known galaxy population. The photometry for all these objects was created and scattered given the latest knowledge of the preformance of the relevant instruments, and the samples were then trimmed to only include significant detections (given our adopted observing strategy). Finally we used the Bayesian SED-fitting code Bagpipes to attempt to reclaim the properties of the galaxies from the scattered photometry, performing the analysis both with and without the inclusion of the MIRI and/or *HST* ACS data.

Our main findings are that **i)** parallel MIRI 7.7 μm imaging is of real value (in some cases crucial), but only for a subset of galaxies at $z \simeq 4-7$ which have high dust obscuration, $A_V > 2$; **ii)** the current EGG simulations suggest that such galaxies only constitute 0.5% of the $z = 0-12$ galaxy population that will be detected by *JWST* NIRCam surveys, but this could easily be an under-estimate, given the known existence of galaxies in the GOODS fields with $A_V \simeq 5$ (e.g.

Dunlop et al. 2007); **iii)** while the MIRI photometry also appears to help with the accurate recovery of the properties of some galaxies at $z < 4$, it transpires that deep *HST* ***B***-band photometry is of more value (and is more efficient) for removing photometric redshift degeneracies for such galaxies.

Given the importance of robustly quantifying the evolution of the high-mass dusty galaxy population out to the highest redshifts, our results still favour the use of MIRI parallels with deep NIRCam surveys, despite the fact that, for the vast majority of the bluer galaxy population, the MIRI photometry struggles to add value to the deeper NIRCam data. Our results also argue strongly for the acquisition of additional deep public *HST* ACS imaging in the key CANDELS fields (e.g. UDS and COSMOS) prior to the commencement of *JWST* operations, to ensure that the power of deep extra-galactic imaging surveys with *JWST* is maximised.

Moreover, in closing we also note that, given the known existence of dusty galaxies such as the example highlighted in Figs. 4.5 and 4.6, even if such objects prove to be rare on the scale of the CANDELS fields, they will undoubtedly be revealed in wider area surveys (*e.g.* in on-going near-infrared or sub-mm/mm surveys). This means that deep pointed MIRI follow-up of such sources will be invaluable, both for resolving redshifts/mass ambiguities, and indeed potentially for delineating their mid-infrared SED's through multi-band MIRI imaging.

5

The Prevalence of Dusty Objects in the High-Redshift Universe

This chapter presents a new search for high-mass dusty star-forming galaxies (highlighted in Chapter 4) using the current deepest ground-based UV/optical/near-IR and far-IR/sub-mm observations. In an attempt to assess the prevalence of dusty objects at high redshift, we combine the UV and IR data from numerous telescopes in the UDS and COSMOS fields and calculate the co-moving number density as a function of cosmic time. Additionally, we calculate the total star-formation rate (SFR) as a function of redshift and compare the contribution from sub-mm galaxies and UV/optically-selected dusty galaxies, extending the results from Madau & Dickinson (2014) for obscured star-formation. This chapter shows that both the UV/optical and sub-mm approach to detecting high-redshift dusty galaxies produce a consistent estimation of the evolving co-moving number density and star-formation rate density (SFRD).

5.1 Introduction

In order to effectively study dusty galaxies at high redshift, observations across a wide range of wavelengths are required. Ideally, a set of observations are available covering the optical, UV and near/mid-IR region of the spectrum, to allow an assessment of how the dust suppresses the UV emission within galaxies across a wide range of redshifts. In addition, comprehensive coverage of the far-IR/sub-mm region of the spectrum is desirable, allowing careful analysis of the level of UV emission that has been absorbed and then re-emitted in the infrared by dust particles. Until twenty years ago, galaxies which emitted primarily in the far-IR/sub-mm were relatively unstudied. Surveys carried out using the James Clerk Maxwell Telescope (JCMT) uncovered a significant population of sub-mm bright galaxies (SMGs - e.g. Smail et al. 1997; Hughes et al. 1998; Barger et al. 1998) where it was concluded that these galaxies show the most extreme levels of star-formation (100-2000 $M_{\odot}$ yr^{-1}) in the entire Universe. This was a significant breakthrough, as approximately half of the star-formation activity in the Universe is undetected by the traditional UV/optical studies of high-redshift galaxies. Since then, the role of SMGs in galaxy evolution and formation has been studied extensively in an attempt to understand what drives the immense star-formation rates (SFR) observed (see reviews; Blain et al. 2002 and Casey et al. 2014).

For high-redshift science, sub-mm galaxies have always been relatively easy to detect, in comparison to their low-redshift counterparts, due to the powerful negative *K*-correction. Effectively, this means distant galaxies are observed at a rest-frame wavelength very close to the peak of their spectral energy distribution (SED). At wavelengths beyond $\lambda > 250\mu$m, the observed flux of galaxies above redshift $z > 1$ no longer decreases at a rate of the inverse square of the distance to the object, and in fact, remains relatively constant as the redshift increases beyond $z > 1$. However, both the high background and poor angular resolution of single dish sub-mm/mm telescopes, limits our ability to detect all but the brightest, rarest and most violently star-forming galaxies.

A step towards understanding the evolution and formation of galaxies across cosmic time is to measure the cosmic star-formation history of the Universe. This is usually quantified through the Star-Formation Rate Density (SFRD), as a function of redshift and/or lookback time, as summarised in the Behroozi et al. (2013) and Madau & Dickinson (2014) reviews. Observationally, this has been

accomplished to extreme redshifts $z \simeq 9$ using the UV light from star-forming galaxies. However, much of the UV emission from young stars is thought to be enshrouded by dust, where the light is scattered and absorbed. Unfortunately, this means that calculations based on rest-frame UV emission require to be corrected to account for dust extinction.

The nature and prevalence of obscured star formation at high redshift is still uncertain. There is evidence suggesting that at lower redshifts ($z < 3$) the evolution of SFRD is dominated by obscured star formation, while at high redshift ($z > 4$) unobscured UV luminous sources are the dominant contributors (e.g. Burgarella et al. 2013;Gruppioni et al. 2013; Dunlop et al. 2017; Bourne et al. 2017; Koprowski et al. 2017; Wang et al. 2019). However, arguably the complete census of obscured star formation at $z > 3$ has yet to be completed. This is because most obscured star formation seems to be concentrated in the rare high mass objects and so large area surveys, with good redshift information are required. In this chapter, we therefore exploit the wealth of sub-mm and optical to near-IR data available in the two best studied degree-scale extragalactic survey fields

This chapter is structured as follows. In Section 5.2 we present a detailed description of the UV/optical and near-IR photometric catalogues constructed for both the UDS and COSMOS fields. We also present the results and analysis of photometric redshift testing calibrated against a high-quality spectroscopic galaxy sample, as well as outlining our methodology for creating sub-samples of the photometric catalogue. In Section 5.3 we present the initial results of fitting the UV/optical and near-IR COSMOS and UDS datasets with Bagpipes. This is followed by Section 5.4 where we provide a detailed introduction to the additional sub-mm data taken with ALMA in the UDS field (based on the ALMA follow-up of SCUBA-2 sources). In Section 5.5, we present the results of fitting this smaller dataset of sub-mm bright galaxies in the UDS with Bagpipes and compare the results to that of the UV/optically and near-IR selected dusty galaxies. Finally, in Section 5.6, we give a summary of our main conclusions.

5.2 Data

5.2.1 COSMOS Catalogue

The COSMOS multi-wavelength photometric catalogue is built using photometry from 4 separate instruments/surveys. The optical data are taken from the Canada-France-Hawaii Telescope Legacy Survey (CFHTLS; `http://www.cfht.hawaii.edu/Science/CFHLS/`) in the U, G, R, I and Z bands, with additional deeper z-band data from as the Subaru/SuprimeCam (z_1; Furusawa et al. 2016). The deep near-IR data was obtained from the UltraVISTA with the VISTA telescope (UVISTA; McCracken et al. 2012, Bowler et al. 2014) in the Y, J, H and Ks bands (DR3 (DR4 for Ks) release). The optical to near-IR imaging was PSF-homogenized to a Moffat profile of FWHM 0.98″. *Spitzer* imaging in the 3.6μm and 4.5μm filters is also available as part of the The *Spitzer* Extended Deep Survey (SEDS; Ashby et al. 2013), The *Spitzer*-Cosmic Assembly Deep Near-Infrared Extragalactic Legacy Survey (S-CANDELS; Ashby et al. 2015) and The *Spitzer* Large Area Survey with Hyper-Suprime-Cam (SPLASH; PI Capak; see e.g. Mehta et al. 2018) programmes, as well as The *Spitzer* Legacy Survey of the Hubble Space Telescope COSMOS Field (S-COSMOS; Sanders et al. 2007) and the *Spitzer* Matching Survey of the Ultra-VISTA Deep Stripes (SMUVS; Ashby et al. 2018). These data sets were all combined into one COSMOS 'supermap', so as to provide the deepest available mid-IR imaging. SPLASH combines observations from both the Subaru/SuprimeCam and *Spitzer* in order to build a catalogue of optical and near/mid IR data across the entirety of the COSMOS field. The 5σ depths for each filter in the COSMOS field are summarised in Table 5.1, where we also state the telescope and survey used to make the observations.

UltraVISTA is an ultra deep near-IR survey with the European Southern Observatory (ESO) VISTA survey telescope. Over the course of 10 years, UltraVISTA has repeatedly imaged the COSMOS field in 4 broad bands and 1 narrow band (Y, J, H, Ks and NB188, respectively) split into 3 separate surveys. The first is an ultra deep broad-band (Y, J, H and Ks) set of strips covering 0.73 deg^2 (1408hr), the second is a contiguous shallower but wider broad band survey (Y, J, H and Ks) covering 1.5 deg^2 (212hr) while the third is a narrow band imaging survey covering the entire ultra deep area.

Field	Filter	Depth (5σ) (Deep/U-Deep)	Telescope	Survey
COSMOS	U	27.0	CFHT	CFHTLS
	G	27.0	CFHT	CFHTLS
	R	26.4	CFHT	CFHTLS
	$i^{'}$	26.1	CFHT	CFHTLS
	$z^{'}$	26.1	CFHT	CFHTLS
	$z_1^{'}$	25.2	Subaru	SPLASH
	Y	25.6/24.8	VISTA	UVISTA
	J	25.4/24.6	VISTA	UVISTA
	H	25.1/24.2	VISTA	UVISTA
	K_s	25.0/23.9	VISTA	UVISTA
	Ch1 3.6μm	26.5	*Spitzer*	SPLASH, SEDS, S-CANDELS, SMUVS, S−CANDELS
	Ch2 4.5μm	26.5	*Spitzer*	SPLASH, SEDS, S-CANDELS, SMUVS, S−CANDELS

Table 5.1 *The 5σ depths of the multiwavelength data used in the COSMOS field assuming a $2''$ diameter aperture.*

5.2.2 UDS Catalogue

The UDS multi-wavelength photometric catalogue is constructed using data from four telescopes/surveys. The optical data are again obtained from the CFHTLS and Subaru/SuprimeCam z-band imaging specifically from the publicly released mosaics in Subaru-XMM-Newton Deep Survey (SXDS)) in the B, V, R, i, z' filters. The near-IR data are taken from the VISTA Deep Extragalactic Observations (VIDEO, Jarvis et al. 2013) survey and the Ultra Deep Survey (UDS) of the United Kingdom Infra-Red Telescope (UKIRT) Infrared Deep Sky Survey (UKIDSS: Lawrence et al. 2007). Specifically the UDS DR11 data release (Almaini et al. in prep), which is comprised of Wide-Field Camera (WFCAM) imaging in J, H, and K. All of the optical to near-IR UDS imaging was PSF-homogenized to a Moffat profile, with FWHM $0.8''$. For longer wavelength coverage extending to the mid-IR, we utilise *Spitzer* IRAC imaging from SEDS, S-CANDELS and SPLASH. A 'supermap' stacked mosaic of all of these datasets was produced using the MOsaicker and Point source EXtractor (MOPEX; Makovoz & Marleau 2005) [1]. The 5σ depths for each filter in the UDS field are summarised in Table 5.2, where we also state the telescope and survey used to make the observations.

5.2.3 Photometry and Photometric Redshifts

In order to generate photometric catalogues, SExtractor (Bertin & Arnouts 1996 [2]) was run in dual-image mode, with the Ks band imaging serving as the detection image. Photometry was primarily measured in both 2 and 3 arcsecond diameter apertures. While detection of objects was on the non-homogenized imaging, photometric measurements were performed on the PSF-homogenized imaging, in order to give a uniform spatial resolution across all bands, and to reduce systematics when SED fitting. Slight corrections (typically at the $\simeq$1% level) were made to cater for any remaining inhomogeneities between bands, based on the flux curve of growth.

By measuring the local aperture-to-aperture rms, accurate photometric uncertainties could be assigned for each object. This analysis was performed for both the 2 and 3 arcsecond photometry. Firstly, a grid of evenly spaced, non-overlapping

[1] `https://irsa.ipac.caltech.edu/data/SPITZER/docs/dataanalysistools/tools/mopex/`

[2] `https://www.astromatic.net/software/sextractor`

Field	Filter	Depth (5σ)	Telescope	Survey
UDS	U	27.0	CFHT	CFHTLS
	B	27.8	Subara	SXDS
	V	27.4	Subara	SXDS
	R_c	27.2	Subara	SXDS
	$i^{'}$	27.0	Subara	SXDS
	$z_1^{'}$	26.0	Subara	SXDS
	$z_2^{'}$	26.4	Subara	SXDS
	NB921	25.8	Subara	SXDS
	Y	25.1	VISTA	VIDEO
	J	25.5	UKIRT	UKIDSS
	H	24.9	UKIRT	UKIDSS
	K	25.1	UKIRT	UKIDSS
	Ch1 3.6μm	26.5	*Spitzer*	SPLASH, S−CANDELS and SEDS
	Ch2 4.5μm	26.5	*Spitzer*	SPLASH, S−CANDELS and SEDS

Table 5.2 *The 5σ depths of the multiwavelength data used in the UDS field assuming a $2''$ diameter aperture*

apertures were placed across the entire field of view. All apertures that contained flux due to sources were removed using a dilated SExtractor segmentation map. Statistics were then run on a sub-grid of 150−200 'blank-sky' apertures around each object in order to derive σ through the median absolute deviation (MAD). In the case of an object being situated near the edge between deep and ultra deep stripes, the statistics were only applied on apertures in the appropriate stripe so as not to bias the depth measurement.

For the lower spatial resolution IRAC imaging at 3.6μm and 4.5μm, photometry was measured by using the de-confusion code TPHOT (Merlin et al. 2015). Briefly, the surface brightness and spatial information of a given object in the high-resolution Ks-band imaging serves as the prior. The algorithm convolves each 2D cutout galaxy template with a transfer kernel in order to produce a model of the object in the low-resolution IRAC imaging. Fluxes of all resulting templates are then fitted simultaneously to produce the longer-wavelength photometry.

In order to find photometric redshifts, SED fitting analyses were performed by employing the fitting codes LePhare (Ilbert et al. 2006, Arnouts & Ilbert 2011), Bayesian Photometric Redshifts (BPZ; Benítez 2000) and EAZY (Brammer et al. 2008 [3]). Six runs were performed: for LePhare, the COSMOS SED library, the Pegase SED library (Fioc & Rocca-Volmerange 1999) and the Bruzual & Charlot (2003) were employed; for EAZY, the default PCA and Pegase libraries were used, and for BPZ the standard Coleman et al. 1980 or CWW libraries were used. For each of the six runs, in order to ensure that accurate photometric redshifts were measured across our samples, training sets were used in order to calculate zero-point offsets which were then applied to the photometry. Extensive testing was performed in order to find the ideal SED fitting setup, which we quantified through measuring the scatter of the photometric to spectroscopic redshift line. Spectroscopic redshifts came from a variety of studies including the Visible Multi Object Spectrograph (VIMOS) Public Extragalactic Redshift Survey (VIPERS; Guzzo et al. 2014), UDSz survey (Bradshaw et al. 2013, McLure et al. 2013a and Almaini et al. in prep) and zCOSMOS (Lilly et al. 2007). Once the optimal set-up was found for each photometric redshift run, the SED fitting was performed on the full catalogues with the calculated offsets included. A final median photometric redshift (z_{med}) was measured for each object based on the six individual runs, and propagated to the next step.

[3] `http://www.astro.yale.edu/eazy/`

By fixing the photometric redshift to the median as found previously, stellar masses were calculated with LePhare. The SED library was based on the Bruzual & Charlot (2003) template set, a Calzetti (2000) dust attenuation model with allowed extinction in the range E(B - V) = 0−0.7 ($A_V \simeq 0-2.1$ mag) with fine steps 0.0125, and IGM absorption according to Madau (1995). Emission lines were also included.

Across both fields, we found our photometric redshifts typically have a 2−3% catastrophic outlier fraction versus the spectroscopic redshifts, with a very tight correlation. If one only considers $z > 1.5$ objects, the outlier fraction typically increases to 4−6% although this corresponds to a relatively small number of objects. Fig. 5.1 and Fig. 5.2 shows photometric redshift as a function of spectroscopic redshift for all runs detailed above. We also show the results produced from Bagpipes, but this will be discussed in more detail in Section 5.2.4.

Corrections to total photometry, and hence total masses, were based on the assumption that FLUX_AUTO encloses approximately 90% of the total flux of a source. The aperture photometry of the optical to near-IR, and the TPHOT-processed photometry in the mid-IR bands were scaled to total according to this measurement for each object.

The entire 1.5 deg^2 deep and ultra deep COSMOS and UDS catalogues containing approximately 600,000 galaxies was initially cut to only include galaxies with a stellar mass $M_* > 10^{9.5} M_\odot$, reducing the total number of galaxies down to approximately ≃180,000 objects. This ensures we are targeting the most massive galaxies within our catalogue, while it also increases the computational efficiency. Further cuts to improve the efficiency further are detailed in Section 5.2.5.

5.2.4 Spectroscopic Sample

A small number of objects in the finalised UDS and COSMOS galaxy catalogues had supplementary spectroscopic observations. Many of these observations were of sufficient brightness so that the signal-to-noise ratios were good enough for solid spectroscopic redshift measurements. In the UDS, we have approximately ≃ 1000 galaxies while in the COSMOS field we have a large sample of ≃ 2100 objects with accurately calculated spectroscopic redshifts. This allowed for rigorous testing of photometric-redshift and stellar-mass estimations using Bagpipes. As previously

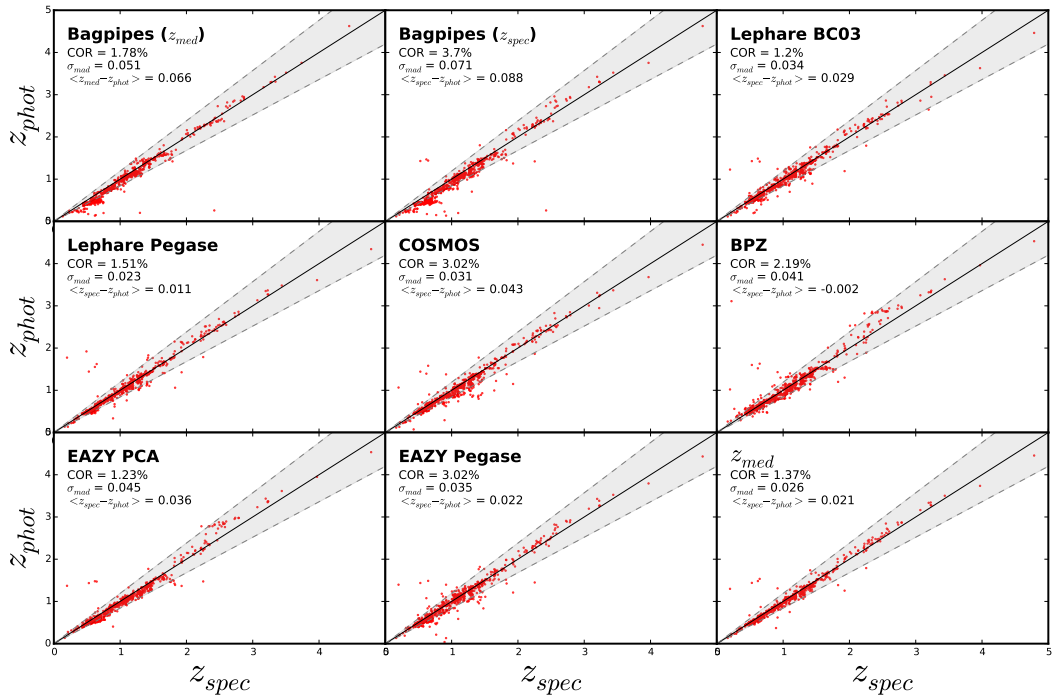

Figure 5.1 *Photometric redshift vs spectrscopic redshift calculated by* BAGPIPES *for the galaxies found in the UDS field. We also plot the photometric redshifts estimated by a number of independent runs, such as EAZY and LePhare. We also plot z_{med}, which represents the average photometric redshift found for each object. For each case, we print the calculated catastrophic outlier rate (COR), the σ_{MAD} and the mean offset between the spectroscopic and photometric redshift ($z_{spec} - z_{phot}$).*

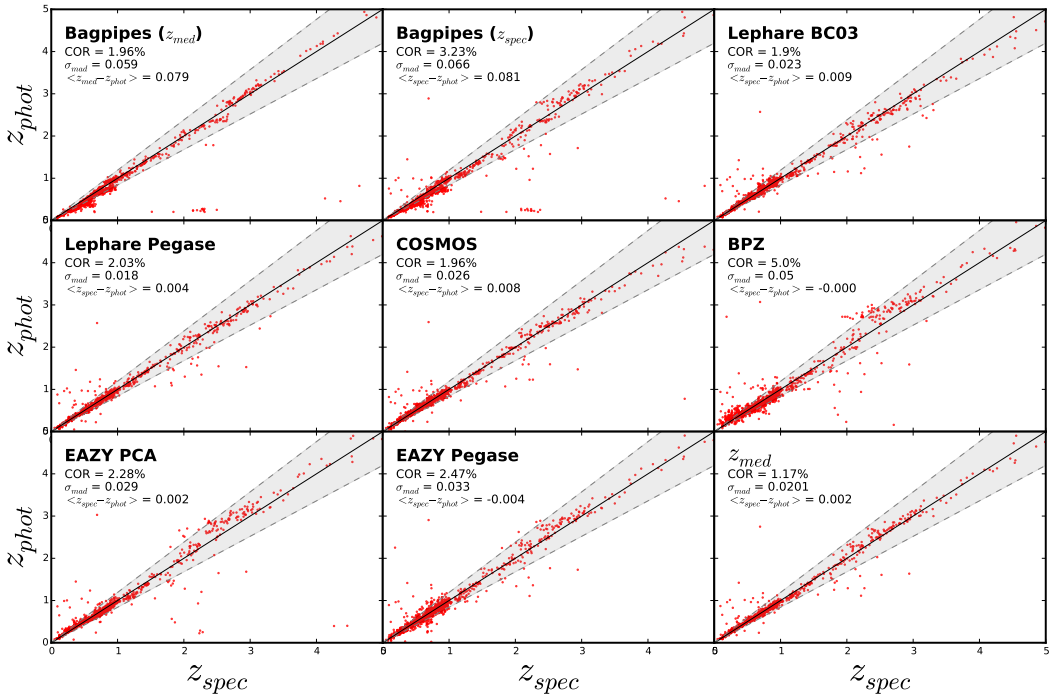

Figure 5.2 *Photometric redshift vs spectroscopic redshift calculated by* BAGPIPES *for the galaxies found in the COSMOS field. We also plot the photometric redshifts estimated by a number of independent runs, such as EAZY and LePhare. We also plot z_{med}, which represents the average photometric redshift found for each object. For each case, we print the calculated catastrophic outlier rate (COR), the σ_{MAD} and the mean offset between the spectroscopic and photometric redshift ($z_{spec} - z_{phot}$).*

stated, there were also 6 other photometric redshift tests completed using LePhare Pegase, LePhare BC03, LePhare COSMOS-SED, EAZY PCA, EAZY Pegase, and BPZ allowing for comprehensive comparison with the infered galaxy properties produced from BAGPIPES.

Fig. 5.1 presents the derived photometric redshift estimations from BAGPIPES, along with all the previous runs for the same set of objects against the spectroscopic redshift in the UDS. We also plot the z_{med} which is the calculated median photometric redshift found by all previous photo-z runs (LePhare Pegase, LePhare BC03, LePhare COSMOS-SED, EAZY PCA, EAZY Pegase, and BPZ.) for our spectroscopic sample the UDS field. In general, BAGPIPES does very well in reclaiming the redshifts of the objects in the spectroscopic sample (*Top Middle Panel*), however, we do see that it tends to underestimate the redshift. This is quantified by the average offset printed in each panel ($z_{spec}-z_{phot}$), in this scenario, the higher this value than the larger the underestimation. BAGPIPES produces a

larger $z_{spec} - z_{phot}$ by approximately a factor of two or three in comparison to the other SED-fitting codes. The catastrophic outlier rate (COR) is good at around $\simeq 3.70\%$ when compared with the spectroscopic sample, however it appears to be very consistent with the median redshift for all the other photometric redshift calculations (*Top Left Panel*) where the COR is $\simeq 1.78$ %, albeit with a slightly larger $\sigma_{MAD} = 0.051$. This general underestimation of the redshift causes a slight underestimation of the reclaimed stellar mass of the galaxy sample. It is important to note that the data has been trained to the spectroscopic redshift where we have calculated the zero-point photometric offsets for each filter and applied a small flux increase or decrease to the respective photometry point.

Fig. 5.2 presents the photometric redshifts inferred using Bagpipes, along with all the previous runs for the same set of objects against the spectroscopic redshift in the COSMOS field. Similarly to the UDS galaxies, we see that Bagpipes performs relatively well when reclaiming the redshifts of the spectroscopic objects (*Top Left Panel*) producing a COR of $\simeq 3.23\%$ with a $\sigma_{MAD} = 0.66$. Interestingly, in COSMOS, Bagpipes does not appear to generally underestimate the redshift of the spectroscopic sample, certainly not as prominently as in the UDS sample. This is shown by the slightly lower values of $z_{spec} - z_{phot}$ in comparison to Fig 5.1. Interestingly, also comparing the other SED-fitting codes to Fig 5.1 we can se that the offset values also decrease, indicating that this feature is likely to be a result of the different filter sets available in the UDS and COSMOS. Like the UDS, in COSMOS Bagpipes also appears to match the z_{med} well, providing a COR of $\simeq 1.96\%$ with a corresponding $\sigma_{MAD} = 0.059$.

5.2.5 UV/optically/near-IR Selected Dusty Galaxies (Gold, Silver and Bronze)

The UDS and COSMOS mass-cut samples comprise $\simeq$ 180,000 galaxies making it incredibly computationally expensive to run Bagpipes on the entire catalogue, across the full parameter space (7 free parameters). In order to cut down the sample further and highlight the likely dusty, massive, high-redshift objects of interest here, an initial set of runs was completed over a smaller region parameter space. The sample was fit with only five free parameters; the redshift (z), stellar mass (M_*), dust obscuration (A_V) and an exponential star-formation history (τ, T). The first SED fit to the photometric data limited the redshift to between $1.5 < z < 8$, while the dust obscuration had a minimum $A_V > 2.0$. The second

Run	Parameter	Description	Range
Run 1	M_*	Stellar Mass	$0 < \log_{10}(M_*/\mathrm{M}_\odot) < 14$
	z	Redshift	$1.5 < z < 8$
	A_V	Dust Obscuration	$A_V/\mathrm{mag} > 2.0$
	τ	Timescale	$-10 < (\tau/\mathrm{Gyr}) < 10$
	T	Age of SFH	$0.001 < (T/\mathrm{Gyr}) < 15$
Run 2	M_*	Stellar Mass	$0 < \log_{10}(M_*/\mathrm{M}_\odot) < 14$
	z	Redshift	$0 < z < 1.5$
	A_V	Dust Obscuration	$A_V/\mathrm{mag} < 2$
	τ	Timescale	$-10 < (\tau/\mathrm{Gyr}) < 10$
	T	Age of SFH	$0.001 < (T/\mathrm{Gyr}) < 15$

Table 5.3 *The free parameters, and their allowed ranges used to initially fit our two photometric catalogues.*

SED fit fixed the redshift to the range $0 < z < 1.5$ and the dust obscuration was limited to a maximum of $A_V < 2.0$; the parameters are summarised for each run in Table 5.3.

Upon completion of the $\simeq$ 180,000 galaxy SED fits across both the UDS and COSMOS fields, we conducted a search for all objects that satisfy the following criteria. We only kept the galaxies that had an overall best-fit redshift $z \geq 1.5$, stellar mass $\log_{10}(M_*/\mathrm{M}_\odot) > 10.0$, and dust obscuration $A_V > 2.0\,\mathrm{mag}$, and also had a satisfactory fit with a $\chi^2 < 100$. Out of the $\simeq$ 180,000 galaxies in the UDS and COSMOS field, 1844 galaxies were left in the UDS while 3263 remained in the COSMOS sample. This is equivalent to $\simeq$ 3% of the population being classified as a galaxy of high mass, high redshift and high dust obscuration.

This $\simeq$ 6000 galaxy sub-sample was further sub-divided into three classes; 'Gold', 'Silver' and 'Bronze'. The 'Gold' sample contained all galaxies where a redshift $z > 1.5$ was the global maximum likelihood fit, corresponding to approximately 1034 and 2119 galaxies in the UDS and COSMOS respectively. 'Silver' represents the sample of galaxies that have a maximum of $\Delta\chi^2 \leq 9.0$ for the $z \geq 1.5$ solution, producing a sub-sample of 295 and 437 galaxies in the UDS and COSMOS fields respectively. The final sub-category, 'Bronze', highlights the galaxies where, although the maximum likelihood solution may not lie in high-redshift $z > 1.5$ region, there was still a significant portion of the posterior distribution lying at $z > 1.5$, with a $\Delta\chi^2 > 9.0$. The 'Bronze' sample was therefore not entirely ruled

Parameter	Description	Range
M_*	Stellar Mass	$0 < \log_{10}(M_*/\mathrm{M}_\odot) < 14$
z	Redshift	$0 < z < 10$
A_V	Dust Obscuration	$0 < A_V/\mathrm{mag} > 10$
Z	Metallicity	$0 < Z_{dpl}/\mathrm{Z}_\odot < 3$
α_{dpl}	Falling Slope	$0.1 < \alpha_{dpl} < 1000$
β_{dpl}	Rising Slope	$0.1 < \beta_{dpl}/ < 1000$
τ_{dpl}	Turnover	$0.1 < (\tau_{dpl}/\mathrm{Gyr}) < t_{obs}$

Table 5.4 *The free parameters, and their allowed ranges, used to build the SED library within* Bagpipes *for fitting to the COSMOS and UDS galaxy photometry.*

out, where opening the parameter space might enable the high-redshift solution to become more favourable. The 'Bronze' sample contained a total of 1222 galaxies, 515 in the UDS and 707 in COSMOS.

Using Bagpipes, the finalised sub-samples of 'Gold', 'Silver' and 'Bronze' galaxies in COSMOS and UDS fields were SED fit to the population synthesis models of Bruzual & Charlot (2003) over a wide parameter space, as defined by Table 5.4. Bagpipes requires defined multiple-model parameterisation to fit against the observational data, with associated uncertainties. The user is required to define a prior probability distribution, describing the free parameters and limits for the fitting process. In this scenario we allow the range of galaxy redshifts to vary between $0 < z < 10$, the range in stellar mass was $0 < \log(M_*/\mathrm{M}_\odot) < 14$, the range in metallicity was $0 < (Z/\mathrm{Z}_\odot) < 3$, while fore dust obscuration the range was $0 < (A_V/\mathrm{mag}) < 10$. Effectively, we aimed to cover the widest possible parameter space within physically realistic limits. A double power law (dpl) star-formation history was used to fit the data, defined by three variables; the falling slope (α_{dpl}), rising slope (β_{dpl}) and turnover (τ_{dpl}). The functional form of the double power law is:

$$SFR(t) = \left[\left(\frac{t}{\tau_{dpl}}\right)^{\alpha_{dpl}} + \left(\frac{t}{\tau_{dpl}}\right)^{-\beta}\right]^{-1} \tag{5.1}$$

The SFH parameters were allowed to vary over the widest possible range, where the falling (α_{dpl}) and rising (β_{dpl}) slopes were both varied between $0.1 < \alpha_{dpl}$ or $\beta_{dpl} < 1000$, respectively, while the turnover (τ_{dpl}) is limited to the maximum

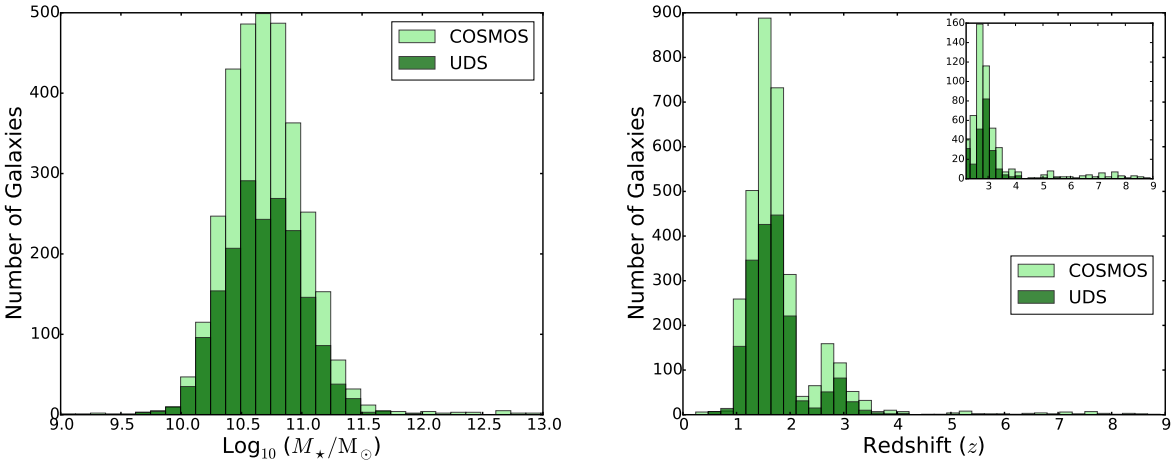

Figure 5.3 **Left Panel** *The fitted mass distirbution for our subset of 'dusty' galaixes within the UVISTA catalogue. These were galaxies selected with a high-mass and re-fitted to find the average stellar mass. We show both the samples within the COSMOS (light green) and UDS (dark green) CANDELS fields.* **Right Panel***: The redshift distribution for our 'dusty' sub-set of galaxies within our UVISTA catalogue of. We show both the COSMOS (light green) and UDS (dark green) CANDELS fields. The inset in the first panel provides a zoom-in of the galaxies with a redshift of $z > 2$.*

time of observation (t_{obs}) starting at 0.1 Gyr ($0.1 < (\tau_{dpl}/\mathrm{Gyr}) < t_{obs}$). More information about the star-formation histories utilised within BAGPIPES and how they are implemented can be found in Carnall et al. 2018b.

5.3 Results

5.3.1 Gold, Silver and Bronze Sample results

Figures 5.3 and 5.4 show the stellar mass, redshift and dust distributions for the 1844 galaxies in the UDS (dark green) and the 3263 galaxies in the COSMOS (light green) sample, respectively. These distributions present the UDS+COSMOS 'Gold', 'Silver' and 'Bronze' galaxies fitted across the entire parameter space with BAGPIPES; see Table 5.4

The mass distribution (Fig. 5.3, left panel) is consistent in shape across both the UDS and COSMOS fields, showing a peak stellar mass of approximately $M_* \simeq 10^{10.75}\mathrm{M}_\odot$, with the COSMOS field extending to the highest stellar masses of $M_* \simeq 10^{12}$ - 10^{13} $\mathrm{M}_\odot$. This may be a consequence of the slightly larger

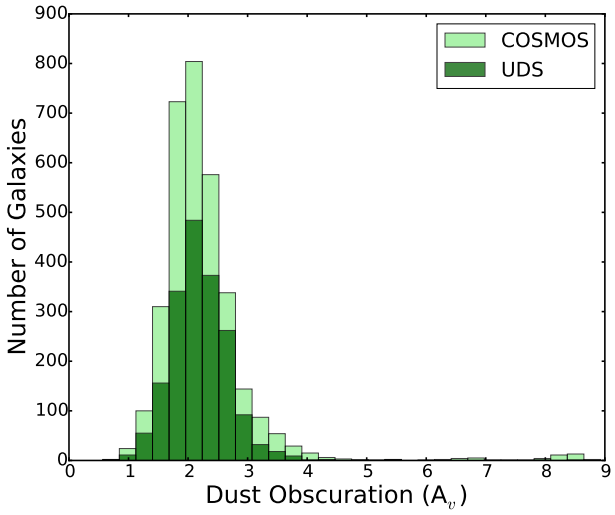

Figure 5.4 *The fitted dust obscuration distribution for our 'dusty' subset of galaxies from the UVISTA catalogue in the COMSOS (light green) and UDS (dark green) CANDELS fields.*

coverage in the COSMOS field, being approximately double the size than the UDS. Therefore the COSMOS field is more likely to detect the rare high-mass galaxies at both high and low redshift. In addition, the UDS and COSMOS have redshift distributions (Fig. 5.3, right panel) consistent in shape with one another where both have 2 peaks at approximately $z \simeq 1.5$ and $z \simeq 2.6{-}2.9$. Interestingly, COSMOS appears to detect the bulk of the high redshift galaxies in the sample. This again, is a consequence of having a wider area compared to that of the UDS field, giving COSMOS an ability to detect the more rare high redshift galaxies. We see a similar trend with the dust obscuration distribution (Fig. 5.4). The peak dust obscuration sits at a peak A_V approximately $\simeq 2.1$ mag for the UDS and COSMOS field, extending with significant numbers up to $A_V \simeq 4$. The COSMOS field then takes over, being the only field with the ability to detect galaxies with a dust obscuration $A_V > 4$.

In total, approximately $\simeq 3900$ galaxies that were fit with BAGPIPES would have classified themselves in the same category as the independent code run prior to the entire sample SED fit. This provides a nominal surface density for high mass ($M_* > 10^{10}\mathrm{M}_\odot$, high redshift ($z > 1.5$), dusty ($A_V > 2.0$) galaxies equalling $\simeq 2590/\mathrm{deg}^2$. This is equivalent to approximately $\simeq 0.72/\mathrm{arcmin}^2$ or $\simeq 90$ high-mass, high-redshift, dusty galaxies in a 125 arcmin^2 field, a similar area coverage to that of GOODS-S/GOODS-N. If the definition of a 'dusty' galaxy is increased to a minimum dust obscuration of $A_V > 3.0$ mag, the total number of

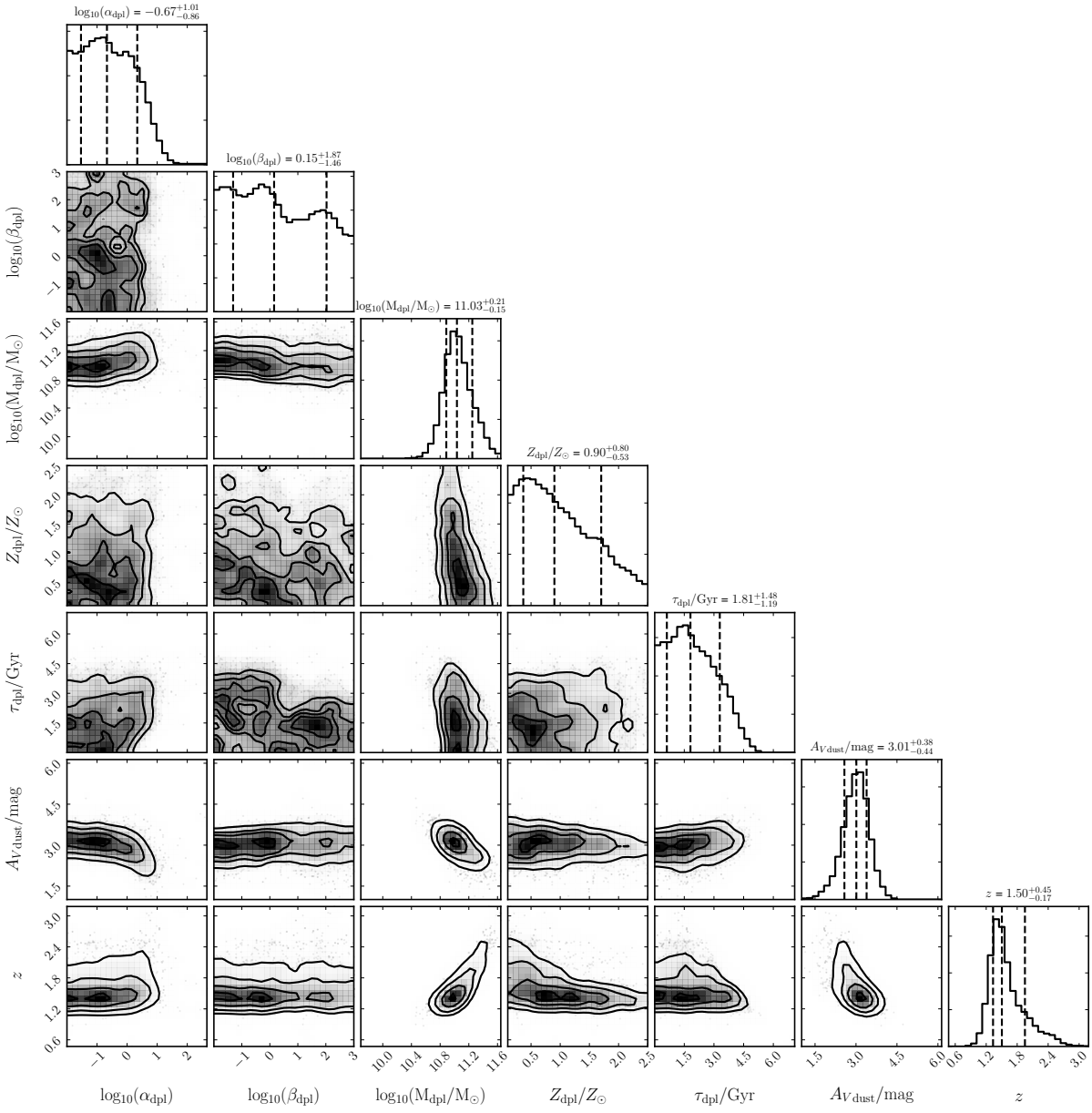

Figure 5.5 *The corner-plot of an example galaxy (selected at random) presenting the resulting posterior distributions of all seven free parameters described in Table 5.4 We also show the inferred age, SFR and SFH. The dashed lines in each panel represent the posterior median along with the ±1-σ solutions.*

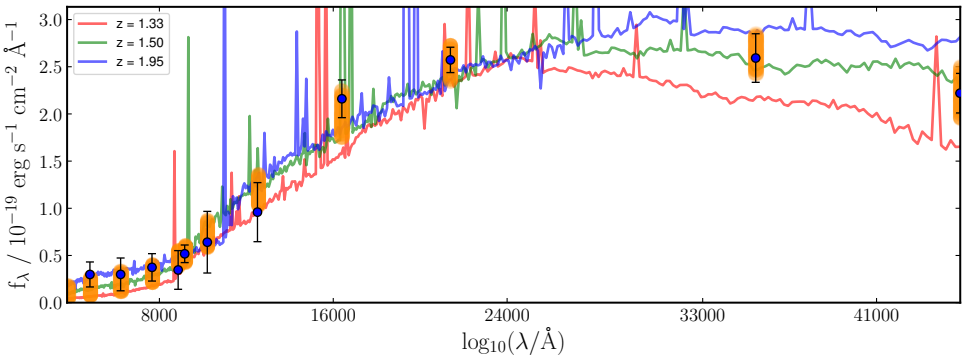

Figure 5.6 *The example galaxy photometry (blue points with error-bars), along with the* Bagpipes *SED fits to the data. The green line represents the SED extracted from the posterior medians of each distribution, in this case, at redshift $z \simeq 1.50$. The red and blue lines show the corresponding -1-σ and $+1$-σ SEDs respectively. In this case, the blue line corresponds to a high-redshift solution (at $z \simeq 1.95$, close to the true value), while the red line corresponds to a low-redshift solution (at $z \simeq 1.33$, close to the stronger low-redshift peak seen in the redshift corner plot)*

dusty galaxies reduces to 540 across both the UDS and COSMOS fields. This dramatically reduces the surface density of dusty galaxies to approximately 365 galaxies/deg^2 or 0.1/arcmin^2, leaving approximately 13 galaxies across an the area of a GOODS-S/GOODS-N field.

When comparing these numbers to the total number of galaxies found in the Empirical Galaxy Generator (EGG v.1.1.0; Schreiber et al. 2017), there were no galaxies with a dust obscuration with an $A_V > 3.0$ across the entire 1.2 deg^2 simulated field. This work shows that there should be a few hundred. When comparing the $A_V > 2.0$ sample, EGG contains a total of 1311 galaxies in the full 1.2 deg^2 field equalling a density of $\simeq 1092$/deg^2. Again, converting to arcmin, EGG has a surface density of $\simeq 0.303$/arcmin^2 providing a total of $\simeq 35$ high mass dusty galaxies in a GOODS-N/GOOD-S field. It is therefore clear that EGG drastically underestimates the total number of dusty galaxies by almost a factor of 3.

Figures 5.5 and 5.6 show an example (object ID - 5073) of using Bagpipes to fit the photometric data of a galaxy from the UDS sample (Table 5.2). The first figure shows the posterior distributions and contour plots for all the fitted free parameters described in Table 5.4. Included in the corner plots are three dashed lines highlighting the posterior median (middle dashed line) and $\pm 1\sigma$ solutions fitted for all free parameters. In this case, we have a reasonably tight fit to the

data, where the posterior distributions tend to be relatively sharply peaked for the stellar mass (M_*), redshift (z) and dust obscuration (A_V) centred on $M_* = 10^{11}$, z=1.50 and $A_V = 3.0$ mag, respectively. This galaxy is therefore consistent with the categorisation of a 'Gold' galaxy, representative of the general 'Gold' galaxies found in our sample.

In Fig. 5.6, we present the median and ±1-σ best-fit SEDs to the photometric data for the same galaxy. The blue points represent the raw photometry (with black error bars), while the orange shaded region depicts the photometric posterior distribution. Three SEDs are shown, with the red, green and blue SEDs representing the best fitting SEDs for the posterior median (green) and ±1-σ (blue and red, respectively). These can be matched to the dashed lines on the posterior distribution found in the corner plot (Fig. 5.5. the blue line is a $z \simeq 1.95$, $M_* \simeq 10^{11.24}\,M_\odot$, $A_V = 2.57$ mag galaxy, while the green line represents the median $z = 1.55$, $M_* = 10^{11.03}\,M_\odot$, $A_V = 3.01$ mag SED fit, and the red line is a $z = 1.33$, $M_* = 10^{10.88}\,M_\odot$, $A_V = 3.39$ mag galaxy. This SED is typical of that displayed by the galaxies found in our 'Gold' and 'Silver' samples.

The possible SEDs are largely constrained by the rest-frame UV/optical data, blue-ward of 24000Å. Beyond this wavelength range, the scatter increases where we see the poorer sensitivity of the first two *Spitzer* IRAC channels, 3.6μm and 4.5μm allowing for a larger range of potential SED fits to the photometric data. The plausible SEDs that fit the data effectively allow the inferred physical properties to extend to vastly different values. The redshift can now be fit to a redshift range $\Delta z = 0.62$, a relatively large disparity for a $z \simeq 1.5$ galaxy.

If we compare this object to the simulated BC03 galaxy in Chapter 4, (Section 4.5.2, Fig. 4.5), these two objects have a very similar shaped SED, albeit, the simulated BC03 galaxy has a higher redshift ($z \simeq 5$). If, however, one were to increase the redshift of object 5073 to that of the of the simulated BC03 galaxy, from Chapter 4 the galaxies would overlap rather well. The 3.6μm photometric data point would now be sitting at approximately $\simeq 8.5\mu$m, slightly blue-ward of the effective wavelength (λ_{effec}) of MIRI's 7.7μm filter. Observing object 5073 with a programme similar to that of the observing strategy described in Chapter 4, Section 4.4.3 it would be possible to secure the redshift, and therefore stellar mass and dust obscuration far more accurately. Effectively, object 5073 is a lower-redshift analogue of the simulated galaxy found in Chapter 4, Section 4.5.2 suggesting that these type of objects do exist and therefore will require MIRI observations to accurately estimate their physical properties.

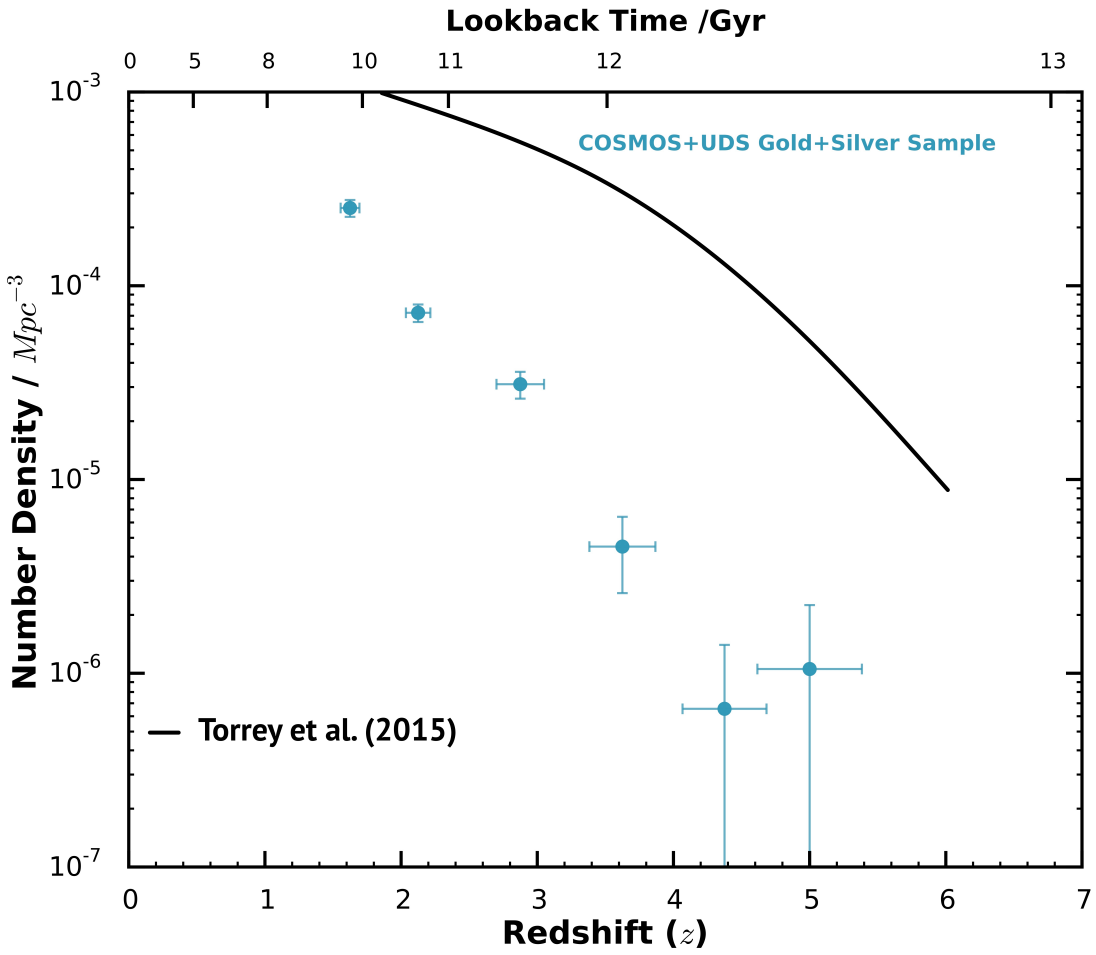

Figure 5.7 *The evolution of the comoving number density of all galaxies within both the COSMOS and UDS field that are secruely identified as a high-mass, dusty and high-redshift galaxy falling within either our 'Gold' of 'Silver' sample as a function of redshift. We also plot the Loockback time on the upper x-axis, highlight how rapid the number density declines over cosmic time. For comparison to the literature, we show the comoving number density predicted by Conselice et al. (2016) based on hydronamical simulations from Torrey et al. (2015).*

Fig. 5.7 shows the comoving number density for all galaxies within the UDS and COSMOS 'Gold' and 'Silver' samples as a function of redshift. We have calculated the number density by counting the number of galaxies in a redshift bin and dividing by the volume of the selected bin, given by the difference in comoving volumes at the upper and lower redshift boundary, scaled to the sampled sky area. To calculate the volume of each redshift bin, we have assumed the combined area of the COSMOS and UDS field with UV/optical coverage of $\simeq 1.5$ deg^2. We have binned by redshift to a maximum $z = 5.5$ ($1.5 < z < 1.75$, $1.75 < z < 2.5$, $2.5 < z < 3.25$, $3.25 < z < 4.0$,$4.0 < z < 4.75$, $4.75 < z < 5.25$), cutting any galaxies that have a redshift below $z < 1.5$ and above $z > 5.5$. This means the bin size is $\Delta z = 0.75$ for all but the first redshift bin where we have selected a finer bin width of $\Delta z = 0.25$. The comoving number density rapidly decreases with increasing redshift, decreasing by over 2 orders of magnitude from $z \simeq 2$ to $z \simeq 4$. In terms of timescale, that is equivalent to about 2 billion years of cosmic time. As the sample is mass-selected, it is inevitable to observe a drop in number density, as the underlying mass function decreases with redshift. Therefore, in order to interpret the drop in number density for dusty objects, we compare our results to the comoving number density for all galaxies with a stellar-mass $M_* \geq 10^{10}\,\mathrm{M}_\odot$ predicted by Conselice et al. (2016) based on hydrodynamical simulations (Illustris) from Torrey et al. (2015), plotted in black. It is clear, therefore, that high-mass, dusty galaxies become very rare at high redshift, consistent with current literature which suggests that dusty galaxies only start to dominate the total star-formation at $z < 4$ (e.g. Dunlop et al. 2017; Koprowski et al. 2017 and Bourne et al. 2017). This is direct contrast to the results of Gruppioni et al. (2013) and Rowan-Robinson et al. (2016) who suggest that the number density of the dusty galaxy population detected in the far-IR stays relatively constant even out to extreme redshifts.

5.4 ALMA Selected Dusty Galaxy Sample

The Atacama Large Millimetre/sub-millimetre Array (ALMA) is a facility capable of studying the dusty star-forming galaxies out to the highest redshifts. Like the James Clerk Maxwell Telescope (JCMT, Scott et al. 2002, 2006; Geach et al. 2013), ALMA studies the far-IR/sub-mm and mm region of the electro-magnetic spectrum uncovering the recycled UV light absorbed and re-emitted/scattered from galaxies enshrouded by dust. Being able to build a link between the optical,

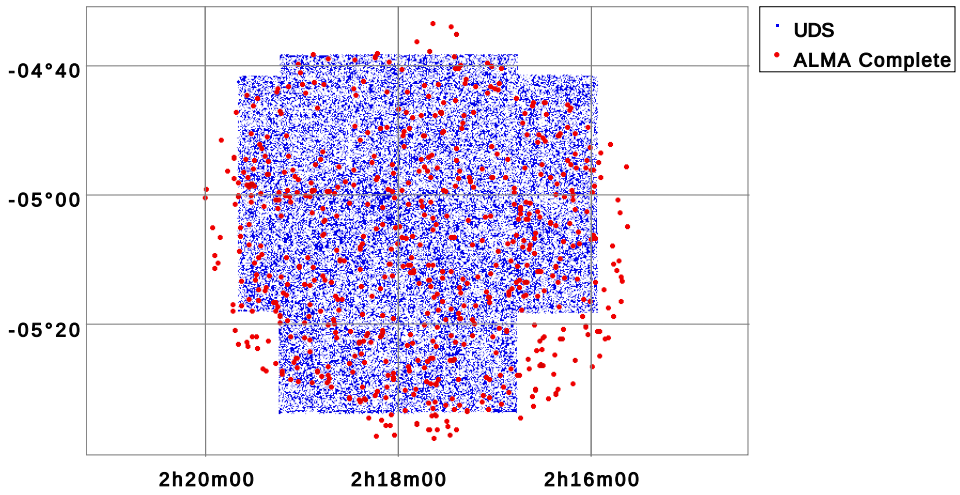

Figure 5.8 *The UDS (UV/optical+IR) and all ALMA detected galaxies (>2mJy) in our catalogue are represented by the blue and red points respectively. The UDS catalogue comprises near-IR imaging from the UDS DR11 release, with optical data from SXDS (Subaru-XMM-Newton Deep Survey) and IRAC imaging taken from S-CANDELS. The UDS (UV/optical+IR) comprises ≃ 70,000 galaxies, while the ALMA catalogue contains ≃ 700 galaxies.*

UV, near/mid/far-IR and mm region of the spectrum is vital in allowing us to understand the complete picture of cosmic star-formation history and the physical mechanisms that drive galaxy formation.

In this work we utilise data from the ALMA SCUBA-2 Ultra Deep Survey (AS2UDS), an 870-μm continuum survey with ALMA imaging 685 single-dish sub-millimetre sources detected in the UKIDSS/UDS field by the SCUBA-2 Cosmology Legacy Survey (S2CLS); see Michałowski et al. (2017) and Stach et al. (2019) for more detailed information. AS2UDS is a high resolution sub-millimetre interferometric follow-up survey of 850-μm sources initially discovered in the SCUBA-2 survey across the entirety of the UDS field ($\simeq$ 1 deg^2). The data were acquired over a number of ALMA cycles (1,3,4 and 5) observing all 685 SCUBA-2 sources which were detected at 4σ.

The resulting ALMA catalogue (685 objects) map is shown in Fig. 5.8, depicted by the red points. The underlying blue points show the full UDS UV/optical+near-IR footprint for our $M_* > 10^{9.5}$M$_\odot$ sample described in Section 5.2.2, equivalent to $\simeq$ 70,000 galaxies. As we can see, the ALMA coverage extends well beyond the area of the shorter wavelength imaging requiring a cut to be made in order to highlight the galaxies that have matching optical, UV, near-IR and sub-mm detections. This was done by matching the RA and Dec for all objects to within

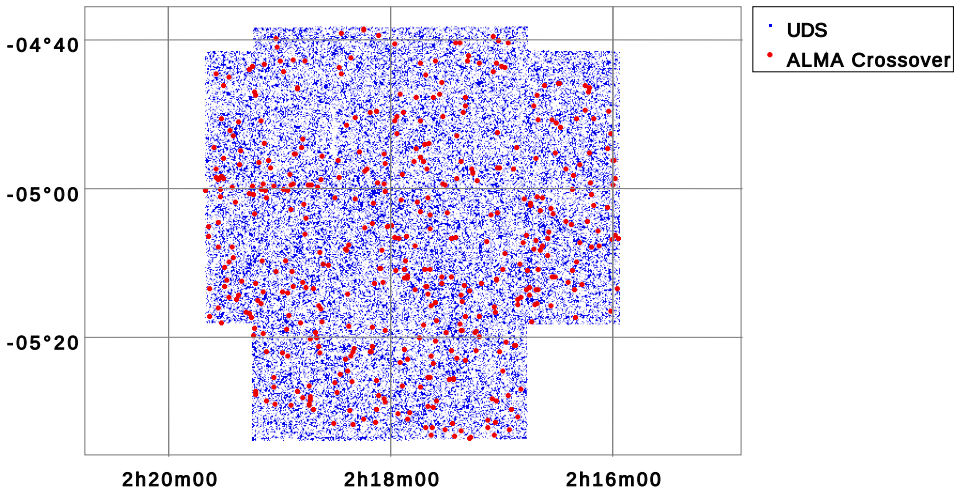

Figure 5.9 *The refined galaxy catalogue where there is both UDS and ALMA detections, again represented by the blue and red points respectively. In-total, I have ≃ 450 galaxies that are have both UV/optical+NIR and ALMA detections, matched by their respective RA and Dec to within a 1 arcsecond accuracy.*

an accuracy 1 arcsec. The resulting data-set is shown in Fig. 5.9, containing only 455 of the original 685 sample. This reduction in numbers is largely down to exclusion of the objects lying out-with the UV/optical+near-IR coverage.

In addition to matching the ALMA detection to our entire ≃ 70,000 galaxy UDS catalogue, we also matched the ALMA-detected galaxies to our 'Gold', 'Silver', and 'Bronze' samples, aiming to assess the total overlap in the methodology of discovering high-mass dusty galaxies. In total 120 ALMA galaxies were found to overlap with the 'Gold' sample, but none were found in the 'Silver' or 'Bronze', giving an overlap percentage of approximately ≃ 26% (arguably somewhat lower than expected). As the 'Gold' sample effectively rules out any galaxies below $z < 1.5$, $M_* < 10^{10} M_\odot$ and dust obscuration $A_V < 2.0$, it may be the case that these ALMA detected galaxies fall under one of these criteria by a small margin. Therefore, the remaining 75% of the ALMA detected galaxies were SED-fit with Bagpipes using the same fitting parameters described in Section 5.2.5 and Table 5.4.

The sample properties are plotted in Figures 5.10 and 5.11. Fig. 5.10 shows the mass distribution in the left panel and the redshift distribution in the right panel, where the light green histogram represents the inferred properties of the 455 ALMA detected galaxies explained above. The darker green histogram highlights the galaxies that overlap with our 'Gold' sample. When comparing with the

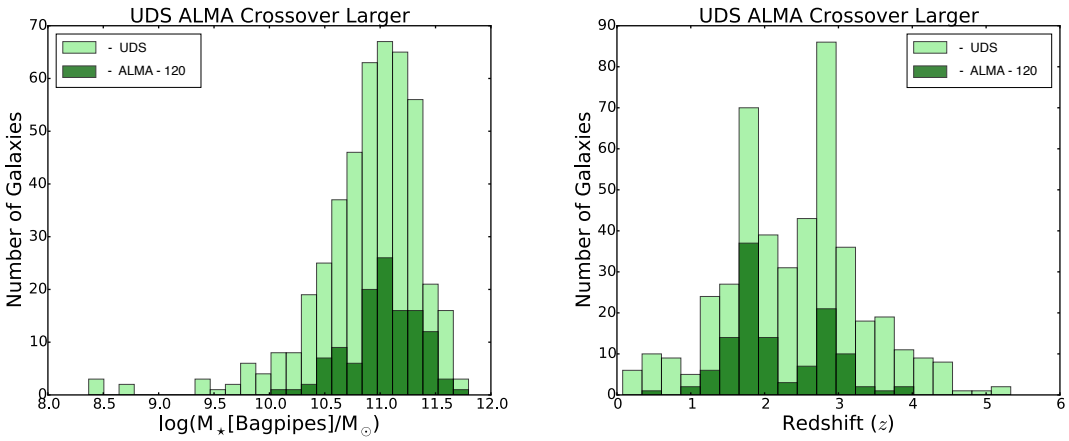

Figure 5.10 **Left**: *The mass distribution inferred from* Bagpipes *for our ALMA galaxy sampl. The light green represents the entire ALMA (>2mJy) galaxy catalogue (455 galaxies), while we also plot the sub-set of galaxies that fall into our 'Gold' galaxy sample in the UDS field.* **Right**: *The redshift distributions for our ALMA galaxy sample and the corresponding crossover with our 'Gold' galaxy catalogue in the light green and dark green respectively.*

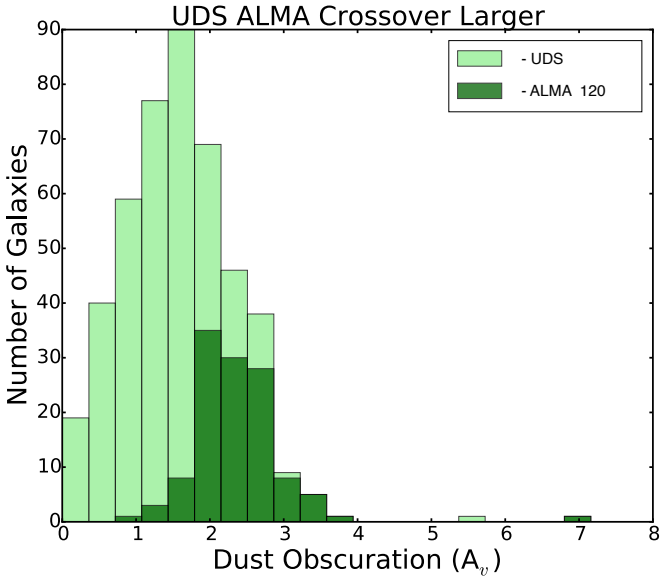

Figure 5.11 *The A_v distribution inferred from* Bagpipes *for our ALMA galaxy sample, the light green represents the entire ALMA (>2mJy) galaxy catalogue (455 galaxies), while we also plot the sub-set of galaxies that fall into our 'Gold' galaxy sample in the UDS field. It is clear that the 'Gold' sample has picked up the majority of the dustiest set of objects from our ALMA catalogue*

original COSMOS and UDS distributions (Fig. 5.3, 5.4) we see a significant shift in the peak of the stellar mass and redshift distribution. The stellar mass peak has shifted from $M_* \simeq 10^{10.75}\mathrm{M}_\odot$ to $M_* \simeq 10^{11.15}\mathrm{M}_\odot$. The dual-peaked redshift distribution also shifts to slightly higher redshifts $z \simeq 1.8$ and $z \simeq 2.9$ - 3.0.

As expected, the 'Gold' sample sits at the massive end of the ALMA mass distribution containing no galaxies $M_* < 10^{10}\mathrm{M}_\odot$. However, we do see that a number of ALMA galaxies fall below the redshift cut for our 'Gold' sample. What is also clear is that, when re-fitting over the full parameter space, Bagpipes fits a redshift for some of the objects in the 'Gold' sample to be lower than $z < 1.5$ and although this is a relatively small number of objects it can partly explain why we see the lack of overlap between the 'Gold' and ALMA galaxy samples.

Fig. 5.11 shows the inferred dust obscuration estimated from Bagpipes, again plotting both the entire ALMA sample (455 galaxies) and the subset of galaxies that fall into the 'Gold' category in the light and dark green, respectively. The initial categorisation of the Gold sample, in general, picks up the majority of the dusty galaxies for which we also have ALMA detections. However, there does also appear to be a number of galaxies detected by ALMA that fall beneath the dust obscuration cut-off $A_V > 2.0$ mag, again giving a potential explanation as to why the overlap only sits at approximately $\simeq 26\%$.

5.5 ALMA UDS Results

In Fig. 5.12 we plot the Bagpipes-inferred dust obscuration (A_V) for all UDS galaxies as a function of the inferred stellar mass ($\log(M_*[\mathrm{fit}]/\mathrm{M}_\odot)$. We colour-code by which category the galaxies fall into, either Gold', Silver' or 'Bronze'. In addition, the ALMA sample is over-plotted in order to highlight which galaxies have ALMA detections; this is represented by the green points. The left panel presents all UDS + the 455 ALMA detected galaxies, while the right panel plots only the ALMA galaxies that have been identified as part of the 'Gold' sample (120 galaxies) and therefore are UV/optically selected dusty, high-mass high-redshift galaxies.

This plot illustrates the effectiveness and accuracy with which we have created the 3 samples of high-mass, dusty and high-redshift galaxies. The galaxies were categorised independently, as explained in Section 5.2.5, where 'Gold' was selected

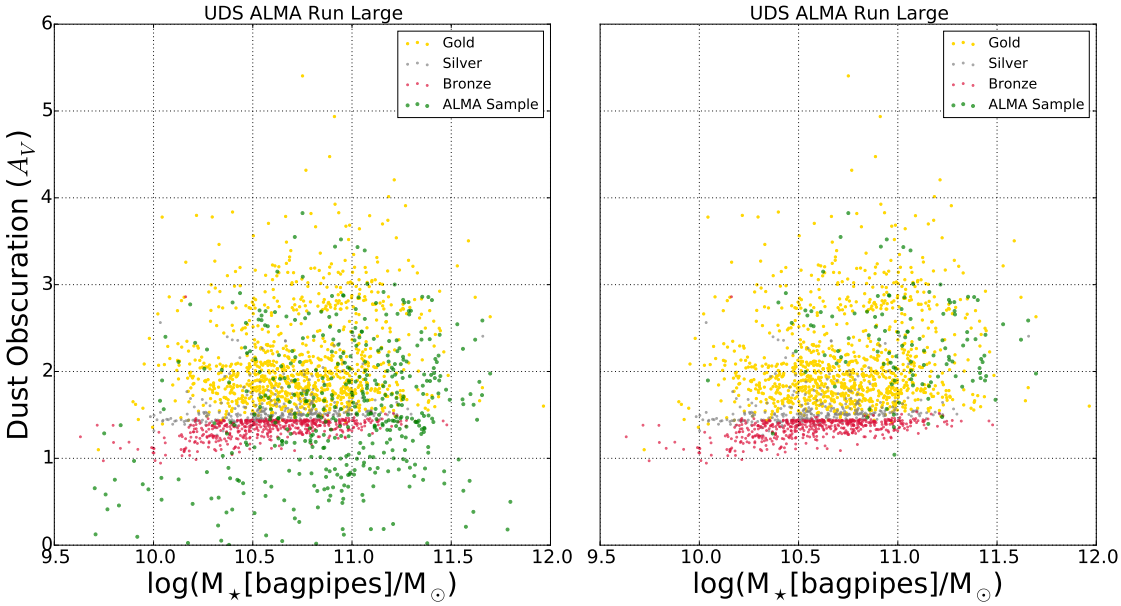

Figure 5.12 *Dust obscuration (A_V) as a function of stellar mass ($\log(M_*[fit]/M_\odot)$) for the 'Gold', 'Silver', 'Bronze' and ALMA galaxy catalogues. In the left panel, we show the entire 455 ALMA galaxy sample represented by the green points, while on the right panel, we only plot the ALMA galaxies that also fall into our 'Gold' sample (120 galaxies).*

on the basis of a maximum-likelihood solution of $z > 1.5$ with a minimum dust obscuration of $A_v > 2.0$ and minimum stellar mass ($\log_{10}(M_*/\mathrm{M}_\odot) > 10$) with 'Silver' and 'Bronze' containing galaxies with hierarchal lower likelihoods. However when re-fit over a wider parameter space with a different SED fitting code (BAGPIPES) we recreate the distinct tiers in the classification of the object. From Fig. 5.12, it is clear that BAGPIPES also selects the 'Gold' sample as the most massive and dusty subset of galaxies from the UDS catalogue with the 'Silver' sample being slightly less massive and dusty and the 'Bronze' containing the galaxies with the lowest level of dust obscuration and stellar mass.

Comparing the two plots, it is clear as to why the overlap between the ALMA detected galaxies and the 'Gold' sample is smaller than perhaps expected. The 'Gold' sample is defined as any galaxy with a good redshift solution of $z > 1.5$ with a minimum stellar mass ($\log_{10}(M_*/\mathrm{M}_\odot) > 10$) and dust obscuration ($A_V > 2.0$). In the first panel, we see a number of objects lying well below the dust obscuration limit, where as on the right hand side, the majority of detected ALMA galaxies fit within/near to the criteria explained above.

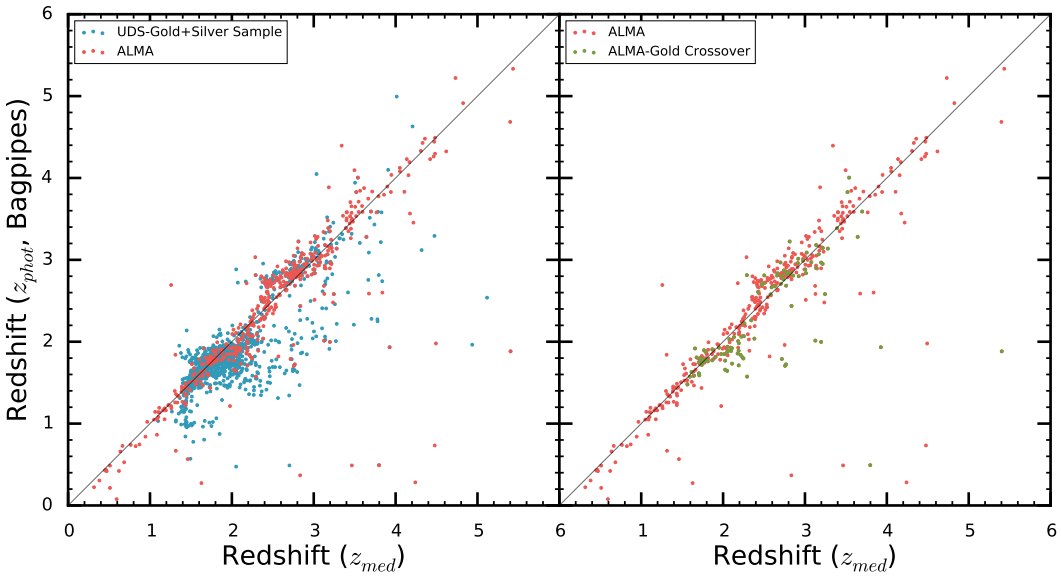

Figure 5.13 **Left Panel**: *The photometric redshift estimated by* Bagpipes *vs the average photometric redshift inferred independently utilising 8 different photometric redshift codes, including EAZY and LePhare, for our ALMA detected UDS galaxies. We plot both the full UDS 'Gold'+'Silver' sample of 1329 galaxies (blue points) with the 455 ALMA detected galaxies overplotted with the red points.* **Right Panel**: *We plot the same 455 detected ALMA galaxies with red points but also highlight the 120 galaxies selected from the UDS 'Gold' + 'Silver' sample that also have an ALMA detection.*

In Fig. 5.13, we show the photometric redshift estimated by Bagpipes as a function of the median photometric redshift estimated by the series of SED fits ran independently using LePhare Pegase, LePhare BC03, LePhare COSMOS-SED, EAZY PCA, EAZY Pegase, and BPZ. The left panel plots the photometric redshift as a function of the median photometric redshift for the 1329 UDS 'Gold'+'Silver' galaxy sample (blue points) and the 455 ALMA detected galaxies (red points). The right panel plots the same 455 ALMA detected galaxies (red points) as the left hand panel, however we also highlight the 120 galaxies that are included in both the UDS UV/optical 'Gold'+'Silver' and the ALMA detected sample, represented by the dark green points.

This plot confirms that Bagpipes recovers the redshifts relatively well and in good agreement with the previous independent SED fits. Interestingly, the ALMA galaxies perform very well, especially in comparison to the general population of the 'Gold'+'Silver' sample in the left panel (blue points). There could be a number of factors in play here. Firstly, the ALMA galaxies are generally of higher stellar mass producing the highest SNR in the optical and UV bands giving us an ability to reclaim the redshift more effectively. Secondly, the optical + UV selected galaxies are selected to have a high dust content and therefore there is an assumption of UV/optical attenuation most likely reducing the potential SNR capabilities in the blue filters. This in turn would make it far more difficult when estimating the redshift.

In the upper panel of Fig. 5.14 we plot the comoving number density as a function of redshift for all galaxies in the UDS 'Gold' + 'Silver' catalogue and all ALMA detected galaxies represented by the blue and red points, respectively. We have binned by redshift to a maximum $z = 5.5$ ($1.5 < z < 1.75$, $1.75 < z < 2.5$, $2.5 < z < 3.25$, $3.25 < z < 4.0$,$4.0 < z < 4.75$, $4.75 < z < 5.25$), cutting any galaxies that have a redshift below $z < 1.5$ and $z > 5.5$. To calculate the volume of each redshift bin, we have assumed the area of the UDS field with both UV/optical and ALMA coverage, equivalent to approximately $\simeq 0.8$ deg^2. The redshift errors are calculated from the average size of the ± 1-σ values in each redshift bin acquired from the SED fit of each galaxy, while we have added Poisson errors for the number density. In the lower panel, we plot the percentage overlap between the two samples (UDS 'Gold'+'Silver' and ALMA) as a function of redshift, with identical bins to the upper panel. The percentage overlap is defined as the fraction of galaxies with a minimum redshift of the minimum bin boundary selected in our UDS 'Gold'+'Silver' sample that also have an ALMA

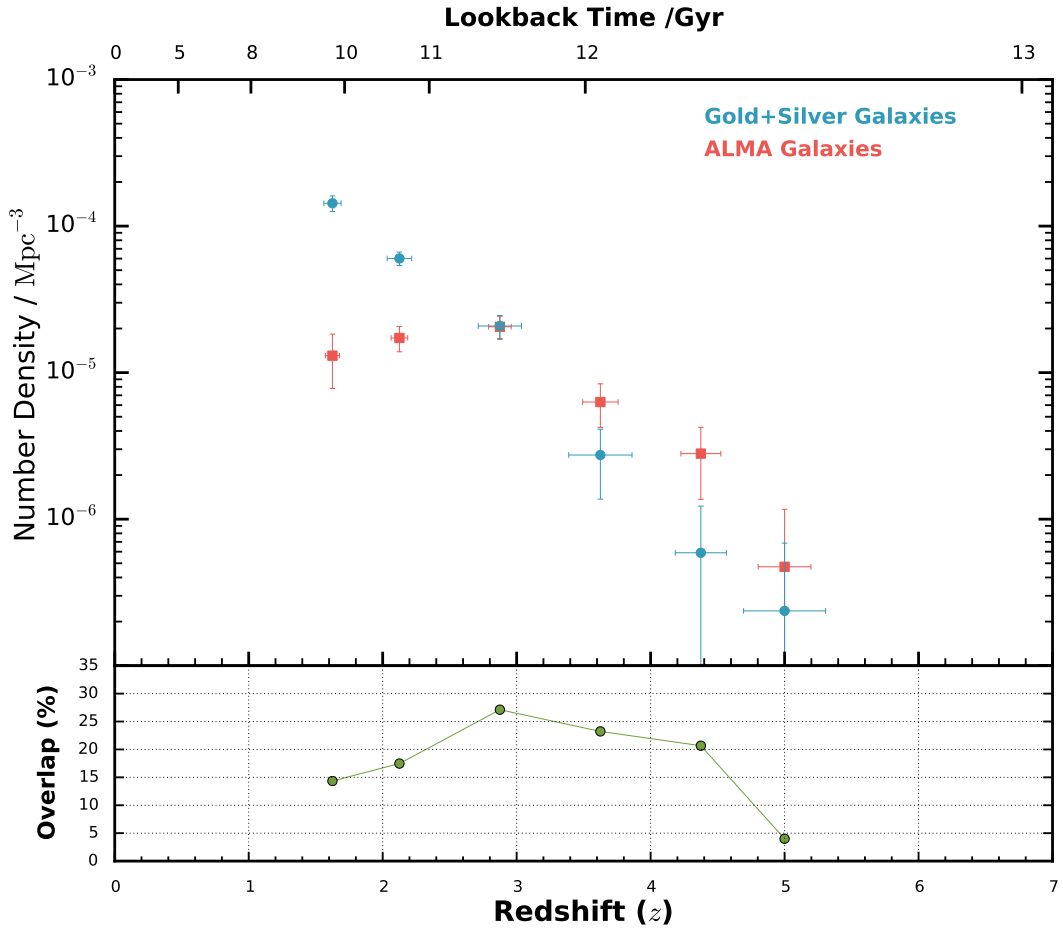

Figure 5.14 **Upper Panel**: *The evolution of the comoving number density for the ALMA galaxies (red points) and the entirety of the UDS 'Gold' sample (green points).* **Lower Panel**: *The percentage overlap of the UDS 'Gold' and ALMA samples. Essentially it defines the number of dusty galaxies from the UDS 'Gold' sample that has an ALMA detection in each redshift bin* ($1.5 < z < 1.75$, $1.75 < z < 2.5$, $2.5 < z < 3.25$, $3.25 < z < 4.0$,$4.0 < z < 4.75$, $4.75 < z < 5.25$).

detection.

In both cases, we see a steady decline in the (logarithm of) comoving number density as we extend to greater redshifts. It is clear that the number density of such dusty objects peaks at approximately $z \simeq 1{-}3$ for both the ALMA and the UV/optical selected galaxy samples with the ALMA sample peaking around $\simeq$2.5−3.5. This is consistent with other studies which indicate the sub-millimetre number density peaks at approximately $\simeq 2{-}3$ (e.g. Chapman et al. 2005; Wardlow et al. 2011). Prior to $z \simeq 2$, the UV/optically selected galaxies continue to rise sharply in number density, while the number density of the ALMA selected galaxies plateaus. The rate of decline is extremely sharp for both galaxy samples beyond $z > 3$, where in the space of $\simeq 1$ Gyr ($3 < z < 5$), the number density of dusty galaxies drops by nearly two orders of magnitude. Dusty galaxies become far rarer at higher redshifts, regardless of whether they are selected by the extinction of UV/optical radiation or detecting the dust emission. The average ± 1-σ values for each redshift bin (x-axis error bars) is significantly lower (smaller) for the ALMA-detected sample in comparison to the UV/optically selected sample. This demonstrates the more accurate photometric redshifts inferred from BAGPIPES for the ALMA sample (see Fig. 5.13).

The overlap between the two galaxy samples at redshift $1.5 < z < 2.5$ is only approximately 15-20%. This rises to a peak percentage overlap of $> 25\%$ at $z \simeq$ 2.5-3.5 as the comoving number density of the ALMA selected galaxies peaks. Beyond this redshift, the overlap appears to slowly decline as we increase in redshift. This indicates that the majority of the 120 UV/optically detected galaxies that have an ALMA detection lie in the intermediate redshift range, $2.5 < z < 4.5$. The relatively low percentage of overlap between the two samples is somewhat surprising as, intuitively, one might think that selecting dusty galaxies from UV/optical data would link closely to the detection of SMGs. This disparity in the overlap between the two methods of selecting dusty galaxies is explained largely from the relatively high cut-off of a minimum dust obscuration of $A_V > 2.0$ mag. Fig. 5.12 shows the dust obscuration as a function of inferred stellar mass and shows that a large number of ALMA galaxies do not have an apparent dust obscuration $A_V > 2.0$ mag and are therefore not making it into our final UDS 'Gold' and 'Silver' samples.

Fig. 5.15 shows the comoving number density as a function of redshift for all galaxies in the UDS 'Gold' + 'Silver' catalogue and all ALMA detected galaxies represented by the blue and red points, respectively. In this figure,

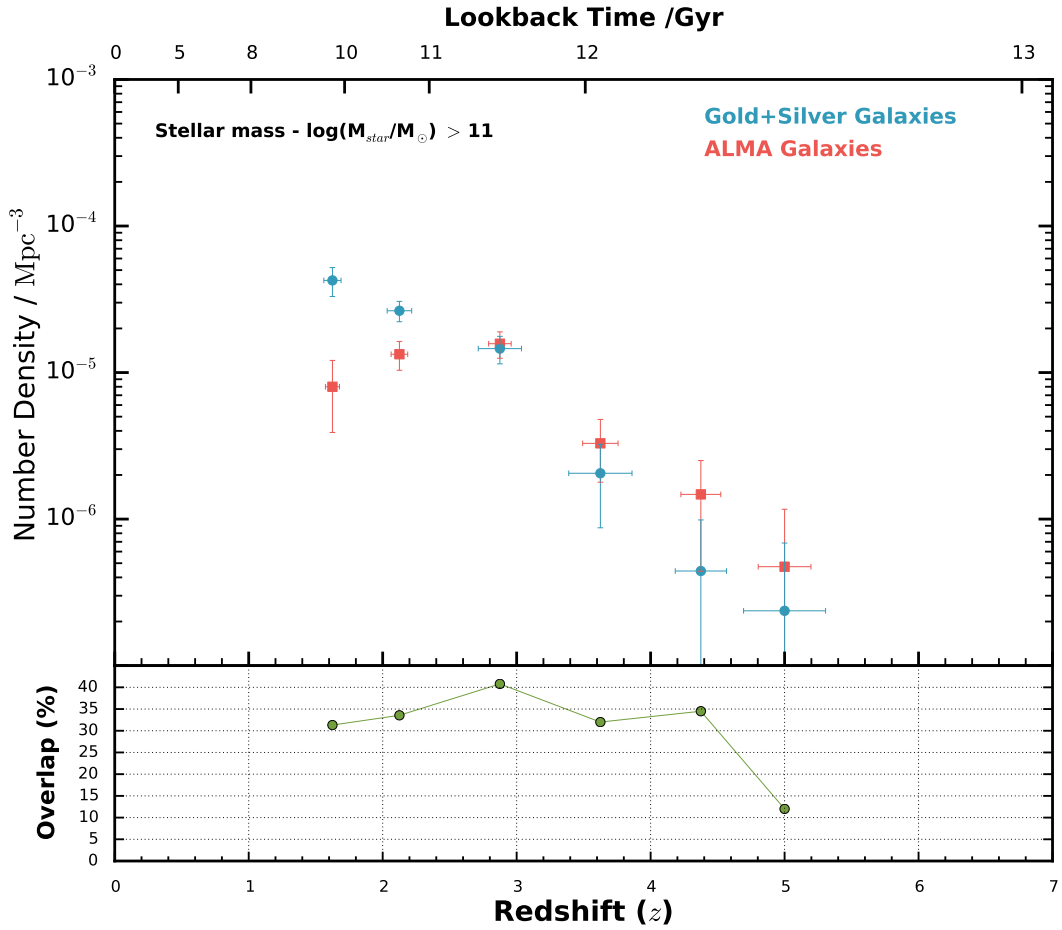

Figure 5.15 **Upper Panel**: *The evolution of the comoving number density for the ALMA galaxies (red points) and the entirety of the UDS 'Gold' sample (green points) with a stellar mass* $\log_{10}(M_*/\mathrm{M}_\odot) > 11$. **Lower Panel**: *The percentage overlap of the UDS 'Gold' and ALMA samples. Essentially it defines the number of dusty galaxies from the UDS 'Gold' sample that has an ALMA detection in each redshift bin (*$1.5 < z < 1.75$, $1.75 < z < 2.5$, $2.5 < z < 3.25$, $3.25 < z < 4.0$,$4.0 < z < 4.75$, $4.75 < z < 5.25$*).*

however, we have removed any galaxy in either sample that have a stellar mass $\log_{10}(M_*/\mathrm{M}_\odot) < 11$, leaving only the highest-mass objects in our catalogues. Again, we plot the percentage overlap between the two high-mass samples in the lower panel, represented by the green points.

Comparing this to Fig. 5.14, we see a similar trend in the decline of the two samples, in particular, the ALMA galaxies have a somewhat shallower decrease in the comoving number density as a function of redshift. Unsurprisingly there is an overall decrease in the comoving number density for all redshifts, however, the peak of the comoving number density is again consistent with previous studies, sitting at approximately $z \simeq 2$–3.5. We see a decrease in the number density for UV/optically selected dusty galaxies in the lower redshift bins in comparison to the ALMA selected galaxies, Another significant difference is apparent when looking at the respective overlap percentages. In the first scenario, we see a peak of approximately 25% at a redshift of $z \simeq 2.5$–3.5, while the mass cut sample produces a peak percentage overlap of approximately 40% at a redshift of $z \simeq 2.5$–3.5.

This could possibly be explained by different inclinations and morphologies of the ALMA selected and UV/optically selected galaxies. Potentially, the UV/optical galaxies could be more inclined and flatter suggesting that we calculate high A_V values when SED-fitting and we would, therefore, categorise more galaxies as dusty, particularly in the low-redshift bins. This would also explain why we may not calculate a very high A_V for the some of the galaxies in the ALMA sample as they appear more round and thus allow a significant amount of UV/optical radiation to be emitted (see Fig. 5.12) and Fig. 5.16) shows the distribution of the axial ratio (b/a) for our ALMA (red) and UV/optically selected (blue) galaxy samples, extracted from SExtractor (b and a are defined as the semi-minor and semi-major axes, respectively). As the axial ratio increases, the galaxy appears more round on-sky. It appears as if the distributions are different, with the UV/optically selected galaxies favouring a more round shape (peaking at a $b/a \simeq 0.9$) while the ALMA galaxies appear to be more elliptical and flatter. This disagrees with the above theory but still suggests there is a link between inclination and the estimate dust obscuration. However, it is important to note that these results are limited by the relatively poor quality of the ground-based images, that do not allow us to measure the axial ratios properly (particularly for small objects). Also, poor resolution tends to make objects appear more round than their intrinsic shape on-sky. This can be seen in the histogram

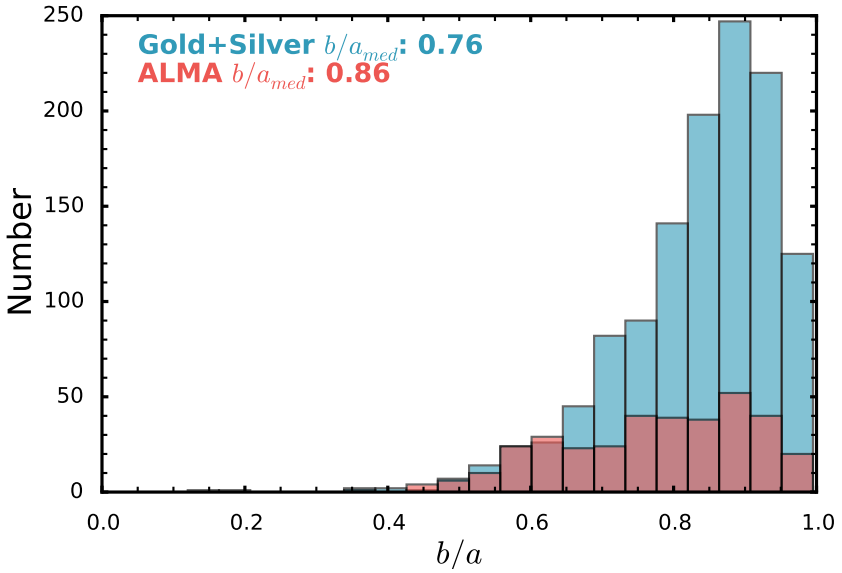

Figure 5.16 *The distribution of axial ratios for both the 'Gold' and 'Silver' UV/optically selected and the ALMA sub-mm detected galaxies, represented by the blue and red distributions respectively. We also show the median axial ratio for each sample. The values were obtained from SExtractor where the axial ratio is defined as b/a with b and a being the semi-minor and semi-major axis, respectively.*

presented (see Fig. 5.16) where both sets of objects have a $b/a > 0.75$ and the shape of both distributions tends towards higher b/a. For these reasons, we ran a Kolmogorov-Smirnov test (K-S test) in order to check the consistency between the two histograms. A critical value $D_{n,m}$ (above which means the two samples are entirely inconsistent) can be found depending on the two sample sizes using:

$$D_{n,m} > c(\alpha)\sqrt{\frac{n+m}{nm}}. \tag{5.2}$$

where n and m are the respective sample sizes and $c(\alpha)$ depends on the confidence level incurred. For our samples, assuming a commonly used α of 0.01, we find a critical D-value of $D(n,m) \simeq 0.088$. Using the statistical python module (`https://docs.scipy.org/doc/scipy-0.14.0/reference/generated/scipy.stats.kstest.html`) we compute a statistical D-value of 0.037, which is well below our critical D-value of $D_{n,m} \simeq 0.088$, suggesting that the two samples/distributions are somewhat consistent.

Fig. 5.17 shows the cosmic evolution of comoving star-formation rate density (SFRD) for both the ALMA-selected galaxies and 'Gold'+'Silver' UV/optically

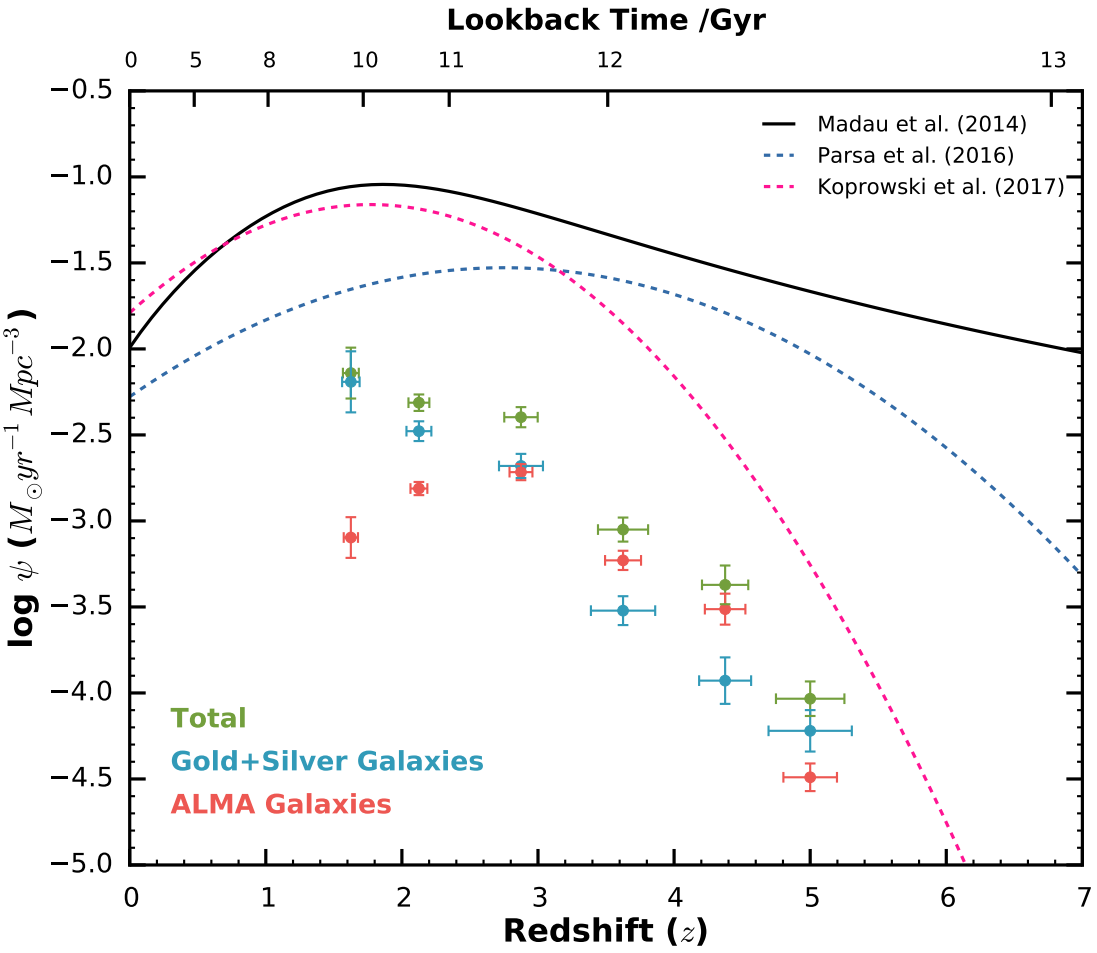

Figure 5.17 *SFRD as a function of redshift. The blue and red points represent the calculated SFRD in each redshift bin for the UV/optically selected and ALMA (> 2 mJy) detected dusty, high mass galaxies, respectively. The green points represent the total SFRD for both the ALMA and UV/optical dusty galaxies, ensuring there are no duplicated objects. We plot the total star-formation rate density as calculated by Madau & Dickinson 2014 (black solid line), IR contributions from Koprowski et al. 2017 (dashed red line) and UV contribution derived by Parsa et al. 2016 (dashed blue line).*

selected galaxies. We estimate the total SFR density (SFRD) of galaxies in each of the redshift bins by taking the sum of SFRs (calculated by BAGPIPES) of galaxies in the bin and dividing by the comoving volume of the bin. This is given by the difference in comoving volumes at the upper and lower redshift boundary, scaled to the sampled sky area (in this case UDS $\simeq 0.8$ deg^2). The blue points represent the 'Gold' and 'Silver' samples while the red represent the ALMA-selected galaxies. The green points are a sum of the total SFR in each bin from both galaxy samples, ensuring that the overlapping galaxies are not duplicated in the calculation. We also plot the total star-formation rate density as calculated by Madau & Dickinson (2014) (black solid line), IR contributions from Koprowski et al. (2017) (dashed red line) and UV contribution defined by Parsa et al. (2016) (dashed blue line). To convert the Madau & Dickinson (2014) line to a Chabrier IMF used in this work (and Koprowski et al. 2017), we have multiplied the function by a factor of 0.68. Parsa et al. (2016) provides an estimation of the unobscured SFRD calculated by converting the rest-frame UV (1500 Å) luminosity to a UV-visible SFR from galaxies in the HUDF, CANDELS/GOODS-South and UltraVISTA/COSMOS survey ($M_{UV} < -15$).

This plot shows the total contribution of obscured star formation across cosmic history from dusty, high-mass galaxies colour-coded by the manner in which these objects were selected. We effectively reproduce the shape of the peak of cosmic SFRD, albeit at a slightly higher redshift to the Madau curve, between $2 < z < 3$ instead of $z \simeq 2$. This is to be expected as there is a large amount of scatter around the peak of cosmic SFRD due to the diverse range of observational techniques used to deduce the SFRD. This is also evidence that the SF in high mass galaxies peaks at higher redshift than average (e.g. Koprowski et al. 2017; Bourne et al. 2017; Dunlop et al. 2017 and Wang et al. 2019). The real difference is between the two results is beyond $z > 3$ where there is a dramatically sharp decrease in the SFRD contributed by obscured star-formation. Between redshift $z \simeq 2 - 5$ (2 Gyrs), the SFRD drops by 2 orders of magnitude. This rate of decline is fairly consistent with Dunlop et al. (2017), Koprowski et al. (2017) and Bourne et al. (2017) who also report a sharp decline in the contribution of obscured star-formation. Parsa et al. (2016) and Dunlop et al. (2017) report that the overall contribution to the SFRD from unobscured star-formation begins to increase at the redshift where the contribution from obscured sources decrease. They show strong evidence of a transitional period of the dominant form of star-formation in the Universe between obscured and unobscured between $3 < z < 4$.

One might assume that this could be explained by an increase in the prevalence of dust in galaxies of certain mass at $z < 4$, however, when comparing Figures 5.17, 5.14 and 5.15, it can be concluded that if the majority of star-formation in the universe is dominated by obscured dusty galaxies at $z < 4$, this is largely down to the sharp increase in the number of dusty star-forming galaxies. The rate of decline beyond $z > 3$ is remarkably similar to that of the decline in SFRD, both dropping by nearly 2 orders of magnitude in the same timescale. This plot is in direct contrast to the result produced by two studies using *Herschel* data, Gruppioni et al. (2013) and Rowan-Robinson et al. (2016) report a shallower/ non-existent decline in dust-obscured SFRD from $z \simeq 3$ to $z \simeq 6$. A more recent *Herschel* study by Wang et al. (2019) also reports a relatively shallow decline in the SFRD as we extend to higher redshifts and suggest there is no evidence for a transitional period of dominating obscured to unobscured star-formation between $3 < z < 4$. Interestingly they suggest that there is a significant reduction of obscured star formation in this redshift range, but provide no explanation as to why this may be the case. Koprowski et al. (2017) conclude that the high star-formation rate values estimated in both Gruppioni et al. (2013) and Rowan-Robinson et al. (2016) are a consequence of the severe over estimations of 850μm number counts arising from inaccurate source identification, faulty SEDs and photometric redshifts. In our case, we do not include the $\simeq$ 150-200 galaxies detected by ALMA with no UV/Optical data resulting in only approximately 70% of all ALMA detected galaxies having addition UV/optical data. One might suggest that this could provide a reason for the discrepancy between these results and those found by Gruppioni et al. (2013) and Rowan-Robinson et al. (2016). However, I would argue that this would not affect the total shape of the comoving number density as the distribution of these galaxies would follow the distribution of our ALMA sample (Fig. 5.10 and 5.11) across all redshifts, in any case. Although we are missing 30% of the objects in the sample, comparing the total amount of flux from our final sample of 455 galaxies and the missing 150-200 galaxies, we have $\simeq$ 80% of the total flux. This would have a very small effect on the total SFHUacross all redshift, particularly if these missing galaxies followed a similar distribution to our original sample (Δ log SFR $\leq$ 0.1). In fact, based on independent redshift estimations of the same sample by Koprowski et al. (2017) and Stach et al. (2019), it is likely that these objects without the UV/optical data are less bright and therefore more likely to sit at lower redshift. We can, therefore, safely conclude that at high-redshift these missing galaxies would have very little impact, if any, on the shape

of the dust-obscured SFHU.

Fig. 5.18 shows the analogous plot to Fig 5.17 if we were to obtain ALMA data of a depth similar to that of Dunlop et al. (2017). The shift in SFRD for each redshift bin was calculated based on the work in Koprowski et al. (2017), where we assumed an ALMA depth of 0.5mJy instead of 2mJy. As we extend further down the luminosity function, we obtain star-formation from a larger number of source increasing the total SFRD in each redshift bin. This correction places the total contribution to the SFRD from obscured star-formation directly onto to the estimated evolution of the SFRD from Koprowski et al. (2017) (dashed red line). Again, this disagrees with the work of Gruppioni et al. (2013) and Rowan-Robinson et al. (2016), who suggest that the evolution of the SFRD beyond $z > 3$ is far shallower than this. This plot shows that even when taking into account the lower luminosity galaxies, the contribution to the SFRD of the Universe from obscured star-formation is very small at high redshifts. This is can be explained further looking at the LF and comoving number density of dusty star-forming galaxies from Koprowski et al. (2017). They suggest that, although the LF increases to higher redshift, the number density decreases at a far more rapid rate. Effectively, as you go to higher redshift, the decline in the number density of far-IR sources overcomes the increasing luminosity producing an overall decrease in the SFRD of the Universe. The continued increase in luminosity means that at high redshift it is still possible to detect luminous dust-enshrouded objects, even when they are very rare.

5.6 Conclusions

In an attempt to asses the prevalence of the type of dusty, high-redshift objects highlighted in Chapter 4, we selected a large sample ($\simeq$ 10,0000 objects) of high mass, high redshift, dusty, star-forming galaxies through UV/optical/near-IR data in the UDS/SXDS and COSMOS/UltraVISTA field covering a total area of 1.5 deg^2. This sample was selected based on redshift, mass and dust parameter fitting over a relatively narrow parameter space in order to highlight the objects that contained a maximum likelihood high mass ($M_* > 10^{10}$ M$_\odot$), high redshift ($z > 1.5$) and high dust obscuration ($A_V > 2.0$ mag) solution. These 10,000 objects were then SED fit with Bagpipes over the full parameter space in order to accurately infer their physical properties and to ensure they are indeed dusty, high-mass, high-redshift star-forming galaxies.

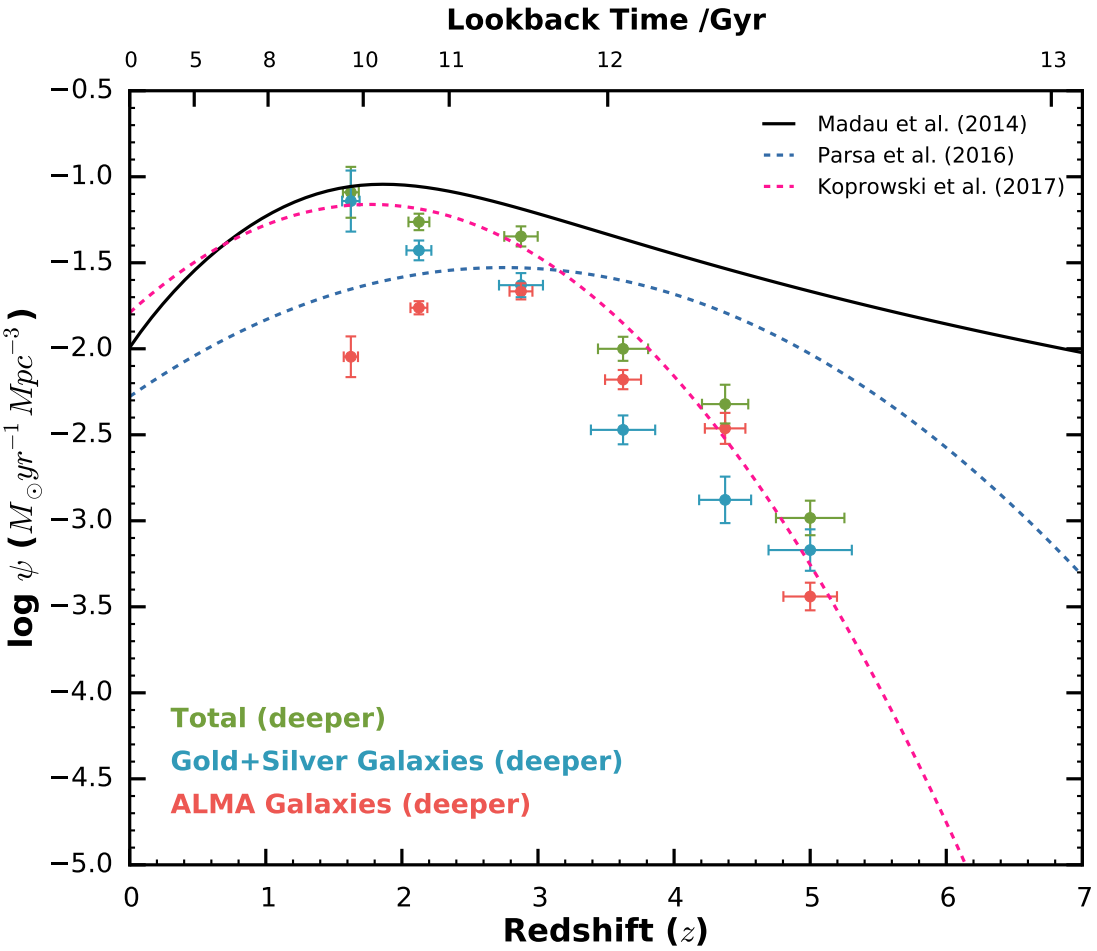

Figure 5.18 *SFRD as a function of redshift. The blue and red points represent the calculated SFRD in each redshift bin for the UV/optically selected and ALMA detected dusty, high mass galaxies, respectively. The green points represent the total SFRD for both the ALMA and UV/optical dusty galaxies, ensuring there are no duplicated objects. We also plot the total star-formation rate density as calculated by Madau & Dickinson 2014 (black solid line), IR contributions from Koprowski et al. 2017 (dashed red line) and UV contribution Parsa et al. 2016 (dashed blue line). Here we have adjusted the SFRD in each redshift by a* $\Delta\psi = 1.05$*, calculated by assuming we extend to a deeper ALMA sample of (>0.5 mJy).*

Using data from the ALMA SCUBA-2 Ultra Deep Survey (AS2UDS), we built an ALMA sample of 455 galaxies and matched them with our initial 68,000 UDS/SXDS galaxy catalogue to extract the UV/optical and near-IR photometric data. We assessed the total overlap of dusty galaxies selected through the dust emission in ALMA and the highlighted dusty galaxy sample selected through the extinction of dust in the UV/optical (our 'Gold', 'Silver' and 'Bronze' samples). We compared the comoving number densities and total contribution to the star-formation rate density (SFRD) throughout cosmic time from dusty, star-forming galaxies (obscured star-formation). The main findings of our work are as follows.

- We assessed Bagpipes ability to accurately estimate the photometric redshift in comparison to a spectroscopic sample taken from from a variety of studies including the Visible Multi-Object Spectrograph (VIMOS) Public Extragalactic Redshift Survey (VIPERS; Guzzo et al. 2014), UDSz survey (Bradshaw et al. 2013, McLure et al. 2013a and Almaini et al. in prep) and zCOSMOS (Lilly et al. 2007). We also compared the photometric redshifts to six independent SED fits LePhare Pegase, LePhare BC03, LePhare COSMOS-SED, EAZY PCA, EAZY Pegase, and BPZ. We show that Bagpipes accurately infers the photometric redshift resembling similar COR and σ_{MAD} to that found independently.

- We calculated the spatial density of the selected high-mass, high-redshift, dusty galaxies in the COSMOS and UDS field. We compared this to the spatial density of dusty galaxies under the same criteria extracted from EGG and show that EGG fails to reproduce the dusty population of galaxies by a factor of three. We show that current observations provide approximately 90 galaxies for a 125 arcmin^2 field while EGG only has approximately 35 galaxies in the same size field. If we extend the minimum dust obscuration to $A_V > 3.0$ mag, we show that there should be around 365 galaxies/deg^2, however, EGG contains zero galaxies with an $A_V > 3.0$ in the entire 1.2 deg^2 field, across all masses and redshifts.

- We plotted the comoving number density for the UDS 'Gold' and 'Silver' sample and show that there is a very sharp decline in the density of dusty, high-mass galaxies between $z = 1{-}5$. Over the timescale of 2 Gyr ($z = 3{-}5$) the comoving number density decreases by a factor of 2.

- We then calculated and plotted the comoving number density for the 'Gold' + 'Silver' and ALMA detected galaxies where we see a remarkably similar

decline above $z > 3$. From this we suggest that at high redshift regardless of whether the dusty galaxies are selected on the basis of the extinction of the UV/optical radiation or the dust emission in the sub-mm the shape of the comoving number density is the same. At lower redshift ($z < 3$) there is a clear discrepancy in the comoving number density. We suggest that this cannot be explained by the shape and morphology of each galaxy sample.

- We showed the resulting SFRD as a function of redshift and compared our results to previous studies. We showed that the comoving number density of obscured star formation decreases in a similar manner to the comoving number density of both the UV/optical and ALMA galaxies. We concluded that the sharp decrease in SFRD contributed by obscured star formation is a direct consequence of the vast decrease in the number density of dusty, high mass galaxies in the high redshift Universe. We also suggest that this result is found whether or not the observations is of the suppressed UV/optical radiation or the far-IR dust emission.

6

Summary and Future Work

6.1 Summary

In this thesis, I have presented a new insight into the potential science capabilities of *JWST*. In particular, I have assessed how effectively the Mid-Infrared Instrument (MIRI), through both spectroscopy and imaging, will be able to observe star-forming galaxies at high redshift. In Chapter 2, I evaluated the capability of the MIRI Medium Resolution Spectrometer (MRS) for observing Hα, an emission line that provides a direct indicator of recent star formation. MIRI is a valuable tool for observing emission lines caused by recent star formation in high-redshift galaxies because, at about $z \simeq 6.5$, Hα is redshifted beyond the wavelength range of NIRCam and NIRSpec ($< 5.0\mu$m). It is thought that the very first galaxies would be of low metallicity meaning that there will be virtually no emission lines between Lyman-α and the Balmer series, adding to the importance of being able to observe the Hα emission line. Using an independently-built simulator (Chapter 3, Section 2.4), tested against the official ETC and MIRI Teams simulator (MIRISim), I showed that for the brightest known $z \simeq 7$ galaxies ($m_{ab} \simeq 25$ mag) the MRS IFU should be able to detect Hα emission line to a SNR

of 11.6 from a $\simeq$ 6-hour integration time within each short channel. If matched with MIRI and NIRCam imaging, very tight constraints on the SFR of selected objects could be measured, and subsequently, improved constraints on the total SFRD of the Universe can be achieved at the very highest redshifts.

In Chapter 3, I present an overview of the Public Release Imaging for Extragalactic Research (PRIMER) proposal submitted as part of the Directors Discretionary Early Release Science (DD-ERS) programme for Cycle-1 of *JWST*. PRIMER is a large (52hr), deep, fully-sampled NIRCam and MIRI imaging programme, designed to efficiently ($\approx$ 75% observing efficiency) observe the faintest galaxies in the best-studied available (Non-GTO Covered) equatorial *HST* CANDELS field, COSMOS. This introduced a specific observing strategy that provided the basis for the work in Kemp et al. (2019) which makes up the entirety of Chapter 4. I then provided a new review of the currently accepted ERS & GTO *JWST* observing programmes that focus on studying galaxies at high-redshift.

In Chapter 4, I then presented an analysis of simulated *JWST*+*HST* photometry for a wide range of model galaxies, in order to explore the ability with which the redshifts and physical properties of galaxies can be reclaimed from different multi-band combinations of photometry. In particular, I have explored the potential value of extending the wavelength baseline of *JWST* NIRCam photometry to longer wavelengths with *JWST* MIRI, and/or to shorter wavelengths with additional *HST* ACS imaging.

I created two different simulated galaxy samples, one (based on the models of Bruzual & Charlot 2003) designed to explore a wide range of possible galaxy properties including very dust-obscured objects, and a second (based on the Empirical Galaxy Generator: EGG) that is designed to be representative of the known galaxy population. The photometry for all these objects was created and scattered given the latest knowledge of the performance of the relevant instruments, and then subsequently SED-fit using Bagpipes to attempt to reclaim the properties of the galaxies from the scattered photometry.

Our main findings are that **i)** parallel MIRI 7.7 μm imaging is of real value (in some cases crucial), but only for a subset of galaxies at $z \simeq 4-7$ which have high dust obscuration, $A_V > 2$; **ii)** the current EGG simulations suggest that such galaxies only constitute 0.5% of the $z = 0-12$ galaxy population that will be detected by *JWST* NIRCam surveys, but this could easily be an underestimate,

given the known existence of galaxies in the GOODS fields with $A_V \simeq 5$ (Dunlop et al. 2007); **iii)** while the MIRI photometry also appears to help with the accurate recovery of the properties of some galaxies at $z < 4$, it transpires that deep *HST B*-band photometry is of more value (and is more efficient) for removing photometric redshift degeneracies for such galaxies.

Finally, in an attempt to asses the prevalence of the dusty, high-redshift objects highlighted in Chapter 4, in Chapter 5 I selected a large sample ($\simeq$ 10,0000 objects) of high mass, high redshift, dusty, star-forming galaxies through UV/optical/near-IR data in the UDS/SXDS and COSMOS/UltraVISTA field covering a total area of 1.5 deg^2. This sample was selected based on redshift, mass and dust parameter fitting over a relatively narrow parameter space in order to highlight the objects that contained a maximum likelihood high mass ($M_* > 10^{10}$ M$_\odot$), high redshift ($z > 1.5$) and high dust obscuration ($A_V > 2.0$ mag) solution. The resulting dataset was split into 'Gold', 'Silver' and 'Bronze' sub-samples depending on the confidence of fitting the criteria. Using additional data from the ALMA SCUBA-2 Ultra Deep Survey (AS2UDS), I built an ALMA sample of 650 galaxies and matched them with our initial 68,000 UDS/SXDS galaxy catalogue to extract the UV/optical and near-IR photometric data. I assessed the total overlap of dusty galaxies selected through the dust emission in ALMA and the highlighted dusty galaxy sample selected through the extinction of dust in the UV/optical (our 'Gold', 'Silver' and 'Bronze' samples).

Initially, I tested Bagpipes ability to accurately estimate the photometric redshift in comparison to a spectroscopic sample. I then calculated the spatial density of the selected high-mass, high-redshift, dusty galaxies in the COSMOS and UDS field and compare this to the spatial density of dusty galaxies under the same criteria extracted from EGG. I show that EGG fails to reproduce the dusty population of galaxies by a factor of three. EGG contains only 35 $A_V > 3.0$ mag galaxies in 125 arcmin^2 while I found > 90 galaxies. Extending the limiting A_V to $A_V > 3.0$ mag, I find 365 galaxies/deg^2, while EGG contains no $A_V > 3.0$ galaxies in the entire 1.2 deg^2 field, indicates that, EGG does not properly reproduce the dusty star-forming galaxy population. I measure and compare the comoving number densities and total contribution to the star-formation rate density (SFRD) throughout cosmic time from dusty, star-forming galaxies (obscured star-formation).

I showed that the comoving number density for the 'Gold' + 'Silver' selected and ALMA detected galaxies samples both show a sharp decline beyond $z > 3$. From

this, I suggest that at high redshift, regardless of whether the dusty galaxies are selected based on the extinction of the UV/optical radiation or the dust emission in the sub-mm, the evolution of the comoving number density is the same. I show the resulting SFRD as a function of redshift and compare our results to previous studies. I show that the comoving number density of obscured star formation decreases similarly to the comoving number density of both the UV/optical and ALMA galaxies. I conclude that the sharp decrease in SFRD contributed by obscured star formation is a direct consequence of the significant decrease in the number density of dusty, high mass galaxies in the high-redshift Universe. I also show that this result is found whether or not you are observing the suppressed UV/optical radiation or the far-IR dust emission.

6.2 Future Work

JWST is now set to launch in 2021, which leaves enough time to gather the required ancillary data. In particular, the results from Chapter 4 and Kemp et al. (2019) highlight the importance of obtaining deeper UV/optical data before the launch of *JWST*. As *JWST's* wavelength coverage begins at 0.7μm, only LBGs with a redshift of $z > 5$ can be selected using NIRCam data alone. However, the shortest wavelength filter in NIRCam provides no real significant increase in sensitivity in comparison to *HST*. This means that NIRCam's effective wavelength coverage begins at 0.9μm pushing the limiting LBG method to $z \simeq 7$. In any case, information blueward of NIRCam wavelength is vital in distinguishing between a Lyman-break and Balmer/4000Å break. This manifests itself in two ways, Fig. 6.1 (taken from Chapter 4) shows two features in the density maps: a vertical arm sitting at redshift $z \simeq 1$ and a horizontal arm sitting at $z_{phot} \simeq 0.5{-}1$. These are both caused by the incorrect confirmation of the Lyman-break and the confirmation of the Lyman-break, respectively. Additional deep (28.4 mag) ACS B_{435} provides enough information to reclaim the photometric redshift accurately.

An *HST* survey, covering necessary CANDELS fields will, therefore, be of the utmost importance in maximising the efficiency of *JWST* observations and the resulting dataset. The limited lifetime of *JWST* will rely on sufficient preparation in order to ensure we can put forward proposals for follow-up observations in later cycles of *JWST*. If this is not accomplished by the launch of *JWST* there is a real possibility of a depth gap between current observations and *JWST* observations where there is not enough multi-wavelength coverage, particularly, blueward of

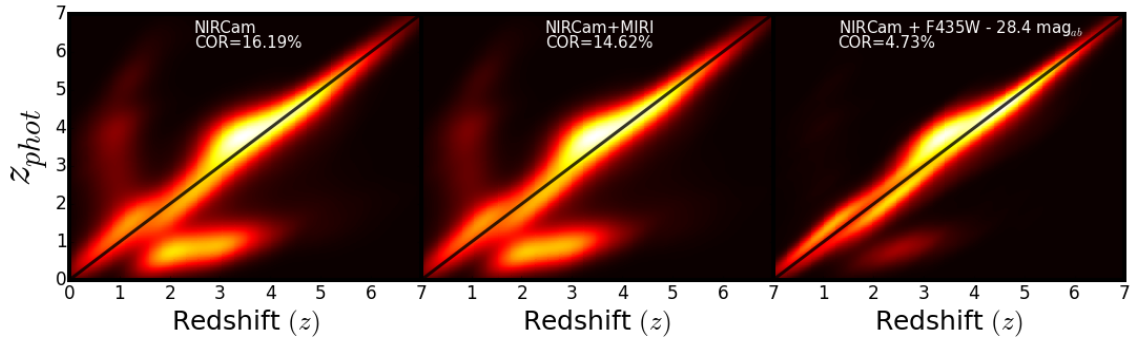

Figure 6.1 *Density maps showing reclaimed photometric redshift as a function of simulated galaxy redshift for our sample of EGG galaxies in multiple filter combinations. Left: Photometric redshifts reclaimed using the 8 NIRcam Bands with existing HST V_{606} and i_{814} imaging. Centre: Photometric redshifts reclaimed using the 8 NIRcam Bands with existing HST V_{606} and i_{814} + MIRI F770W photometry. Right: Photometric redshifts reclaimed using the 8 NIRcam Bands with HST V_{606} and i_{814} + B_{435} (28.4 mag) imaging. The catastrophic outlier rate (COR) in each case is also given, defined as the percentage of galaxies with $|\Delta z| > 0.15$, where $|\Delta z| = |(z_{phot} - z_{input})/(1 + z_{input})|$.*

NIRCam to effectively analyse high-redshift galaxies. In any case, in the run-up to the launch of *JWST*, the community should work harder in gaining an understanding of the realistic possibilities of *JWST*.

Deep wide surveys using *JWST's* NIRCam and MIRI imagers (Fig. 6.2) will observe the rest-frame UV-optical and near-IR. In theory, this should allow good estimations of photometric redshifts for the majority of bright galaxies at $z < 5$ with $m_{AB} < 30$. Upon completion of the SED-fitting analysis of these objects, we can highlight several objects that can be observed with NIRSpec to measure the exact SFR of massive galaxies, specifically using the Hα line. Spectroscopic observations will also allow us to determine accurate (≤ 0.2 dex) metallicities for the objects found in a deep, wide imaging survey. NIRSpec will be able to observe strong emission lines to a resolution of R $\sim$ 1000, produced in star-forming gas: [OII] λ3727, Hβ, [OIII] $\lambda\lambda$4959, 5007, Hα , [NII] λ6583, [SII] $\lambda\lambda$6717, 6731. This sort of science is also applicable to planetary and stellar astrophysics, as planets form from the same material. More importantly, *JWST* will be able to complement line studies that have been carried out by ground-based optical telescopes (VANDELS; McLure et al. 2017, Carnall et al. 2018b).

The Lyman-α forest presents critical signatures for the Epoch of Re-ionisation (EoR); the Lyman-α Gunn-Peterson trough, islands in the Lyman-α forest, and the appearance of a Lyman-α damping wing. Using deep NIRCam+MIRI imaging

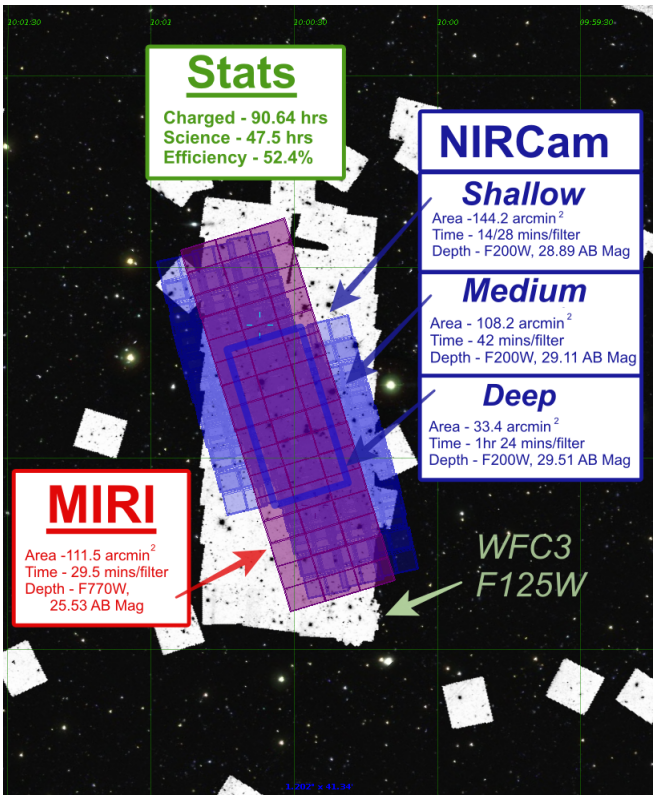

Figure 6.2 *A potential JWST NIRCam and MIRI imaging survey conducted over the well studied HST COSMOS CANDELS field. The blue and red tiles represent the NIRCam and MIRI observations, respectively. While the dark blue line represents a region of deep NIRCam imaging constructed by multiple exposures (× 4) of NIRCam prime observations. The constructed mosaic overplots the current HST imaging in the COSMOS CANDELS field. The ability to drag the MIRI imaging over the NIRCam prime imaging allows efficient coverage for both instruments, and this produces multi-wavelength data enabling detection and analysis of dusty star-forming galaxies.*

surveys, we can identify a sample of Lyman-break galaxies at extreme redshift while ancillary and shorter wavelength NIRCam data ($\lambda < 0.1\mu$m) will be used to study lower redshift samples. In addition, a search for Quasi-Stellar Objects (QSOs) and Gamma-Ray Bursts (GRBs) afterglow will allow us to probe the intervening IGM between the source and observer. If we can also identify the Lyman-α emitters, within the global Lyman-break population, and measure the evolution of their LF, it is possible to constrain the progress of cosmic reionisation. Unfortunately, observations in the UV are hampered by the impact of dust, along with the kinematics and geometry of the surrounding gas encompassing LAEs. NIRSpec will, however, help characterise the physical properties of the gas and dust surrounding these objects. Primarily this will be done through studying the nebular emission lines in the spectra of high redshift LAEs, similar to the work done by ground-based telescopes such as MUSE and VLT at lower redshifts.

Merger events can cause Super Massive Black Holes (SMBHs) to begin accreting the surrounding matter producing vast amounts of radiated energy. These are known as Active Galactic Nuclei (AGN). Often, these objects are obscured by dust and gas, preventing the majority of UV/optical light escaping. MIRI observes the mid-IR light from sources meaning that MIRI will have a relatively unobscured view of the centres of AGN. In particular, the aim is to look at the epoch where quasar activity was at its highest, between redshifts $z \simeq 2{-}3$. Most of these quasars are heavily obscured, recognised as type II. They distinguish themselves from type I solely through the spectrum we observe when studying them, yet the physics behind this is still not fully understood. It is essential to try and work out the star formation and how this relates to the accretion of matter by the SMBH. MIRI will also be able to observe the dust-obscured Ultra Luminous Infra-Red Galaxies (ULIRGs), while NIRSpec can accurately determine the redshift through emission line measurements. Another aim is to probe the morphologies of star-forming galaxies at relatively high redshift ($z \simeq 2$), especially for objects that are gravitationally lensed by an intervening object. In this case, the MIRI imager has a good enough resolving power to reconstruct these images in the mid-IR.

In Chapter 4, I highlighted the importance of MIRI imaging in observing the dustiest galaxies in the Universe, even though, for the vast majority of the bluer galaxy population, the MIRI photometry struggles to add value to the deeper NIRCam data. Initial estimates, based on EGG, of the prevalence of these dusty objects showed that they make up a tiny fraction of the high-redshift galaxy population. Subsequently, however, in Chapter 5, I showed that

EGG does not sufficiently reproduce the DSFG population, underestimating the total number by a factor of $\simeq 3$. When studying the dustiest galaxies in the Universe, one can observe the far-IR/sub-mm to estimate the SFR accurately. However, to contextualise this in terms of cosmic time, and thus create the SFHD for obscured star-formation, accurate redshift estimations of these objects are required. Ultimately this comes from SED-fitting the UV/optical and near-IR data. For these objects, I have shown that MIRI will be vital for estimating the redshift accurately. One of the remaining questions about the SFH of the Universe in constraining the contribution of obscured SF beyond $z > 3$. There is much debate as to how flat or steep the drop off is, and thus the total fraction of obscured to unobscured star-formation at high redshift (e.g. Burgarella et al. 2013;Gruppioni et al. 2013; Dunlop et al. 2017; Bourne et al. 2017; Koprowski et al. 2017; Wang et al. 2019). In this case, MIRI will play a vital role in completing the census of obscured star formation beyond $z > 3$ and should, therefore, be carefully considered for any large *JWST* imaging survey with NIRCam. Fig. 6.2 shows a potential Cycle-1 imaging survey covering the COSMOS CANDELS field that would benefit greatly from the addition of parallel MIRI imaging to enable the detection of dusty galaxies. This means that deep pointed MIRI follow-up of such sources will be invaluable, both for resolving redshifts/mass ambiguities and indeed potentially for delineating their mid-infrared SEDs through multi-band MIRI imaging.

In order to complete the census of dusty star-forming galaxies and the contribution to the SFHU of the Universe by obscured star-formation, deeper and wider far-IR/sub-mm surveys are required, in particular with ALMA. At the end of Chapter 5, I estimated the potential benefits of obtaining deeper ALMA data, in order to probe the faint-end of the FIRLF. Ultimately, redshift estimations will be accurately determined using the shorter wavelength data, but analogous longer wavelength data is an excellent tool for completing our census of cosmic star formation.

Bibliography

Abel T., Bryan G. L., Norman M. L., 2002, Science, 295, 93

Ajiki M., Mobasher B., Taniguchi Y., Shioya Y., Nagao T., Murayama T., Sasaki S. S., 2006, ApJ, 638, 596

Almaini O., et al., 2017, MNRAS, 472, 1401

Arnouts S., Ilbert O., 2011, LePHARE: Photometric Analysis for Redshift Estimate, Astrophysics Source Code Library (ascl:1108.009)

Ashby M. L. N., et al., 2013, ApJ, 769, 80

Ashby M. L. N., et al., 2015, ApJS, 218, 33

Ashby M. L. N., et al., 2018, ApJS, 237, 39

Atek H., Kunth D., Schaerer D., Hayes M., Deharveng J. M., Östlin G., Mas-Hesse J. M., 2009, A&A, 506, L1

Atek H., et al., 2014, ApJ, 786, 60

Barger A. J., Cowie L. L., Sanders D. B., Fulton E., Taniguchi Y., Sato Y., Kawara K., Okuda H., 1998, Nature, 394, 248

Barrow K. S. S., Wise J. H., Norman M. L., O'Shea B. W., Xu H., 2017, MNRAS, 469, 4863

Beckwith S. V. W., et al., 2006, AJ, 132, 1729

Behroozi P. S., Wechsler R. H., Conroy C., 2013, ApJ, 770, 57

Benítez N., 2000, ApJ, 536, 571

Bertin E., Arnouts S., 1996, A&AS, 117, 393

Béthermin M., Dole H., Beelen A., Aussel H., 2010, A&A, 512, A78

Bisigello L., et al., 2016, ApJS, 227, 19

Bisigello L., et al., 2017, ApJS, 231, 3

Blain A. W., Smail I., Ivison R. J., Kneib J.-P., Frayer D. T., 2002, Phys. Rep., 369, 111

Bouchet P., et al., 2015, PASP, 127, 612

Boulade O., et al., 2003, in Iye M., Moorwood A. F. M., eds, Proc. SPIEVol. 4841, Instrument Design and Performance for Optical/Infrared Ground-based Telescopes. pp 72–81, doi:10.1117/12.459890

Bourne N., et al., 2017, MNRAS, 467, 1360

Bouwens R. J., Illingworth G. D., Blakeslee J. P., Franx M., 2006, ApJ, 653, 53

Bouwens R. J., Illingworth G. D., Franx M., Ford H., 2007, ApJ, 670, 928

Bouwens R. J., et al., 2010, ApJ, 709, L133

Bouwens R. J., et al., 2011, ApJ, 737, 90

Bouwens R. J., et al., 2012, ApJ, 754, 83

Bouwens R. J., et al., 2014, ApJ, 795, 126

Bouwens R. J., et al., 2015, ApJ, 803, 34

Bouwens R. J., Oesch P. A., Illingworth G. D., Ellis R. S., Stefanon M., 2017, ApJ, 843, 129

Bowler R. A. A., et al., 2012, MNRAS, 426, 2772

Bowler R. A. A., et al., 2014, MNRAS, 440, 2810

Bowler R. A. A., et al., 2015, MNRAS, 452, 1817

Bowler R. A. A., Dunlop J. S., McLure R. J., McLeod D. J., 2017, MNRAS, 466, 3612

Bradshaw E. J., et al., 2013, MNRAS, 433, 194

Brammer G. B., van Dokkum P. G., Coppi P., 2008, ApJ, 686, 1503

Brammer G. B., et al., 2016, ApJS, 226, 6

Bromm V., Yoshida N., 2011, ARA&A, 49, 373

Bromm V., Coppi P. S., Larson R. B., 1999, ApJ, 527, L5

Bruzual G., Charlot S., 2003, MNRAS, 344, 1000

Bruzual A. G., Charlot S., 1993, ApJ, 405, 538

Burgarella D., et al., 2013, A&A, 554, A70

Calzetti D., Kinney A. L., Storchi-Bergmann T., 1994, ApJ, 429, 582

Calzetti D., Kinney A. L., Storchi-Bergmann T., 1996, ApJ, 458, 132

Calzetti D., Armus L., Bohlin R. C., Kinney A. L., Koornneef J., Storchi-Bergmann T., 2000, ApJ, 533, 682

Calzetti D., et al., 2010, ApJ, 714, 1256

Cardelli J. A., Clayton G. C., Mathis J. S., 1989, ApJ, 345, 245

Carnall A. C., Leja J., Johnson B. D., McLure R. J., Dunlop J. S., Conroy C., 2018a, arXiv e-prints,

Carnall A. C., McLure R. J., Dunlop J. S., Davé R., 2018b, MNRAS, 480, 4379

Casey C. M., Narayanan D., Cooray A., 2014, Phys. Rep., 541, 45

Chabrier G., 2003, PASP, 115, 763

Chapman S. C., Blain A. W., Smail I., Ivison R. J., 2005, ApJ, 622, 772

Cirasuolo M., McLure R. J., Dunlop J. S., Almaini O., Foucaud S., Simpson C., 2010, MNRAS, 401, 1166

Clements D. L., Sutherland W. J., Saunders W., Efstathiou G. P., McMahon R. G., Lawrence A., Rowan-Robinson M., 1996, Vistas in Astronomy, 40, 215

Coe D., et al., 2013, ApJ, 762, 32

Coleman G. D., Wu C.-C., Weedman D. W., 1980, ApJS, 43, 393

Conroy C., 2013, ARA&A, 51, 393

Conselice C. J., Wilkinson A., Duncan K., Mortlock A., 2016, ApJ, 830, 83

Cowley W. I., Baugh C. M., Cole S., Frenk C. S., Lacey C. G., 2018, MNRAS, 474, 2352

Crosby B. D., O'Shea B. W., Beers T. C., Tumlinson J., 2016, ApJ, 820, 71

Cucciati O., et al., 2012, A&A, 539, A31

Cullen F., McLure R. J., Khochfar S., Dunlop J. S., Dalla Vecchia C., 2017, MNRAS, 470, 3006

Curtis-Lake E., et al., 2012, MNRAS, 422, 1425

Curtis-Lake E., et al., 2016, MNRAS, 457, 440

Dahlen T., Mobasher B., Dickinson M., Ferguson H. C., Giavalisco M., Kretchmer C., Ravindranath S., 2007, ApJ, 654, 172

Dahlen T., et al., 2013, ApJ, 775, 93

Damen M., et al., 2011, ApJ, 727, 1

Davidzon I., et al., 2017, A&A, 605, A70

Dayal P., Ferrara A., Dunlop J. S., Pacucci F., 2014, MNRAS, 445, 2545

Dey A., Spinrad H., Stern D., Graham J. R., Chaffee F. H., 1998, ApJ, 498, L93

Doyon R., et al., 2012, in Space Telescopes and Instrumentation 2012: Optical, Infrared, and Millimeter Wave. p. 84422R, doi:10.1117/12.926578

Dunlop J. S., 2013, in Wiklind T., Mobasher B., Bromm V., eds, Astrophysics and Space Science Library Vol. 396, The First Galaxies. p. 223 (arXiv:1205.1543), doi:10.1007/978-3-642-32362-1_5

Dunlop J. S., Cirasuolo M., McLure R. J., 2007, MNRAS, 376, 1054

Dunlop J. S., et al., 2013, MNRAS, 432, 3520

Dunlop J. S., et al., 2017, MNRAS, 466, 861

Ellis R. S., 1997, ARA&A, 35, 389

Ellis R. S., et al., 2013, ApJ, 763, L7

Fan X., et al., 2006, AJ, 132, 117

Feng Y., Di-Matteo T., Croft R. A., Bird S., Battaglia N., Wilkins S., 2016, MNRAS, 455, 2778

Ferland G. J., et al., 2017, Rev. Mex. Astron. Astrofis., 53, 385

Finkelstein S. L., 2016, Publ. Astron. Soc. Australia, 33, e037

Finkelstein S. L., Papovich C., Giavalisco M., Reddy N. A., Ferguson H. C., Koekemoer A. M., Dickinson M., 2010, ApJ, 719, 1250

Finkelstein S. L., Dunlop J., Le Fevre O., Wilkins S., 2015, preprint, (arXiv:1512.04530)

Finkelstein S., et al., 2017, The Cosmic Evolution Early Release Science (CEERS) Survey, JWST Proposal ID 1345. Cycle 0 Early Release Science

Finlator K., Oppenheimer B. D., Davé R., 2011, MNRAS, 410, 1703

Fioc M., Rocca-Volmerange B., 1999, arXiv Astrophysics e-prints,

Fitzpatrick E. L., 1986, AJ, 92, 1068

Fontana A., et al., 2006, A&A, 459, 745

Fontana A., et al., 2009, A&A, 501, 15

Fontana A., et al., 2014, A&A, 570, A11

Furusawa H., et al., 2008, ApJS, 176, 1

Furusawa H., et al., 2016, ApJ, 822, 46

Gallagher J. S., Hege E. K., Kopriva D. A., Butcher H. R., Williams R. E., 1980, ApJ, 237, 55

Gardner J. P., et al., 2006, Space Science Reviews, 123, 485

Geach J. E., et al., 2013, MNRAS, 432, 53

Geach J. E., et al., 2016, ApJ, 832, 37

Giavalisco M., et al., 2004, ApJ, 600, L93

Glasse A., et al., 2015, PASP, 127, 686

Glazebrook K., et al., 2017, Nature, 544, 71

Grazian A., et al., 2015, A&A, 575, A96

Grogin N. A., et al., 2011, ApJS, 197, 35

Gruppioni C., et al., 2010, A&A, 518, L27

Gruppioni C., et al., 2013, MNRAS, 432, 23

Guhathakurta P., Tyson J. A., Majewski S. R., 1990, ApJ, 357, L9

Guzzo L., et al., 2014, A&A, 566, A108

Hao C.-N., Kennicutt R. C., Johnson B. D., Calzetti D., Dale D. A., Moustakas J., 2011, ApJ, 741, 124

Hartley W. G., Almaini O., Foucaud S., 2013, in Adamson A., Davies J., Robson I., eds, Astrophysics and Space Science Proceedings Vol. 37, Thirty Years of Astronomical Discovery with UKIRT. p. 309, doi:10.1007/978-94-007-7432-2_29

Hayes M., Schaerer D., Östlin G., Mas-Hesse J. M., Atek H., Kunth D., 2011, ApJ, 730, 8

Hoag A., et al., 2019, ApJ, 878, 12

Hogg D. W., Cohen J. G., Blandford R., Pahre M. A., 1998, ApJ, 504, 622

Hopkins A. M., Beacom J. F., 2006, ApJ, 651, 142

Horner S. D., Rieke M. J., 2004, in Mather J. C., ed., Proc. SPIEVol. 5487, Optical, Infrared, and Millimeter Space Telescopes. pp 628–634, doi:10.1117/12.552281

Hu E. M., Cowie L. L., McMahon R. G., 1998, ApJ, 502, L99

Hu E. M., Cowie L. L., McMahon R. G., Capak P., Iwamuro F., Kneib J.-P., Maihara T., Motohara K., 2002, ApJ, 568, L75

Hubble E., 1929, Proceedings of the National Academy of Science, 15, 168

Hughes D. H., et al., 1998, Nature, 394, 241

Ilbert O., et al., 2006, A&A, 457, 841

Ilbert O., et al., 2013, A&A, 556, A55

Illingworth G. D., et al., 2013, ApJS, 209, 6

Inoue A. K., Shimizu I., Iwata I., Tanaka M., 2014, MNRAS, 442, 1805

Ishigaki M., Kawamata R., Ouchi M., Oguri M., Shimasaku K., Ono Y., 2018, ApJ, 854, 73

Iye M., et al., 2006, Nature, 443, 186

Iye M., Kashikawa N., Furusawa H., Ota K., Ouchi M., Shimasaku K., 2008, in Kodama T., Yamada T., Aoki K., eds, Astronomical Society of the Pacific Conference Series Vol. 399, Panoramic Views of Galaxy Formation and Evolution. p. 61

Jarvis M. J., et al., 2013, MNRAS, 428, 1281

Kashikawa N., et al., 2006, ApJ, 648, 7

Kemp T. W., Dunlop J. S., McLure R. J., Schreiber C., Carnall A. C., Cullen F., 2019, MNRAS, 486, 3087

Kendrew S., et al., 2015, PASP, 127, 623

Kennicutt Jr. R. C., 1998, ARA&A, 36, 189

Kennicutt R. C., Evans N. J., 2012, ARA&A, 50, 531

Kennicutt Jr. R. C., Kent S. M., 1983, AJ, 88, 1094

Koekemoer A. M., et al., 2011, ApJS, 197, 36

Konno A., et al., 2014, ApJ, 797, 16

Koprowski M. P., Dunlop J. S., Michałowski M. J., Coppin K. E. K., Geach J. E., McLure R. J., Scott D., van der Werf P. P., 2017, MNRAS, 471, 4155

Koprowski M. P., et al., 2018, MNRAS, 479, 4355

Kroupa P., 2001, MNRAS, 322, 231

Labbé I., et al., 2013, ApJ, 777, L19

Labbé I., et al., 2015, ApJS, 221, 23

Lacey C. G., et al., 2016, MNRAS, 462, 3854

Laigle C., et al., 2016, ApJS, 224, 24

Lawrence A., Walker D., Rowan-Robinson M., Leech K. J., Penston M. V., 1986, MNRAS, 219, 687

Lawrence A., et al., 2007, MNRAS, 379, 1599

Lilly S. J., Le Fevre O., Hammer F., Crampton D., 1996, ApJ, 460, L1

Lilly S. J., et al., 2007, ApJS, 172, 70

Livermore R. C., Finkelstein S. L., Lotz J. M., 2017, VizieR Online Data Catalog, 183

Lotz J. M., et al., 2017, ApJ, 837, 97

Lovell M. R., et al., 2018, arXiv e-prints,

Madau P., 1995, ApJ, 441, 18

Madau P., Dickinson M., 2014, ARA&A, 52, 415

Madau P., Ferguson H. C., Dickinson M. E., Giavalisco M., Steidel C. C., Fruchter A., 1996, MNRAS, 283, 1388

Madau P., Pozzetti L., Dickinson M., 1998, ApJ, 498, 106

Magnelli B., Elbaz D., Chary R. R., Dickinson M., Le Borgne D., Frayer D. T., Willmer C. N. A., 2011, A&A, 528, A35

Magnelli B., et al., 2013, A&A, 553, A132

Makovoz D., Marleau F. R., 2005, PASP, 117, 1113

Martin D. C., et al., 2005, ApJ, 619, L1

Mason C. A., Trenti M., Treu T., 2015, ApJ, 813, 21

Mason C. A., Treu T., Dijkstra M., Mesinger A., Trenti M., Pentericci L., de Barros S., Vanzella E., 2018, ApJ, 856, 2

Mason C. A., et al., 2019, MNRAS, 485, 3947

McCracken H. J., et al., 2012, A&A, 544, A156

McLeod D. J., McLure R. J., Dunlop J. S., Robertson B. E., Ellis R. S., Targett T. A., 2015, MNRAS, 450, 3032

McLeod D. J., McLure R. J., Dunlop J. S., 2016, MNRAS, 459, 3812

McLure R. J., et al., 2006, MNRAS, 372, 357

McLure R. J., Cirasuolo M., Dunlop J. S., Foucaud S., Almaini O., 2009, MNRAS, 395, 2196

McLure R. J., Dunlop J. S., Cirasuolo M., Koekemoer A. M., Sabbi E., Stark D. P., Targett T. A., Ellis R. S., 2010, MNRAS, 403, 960

McLure R. J., et al., 2013a, MNRAS, 428, 1088

McLure R. J., et al., 2013b, MNRAS, 432, 2696

McLure R., Pentericci L., VANDELS Team 2017, The Messenger, 167, 31

McLure R. J., et al., 2018a, MNRAS, 476, 3991

McLure R. J., et al., 2018b, MNRAS, 479, 25

Mehta V., et al., 2018, ApJS, 235, 36

Merlin E., et al., 2015, A&A, 582, A15

Merlin E., et al., 2018, MNRAS, 473, 2098

Mesinger A., Furlanetto S. R., 2008, MNRAS, 386, 1990

Michałowski M. J., et al., 2017, MNRAS, 469, 492

Mortier A. M. J., et al., 2005, MNRAS, 363, 563

Murphy E. J., et al., 2011, ApJ, 737, 67

Muzzin A., et al., 2013, ApJ, 777, 18

Nakajima K., Ellis R. S., Iwata I., Inoue A. K., Kusakabe H., Ouchi M., Robertson B. E., 2016, ApJ, 831, L9

Oesch P. A., et al., 2010, ApJ, 709, L21

Oesch P. A., et al., 2013, ApJ, 773, 75

Oesch P. A., et al., 2014, ApJ, 786, 108

Oesch P. A., et al., 2016, ApJ, 819, 129

Oesch P. A., Bouwens R. J., Illingworth G. D., Labbé I., Stefanon M., 2018, ApJ, 855, 105

Oke J. B., 1974, ApJS, 27, 21

Oke J. B., Gunn J. E., 1983, ApJ, 266, 713

Ouchi M., et al., 2004, ApJ, 611, 660

Ouchi M., et al., 2005, ApJ, 620, L1

Ouchi M., et al., 2010, ApJ, 723, 869

Paardekooper J.-P., Khochfar S., Dalla Vecchia C., 2013, MNRAS, 429, L94

Papovich C., et al., 2004, ApJS, 154, 70

Parsa S., Dunlop J. S., McLure R. J., Mortlock A., 2016, MNRAS, 456, 3194

Pentericci L., et al., 2018, A&A, 619, A147

Planck Collaboration et al., 2014, A&A, 571, A16

Planck Collaboration et al., 2018, arXiv e-prints,

Pontoppidan K. M., et al., 2016, MNRAS, 9910, 991016

Posselt W., Holota W., Kulinyak E., Kling G., Kutscheid T., Le Fevre O., Prieto E., Ferruit P., 2004, in Mather J. C., ed., Proc. SPIEVol. 5487, Optical, Infrared, and Millimeter Space Telescopes. pp 688–697, doi:10.1117/12.555659

Postman M., et al., 2012, ApJS, 199, 25

Prevot M. L., Lequeux J., Maurice E., Prevot L., Rocca-Volmerange B., 1984, A&A, 132, 389

Ranalli P., Comastri A., Setti G., 2003, A&A, 399, 39

Reddy N. A., Steidel C. C., 2009, ApJ, 692, 778

Rieke G. H., Lebofsky M. J., 1978, ApJ, 220, L37

Rieke G. H., Alonso-Herrero A., Weiner B. J., Pérez-González P. G., Blaylock M., Donley J. L., Marcillac D., 2009, ApJ, 692, 556

Rieke G. H., et al., 2015, PASP, 127, 584

Roberts M. S., 1963, ARA&A, 50, 149

Robertson B. E., et al., 2013, ApJ, 768, 71

Robertson B. E., Ellis R. S., Furlanetto S. R., Dunlop J. S., 2015, ApJ, 802, L19

Robotham A. S. G., Driver S. P., 2011, MNRAS, 413, 2570

Rogers A. B., et al., 2014, MNRAS, 440, 3714

Rowan-Robinson M., et al., 2016, MNRAS, 461, 1100

Rowlands K., et al., 2018, MNRAS, 473, 1168

Salmon B., et al., 2016, ApJ, 827, 20

Salpeter E. E., 1955, ApJ, 121, 161

Sanders D. B., 2003, Journal of Korean Astronomical Society, 36, 149

Sanders D. B., et al., 2007, ApJS, 172, 86

Santini P., et al., 2015, ApJ, 801, 97

Schaye J., et al., 2010, MNRAS, 402, 1536

Schechter P., 1976, ApJ, 203, 297

Schenker M. A., et al., 2013, ApJ, 768, 196

Schiminovich D., et al., 2005, ApJ, 619, L47

Schreiber C., et al., 2017, A&A, 602, A96

Scott S. E., et al., 2002, MNRAS, 331, 817

Scott S. E., Dunlop J. S., Serjeant S., 2006, MNRAS, 370, 1057

Scoville N., et al., 2007, ApJS, 172, 38

Shibuya T., Kashikawa N., Ota K., Iye M., Ouchi M., Furusawa H., Shimasaku K., Hattori T., 2012, ApJ, 752, 114

Shimasaku K., Ouchi M., Furusawa H., Yoshida M., Kashikawa N., Okamura S., 2005, PASJ, 57, 447

Shimasaku K., et al., 2006, PASJ, 58, 313

Simpson J. M., et al., 2014, ApJ, 788, 125

Simpson J. M., et al., 2017, ApJ, 839, 58

Slipher V. M., 1912, Lowell Observatory Bulletin, 2, 26

Slipher V. M., 1913, Lowell Observatory Bulletin, 2, 56

Slipher V. M., 1914, Popular Astronomy, 22, 19

Slipher V. M., 1915, Popular Astronomy, 23, 21

Slipher V. M., 1917, Lowell Observatory Bulletin, 3, 59

Slipher V. M., 1921, Popular Astronomy, 29, 128

Slipher V. M., 1922, in Publications of the American Astronomical Society. p. 232

Slipher V. M., 1924, Popular Astronomy, 32, 622

Smail I., Ivison R. J., Blain A. W., 1997, ApJ, 490, L5

Smit R., et al., 2015, ApJ, 801, 122

Soifer B. T., Sanders D. B., Madore B. F., Neugebauer G., Danielson G. E., Elias J. H., Lonsdale C. J., Rice W. L., 1987, ApJ, 320, 238

Soifer B. T., et al., 2000, AJ, 119, 509

Spergel D. N., et al., 2003, ApJS, 148, 175

Stach S. M., et al., 2019, arXiv e-prints,

Stacy A., Bromm V., 2014, ApJ, 785, 73

Stark D. P., 2016, ARA&A, 54, 761

Steidel C. C., Hamilton D., 1992, AJ, 104, 941

Steidel C. C., Giavalisco M., Pettini M., Dickinson M., Adelberger K. L., 1996, ApJ, 462, L17

Steidel C. C., Adelberger K. L., Giavalisco M., Dickinson M., Pettini M., 1999, ApJ, 519, 1

Steidel C. C., Adelberger K. L., Shapley A. E., Pettini M., Dickinson M., Giavalisco M., 2000, ApJ, 532, 170

Steidel C. C., Shapley A. E., Pettini M., Adelberger K. L., Erb D. K., Reddy N. A., Hunt M. P., 2004, ApJ, 604, 534

Swinyard B. M., Rieke G. H., Ressler M., Glasse A., Wright G. S., Ferlet M., Wells M., 2004,] 10.1117/12.551223, 5487, 785

Takeuchi T. T., Yoshikawa K., Ishii T. T., 2003, ApJ, 587, L89

Taniguchi Y., et al., 2005, PASJ, 57, 165

Taniguchi Y., et al., 2007, ApJS, 172, 9

Targett T. A., Dunlop J. S., McLure R. J., 2012, MNRAS, 420, 3621

Telesco C. M., Harper D. A., 1980, ApJ, 235, 392

Tinsley B. M., 1968, ApJ, 151, 547

Tomczak A. R., et al., 2014, ApJ, 783, 85

Torrey P., et al., 2015, MNRAS, 454, 2770

Wang L., Pearson W. J., Cowley W., Trayford J. W., Béthermin M., Gruppioni C., Hurley P., Michałowski M. J., 2019, A&A, 624, A98

Wardlow J. L., et al., 2011, MNRAS, 415, 1479

Wells M., et al., 2015, PASP, 127, 646

Whitaker K. E., et al., 2017, ApJ, 838, 19

Wilkins S. M., Feng Y., Di Matteo T., Croft R., Lovell C. C., Waters D., 2017, MNRAS, 469, 2517

Williams C. C., et al., 2018, ApJS, 236, 33

Wuyts S., et al., 2012, ApJ, 753, 114

Wyder T. K., et al., 2005, ApJ, 619, L15

Yung L. Y. A., Somerville R. S., Finkelstein S. L., Popping G., Davé R., 2019, MNRAS, 483, 2983

Zitrin A., et al., 2014, ApJ, 793, L12

van Dokkum P. G., et al., 2015, ApJ, 813, 23